University of Trento

Doctoral Thesis

Simulation of curved-space quantum field theories with two-component Bose-Einstein condensates: from black hole physics to cosmology

Anna Berti

April 2024

University of Trento

Department of Physics

Simulation of curved-space quantum field theories with two-component Bose-Einstein condensates: from black hole physics to cosmology

A thesis submitted to the
Doctoral School of Physics - XXXVI cycle

in fulfillment of the requirements for the degree of
Doctor of Philosophy

by

Anna Berti

April 2024

Supervisors: Dr. Iacopo Carusotto (University of Trento)
Prof. Gabriele Ferrari (University of Trento)

Referees: Prof. Nicolas Pavloff (LPTMS and Universitè Paris-Saclay)
Prof. Roberto Balbinot (University of Bologna)
Prof. Massimiliano Rinaldi (University of Trento)

"*So long, and thanks for all the fish*"

Douglas Adams
(The Hitchhiker's Guide to the Galaxy)

Contents

1 Introduction

In 1981, Unruh [1, 2] suggested the possibility of simulating the dynamics of quantum fields in curved spacetimes through the propagation of sound-waves in moving fluids. Imagine a fish emitting sound while plunging down a waterfall (see Fig.1.1): if the velocity of the fluid exceeds the sound speed, the emitted waves are not able to reach the river at the top of the waterfall. This behaviour is qualitatively *analogous* to that of radiation emitted inside a black hole. In other words, a supersonic flow in a fluid would influence the dynamics of sound similarly to what happens to light when it's dragged by the spacetime geometry in strong gravity environments. This simple yet groundbreaking observation has lead to the beginning of a whole new field of research, nowadays known as *Analog Gravity* [3].

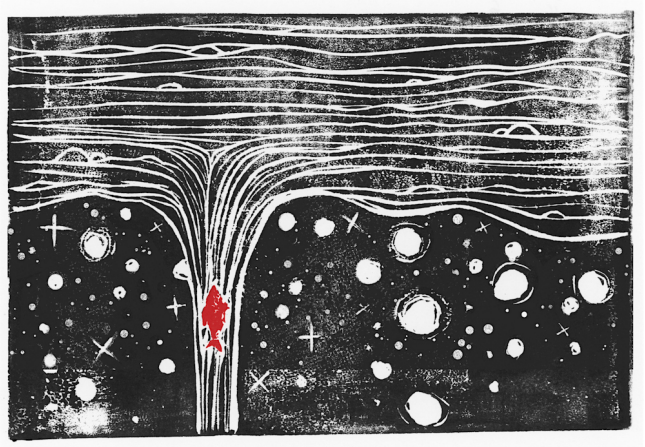

FIGURE 1.1: A fish plunging down a waterfall emits sound waves which cannot reach the river at the top, similarly to light trapped inside a black hole. Credits: Olena Shmahalo (Quanta Magazine).

In quantitative terms, the hydrodynamic equations for a perfect fluid can be cast in the form of the Klein-Gordon equation for a massless scalar field on a curved spacetime, provided the identification of an acoustic metric tensor, which depends on the properties of the fluid. In its original derivation, the analogy is therefore exploited to simulate gravitational processes involving a non-interacting field in a fixed background geometry. Over the years, proposals have been made to take into account effects coming from interactions between the fields and backreaction [4, 5], or even to gain insight on modified theories of gravity, where, for instance, Lorentz invariance is broken or quantum effects cannot be neglected [6, 7].

Although the analogy can be pushed only up to some limit, analog models provide an experimentally accessible platform to study the dynamics of quantum fields and

to gain insight on physical phenomena that escape direct astrophysical investigation, as those occurring in the vicinity of a black hole or during the fast expansion of the early universe.

Curved space-time geometries have been realized in a large variety of systems, including surface waves on classical fluids [8, 9], ultra-cold atoms [10], polariton fluids [11, 12] and optical systems [13]. Thanks to their impressive experimental tunability and superfluid character, atomic Bose-Einstein condensates (BECs) [14, 15] represent one of the most promising analogs. The effective metric associated to a condensate is fully determined by its irrotational velocity flow and by the sound speed for low-frequency elementary excitations, which depends on its density; both these quantities are controlled in space and time via manipulations of the trapping potential and/or of some externally applied electromagnetic fields. It is therefore possible to generate analog black-hole geometries with horizons and ergoregions [10, 12, 16], as well as time-dependent spacetimes, analog to an oscillating [17–20] or expanding [21–23] universe.

In the last decades, the technological advances in the field of ultracold gases have made it possible to experimentally realize and control multicomponent BECs [24]. It is natural to ask whether such mixtures can be exploited as analogs [25–27]: the availability of various branches of elementary excitations with different sound speed and effective mass may in fact lead to advantages in the implementations of interesting geometries and, eventually, thanks to the possibility of coupling the different components, to the exploration of a broader spectrum of physical processes. This Thesis aims to address this question, focusing specifically on coherently-coupled two-component BEC mixtures. We first consider analog geometries that have already been analysed with single-component systems, generalising the results to mixtures and pointing out the differences; we then proceed to tackle problems which instead require the additional degrees of freedom that only a mixture displays.

1.1 Structure of the Thesis

The Thesis is structured as follows: in Chapters 2 and 3 we review the main theoretical tools which are typically used to describe Bose-Einstein condensates (Gross-Pitaevskii and Bogoliubov theories) and use them to derive the most relevant properties of coherently-coupled superfluid mixtures; we also briefly discuss the numerical techniques we exploited to obtain the results of this work.

Chapter 4 is devoted to *analog Hawking radiation*. First predicted by Hawking in 1974 [28, 29], thermal emission from astrophysical black-holes (and their subsequent evaporation) remains one of the most fascinating yet untested phenomena stemming from quantum effects in curved spacetime geometries. Its experimental observation, at least in the analog context, was the main subject of interest for the analog gravity community for many years [30–37]. Curved spacetime configurations mimicking the properties of an event horizon have been realized with a variety of platform [8–13]. The simplest (one-dimensional) analog black-hole configuration for a BEC is obtained by moving a step-like potential through an elongated atomic cloud [10]: the step position marks the location of the analog horizon, namely an interface separating two regions with supersonic and subsonic fluid flow, which represent the interior and

exterior of the black-hole, respectively. Within this setup, it has been shown that spontaneous Hawking radiation can be detected through equal-time correlations of density perturbations emitted on the two sides of the horizon [38, 39]: a first experimental measurement was performed in 2016 [40], and then improved in the following years [41, 42]. So far, Hawking emission has escaped observation in any other analog system, as well as in the astrophysical context. Its elusive nature resides in the weakness of the signal with respect to any source of noise.

We analyse Hawking radiation emitted from a spin-sonic horizon in an unpolarized binary mixture in the simplest one-dimensional geometry considered in previous literature [43–45]. Our purpose is twofold: from a conceptual point of view, contrary to the case of a single-component systems, spin excitations in binary mixtures can be made massive in the presence of a coherent coupling, with the mass being tunable through the Rabi frequency; moreover, the experimental accessibility of additional degrees of freedom, such as the relative phase between the two components, opens the possibility of identifying observables in which the intensity of the Hawking signal overcomes by orders of magnitude that of the typical *mustache* observed in density correlations, thus potentially facilitating experimental measurements.

In Chapter 5 we consider two-dimensional analog black-hole geometries, which can be realised through draining vortices [12]. With respect to the one-dimensional configuration discussed above, vortices allow to analyse the effect of rotation: in formal terms, the analog metric of the system can display both an horizon and an ergoregion. In the gravitational context, spacetimes with an ergoregion (such as Kerr black-holes) are predicted to superradiate [46, 47], namely to lose rotational energy via the amplified reflection of incoming radiation, similarly to what happens with electromagnetic waves impinging on a rotating cylinder [48]. Although pioneering experiments have lead to the experimental measurement of superradiant amplification on several classical platforms [49–51], other superradiance-related phenomena still remain untested.

In the presence of reflecting boundaries on either side of the ergosurface, self-stimulated superradiance gives rise to dynamical instabilities [52–54]: from a microscopic perspective, these can be interpreted as the excitation of exponentially growing modes either inside or outside the ergoregion. For astrophysical black-holes, instabilities might arise if the horizon does not behave as a perfectly absorbing surface, or if the black-hole is surrounded by an accretion disk. In the analog context, this translates into the absence of a drain term or the confinement of the condensate by some trapping potential. Both these conditions are naturally realized in atomic BECs, that indeed represent, at least in principle, the ideal platform to study analog superradiant instabilities [55].

Numerical studies [56] on the stability of vortex configurations in single-component condensates have shown that analog ergoregion instabilities are always associated to high-frequency modes that evolve into splitting or displacement of the vortex itself. The development of such instabilities is however challenging to observe experimentally, due to the small size of the vortex, typically comparable with the imaging resolution, and to the vanishing atomic density in the vortex core.

In this Thesis we extend the same numerical analysis to binary mixtures. Two-component condensates have two independent branches of elementary excitations, associated to perturbations of the total density and of the relative density, featuring with different values of the speed of sound and of the healing length [57]. Thanks to this additional degree of freedom, as well as to the availability of interferometric techniques based on a coherent mixing of the two components which allow to image all quadratures of the quantum field, we expect both conceptual and practical advantages with respect to the single-component case. Indeed, within some parameters' range, we find anomalous low-frequency modes that not only are associated with a much larger ergoregion and thus easier to access in experiments, but also involve, at long times, phononic emission from the ergosurface rather that vortex deformation, in closer analogy with the expected behaviour in the astrophysical context.

Chapter 6 is devoted to a prediction of quantum field theory with relevant applications to cosmology, known as *false vacuum decay* (FVD), that has recently attracted the attention of the analog gravity community [58–68]. The term *false vacuum decay* refers to the decay of a quantum field from a metastable state (or false vacuum) to its ground state (or true vacuum), triggered by quantum or thermal fluctuations [69–71]. In an extended system the tunnelling process is expected to occur locally through the formation of one or more bubbles of true vacuum, which then expand in time while releasing energy.

According to the latest measurements of the Higgs boson mass, the standard model predicts the Higgs field to be in a metastable state of the Higgs potential [72–74], so our Universe could (and eventually will) be annihilated by a FVD process. While the decay rate is believed to be extremely small at present times, the metastability of electroweak vacuum has strong implications on cosmological models describing the inflationary and post-inflationary phases, due to the presence of additional mechanisms that could have triggered FVD in the Early Universe [75], such as high temperatures and fast accelerated expansion. Inflation itself might have been the the result of a false vacuum decay process: if this was the case, signatures of it might be found in the cosmic microwave background (CMB) spectrum [76]. In general however, an experimental observation of FVD in the astrophysical context seems extremely challenging.

Here, we discuss the realization of thermally-induced false vacuum decay with a coherently-coupled two-component mixture. The project was carried on within a collaboration with the experimental group at the Pitaevskii BEC Center and Ian Moss (and collaborators), from the University of Newcastle; in this Thesis we will focus on the numerical analysis of the problem, which was our main contribution to this work.

One of the basic ingredients to observe false vacuum decay is a mean-field energy landscape with an asymmetric double-well profile: absolute and relative minimum of the potential represent the true and false vacuum states, respectively. The most natural way to achieve this is to exploit spontaneous symmetry-breaking in a system in the vicinity of a phase transition. Coherently-coupled BEC mixtures display a magnetic quantum phase transition [77]: hence their mean-field energy can be engineered to have a double well profile, whose shape is controllable by changing the strength and detuning of the coherent coupling. The tunability of the double-well potential makes it possible to determine how the tunnelling time depends on the height of the

potential barrier between the two minima, and compare the numerical results both with the theoretical prediction and the experimental data.

The last Chapter 7 is devoted to concluding remarks and to a brief discussion of future perspectives in the field.

2 Bose-Einstein condensates as gravitational analogs

Bose-Einstein condensation was first predicted by Einstein in 1925, building upon an idea of Bose: when a dilute and non-interacting gas of bosons is cooled down to temperatures close to the absolute zero, a phase transition takes place, with the ordered phase being characterized by a macroscopic occupation of the lowest-energy single-particle state. The resulting phase coherence and long-range order make BECs the ideal platform to study quantum effects on a macroscopic scale.

Over the years the theoretical description of Bose-Einstein condensation has been extended to include the presence of interactions and confinement, as well as to mixtures and photonic systems [14, 78]. The first experimental observation of an atomic BEC dates back to 1995 [79, 80]; since then the technological advances in the field have allowed to realize condensation with various atomic species, molecules and photons, to manipulate both the strength and range of interactions, and to accurately control the confining potentials to engineer arbitrary geometries and configurations.

The relatively simple theoretical description of these systems, together with the remarkable level of control in experiments, make Bose-Einstein condensates a powerful platform in the study or simulation of a wide variety of physical phenomena.

2.1 The Gross-Pitaevskii equation

The main theoretical tools we will be using throughout the Thesis are Gross-Pitaevskii and Bogoliubov theory, that is, the mean-field description of a BECs and its lowest-order quantum correction. All the results that we present in this section can be found in Refs. [14, 15]. Both Gross-Pitaevskii and Bogoliubov theory rely on the same set of assumptions, that we list and discuss in the following:

(a) Since Bose-Einstein condensation, as all phase transitions, occurs only in the thermodynamic limit, the number of atoms N has to be macroscopically large;

(b) We consider *dilute* and *weakly interacting* gases: this condition guarantees that only contact two-body interactions take place and that the only relevant parameter describing such interactions is the s-wave scattering length a. Hence, the full quantum Hamiltonian of the system reads:

$$\hat{H} = \int \mathrm{d}\mathbf{r}\hat{\Psi}^\dagger(\mathbf{r}) \left[-\frac{\hbar^2}{2m}\nabla^2 + V(\mathbf{r}) + \frac{g}{2}\hat{\Psi}^\dagger(\mathbf{r})\hat{\Psi}(\mathbf{r}) \right] \hat{\Psi}(\mathbf{r}) \tag{2.1}$$

where $\hat{\Psi}(\mathbf{r})$ is a complex quantum field, $g \equiv 4\pi\hbar^2 a/m$ is referred to as interaction constant, m is the atomic mass and $V(\mathbf{r})$ the confining external potential. From

(2.1) one can easily derive an Heisenberg equation for the field:

$$i\hbar\frac{\partial\hat{\Psi}}{\partial t} = [\hat{\Psi}(\mathbf{r}), \hat{H}] = \left[-\frac{\hbar^2}{2m}\nabla^2 + V(\mathbf{r}) + g\hat{\Psi}^\dagger(\mathbf{r})\hat{\Psi}(\mathbf{r})\right]\hat{\Psi}(\mathbf{r}) \tag{2.2}$$

by exploiting the canonical commutation relation $[\hat{\Psi}(\mathbf{r}), \hat{\Psi}^\dagger(\mathbf{r}')] = \delta(\mathbf{r}-\mathbf{r}')$.

(c) Temperature T is much lower than the condensation temperature, so that the number of condensed particles $N_0 = \langle\hat{a}_0^\dagger\hat{a}_0\rangle$ ($\hat{a}_0$ being the annihilation operator for the lowest-energy single-particle state) is much larger than the number of non-condensed particles $\delta N = N - N_0 \ll N_0$.

(d) The crucial point in the theoretical derivation is the so-called *Bogoliubov prescription*, namely the substitution of $\hat{a}_0$ with a complex number $\sqrt{N_0}e^{i\alpha}$, where N_0 is the (macroscopic) occupation of the lowest-energy single-particle state and α is an arbitrary phase. Such a replacement is justified as follows: the operatorial nature of $\hat{a}_0, \hat{a}_0^\dagger$ stands in their commutator being non-zero, that is $\langle\hat{a}_0^\dagger a_0\rangle = N_0 \neq N_0 + 1 = \langle\hat{a}_0\hat{a}_0^\dagger\rangle$; however, in the limit of macroscopic occupation of the lowest-energy state $N_0 \to \infty$, the difference between the two averages becomes negligible and $\hat{a}_0$ can be treated as a number.

More rigorously, we are assuming that the average value of the annihilator operator $\langle\hat{a}_0\rangle$ over the state of the system is non-zero below the critical temperature: this is straightforwardly verified if the condensate is in a coherent state, characterized by a well-defined phase rather than a well-defined particle number. Such phase locking is responsible for the spontaneous symmetry breaking of Gauge symmetry at the BEC phase transition.

Based on the above assumptions, let us separate the condensed and non-condensed components of the field: $\hat{\Psi}(\mathbf{r}) = \sqrt{N_0}\psi(\mathbf{r}) + \delta\hat{\Psi}(\mathbf{r})$, where $\psi(\mathbf{r})$ is the lowest-energy single particle wavefunction, orthogonal to $\delta\hat{\Psi}$. Expansion of the full Hamiltonian (2.1) up to second order in $\delta\hat{\Psi}$ leads to the result:

$$\hat{H} = E + \delta E^{(2)} + \hat{H}^{(1)} + \hat{H}^{(2)} + O\Big(\frac{\delta N}{N}\Big) \tag{2.3}$$

The first term of the expansion is the Gross-Pitaevskii mean-field energy contribution:

$$E = N\int \mathrm{d}\mathbf{r}\left[\frac{\hbar^2}{2m}|\vec{\nabla}\psi|^2 + V|\psi|^2 + \frac{N}{2}g|\psi|^4\right] \tag{2.4}$$

It can be obtained directly by replacing the field operator with a classical wavefunction, thus neglecting both thermal and quantum depletion of the condensate. A second order correction $\delta E^{(2)}$ to this mean field energy can be computed, but is typically discarded since it is neither dependent on the field perturbation $\delta\hat{\Psi}$ nor extensive with respect to N. With the same replacement of the field $\hat{\Psi}$ with the wavefunction $\sqrt{N}\psi$, one derives, from Eq.(2.2), the Gross-Pitaevskii (GP) equation:

$$i\hbar\frac{\partial\psi}{\partial t} = \left[-\frac{\hbar^2}{2m}\nabla^2 + V + gN|\psi|^2\right]\psi := \mathcal{H}\psi \tag{2.5}$$

Stationary solutions fulfil $\mathcal{H}\psi = \mu\psi$, where μ is the chemical potential of the system:

$$\mu = \frac{\partial E}{\partial N} = \int \mathrm{d}\mathbf{r} \left[\frac{\hbar^2}{2m}|\nabla\psi|^2 + V|\psi|^2 + gN|\psi|^4\right] = \int \mathrm{d}\mathbf{r}\psi^*\mathcal{H}\psi \tag{2.6}$$

As expected, stationary solutions are also minima of the energy functional: indeed, if we assume the time-independent Gross-Pitaevskii equation is fulfilled, the linear contribution $\hat{H}^{(1)}$ vanishes due to the orthogonality of ψ and $\delta\hat{\Psi}$:

$$\hat{H}^{(1)} = \sqrt{N}\int \mathrm{d}\mathbf{r}\big(\mathcal{H}\psi\big)\delta\hat{\Psi}^\dagger + \text{h.c.} = \sqrt{N}\mu\int \mathrm{d}\mathbf{r}\psi\delta\hat{\Psi}^\dagger + \text{h.c.} = 0 \tag{2.7}$$

2.2 Bogoliubov theory

Bogoliubov theory builds up on the next order of approximation, which coincides with the quadratic terms in the field perturbation:

$$\hat{H}^{(2)} = \frac{1}{2}\int \mathrm{d}\mathbf{r}\big(\delta\hat{\Psi}^\dagger, \delta\hat{\Psi}\big)\sigma_3\mathcal{L}[\psi]\begin{pmatrix}\delta\hat{\Psi}\\ \delta\hat{\Psi}^\dagger\end{pmatrix} \tag{2.8}$$

where $\sigma_3 = \mathrm{diag}(1,-1)$ is the third Pauli matrix and the $\mathcal{L}$ is the *Bogoliubov matrix*:

$$\mathcal{L}[\psi] = \begin{pmatrix}\mathcal{H} + gN|\psi|^2 - \mu & gN\psi^2\\ -gN\psi^{*2} & -(\mathcal{H} + gN|\psi|^2 - \mu)\end{pmatrix} \tag{2.9}$$

It is worth noticing that the Bogoliubov matrix is *pseudo-hermitian*, since $\mathcal{L}^\dagger = \sigma_3\mathcal{L}\sigma_3$. This has interesting implications on its spectrum, which will be discussed later. Moreover, it guarantees that the Hamiltonian is hermitian, $\sigma_3\mathcal{L} = \mathcal{L}^\dagger\sigma_3$.

The equation of motion for the field perturbations is derived either by linearizing (2.2) or as the Heisenberg equation associated to the Hamiltonian $\hat{H}^{(2)}$ in Eq. (2.8):

$$i\hbar\frac{\partial}{\partial t}\begin{pmatrix}\delta\hat{\Psi}\\ \delta\hat{\Psi}^\dagger\end{pmatrix} = \mathcal{L}[\psi]\begin{pmatrix}\delta\hat{\Psi}\\ \delta\hat{\Psi}^\dagger\end{pmatrix} \tag{2.10}$$

Stationary solutions of this equation coincide with the eigenstates of the Bogoliubov matrix and therefore diagonalize the Bogoliubov Hamiltonian $\hat{H}^{(2)}$. To prove this, it is convenient to write the field perturbations in terms of single-particle creation/annihilation operators $\hat{a}_\lambda, \hat{a}_\lambda^\dagger$: let λ be a set of quantum numbers labelling single-particle states, and $\lambda = 0$ indicate the lowest-energy one. Moreover, let us expand the field perturbation in terms of *quasi-particle* creation/annihilation operators:

$$\delta\hat{\Psi}(\mathbf{r},t) = \sum_{\lambda\neq 0}\psi_\lambda(\mathbf{r},t)\hat{a}_\lambda := \sum_{\lambda\neq 0}\Big[u_\lambda(\mathbf{r},t)\hat{b}_\lambda + v_\lambda^*(\mathbf{r},t)\hat{b}_{-\lambda}^\dagger\Big] \tag{2.11}$$

where u_λ, v_λ are usually referred to as the particle and antiparticle components of the mode. With this expansion, we transfer the space and time dependence of $\delta\hat{\Psi}$ to the

spinor $(u_\lambda, v_\lambda)^\top$, so that Eq.(2.10) translates to:

$$i\hbar\frac{\partial}{\partial t}\begin{pmatrix}u_\lambda\\ v_\lambda\end{pmatrix} = \mathcal{L}[\psi]\begin{pmatrix}u_\lambda\\ v_\lambda\end{pmatrix} \tag{2.12}$$

These are known as Bogoliubov-de Gennes equations. They can also be obtained from a linearization of the Gross-Pitaevskii equations by expanding the order parameter as $\psi \to \psi + \delta\psi$, with

$$\delta\psi(\mathbf{r},t) = \sum_{\lambda\neq 0}\left[u_\lambda(\mathbf{r},t) + v^*_\lambda(\mathbf{r},t)\right]e^{-i\mu t/\hbar} \tag{2.13}$$

Moreover, if we expand the Gross-Pitaevskii energy functional keeping only up to quadratic terms in $\delta\psi$, we get the same expression as (2.8), provided the substitution of the field perturbation with the wave-function variation, $\delta\hat{\Psi} \to \sqrt{N}\delta\psi$.

Note that the expansion of the field perturbation as in (2.11), or equivalently (2.13), allows to transfer the normalization and orthogonality condition from the field to the spinor (u_λ, v_λ). In particular, if:

$$\langle\psi_\lambda|\sigma_3|\psi_{\lambda'}\rangle := \int \mathrm{d}\mathbf{r}\Big[u^*_\lambda(\mathbf{r})u_{\lambda'}(\mathbf{r}) - v^*_{-\lambda}(\mathbf{r})v_{-\lambda'}(\mathbf{r})\Big] \tag{2.14}$$

is the Bogoliubov inner product, the spinor components must satisfy $\langle\psi_\lambda|\sigma_3|\psi_{\lambda'}\rangle = 0$ for all $\lambda \neq \lambda'$ and $\langle\psi_\lambda|\sigma_3|\psi_\lambda\rangle[\hat{b}_\lambda, \hat{b}^\dagger_\lambda] = 1$. Despite being a conserved quantity during the time evolution, the Bogoliubov product is not positive-definite; collective excitations can therefore be classified into positive- and negative-norm modes: while the former fulfil canonical commutation relations, for the latter the role of creation and annihilation operators is exchanged. In physical terms, this means that creating a quasi-particle with positive energy is equivalent to destroying one with negative energy, and vice-versa.

The quadratic hamiltonian $\hat{H}^{(2)}$ can be expressed in terms of creation/annihilation operators for quasi-particle excitations:

$$\hat{H}^{(2)} = \frac{1}{2}\sum_{\lambda,\lambda'\neq 0}(\hat{b}^\dagger_\lambda, \hat{b}_\lambda)\begin{pmatrix}\varepsilon_{\lambda\lambda'} & f^*_{\lambda\lambda'}\\ f_{\lambda\lambda'} & \varepsilon^*_{\lambda\lambda'}\end{pmatrix}\begin{pmatrix}\hat{b}_{\lambda'}\\ \hat{b}^\dagger_{\lambda'}\end{pmatrix} \tag{2.15}$$

where the diagonal and off-diagonal coefficients are:

$$\varepsilon_{\lambda\lambda'} = i\hbar\int \mathrm{d}\mathbf{r}\left(u^*_\lambda\frac{\partial u_{\lambda'}}{\partial t} - v^*_{-\lambda}\frac{\partial v_{-\lambda'}}{\partial t}\right) \tag{2.16}$$

$$f_{\lambda\lambda'} = i\hbar\int \mathrm{d}\mathbf{r}\left(v_{-\lambda}\frac{\partial u_{\lambda'}}{\partial t} - u_\lambda\frac{\partial v_{-\lambda'}}{\partial t}\right) \tag{2.17}$$

Let us now assume the spinor (u_λ, v_λ) is an eigenstate of the Bogoliubov matrix $\mathcal{L}$ with eigenvalue $\hbar\omega_\lambda$; the off-diagonal contributions due to $f_{\lambda\lambda'}$, after being summed over λ, λ' vanish, while the diagonal coefficients simplify to $\varepsilon_{\lambda\lambda'} = \hbar\omega_\lambda\langle\psi_\lambda|\sigma_3|\psi_\lambda\rangle\delta_{\lambda\lambda'}$.

Hence, eigenstates of the Bogoliubov matrix diagonalize the Bogoliubov Hamiltonian:

$$\hat{H}^{(2)} = \sum_{\lambda\neq 0} \hbar\omega_\lambda \langle\psi_\lambda|\sigma_3|\psi_\lambda\rangle \left(\hat{b}_\lambda^\dagger \hat{b}_\lambda + \frac{1}{2}\right) := \sum_{\lambda\neq 0} E_\lambda \left(\hat{b}_\lambda^\dagger \hat{b}_\lambda + \frac{1}{2}\right) \tag{2.18}$$

Notice how the energy E_λ of a mode is given by the product between its norm and its frequency. Therefore, the nature of elementary excitations over a stationary BEC depends on the spectral properties of the Bogoliubov matrix $\mathcal{L}$. As already mentioned, it is not hermitian: as a consequence, its eigenvalues are not necessarily real. However pseudo-hermiticity guarantees that, for each eigenmode:

$$(\omega_\lambda - \omega_\lambda^*)\langle\psi_\lambda|\sigma_3|\psi_\lambda\rangle = 0 \tag{2.19}$$

Modes with positive or negative norm are necessarily associated to a real eigenvalue. For each positive-norm mode $(u_\lambda, v_\lambda)^\top$ with frequency ω_λ there exist a negative-norm mode $(v_\lambda^*, u_\lambda^*)^\top$ with frequency $-\omega_\lambda$: the two correspond to the same physical oscillation and have the same energy E_λ. Such redundancy, also referred to as *particle-hole symmetry*, is due to the expansion (2.11) and is easily cured by either including in the sum only modes with positive frequency, but both norm signs, or vice-versa (only positive norm, but both frequency signs).

According to (2.18), the energy of each eigenmode is given by the product between its eigenfrequency $\hbar\omega_\lambda$ and its norm. If ψ is the ground state, all excitations on top of it must have positive energy: the class of positive (negative) norm modes coincides with the class of positive (negative) frequency modes. The presence of an excitation with negative energy (that is, norm and frequency of different signs) is the signal of an energetic or thermodynamical instability: these modes cannot be excited in an energy-conserving setup, but would destabilize the system if dissipation was included in the GP equation and the system let to thermalize.

Remarkably, Eq.(2.19) suggests that modes with complex frequency can exist if they have zero norm. Due to the pseudo-hermiticity of $\mathcal{L}$, these modes come in pseudo-degenerate pairs with complex-conjugates frequencies: such excitations are either exponentially growing or suppressed in time. Hence, their existance signals a dynamical instability of the system in the state ψ. Dynamically unstable modes can be populated even in the absence of dissipation, since they carry zero energy. Physically, they correspond to the simultaneous excitation of modes with opposite energy.

2.2.1 The homogeneous condensate

The simplest configuration that can be discussed using the above formalism is the uniform condensate in a box of volume V. The ground state of the system is described by $\psi(\mathbf{r}, t) = e^{-i\mu t/\hbar}/\sqrt{V}$, where $\mu = gn$ is the chemical potential and $n = N/V$ is the condensate density. The mean field energy is $E = gNn/2$. Elementary excitations are plane waves with wavevector $\mathbf{k}$, so that $(u_\lambda, v_\lambda)^\top = (U_k, V_k)^\top e^{i\mathbf{k}\cdot\mathbf{r}}/\sqrt{V}$. Notice that U_k, V_k are now constants in both space and time and depend only on $k = |\mathbf{k}|$. Since the kinetic energy operator becomes a multiplicative factor, $-\nabla^2 = k^2$, the

Bogoliubov matrix takes the simple form:

$$\mathcal{L} = \begin{bmatrix} \hbar^2 k^2/2m + \mu & \mu \\ -\mu & -\left(\hbar^2 k^2/2m + \mu\right) \end{bmatrix} \tag{2.20}$$

Its diagonalization is straightforward and gives the well-known *Bogoliubov dispersion*:

$$(\hbar\omega_k)^2 = \frac{\hbar^2 k^2}{2m}\left(\frac{\hbar^2 k^2}{2m} + 2\mu\right) \tag{2.21}$$

There exist a positive- and a negative-frequency eigenvalue, whose associated Bogoliubov spinors $(U_k, V_k)^\top$ have positive and negative norm, respectively. Each branch has phononic behaviour at low momenta, with speed of sound $c = \sqrt{\mu/m}$, and a particle-like behaviour at high momenta. The threshold between the two regimes is found at $k \sim 1/\xi$, where $\xi = \hbar/mc$ is the healing length of the condensate.

The Bogoliubov norm simplifies to $\langle\psi_{\mathbf{k}}|\sigma_3|\psi_{\mathbf{k}}\rangle = |U_k|^2 - |V_k|^2 = \pm 1$: the Bogoliubov transformations, which relate particle to quasi-particle operators:

$$\hat{a}_{\mathbf{k}} = U_k \hat{b}_{\mathbf{k}} + V_k^* \hat{b}^\dagger_{-\mathbf{k}} \tag{2.22}$$

are therefore hyperbolic rotations or, equivalently, squeezing transformations. The diagonal and off-diagonal terms appearing in the expansion (2.15) of $\hat{H}^{(2)}$ are:

$$\varepsilon_{\mathbf{k}\mathbf{k}'} = \left[\frac{\hbar^2 k^2}{2m}\left(|U_k|^2 + |V_k|^2\right) + \mu|U_k + V_k|^2\right]\delta_{\mathbf{k}\mathbf{k}'} := \varepsilon_k\,\delta_{\mathbf{k}\mathbf{k}'} \tag{2.23}$$

$$f_{\mathbf{k}\mathbf{k}'} = \left[\frac{\hbar^2 k^2}{m} U_k V_k + \mu(U_k + V_k)^2\right]\delta_{\mathbf{k},-\mathbf{k}'} := f_k\,\delta_{\mathbf{k},-\mathbf{k}'} \tag{2.24}$$

As expected, only terms fulfilling momentum conservation survive, leading to:

$$\hat{H}^{(2)} = \frac{1}{2}\sum_{\mathbf{k}\neq 0} (\hat{b}^\dagger_{\mathbf{k}}, \hat{b}_{-\mathbf{k}}) \begin{pmatrix} \varepsilon_k & f_k^* \\ f_k & \varepsilon_k \end{pmatrix} \begin{pmatrix} \hat{b}_{\mathbf{k}} \\ \hat{b}^\dagger_{-\mathbf{k}} \end{pmatrix} \tag{2.25}$$

In order to diagonalize this Hamiltonian, we choose the spinor components such that $f_k = 0$ and $\varepsilon_k = \hbar\omega_k$. Such requirements are satisfied if $2U_kV_k = -\mu/\hbar\omega_k$ and:

$$\mathcal{S}(k) := (U_k + V_k)^2 = \frac{\hbar^2 k^2}{2m\hbar\omega_k} = \sqrt{\frac{\hbar^2 k^2/2m}{\hbar^2 k^2/2m + \mu}} \tag{2.26}$$

The quantity $\mathcal{S}(k)$ is called *structure factor* of the condensate, and it describes the response of the system to density perturbations: it vanishes linearly with k at small momenta ($k < 1/\xi$), while it tends to a unit constant value for high-momentum modes.

The Heisenberg equations associated to (2.25), governing the dynamics of quasi-particle creation/annihilation operators, are:

$$i\hbar\frac{\partial}{\partial t}\begin{pmatrix} \hat{b}_{\mathbf{k}} \\ \hat{b}^\dagger_{-\mathbf{k}} \end{pmatrix} = \begin{pmatrix} \varepsilon_k & f_k^* \\ -f_k & -\varepsilon_k \end{pmatrix} \begin{pmatrix} \hat{b}_{\mathbf{k}} \\ \hat{b}^\dagger_{-\mathbf{k}} \end{pmatrix} \tag{2.27}$$

If the Hamiltonian is diagonalized by the choice of $\{U_k, V_k\}$, the result is trivially an oscillation at frequency ω_k^+.

2.3 The gravitational analogy

All the results derived in the previous Section can be expressed in terms of density and phase of the condensate and their perturbations [14, 15]. This will allow to describe a condensate in terms of generalized hydrodynamic equations, which are at the basis of the gravitational analogy. If we write the order parameter in the Madelung representation as $\sqrt{N}\psi = \sqrt{n}\exp(i\phi)$, the mean field energy of the condensate reads:

$$E = \int \mathrm{d}\mathbf{r} \left[\frac{\hbar^2}{2m} \left(\vec{\nabla}\sqrt{n}\right)^2 + \frac{\hbar^2 n}{2m} \left(\vec{\nabla}\phi\right)^2 + Vn + \frac{1}{2} g n^2 \right] \tag{2.28}$$

and the real and imaginary parts of the Gross-Pitaevskii equations translate to:

$$\frac{\partial n}{\partial t} + \vec{\nabla}\left(n \frac{\hbar}{m} \vec{\nabla}\phi \right) = 0 \tag{2.29}$$

$$\hbar \frac{\partial \phi}{\partial t} + \frac{\hbar^2}{2m} \left(\vec{\nabla}\phi\right)^2 + V + gn = \frac{\hbar^2}{2m} \frac{\nabla^2\sqrt{n}}{\sqrt{n}} \tag{2.30}$$

It is worth mentioning that, if we treat the quantity in squared brackets of (2.28) as a classical Hamiltonian density, n and $\hbar\phi$ behave as canonically conjugated variables: Eqs.(2.29), (2.30) can indeed be derived as Lagrange equations from (2.28).

Eq.(2.29) is a continuity equation for the total density if we define the (irrotational) velocity flow of the condensate as $\mathbf{v} = (\hbar/m)\vec{\nabla}\phi$. Consistently, $n\mathbf{v}$ is the quantum mechanical current associated to the state ψ. Eq.(2.30) can be written as:

$$m \left[\partial_t + \mathbf{v} \cdot \vec{\nabla} \right] \mathbf{v} + \vec{\nabla}\left(V + gn\right) = \frac{\hbar^2}{2m} \vec{\nabla} \left(\frac{\nabla^2\sqrt{n}}{\sqrt{n}} \right) := P \tag{2.31}$$

and is analogous to the Euler equation for a perfect fluid subject to an external force. The additional term P is typically called *quantum pressure* since it is the only term in which $\hbar$ appears explicitly. The limit in which quantum pressure can be ignored is referred to as *hydrodynamic regime*.

At linear order, small perturbations of density and phase represent the real and imaginary part of the wave-function perturbation $\delta\psi$:

$$\delta\psi = \psi \left(\frac{\delta n}{2n} + i\delta\phi \right) := \psi \left(\varepsilon_1 + i\varepsilon_2 \right) \tag{2.32}$$

The Bogoliubov-de Gennes equations (2.12) translate to:

$$\begin{pmatrix} \partial_t + \mathbf{v} \cdot \vec{\nabla} & -\mathcal{D} \\ 2gn/\hbar + \mathcal{D} & \partial_t + \mathbf{v} \cdot \vec{\nabla} \end{pmatrix} \begin{pmatrix} \varepsilon_1 \\ \varepsilon_2 \end{pmatrix} = 0 \tag{2.33}$$

where the operator appearing on the off-diagonal terms is:

$$\mathcal{D}(\cdot) = -\frac{\hbar}{2mn}\vec{\nabla}\left[n\vec{\nabla}(\cdot)\right] \tag{2.34}$$

In the case of a uniform background ($\vec{\nabla}n = 0$), $\hbar\mathcal{D}$ coincides with the kinetic energy operator. Moreover, since the perturbations $\varepsilon_1, \varepsilon_2$ can be expanded in plane waves, Eqs.(2.33) become algebraic: $\partial_t \to -i\omega_k$, $\vec{\nabla} \to i\mathbf{k}$, $\mathcal{D} \to \hbar k^2/2m$. Their solution gives the Bogoliubov dispersion relation for a condensate moving at velocity $\mathbf{v}$: as expected, the only difference with respect to (2.21) is a Doppler shift of the frequencies: $\omega_k \to \omega_k - \mathbf{k}\cdot\mathbf{v}$.

The second equation of the system (2.33) is, once again, an Euler equation for a perfect fluid provided the term $\mathcal{D}\varepsilon_1$, coming from the linearization of quantum pressure, is negligible, that is, $\hbar\mathcal{D}\varepsilon_1 \ll 2gn\varepsilon_1$. Such condition is satisfied if δn varies over length scales larger than the healing lenght of the condensate ξ, namely for long-wavelength perturbations. In what follows we show that, within this hydrodynamic regime, the Bogoliubov equations (2.33) can be cast in the form of Klein-Gordon equations for a scalar massless field in a curved spacetime, with the speed of light replaced by the speed of sound in the condensate $c = \sqrt{gn/m}$.

The proof of the gravitational analogy starts from the definition of a four dimensional tensor and its inverse [3]:

$$f_{\mu\nu} = \frac{1}{n}\begin{pmatrix} -(c^2 - |\mathbf{v}|^2) & -\mathbf{v}^\top \\ -\mathbf{v} & \mathbb{I} \end{pmatrix} \qquad f^{\mu\nu} = \frac{n}{c^2}\begin{pmatrix} -1 & -\mathbf{v}^\top \\ -\mathbf{v} & c^2\mathbb{I} - \mathbf{v}\mathbf{v}^\top \end{pmatrix} \tag{2.35}$$

where $(\mathbf{v}\mathbf{v}^\top)_{ij} = v_i v_j$. Let us then compute the following quantity:

$$\partial_\mu\left[f^{\mu\nu}\partial_\nu\varepsilon_2\right] = -\left(\partial_t + \vec{\nabla}\cdot\mathbf{v}\right)\left[\frac{n}{c^2}\left(\partial_t + \mathbf{v}\cdot\vec{\nabla}\right)\varepsilon_2\right] + \vec{\nabla}\cdot\left[n\vec{\nabla}\varepsilon_2\right] \tag{2.36}$$

where $(\vec{\nabla}\cdot\mathbf{v})(x) = \vec{\nabla}(\mathbf{v}x) = \mathbf{v}\cdot\vec{\nabla}x + x(\vec{\nabla}\cdot\mathbf{v})$. According to the Bogoliubov equation for the phase perturbation, we can replace $(\partial_t + \mathbf{v}\cdot\nabla)\varepsilon_2 = -(2gn/\hbar)\varepsilon_1 = -(2mc^2/\hbar)\varepsilon_1$:

$$\partial_\mu\left[f^{\mu\nu}\partial_\nu\varepsilon_2\right] = \frac{2m}{\hbar}\left[\left(\partial_t + \vec{\nabla}\cdot\mathbf{v}\right)(n\varepsilon_1) - n\mathcal{D}\varepsilon_2\right] = \tag{2.37}$$

$$= \frac{2m}{\hbar}\varepsilon_1\left[\partial_t n + \vec{\nabla}\cdot(n\mathbf{v})\right] + \frac{2m}{\hbar}n\left[\left(\partial_t + \mathbf{v}\cdot\vec{\nabla}\right)\varepsilon_1 - \mathcal{D}\varepsilon_2\right] \tag{2.38}$$

The first square bracket vanishes thanks to the continuity equation (2.29) for the total density, while the second one is zero due to the Bogoliubov equation for ε_1:

$$\partial_\mu\left[f^{\mu\nu}\partial_\nu\varepsilon_2\right] = 0 \tag{2.39}$$

The final result is therefore a Klein-Gordon equation for a massive field in a curved spacetime if we define the analog inverse metric so that $\sqrt{-g}g^{\mu\nu} = f^{\mu\nu}$, g being the determinant of $g_{\mu\nu} = \sqrt{-g}f_{\mu\nu}$. The value of g can be easily determined by solving:

$$\det(f^{\mu\nu}) = \left(\sqrt{-g}\right)^4 g^{-1} = -\left(\sqrt{-g}\right)^2 = -n^4/c^2 \tag{2.40}$$

which implies $\sqrt{-g} = n^2/c$. The analog metric takes then the form:

$$g_{\mu\nu} = \frac{n}{c}\begin{pmatrix} -(c^2 - |\mathbf{v}|^2) & -\mathbf{v}^\top \\ -\mathbf{v} & \mathbb{I} \end{pmatrix} \tag{2.41}$$

and the Klein-Gordon equation reads:

$$\frac{1}{\sqrt{-g}}\partial_\mu\left[\sqrt{-g}g^{\mu\nu}\partial_\nu\varepsilon_2\right] = 0 \tag{2.42}$$

The phase perturbation $\varepsilon_2 := \delta\phi$ plays the role of a massless (possibly quantum) field propagating on a curved spacetime, whose geometry is fully determined by the velocity of the condensate flow and by the speed of sound.

The analogy between Eq. (2.33) and Eq. (2.42) is the core idea behind Analog Gravity: the density and phase of the order parameter, which determine the speed of sound and velocity flow of the condensate, can be manipulated in space and time to simulate geometries of interest. However, it is worth pointing out that the gravitational analogy has limitations. The major one resides evidently in the validity of the hydrodynamic approximation: the quantum pressure term is safely neglected only for perturbations whose wavelength is larger than the healing length ξ, that is, phononic excitations. Strictly speaking, we are restricted to the analysis of physical phenomena in which the dynamics is dominated by low-frequency modes.

Another assumption that was made to get to Eq. (2.33) is the linearization of the Gross-Pitaevskii equations: we considered perturbations which are small enough to not perturb the background order parameter of the condensate. In other words, we can simulate the dynamics of fields on top of a fixed spacetime geometry, not the full Einstein's equations.

Even when the above requirements are fulfilled, it is not possible to engineer arbitrary spacetimes, due to the limited number of degrees of freedom of the analog metric (2.41), but rather toy models [81] that reproduce the main features of geometries of interest, such as the presence of an event horizon, for instance.

Despite these limitations might appear as major drawbacks in the field, they could also be seen as an occasion to exploit analog systems to go beyond the dynamics of scalar fields propagating in curved spacetimes: for instance, deviations from a linear dispersion can be seen as Lorentz symmetry breaking at length scales below the healing length ξ, which plays the role of the Planck length [6, 7]; indeed analog models appear particularly suited to investigate the so-called *transplankian problem* associated to Hawking emission from black-holes [82, 83]. Moreover, if the perturbation amplitude exceeds the linear regime and acts on the background metric, one could analyse the *backreaction* of quantum fields on the geometry [5].

Throughout this Thesis, we analyse the analog counterpart of astrophysical phenomena in configurations that violate at least one of the above assumptions, and to which, as a consequence, the gravitational analogy cannot be straightforwardly applied; this is the reason why we use theoretical tools and methods which come from the physics of ultracold gases, rather than from quantum field theories on curved spacetimes. Remarkably, even though we mostly consider regimes that do not properly fulfill the hydrodynamic approximation, the main features of the astrophysical

phenomenon of interest are preserved.

As already mentioned, this Thesis is focused on *coherently-coupled binary mixtures of Bose-Einstein condensates*; before proceeding to the study of a few analog phenomena in these systems, it is therefore necessary to review their main properties and understand how and when the gravitational analogy applies to them. This will be the subject of next Chapter.

3 Coherently-coupled two-component mixtures

This Chapter is devoted to a summary of the relevant properties of two-component BEC mixtures: we review the main theoretical tools that will be employed throughout the Thesis, that is Gross-Pitaevskii and Bogoliubov theories. The last two Sections are dedicated to a brief discussion of numerical techniques and experimental protocols that have been used to produce some of the results we show in the next Chapters.

Multicomponent Bose-Einstein condensates can be obtained by either condensing different atomic species (heterospecies mixtures) or by exploiting the internal level structure of a single atomic species. We focus on the latter case, so that atoms belonging to the two components have equal masses $m_1 = m_2 \equiv m$, are subject to the same external potential $V(\mathbf{r}, t)$ and can be interconverted using an external field. Contact inter-species and intra-species interactions are described by the constants g_{12} and $\{g_{11} > 0, g_{22} > 0\}$, respectively, proportional to the s-wave scattering length associated to the interaction potentials [14]. The values of these interaction constants depends on the internal levels of the atomic structures which are chosen to produce the mixture.

Two-component condensates are either miscible if $|g_{12}| < \sqrt{g_{11} g_{22}}$ or immiscible, if vice-versa [14]. The physics becomes much richer if we allow atoms to be transferred from one component to the other by means of a coherent coupling of Rabi strength $\Omega \geq 0$, possibly detuned with respect to the atomic transition by a frequency δ. As we will see, this further degree of freedom affects the magnetic properties of the BEC, as well as the nature of its elementary excitations.

3.1 Gross-Pitaevskii theory

The mean field dynamics of a two-component BEC mixture is described by two coupled Gross-Pitaevskii equations [14], that, in the reference frame rotating with the coherent coupling, read:

$$i\hbar \frac{\partial}{\partial t} \begin{pmatrix} \psi_1 \\ \psi_2 \end{pmatrix} = \begin{pmatrix} \mathcal{H}_1 & -\hbar\Omega/2 \\ -\hbar\Omega/2 & \mathcal{H}_2 \end{pmatrix} \begin{pmatrix} \psi_1 \\ \psi_2 \end{pmatrix} \tag{3.1}$$

where the two diagonal operators are defined as:

$$\mathcal{H}_j := -\frac{\hbar^2 \nabla^2}{2m} + V + \frac{\hbar\delta}{2}(-1)^{3-j} + g_{jj} N |\psi_j|^2 + g_{12} N |\psi_{3-j}|^2 \tag{3.2}$$

The order parameters ψ_1, ψ_2 associated to the two species are normalized to N_j/N, where N_j is the number of atoms in the j-th component and $N = N_1 + N_2$. In the

presence of the coupling ($\Omega \neq 0$), N_1, N_2 are not necessarily conserved separately, but the total number of atoms N is. The two atomic densities are $n_1 = N|\psi_1|^2$ and $n_2 = N|\psi_2|^2$. The energy functional of the system, from which it is possible to derive equations (3.1), takes the form:

$$E = N \int \mathrm{d}\mathbf{r} \Big[\frac{\hbar^2}{2m} \big(|\vec{\nabla}\psi_1|^2 + |\vec{\nabla}\psi_2|^2 \big) + V\big(|\psi_1|^2 + |\psi_2|^2\big) + \frac{\hbar\delta}{2}\big(|\psi_1|^2 - |\psi_2|^2\big) + \\ + \frac{N}{2} g_{11}|\psi_1|^4 + \frac{N}{2} g_{22}|\psi_2|^4 + N g_{12}|\psi_1|^2|\psi_2|^2 - \hbar\Omega \mathrm{Re}(\psi_1^* \psi_2) \Big] \tag{3.3}$$

Energetic arguments based on (3.3) show that, if $\Omega = 0$ and $|g_{12}| > \sqrt{g_{11} g_{22}}$, it is convenient for the two components to occupy different volumes and do not interact, rather than stay mixed [14]. Moreover, given the dependence of the energy functional on the relative phase $\varphi := \arg(\psi_1 \psi_2^*)$, which only appears in the last term of (3.3) as $-\hbar\Omega|\psi_1||\psi_2|\cos\varphi$, the ground state is characterized by $\varphi = 0$: in other words, the relative phase must be counter-aligned with the Rabi field in order to minimize the energy of the system. In the absence of coherent coupling, the energy is instead independent on φ, which can arbitrarily change without energy cost. This gauge freedom reflects the conservation of the relative number of particles $N_1 - N_2$, which, in the presence of a coherent coupling, is not fulfilled due to the possibility of transfer atoms from one component to the other. The gauge freedom in the choice of the global phase is instead associated to the conservation of the total number of particles N, which is always satisfied.

Total density	n	$n_1 + n_2$
Magnetization	Z	$(n_2 - n_1)/n$
Relative phase	φ	$\arg(\psi_1 \psi_2^*)$
Average intraspecies interactions	g	$(g_{11} + g_{22})/2$
Intraspecies interaction imbalance	Δ	$(g_{11} - g_{22})/2$
Density interaction strength	G	$g + g_{12}$
Spin interaction strength	κ	$g - g_{12}$
Effective detuning	δ_{eff}	$\delta + \Delta n/\hbar$

TABLE 3.1: Definitions of the relevant physical quantities.

3.2 Spin vector formalism

At the mean-field level, the state of a two-component mixture is fully determined by the total density $n = n_1 + n_2$, polarization $Z \equiv (n_2 - n_1)/n$ and relative phase φ; the one-body density matrix ρ of the system:

$$\rho = N \begin{pmatrix} |\psi_2|^2 & \psi_1^* \psi_2 \\ \psi_1 \psi_2^* & |\psi_1|^2 \end{pmatrix} = \frac{1}{2}\big[n\mathbb{I} + \mathbf{S} \cdot \vec{\sigma} \big] \tag{3.4}$$

can be expanded in the basis of Pauli matrices provided the definition of a spin vector:

$$\mathbf{S} = \mathrm{Tr}(\vec{\sigma}\rho) = n\left(\sqrt{1-Z^2}\cos\varphi, \sqrt{1-Z^2}\sin\varphi, Z\right) \tag{3.5}$$

If $\theta = \arccos(Z)$, the state of a mixture can be locally represented as a point (θ, φ) on the surface of a Bloch sphere of radius $n = \mathrm{Tr}(\rho)$.

The equation of motion for the one-body density matrix is obtained by direct calculation from (3.1). The kinetic term can be expressed as the divergence of a $2 \times 2 \times d$ quantum-mechanical current tensor $\mathcal{J}$ (d being the dimensionality of the system):

$$\mathcal{J}^{\mu}_{ab} = \frac{N\hbar}{2mi}\left[(\partial_\mu \psi_a)\psi^*_b - \psi_a(\partial_\mu \psi^*_b)\right] \tag{3.6}$$

The decomposition of $\mathcal{J}$ in the basis of Pauli matrices requires the definition of the total current vector K^μ and of a spin current matrix F^μ_ν:

$$K^\mu := \mathrm{Tr}(\mathcal{J}^\mu_{\bullet\bullet}) = \mathcal{J}^\mu_{11} + \mathcal{J}^\mu_{22} \tag{3.7}$$

$$F^\mu_\nu := \mathrm{Tr}(\sigma_\nu \mathcal{J}^\mu_{\bullet\bullet}) \tag{3.8}$$

(along the rows we span the spin space coordinates $\nu = 1, 2, 3$, while along the columns we span the real space coordinates $\mu = x, y, z$).

By direct computation, exploiting the definitions of $\mathbf{S}, \mathcal{J}, K^\mu, F^\mu_\nu$, one also finds that the total and spin currents are related through the identity:

$$nF^\mu_\nu = K^\mu S_\nu + \frac{\hbar}{2m}(\partial_\mu \mathbf{S} \times \mathbf{S})_\nu \tag{3.9}$$

With these definitions, the equation of motion for the density matrix takes the form:

$$\partial_t \rho + \vec{\nabla} \cdot \mathcal{J} = \frac{1}{2i}\left[\rho, \mathbf{H}\cdot\vec{\sigma}\right] = \frac{1}{2}(\mathbf{S}\times\mathbf{H})\cdot\vec{\sigma} \tag{3.10}$$

where the notation stands for $(\vec{\nabla}\cdot\mathcal{J})_{ab} = \partial_\mu \mathcal{J}^\mu_{ab}$ and the last equality is a consequence of the following property of Pauli matrices: $[\mathbf{a}\cdot\vec{\sigma}, \mathbf{b}\cdot\vec{\sigma}] = 2i(\mathbf{a}\times\mathbf{b})\cdot\vec{\sigma}$. Moreover, we have defined the (spin-dependent) external field [77, 84, 85]:

$$\mathbf{H} = \left(\Omega,\, 0,\, \delta_{\mathrm{eff}} - \kappa S_3/\hbar\right) \tag{3.11}$$

whose components depend on the coherent coupling and on the interaction constants through the quantities defined in Table 3.1.

It is sufficient to exploit the Pauli decomposition and separate the terms proportional to $\mathbb{I}$ from those proportional to $\vec{\sigma}$ to obtain a continuity equation for the total density and the equation of motion for the spin vector [77, 84, 85]:

$$\partial_t n + \partial_\mu K^\mu = 0 \tag{3.12}$$

$$\partial_t \mathbf{S} + \vec{\nabla}\cdot F = \mathbf{S}\times\mathbf{H} \tag{3.13}$$

where the notation stands for $(\vec{\nabla}\cdot F)_\nu = \partial_\mu F^\mu_\nu$. The continuity equation (3.12) is associated to the conservation of the total number of particles; Eq. (3.13) implies that a

conservative spin dynamics can only be observed in the absence of the external field **H** (that is, without coherent coupling and in a perfectly symmetric configuration) or, in general, if the spin vector is aligned with the field. If this is true, the Noether currents F are associated to the conservation of the three components of the spin vector, or, equivalently, magnetization (relative number of particles) and relative phase.

3.3 Bogoliubov theory of collective excitations

A deep insight on the physical properties of the system is given by the Bogoliubov theory of small excitations over a stationary state. As for a single BEC, this perturbative approach consists in the linearization of the Gross-Pitaevskii equations (3.1), and can be easily quantized to include the lowest order corrections to the mean field hamiltonian [14]. If (ψ_1, ψ_2) is a stationary solution of (3.1) with chemical potential μ, and $(\delta\psi_1, \delta\psi_2)$ are small perturbations of such stationary state, the Bogoliubov-de Gennes equations take the form:

$$i\hbar\frac{\partial}{\partial t}\begin{pmatrix}\delta\psi_1\\ \delta\psi_1^*\\ \delta\psi_2\\ \delta\psi_2^*\end{pmatrix} = \mathcal{L}\begin{pmatrix}\delta\psi_1\\ \delta\psi_1^*\\ \delta\psi_2\\ \delta\psi_2^*\end{pmatrix} := \left(\begin{array}{c|c}\mathcal{L}_{11} & \mathcal{L}_{12}\\ \hline \mathcal{L}_{21} & \mathcal{L}_{22}\end{array}\right)\begin{pmatrix}\delta\psi_1\\ \delta\psi_1^*\\ \delta\psi_2\\ \delta\psi_2^*\end{pmatrix} \tag{3.14}$$

where the 2×2 blocks of the Bogoliubov matrix $\mathcal{L}$ are defined as:

$$\mathcal{L}_{jj} = \begin{bmatrix}\mathcal{H}_j + g_{jj}N|\psi_j|^2 - \mu & g_{jj}N\psi_j^2\\ -g_{jj}N\psi_j^{*2} & -\big(\mathcal{H}_j + g_{jj}N|\psi_j|^2 - \mu\big)\end{bmatrix} \tag{3.15}$$

$$\mathcal{L}_{12} = \begin{bmatrix}g_{12}N\psi_1\psi_2^* - \hbar\Omega/2 & g_{12}N\psi_1\psi_2\\ -g_{12}N\psi_1^*\psi_2^* & -g_{12}N\psi_1^*\psi_2 + \hbar\Omega/2\end{bmatrix} \tag{3.16}$$

and $\mathcal{L}_{21} = \mathcal{L}_{12}[\psi_1 \leftrightarrow \psi_2]$. Notice that the two diagonal blocks have the same general structure of (2.9). The matrix $\mathcal{L}_{12}$ contains instead terms arising from interspecies interaction and from the coherent coupling.

As for a single-component BEC, the spectrum of the Bogoliubov matrix gives the dispersion relation for elementary excitations over the stationary state, and allows to study the stability of such configuration. Once again, the Bogoliubov matrix is not hermitian, but pseudo-hermitian, that is $\mathcal{L} = \eta^{-1}\mathcal{L}^\dagger\eta$ for $\eta = \mathrm{diag}(1,-1,1,-1)$. This implies that the standard norm is not a conserved quantity in the dynamics described by (3.14); on the other hand, the conserved Bogoliubov pseudo-norm is not positive definite. The energy of an eigenmode is given by the product between its norm and its eigenfrequency. Eigenstates of the Bogoliubov matrix $\mathcal{L}$ are therefore classified into three groups:

1. *Stable modes* with positive (negative) norm and positive (negative) frequency, so that their energy is positive.

2. *Energetically unstable modes* with positive (negative) norm and negative (positive) frequency, and consequently, negative energy. The existance of these modes signals that the considered stationary state is not the ground state of the system.

However, they can only be excited in the presence of a dissipation mechanism, leaving the mixture dynamically stable in an energy-conserving setup.

3. *Dynamically unstable modes* with complex frequency and zero norm. They come in pseudo-degenerate pairs: one is evanescent, while the other is exponentially growing in time; moreover, can be populated even in the absence of dissipation, since they carry zero energy. Physically, they correspond to the simultaneous excitation of modes with opposite energy.

In order to avoid double-counting of the modes, throughout this Thesis we will only considered positive and complex frequency solutions, but keep both norm signs.

A solution to both the mean-field dynamics and the Bogoliubov problem is hardly found in the most general case. Hence, in the following Sections we focus on two specific cases of interest:

(a) *Resonantly-coupled unpolarized mixtures*, defined by $g_{11} = g_{22} := g$, $\delta = 0$ and $N_1 = N_2$; stationary states are characterized by the two components being associated to the same order parameter $\psi_1 = \psi_2 := \psi$. As we prove in Section 3.4, there exist two independent branches of collective modes, and an analog metric can be defined for both.

(b) *Polarized uniform mixtures*: the most generic case $\delta \neq 0, g_{11} \neq g_{22}$ can be treated semi-analytically for uniform mixtures (see Section 3.5), whose total density and global phase dynamics is assumed to be trivial.

3.4 Unpolarized mixtures

Let us first focus on the peculiar case of a resonantly coupled balanced mixture, that is, let us assume $g_{11} = g_{22} := g$ and $\delta = 0$ [14, 86]. We will show that there exist some parameters' range in which the two components are described by the same order parameter ψ and $N_1 = N_2 = N/2$. Stationary states satisfy the time-independent Gross-Pitaevskii equation for some chemical potential μ:

$$\mu\psi = \left[-\frac{\hbar^2\nabla^2}{2m} + V + GN|\psi|^2 - \frac{\hbar\Omega}{2}\right]\psi := \mathcal{H}\psi \tag{3.17}$$

Notice that, in contrast to the case of a single condensate considered in the previous Chapter, ψ is now normalized to $1/2$, or, equivalently, that the total density is $n = 2N|\psi|^2$. The energy of a generic configuration is given by:

$$E = 2N\int \mathrm{d}\mathbf{r}\left[\frac{\hbar^2}{2m}|\vec{\nabla}\psi|^2 + V|\psi|^2 + \frac{N}{2}G|\psi|^4 - \frac{\hbar\Omega}{2}|\psi|^2\right] \tag{3.18}$$

In terms of the spin analogy [see Eq.(3.5)], balanced mixtures live on the equator of the Bloch sphere ($Z = 0$): if $\Omega = 0$ the relative phase is undetermined, while in the presence of the coupling, the spin vector is forced to remain aligned with the external field $\mathbf{H} = -\Omega\hat{e}_1$, that is, $\mathbf{S} = n\hat{e}_1$. Spin currents can all be trivially written in terms of $K^\mu = nv^\mu$ [see Eq.(3.7)], with $\mathbf{v} = (\hbar/m)\vec{\nabla}\arg(\psi)$ being the global (irrotational) velocity of the BEC.

Collective excitations of the mixture can be classified into density (d) and spin (s) modes, namely perturbations of the total density and global phase, and perturbations of the relative density and relative phase. Indeed if we perform a $\pi/4$-rotation of the Bogoliubov spinor (and, consequently, of its u, v components):

$$\begin{pmatrix} \delta\psi_d \\ \delta\psi_d^* \\ \delta\psi_s \\ \delta\psi_s^* \end{pmatrix} = M \begin{pmatrix} \delta\psi_1 \\ \delta\psi_1^* \\ \delta\psi_2 \\ \delta\psi_2^* \end{pmatrix} \qquad M = \frac{1}{\sqrt{2}} \begin{pmatrix} 1 & 0 & 1 & 0 \\ 0 & 1 & 0 & 1 \\ -1 & 0 & 1 & 0 \\ 0 & -1 & 0 & 1 \end{pmatrix} \tag{3.19}$$

the transformed Bogoliubov matrix takes a block-diagonal form:

$$M\mathcal{L}M^{-1} = \left(\begin{array}{c|c} \mathcal{L}_d & 0 \\ \hline 0 & \mathcal{L}_s \end{array}\right) \tag{3.20}$$

where the two diagonal blocks are:

$$\mathcal{L}_d = \begin{bmatrix} \mathcal{H} + GN|\psi|^2 - \mu & GN\psi^2 \\ -GN\psi^{*2} & -\big(\mathcal{H} + GN|\psi|^2 - \mu\big) \end{bmatrix} \tag{3.21}$$

$$\mathcal{L}_s = \begin{bmatrix} \mathcal{H} + \kappa N|\psi|^2 - \mu + \hbar\Omega & \kappa N\psi^2 \\ -\kappa N\psi^{*2} & -\big(\mathcal{H} + \kappa N|\psi|^2 - \mu + \hbar\Omega\big) \end{bmatrix} \tag{3.22}$$

The 4×4 Bogoliubov problem for a symmetric mixture reduces therefore to two independent 2×2 Bogoliubov problems for density and spin modes, both completely analogous to that of a single-component Bose-Einstein condensate. In formal terms, the quadratic correction to the energy of the system can be written as the sum of two independent contributions $H^{(2)} = H_d^{(2)} + H_s^{(2)}$, where:

$$H_j^{(2)} = \frac{N}{2} \int \mathrm{d}\mathbf{r} (\delta\psi_j^*, \delta\psi_j) \sigma_3 \mathcal{L}_j \begin{pmatrix} \delta\psi_j \\ \delta\psi_j^* \end{pmatrix} \tag{3.23}$$

Each of the two terms is diagonalized by the eigenmodes of the associated Bogoliubov matrix. Both $\mathcal{L}_d$ and $\mathcal{L}_s$ have the same structure of (2.9), thus they share the same spectral properties. More specifically, results for density and spin modes can be obtained from those of a single BEC by making some substitutions

$$(d) \qquad g \to G/2 := (g + g_{12})/2 \tag{3.24}$$

$$(s) \qquad \begin{array}{l} g \to \kappa/2 := (g - g_{12})/2 \\ (\mathcal{H} - \mu) \to (\mathcal{H} - \mu) + \hbar\Omega \end{array} \tag{3.25}$$

The factors 2 come from the different normalization of ψ with respect to the case of a single-component condensate. Notice that the presence of the coherent coupling only affects spin excitations.

Uniform unpolarized mixture Let us discuss more in detail the differences between the two branches of collective excitations by analysing the simplest case of a uniform mixture of total density n. For plane wave excitations $\mathcal{H} - \mu$ is simply the kinetic energy, thus the substitution $\mathcal{H} - \mu \to \mathcal{H} - \mu + \hbar\Omega$ translates to $\hbar^2 k^2/2m \to \hbar^2 k^2/2m +$

$\hbar\Omega$. Hence, the Bogoliubov dispersion relation for density and spin modes are:

$$\hbar\omega_d^{\pm}(k) = \pm\sqrt{\frac{\hbar^2k^2}{2m}\left(\frac{\hbar^2k^2}{2m} + Gn\right)} \tag{3.26}$$

$$\hbar\omega_s^{\pm}(k) = \pm\sqrt{\left(\frac{\hbar^2k^2}{2m} + \hbar\Omega\right)\left(\frac{\hbar^2k^2}{2m} + \hbar\Omega + \kappa n\right)} \tag{3.27}$$

By analogy with the single-component case, let us define $\mu_d := Gn/2$ and $\mu_s := \kappa n/2$.

There exist both positive and negative frequency modes, whose norm has the same sign as the frequency. Dynamically unstable density modes appear if $G < 0$, namely $g_{12} < -g$: indeed the system becomes unstable against collapse. Similarly, the symmetric state $\psi_1 = \psi_2$ is unstable in the spin channel if $\kappa n + \hbar\Omega < 0$. Without the coherent coupling, this condition reads $g_{12} > g$: the mixture is unstable against separation of the two components; immiscible mixtures with $\kappa < 0$ are instead stabilized by a sufficiently strong coupling $\hbar\Omega > |\kappa|n$. As we will see in Section 3.5, dynamical instabilities arise if $\hbar\Omega < |\kappa|n$, because the ground state of the system is a polarized state with non-zero magnetization, while the stationary state with $Z = 0$ becomes a maximum of the energy functional (see Sec. 3.5).

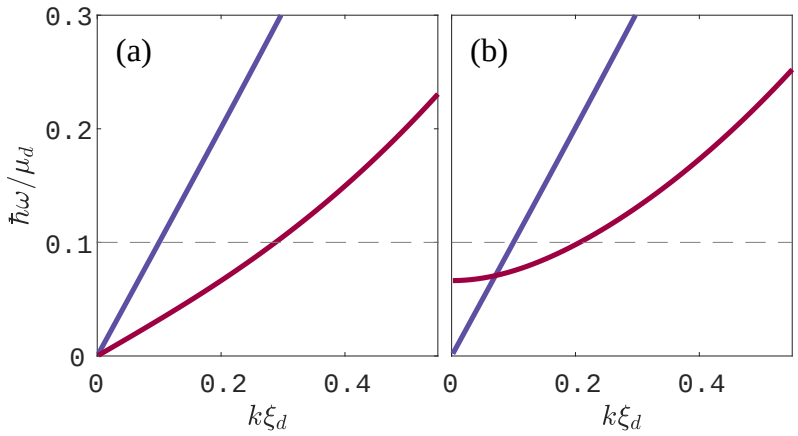

FIGURE 3.1: Bogoliubov dispersion relation for density (blue solid line) and spin (red solid line) modes. Obtained with $\kappa/G = 0.1$ (dotted horizontal line) and different values of the coherent coupling $\hbar\Omega/\kappa n = 0, 0.1$. The dashed line indicates the value of μ_s. In the absence of a coherent coupling [panel (a)], both dispersion relations are gapless and phononic at small momenta, with different sound speeds. The coherent coupling only affects the spin dispersion, opening a gap at $k = 0$ [panel (b)]. Notice that the same dispersion relations could be obtained by changing the sign of κ to negative and tuning the Rabi frequency $\hbar\Omega > |\kappa|n$ such that the spin gap ω_p is unchanged. For panels (a) and (b) this is achieved by setting $\kappa/G = -0.1$ and $\hbar\Omega/\kappa n = -1, -10$, respectively.

Examples of the two dispersion relations both for $\Omega = 0$ and $\Omega \neq 0$ are given in panels (a) and (b) of Fig.3.1, respectively. Density modes are unaffected by the

coupling and long wavelength excitations are phononic, with speed of sound $c_d = \sqrt{Gn/2m} = \sqrt{\mu_d/m}$. The threshold momentum defining the phononic vs. particle behaviour of density modes is $k \sim 1/\xi_d$, where $\xi_d = \hbar/mc_d$. The gapless nature of the dispersion is associated, through the Goldstone theorem, to the conservation of the total number of particles, which holds regardless of the value of Ω. The static structure factor for density modes is analogous to that of a single-component system and vanishes linearly with k at small momenta:

$$\mathcal{S}_d(k) = \sqrt{\frac{\hbar^2k^2/2m}{\hbar^2k^2/2m + 2\mu_d}} \tag{3.28}$$

The nature of long-wavelength spin modes depends instead on Ω: indeed a gap of size $\hbar\omega_p = \sqrt{\hbar\Omega(\hbar\Omega + \kappa n)}$ opens in the presence of the coherent coupling, due to the broken U(1) symmetry associated to the conservation of $N_1 - N_2$. This reflects on the static structure factor for spin modes, which is also gapped at $k = 0$:

$$\mathcal{S}_s(k) = \sqrt{\frac{\hbar^2k^2/2m + \hbar\Omega}{\hbar^2k^2/2m + \hbar\Omega + \kappa n}} \tag{3.29}$$

If $|\kappa|n \ll \hbar\omega_p$, spin modes behave like free particles, with a gapped ($\omega_p \sim \Omega$) almost quadratic dispersion and an almost unitary static structure factor for all k. The phononic nature of long-wavelength spin excitations is instead trivially recovered when $\Omega = 0$ (and $\kappa > 0$): the speed of spin-sound is $c_s = \sqrt{\kappa n/2m} = \sqrt{\mu_s/m}$ and the hydrodynamic regime is reached for $k < 1/\xi_s$ where $\xi_s = \hbar/mc_s$. In this limit the structure factor (3.29) is, once again, linear with k: the mixture responds very weakly to small-frequency relative density perturbations, while relative phase fluctuations are critical: this confirms that the gap closing at $\Omega = 0$ is associated to a U(1) symmetry for the relative phase, or, equivalently, to the conservation of the relative number of particles $N_1 - N_2$, recovered in the absence of coherent coupling.

Remarkably, the gap in the spin dispersion ω_p also closes if $\hbar\Omega + \kappa n = 0$; this necessarily requires $\kappa < 0$. Similarly to the case $\Omega = 0$, spin modes are phononic with speed of sound $c_s = \sqrt{|\kappa|n/2m} = \sqrt{|\mu_s|/m}$; however, while the dispersion relation is identical, the physical properties of the mixture are entirely different, due to the different sign of κ. Such difference becomes appreciable when computing the Bogoliubov amplitudes. In particular, the sign of the product U_kV_k is opposite with respect to κ. A change of the sign of κ that leaves the frequency unaffected (this is possible in the spin channel by properly modifying the Rabi strenght) is equivalent to the transformation: $(U_k + V_k) \to (U_k - V_k) = (U_k + V_k)^{-1}$. In terms of static structure factors, it is equivalent to the transformation $\mathcal{S}_s(k) \to 1/\mathcal{S}_s(k)$: if $\kappa < 0$ and $\hbar\Omega = |\kappa|n$, then $\mathcal{S}_s$ diverges as $1/k$ in the long-wavelength limit. This is shown in Fig. 3.2, where we report the static structure factor of both density and spin excitations, for different values of the parameters.

In other words, we can say that, if $\hbar\Omega + \kappa n = 0$, the mixture becomes extremely sensitive to relative density perturbations. As we will prove in Section 3.5, this happens because $\hbar\Omega + \kappa n = 0$ defines the critical point for a para-to-ferromagnetic quantum phase transition: the gap closing is thus due to the spontaneous breaking of the $\mathbb{Z}_2$ symmetry for the exchange of the two components.

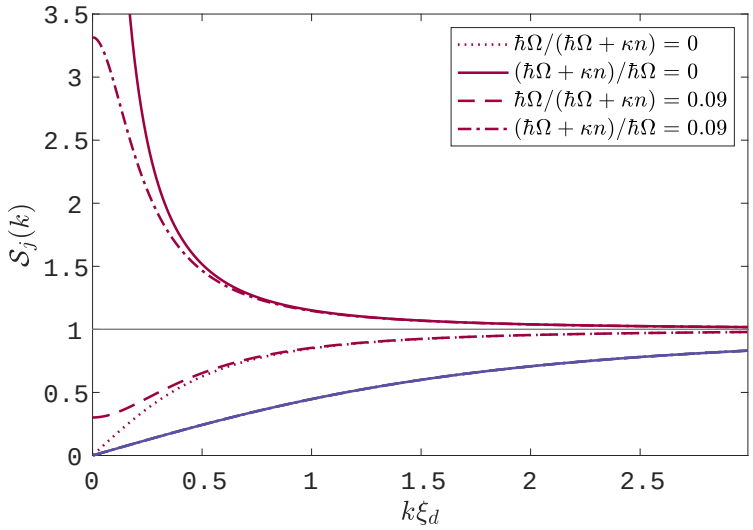

FIGURE 3.2: Static structure factor associated to total density (blue curves) and spin density (red curves) perturbations for different values of the parameters. In particular: $\hbar\Omega/\kappa n = 0$ (dotted), -1 (solid), 0.1 (dashed), -10 (dash-dotted); in all cases $|\kappa|/G = 0.1$. The density structure factor is not affected by the presence of a coherent coupling (all four curves are superimposed). The parameters that give the solid and dotted (dashed and dashdotted) curves are both associated to the dispersion relation in panel (a) [(b)] of Fig. 3.1: a change of sign in κ that leaves the dispersion unchanged is equivalent to the transformation $\mathcal{S}_s(k) \to \mathcal{S}_s^{-1}(k)$.

3.4.1 Measurement of the Bogoliubov dispersion relation through the excitation of Faraday patterns

The Bogoliubov dispersion relation and structure factor of a single-component BEC were first measured by means of Bragg spectroscopy [87]. Another experimental protocol that is widely used to excite modes in ultracold atoms is through parametric resonance [18, 88–95]. In particular, such technique can be be exploited to measure the Bogoliubov dispersion relation for elementary excitations in a spin-symmetric binary mixture, both with and without a coherent coupling between the two components. An exhaustive explanation of the experimental protocol and an analysis of the results can be found in Refs. [57, 96]; we contributed to this work by providing theoretical and numerical support.

In an intuitive way, one can understand the parametric excitation process as the emission of pairs of phonons (of frequency $\omega_M/2$ and opposite wave vectors $\pm k$) as a response to a periodic modulation of the chemical potential of the mixture with driving frequency ω_M[1] (see the sketch in Fig. 3.3); the interference of the two emitted waves with the underlying condensate leads to the development of a stationary pattern, known as Faraday wave, whose spatial periodicity is $2\pi/k$ and whose visibility

[1] In experiments, this is achieved either through a modulation of the interaction constants or through a periodic driving of the external trapping potential, which immediately transfers to the total density.

oscillates in time with frequency ω_M [90, 94]. The frequency of the modulation is therefore related to the periodicity of the Faraday wave through the Bogoliubov dispersion relation; moreover, since binary mixtures display two independent channels of elementary excitations, Faraday patterns with different wave-vector, given by the solutions of $\omega_{d,s}(k) = \omega_M/2$, will appear in both the total and relative density [57].

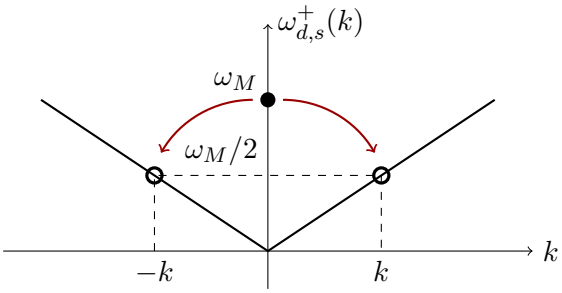

FIGURE 3.3: Parametric excitations of two counter-propagating Bogoliubov modes due to a modulation of frequency ω_M.

More rigorously, one can prove that the Heisenberg equations for creation and annihilation operators of spin modes (2.27) can be cast in the form of a Mathieu equation (see Ref.[57] for the complete calculation). A stability analysis of such equation reveals the presence of a series of instability bubbles centred around momenta satisfying the condition $\omega(k) = l\omega_M/2$, with integer l. The largest lobe is the one associated with $l = 1$, thus the mostly excited momentum is defined by $\omega(k) = \omega_M/2$, as expected. Nonetheless, higher harmonics ($l > 1$) might also be excited by the periodic modulation.

The experimental data, obtained with a periodic driving the transverse trapping frequency of a cigar-shaped two-component mixture, are reported in Fig. 3.4, which shows the Fourier transform of the effectively-1D total [panel (a)] and relative [panel (b)] density profiles of the mixture, against the modulation frequency. As expected, the signal is peaked at specific momenta, which are related to ω_M through the Bogoliubov dispersion relation: notice that the spin dispersion appears also in the total density because of a small imbalance in the two populations n_1, n_2, which induces a coupling between the two otherwise independent channels of excitations.

It is worth noticing that, since the growth rate of the unstable mode depends on the structure factor [57], the same experimental protocol that lead to the measurement of the Bogoliubov dispersion could also be used to measure $S_{d,s}(k)$ through an analysis of the visibility of the pattern in time.

The potential application of the parametric excitation of modes in the analog gravity context has been highlighted in several works, see Refs. [4, 5, 17, 18, 97, 98]. More specifically, this technique could be used to investigate cosmological particle creation during *preheating*; this term refers indeed to a post-inflationary phase in which the inflaton field oscillates near the minimum of its potential, and particles are created in pairs due to a parametric resonance [99, 100].

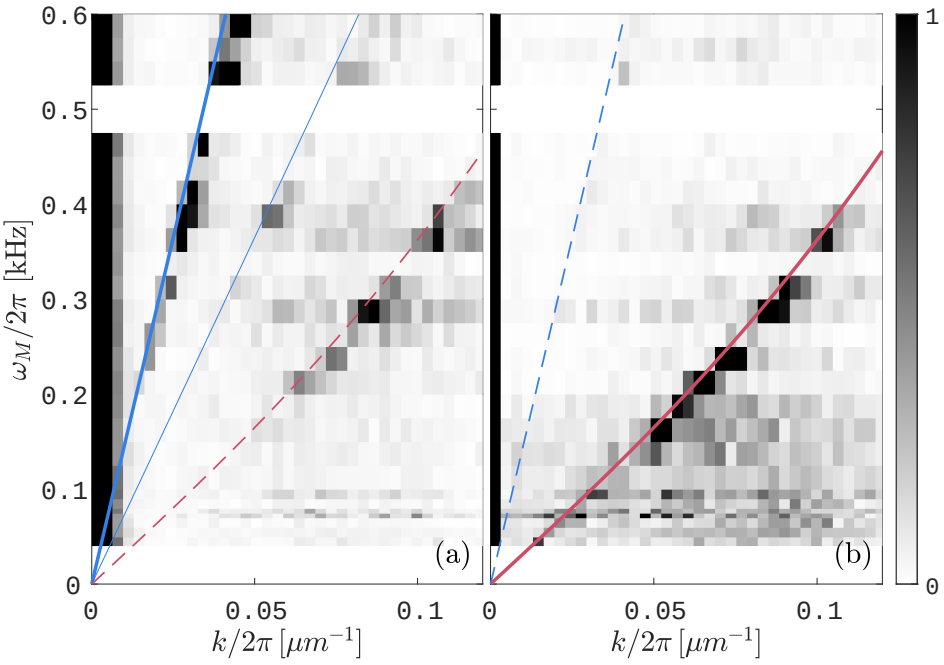

FIGURE 3.4: Measurement of the Bogoliubov dispersion relations in a spin-symmetric binary mixture through the excitation of Faraday patterns [57, 96]. Panels (a) and (b) show the Fourier transforms of the effectively one-dimensional total density and relative density profiles, respectively. Blue (red) lines indicate the expected dispersion relation for density (spin) modes with $\mu_d/2\pi \simeq 3$ kHz ($\mu_s/2\pi \simeq 145$ Hz); these values are computed from the measured peak 3D density by taking into account the geometric renormalization of the interaction constants due to the transverse harmonic trap, see Eqs.(3.78) and (3.82).

3.4.2 Quantization of the modes

As already mentioned, Bogoliubov theory can be easily quantized by promoting the perturbations $\delta\psi_j$ to quantum fields $\delta\hat{\Psi}_j$ in the density and spin quadratic Hamiltonians (3.23): the Bogoliubov-de-Gennes equations are derived from these operators as Heisenberg equations for the field perturbation.

Each of the field perturbation for density and spin modes can be expanded in terms of single-particle or quasi-particle creation/annihilation operators:

$$\delta\hat{\Psi}_j(\mathbf{r},t) = \sum_{\lambda\neq 0} \psi_{j\lambda}(\mathbf{r},t)\hat{a}_{j\lambda} := \sum_{\lambda\neq 0}\left[u_{j\lambda}(\mathbf{r},t)\hat{b}_{j\lambda} + v^*_{j\lambda}(\mathbf{r},t)\hat{b}^\dagger_{j,-\lambda}\right] \tag{3.30}$$

where the Bogoliubov coefficients $\{u_{j\lambda}, v_{j\lambda}\}$ can be chosen so to diagonalize the quadratic Hamiltonians (3.23) and $j = d, s$.

The same decomposition can be applied to the components of the spin vector $\mathbf{S}$, which contains all the quadrature of the fields. As already mentioned, a symmetric mixture is characterized, at the mean field level, by $\mathbf{S} = (n, 0, 0)$. It is therefore interesting to look at the expansion of $S_2 \sim n\delta\varphi$ and $S_3 \sim n\delta Z$ in terms of spin

modes, in the regime of small perturbations of the relative phase φ and magnetization Z. It is straightforward to show that, to the lowest order in the perturbations:

$$\hat{S}_2 \simeq i\sqrt{n}\big(\delta\hat{\Psi}_s - \delta\hat{\Psi}_s^\dagger\big) = \sqrt{n}\sum_{\lambda\neq 0}\Big[i\big(u_{s\lambda} - v_{s,-\lambda}\big)\hat{b}_{s\lambda} + h.c.\Big] \tag{3.31}$$

$$\hat{S}_3 \simeq \sqrt{n}(\delta\hat{\Psi}_s + \delta\hat{\Psi}_s^\dagger) = \sqrt{n}\sum_{\lambda\neq 0}\Big[\big(u_{s\lambda} + v_{s,-\lambda}\big)\hat{b}_{s\lambda} + h.c.\Big] \tag{3.32}$$

The first component is perturbed instead by density modes: $\hat{S}_1 = n + \sqrt{n}(\delta\hat{\Psi}_d + \delta\hat{\Psi}_d^\dagger)$. As expected, all the components of the spin vector are hermitian operators.

Uniform unpolarized mixture Let us consider the simplest case of a uniform mixture: once again, λ coincides with the momentum $\mathbf{k}$ of the modes; single-particle states are $\psi_{\mathbf{k}}(\mathbf{r}) = e^{i\mathbf{k}\cdot\mathbf{r}}/\sqrt{V}$, while the Bogoliubov spinor takes the simple form $(u_{j\lambda}, v_{j\lambda}) \to (U_{jk}, V_{jk})\psi_{\mathbf{k}}(\mathbf{r})$, where the coefficients (U_{jk}, V_{jk}) are real constant in space and time and only depend on $k = |\mathbf{k}|$. The Bogoliubov transformations read:

$$\hat{a}_{j\mathbf{k}} = U_{jk}\hat{b}_{j\mathbf{k}} + V_{jk}\hat{b}^\dagger_{j,-\mathbf{k}} \tag{3.33}$$

with the constraint $U_{jk}^2 - V_{jk}^2 = 1$ (we expect only positive energy modes, because the uniform density profile is the ground state). The quadratic Bogoliubov Hamiltonians only contain momentum-conserving terms:

$$\hat{H}_j^{(2)} = \frac{1}{2}\sum_{\mathbf{k}\neq 0}\big(\hat{b}^\dagger_{j\mathbf{k}}, \hat{b}_{j,-\mathbf{k}}\big)\begin{pmatrix}\varepsilon_{jk} & f_{jk}\\ f_{jk} & \varepsilon_{jk}\end{pmatrix}\begin{pmatrix}\hat{b}_{j\mathbf{k}}\\ \hat{b}^\dagger_{j,-\mathbf{k}}\end{pmatrix} \tag{3.34}$$

The diagonal and off-diagonal contributions are defined as:

$$\varepsilon_{jk} := \left(\frac{\hbar^2k^2}{2m} + \hbar\Omega\delta_{js}\right)\big(U_{jk}^2 + V_{jk}^2\big) + \mu_j(U_{jk} + V_{jk})^2 \tag{3.35}$$

$$f_{jk} := \left(\frac{\hbar^2k^2}{2m} + \hbar\Omega\delta_{js}\right)2U_{jk}V_{jk} + \mu_j(U_{jk} + V_{jk})^2 \tag{3.36}$$

Diagonalization of the two Bogoliubov Hamiltonians is straightforwardly obtained by setting $f_{jk} = 0$ and $\varepsilon_{jk} = \hbar\omega_j^+(k)$, or equivalently, if (3.28) and (3.29) are fulfilled.

3.4.3 Hydrodynamic theory and the gravitational analogy

The hydrodynamic equations for density and spin perturbations are found, once again, by straightforwardly generalizing those of a single-component condensate (2.33).

In particular, for density modes we have to replace $2g \to G$:

$$\begin{pmatrix}\partial_t + \mathbf{v}\cdot\vec{\nabla} & -\mathcal{D}\\ Gn/\hbar + \mathcal{D} & \partial_t + \mathbf{v}\cdot\vec{\nabla}\end{pmatrix}\begin{pmatrix}\varepsilon_1\\ \varepsilon_2\end{pmatrix} = 0 \tag{3.37}$$

where $\varepsilon_1 = \delta n_d/n := (\delta n_1 + \delta n_2)/n$ and $\varepsilon_2 = \delta\phi_d := \delta\phi_1 + \delta\phi_2$ are the real and imaginary part of the wavefunction perturbation, defined in terms of the density and

phase perturbations of the two components, $\delta\psi_j = \sqrt{n/2+\delta n_j}\exp(i\delta\phi_j)$.

As we already proved in Chapter 2, this is equivalent, within the hydrodynamic approximation ($\hbar\mathcal{D}\varepsilon_1 \ll Gn\varepsilon_1$), to a Klein-Gordon equation equation for the global phase perturbation ε_2, while the total density dynamics trivially follows the global phase: $\varepsilon_1 = -(\hbar/Gn)(\partial_t + \mathbf{v}\cdot\vec{\nabla})\varepsilon_2$. The analog spacetime is described by the metric (2.41) with speed of sound $c_d = \sqrt{Gn/2m}$.

For spin modes, the equations are found by replacing both $2g \to \kappa$ and $\mathcal{D} \to \mathcal{D}+\Omega$:

$$\begin{pmatrix} \partial_t + \mathbf{v}\cdot\vec{\nabla} & -(\Omega+\mathcal{D}) \\ \kappa n/\hbar + \Omega + \mathcal{D} & \partial_t + \mathbf{v}\cdot\vec{\nabla} \end{pmatrix} \begin{pmatrix} \varepsilon_1 \\ \varepsilon_2 \end{pmatrix} = 0 \tag{3.38}$$

with $\varepsilon_1 = \delta n_s/n := (\delta n_1 - \delta n_2)/n$ and $\varepsilon_2 = \delta\phi_s := \delta\phi_1 - \delta\phi_2$. If $\Omega = 0$, the system of Eqs.(3.38) is analogous to (3.37): the hydrodynamic approximation, $\hbar\mathcal{D}\varepsilon_1 \ll \kappa n\varepsilon_1$, allows to rewrite it in the form of a Klein-Gordon equation for a massless scalar field $\varepsilon_2 = \delta\phi_s$, provided the speed of light is replaced with the speed of spin sound $c_s = \sqrt{\kappa n/2m}$.

In the presence of the coherent coupling, the system of Eqs.(3.38) can be cast in the form of a Klein-Gordon equation for a massive scalar field in two limits:

$$(a) \quad \frac{\hbar\Omega}{\kappa n + \hbar\Omega} \ll 1,\ \kappa > 0 \qquad (b) \quad \frac{\hbar\Omega + \kappa n}{\hbar\Omega} \ll 1,\ \kappa < 0 \tag{3.39}$$

Not surprisingly, these are the conditions under which the spin Bogoliubov dispersion, despite being gapped, has a linear behaviour for intermediate k, and a speed of sound $c_s \simeq \sqrt{|\kappa|n/2m}$ can be identified. From a mathematical point of view, the gravitational analogy relies on the possibility of neglecting the derivative $\mathcal{D}$ in either one of the two equations (3.38). If the conditions (3.39)(a) and $\hbar\mathcal{D}\varepsilon_1 \ll \kappa n\varepsilon_1$ are fulfilled, the same derivation of Chapter 2 leads to:

$$(a) \quad \frac{1}{\sqrt{-g}}\partial_\mu\Big[\sqrt{-g}g^{\mu\nu}\partial_\nu\varepsilon_2\Big] - \frac{2m\Omega}{\hbar}\left(\frac{c_s}{n}\right)\varepsilon_2 = 0 \tag{3.40}$$

with $c_s = \sqrt{(\kappa n + \hbar\Omega)/2m} \simeq \sqrt{\kappa n/2m}$. The magnetization ε_1 follows the dynamics of the relative phase according to $(\kappa n/\hbar + \Omega)\varepsilon_1 = -(\partial_t + \mathbf{v}\cdot\vec{\nabla})\varepsilon_2$.

If instead we assume (3.39)(b) and $\hbar\mathcal{D}\varepsilon_2 \ll \hbar\Omega\varepsilon_2 \simeq |\kappa|n\varepsilon_2$, by exchanging the roles of the field perturbations $\varepsilon_1, \varepsilon_2$, we find:

$$(b) \quad \frac{1}{\sqrt{-g}}\partial_\mu\Big[\sqrt{-g}g^{\mu\nu}\partial_\nu\varepsilon_1\Big] - \frac{2m(\hbar\Omega + \kappa n)}{\hbar^2}\left(\frac{c_s}{n}\right)\varepsilon_1 = 0 \tag{3.41}$$

where the speed of spin-sound is $c_s = \sqrt{\hbar\Omega/2m} \simeq \sqrt{|\kappa|n/2m}$, while the dynamics of relative phase perturbations is trivially given by $\Omega\varepsilon_2 = (\partial_t + \mathbf{v}\cdot\vec{\nabla})\varepsilon_1$.

Both Eqs. (3.40), (3.41) are relativistic Klein-Gordon equations for a massive scalar field subject to a curved spacetime geometry, and whose mass is tunable via the strength Ω of the coherent coupling:

$$(a) \quad \frac{M}{2m} = \sqrt{\frac{\hbar\Omega}{\kappa n + \hbar\Omega}} \ll 1 \qquad (b) \quad \frac{M}{2m} = \sqrt{\frac{\hbar\Omega + \kappa n}{\hbar\Omega}} \ll 1 \tag{3.42}$$

More specifically, if $\hbar\Omega \ll \kappa n$ (with $\kappa > 0$) the role of the scalar field is played by long-wavelength relative phase perturbations, while if $\hbar\Omega \sim |\kappa| n$ (with $\kappa < 0$), the relevant dynamical variable is the magnetization $\varepsilon_1 \sim \delta Z$. The gravitational analogy breaks down instead if $|\kappa| n \ll \hbar\Omega$, for which neither of the two conditions (3.39) is satisfied; consistently, in the same regime the Bogoliubov dispersion is quadratic for all k and no speed of sound can be defined.

To summarize, the gravitational analogy can be exploited with symmetric mixtures, both for density and spin modes; the two branches of collective excitations are subject to an analog metric with structure given by (2.41): while the velocity flow $\mathbf{v}$ of the condensate is fixed by the total density profile and is therefore the same for both channels, the speed of sound c is different. In certain limits [see Eq. (3.39)], a coherent coupling allows to simulate the dynamics of massive fields, with the (possibly position-dependent) mass being tunable through the value of the Rabi frequency Ω. These results were first derived in Refs.[25–27] for the most general case of a coherently coupled mixture of atoms with different masses and intraspecies interactions: we have restricted here to our specific case of interest.

As a last observation, we point out that the diagonalization of (3.37), (3.38) allows to find the Bogoliubov dispersion relations for density and spin modes in a frame moving with velocity $\mathbf{v}$. For uniform systems $\mathcal{D}$ coincides with the kinetic energy and therefore acts as a multiplicative factor $\hbar^2 k^2/2m$; hence the only difference with respect to (3.26) and (3.27) is a Doppler shift of the mode frequencies: $\omega \to \omega - \mathbf{k}\cdot\mathbf{v}$.

It is worth noticing that, if the velocity $\mathbf{v}$ of the condensate is sufficiently large, positive norm modes can acquire a negative frequency (and vice-versa) in the laboratory frame. The existance of negative energy modes is a key ingredient to observe spontaneous or stimulated particle creation, allowing for the realization of the analog version of gravitational processes (Hawking radiation from sonic black-holes, to cite one). From the cold gases perspective, it is a manifestation of the Landau criterion for superfluidity: if the speed of the condensate exceeds the Landau velocity (that, in our case, coincides with the speed of sound), superfluidity breaks down and excitations can be created.

3.5 Uniform polarized mixtures

Symmetric mixtures represent the only parameter configuration for which spin and density channels decouple regardless of the total density profile. However, as anticipated in Sec. 3.4, mixtures with non-vanishing magnetization Z show magnetic properties. If combined with the superfluid character of the system, these allow to investigate magnetism in a dissipationless and collisionless regime that is extremely hard to achieve with other condensed matter platforms; examples range from the dynamics of domain-walls [77] to the relaxation mechanism from a metastable state [101]. We will discuss the latter in detail in Chapter 6.

In what follows, we analyse the stationary states and elementary excitations of uniform binary mixtures. The results presented here were derived in [86] for a resonant coherent coupling ($\delta = 0$); here we generalize the treatment by allowing a non-zero detuning of the coupling from the atomic transition.

In order to simplify the calculations, we assume that there is no background velocity and the density is uniform in space (no external potentials). These requirements allow to neglect the dynamics of total density and global phase and reduce the number of dynamical variables to two: relative phase φ and magnetization Z.

The two order parameters can be expressed in terms of the (constant) total density n, the global phase φ_{tot}, the magnetization Z and the relative phase φ:

$$\sqrt{N}\begin{pmatrix}\psi_1\\ \psi_2\end{pmatrix} = \sqrt{\frac{n}{2}}\begin{pmatrix}\sqrt{1+Z}e^{-i\frac{\varphi}{2}}\\ \sqrt{1-Z}e^{i\frac{\varphi}{2}}\end{pmatrix} e^{i\frac{\varphi_{tot}}{2}} \tag{3.43}$$

According to the continuity equation (3.12), the total density is constant if there is no global background flow, namely if the total current, defined in Eq. (3.7),

$$K^\mu = \frac{\hbar n}{2m}\left[\partial_\mu\varphi_{tot} - Z\partial_\mu\varphi\right] \tag{3.44}$$

is vanishing. This condition imposes a constraint on the dynamics of the global phase: $\vec{\nabla}\varphi_{tot} = Z\vec{\nabla}\varphi$, which can thus be eliminated from the equations of motion. Under this assumption, the Gross Pitaevskii Hamiltonian density reads:

$$\mathscr{H} = \frac{n}{2}\left\{\frac{\hbar^2}{4m}\left[\frac{|\vec{\nabla}Z|^2}{1-Z^2} + (1-Z^2)|\vec{\nabla}\varphi|^2\right] + U(Z,\varphi)\right\} \tag{3.45}$$

where we have separated the kinetic energy contribution from the effective potential:

$$U(Z,\varphi) = \frac{1}{2}\kappa n Z^2 - \hbar\delta_{\text{eff}}Z - \hbar\Omega\sqrt{1-Z^2}\cos\varphi \tag{3.46}$$

The equations of motion are derived from (3.13) or directly from the Hamiltonian density (3.45) (indeed $nZ/2$ and $\hbar\varphi$ behave as canonically conjugate variables):

$$\hbar\frac{\partial Z}{\partial t} - \frac{\hbar^2}{2m}\vec{\nabla}\left[(1-Z^2)\vec{\nabla}\varphi\right] = -\frac{\partial U}{\partial\varphi} = -\hbar\Omega\sqrt{1-Z^2}\sin\varphi \tag{3.47}$$

$$\hbar\frac{\partial\varphi}{\partial t} + \frac{\hbar^2}{2m}\left[\frac{\vec{\nabla}^2 Z}{1-Z^2} + \frac{Z\,|\vec{\nabla}Z|^2}{(1-Z^2)^2} + Z|\vec{\nabla}\varphi|^2\right] = \frac{\partial U}{\partial Z} = -\delta_{\text{eff}} + Z\left(\kappa n + \frac{\hbar\Omega\cos\varphi}{\sqrt{1-Z^2}}\right) \tag{3.48}$$

Algebraic manipulation of (3.48),(3.47) leads to the following identity:

$$\vec{\nabla}\left\{\frac{\hbar^2}{4m}\left[\frac{|\vec{\nabla}Z|^2}{1-Z^2} + (1-Z^2)|\vec{\nabla}\varphi|^2\right] - U(Z,\varphi)\right\} = \hbar\frac{\partial Z}{\partial t}\vec{\nabla}\varphi - \hbar\frac{\partial\varphi}{\partial t}\vec{\nabla}Z \tag{3.49}$$

according to which, if the right-hand-side is vanishing, the quantity appearing inside the braces is position independent. This condition is satisfied for stationary configurations ($\partial_t Z = \partial_t\varphi = 0$), or if the dynamics of one of the two fields is irrelevant (for instance $\partial_t\varphi = \vec{\nabla}\varphi = 0$) or for solitonic solutions (such that time derivatives and space derivatives are proportional to one another, for both the fields). In all these cases, estimating the kinetic energy contribution becomes trivial: the result only depends

on the local value of the potential U.

Notice that, if both the fields and their variations are small and $\delta_{\text{eff}} = 0$, expansion to the first order of (3.48) and (3.47) leads to the spin Bogoliubov-de-Gennes equations, that we derived in the previous section, in the peculiar case $\vec{\nabla} n = 0, \mathbf{v} = 0$. In order words the Hamiltonian density (3.45) reduces to the Klein-Gordon one if we consider only terms up to second order in both the fields. Instead, by assuming that the mixture is unpolarized, $Z \sim 0$, but relative phase variations are not negligible, the potential reduces to $U(Z \sim 0, \varphi) = -\hbar\Omega \cos\varphi$ and one obtains a sine-Gordon field theory [102].

3.5.1 Stationary states and the phase diagram

Let us first analyse the properties of uniform stationary states. This amounts to assume all time and space derivatives are vanishing, namely that both magnetization and relative phase are uniform and constant in time. The equations of motion (3.47), (3.48) are therefore satisfied if the spin vector $\mathbf{S}$ is aligned with the effective external field $\mathbf{H}$, or equivalently:

$$\frac{\partial U}{\partial Z} = \frac{\partial U}{\partial \varphi} = 0 \tag{3.50}$$

The potential is trivially minimized with respect to φ: due to the presence of the coherent coupling, the two components are forced to stay in phase, $\varphi = 0$.

The stationary condition for the magnetization then reads:

$$\hbar\delta_{\text{eff}} = Z\left(\kappa n + \frac{\hbar\Omega}{\sqrt{1-Z^2}}\right) \tag{3.51}$$

The phase diagram of the uniform mixture is visualized in Fig. 3.5: the central color plot represents the value(s) of Z that correspond to minima of the potential U for each point in the plane $(-\kappa n/\hbar\Omega, \delta_{\text{eff}}/\Omega)$; vertical and horizontal cuts of the surface plot are shown on its left ($\kappa n/\hbar\Omega = 0.5$), right ($\kappa n/\hbar\Omega = -3.5$) and below it ($\delta_{\text{eff}} = 0$); panels A-H show the potential landscape, computed using (3.46), as a function of Z, for some relevant points in the plane.

Let us analyse Fig. 3.5 more in detail: equation (3.51) has either a single solution, corresponding to a minimum of the potential U and, thus, to the true ground state of the mixture, or three different solutions, corresponding to an absolute minimum (the ground state), a relative minimum (a metastable state) and an unstable maximum. These features are easily proved in the simplest case $\delta_{\text{eff}} = 0$, for which the energy profile is symmetric with respect to $Z = 0$: if $-\kappa n/\hbar\Omega < 1$ (that is either if $\kappa > 0$ or, for $\kappa < 0$, $|\kappa| n < \hbar\Omega$) a single mininum exists at $Z = 0$ (see panel B); this is the balanced mixture we considered in Section 3.4. For $-\kappa n/\hbar\Omega > 1$ (that is $|\kappa| n > \hbar\Omega$, with $\kappa < 0$), the solution $Z = 0$ becomes an unstable maximum and two degenerate ground states are found at $\pm Z_0$ (see panel F), with:

$$Z_0 = \sqrt{1 - \left(\frac{\hbar\Omega}{|\kappa| n}\right)^2} \tag{3.52}$$

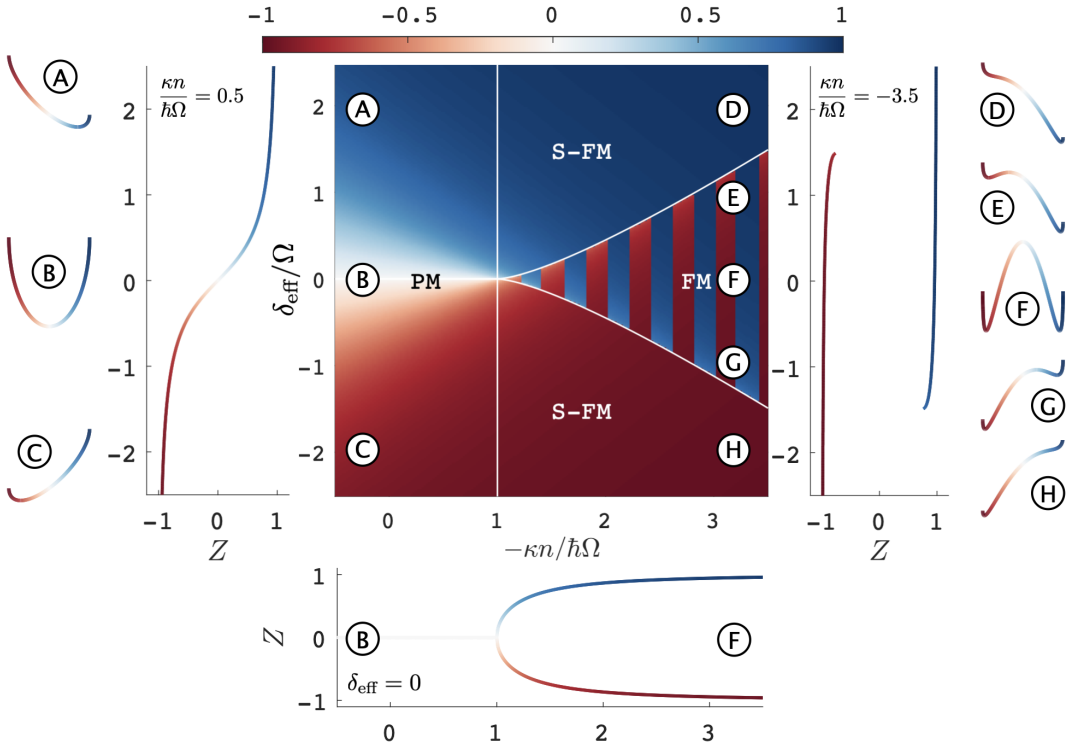

FIGURE 3.5: Phase diagram of a uniform superfluid mixture subject to a non-resonant coherent coupling. The color scale refers to the value(s) of magnetization Z associated to the minima of the potential $U(Z, \varphi = 0)$ as a function of the physical parameters $\Omega, \delta_{\rm eff}, \kappa n$. White solid lines separate the regions of the phase diagram in which the mixture shows different phases: paramagnetic (PM), ferromagnetic (FM) and saturated-ferromagnetic (S-FM). Cuts of the surface plot at fixed $\kappa n/\hbar\Omega$ and at fixed $\delta_{\rm eff}/\Omega$ are also shown. Panels A-H show the profile of $U(Z, \varphi = 0)$ for some relevant locations in the plane $(-\kappa n/\hbar\Omega, \delta_{\rm eff}/\Omega)$.

The phase transition between an unpolarized (paramagnetic, PM) mixture and a polarized (ferromagnetic, FM) one is signalled by the spontaneously broken $\mathbb{Z}_2$ symmetry, as visible in the lower panel of Fig. 3.5: the parameter governing the transition is not temperature, but the non-linearity κ, and the order parameter is the magnetization Z which becomes non-zero in the ferromagnetic phase.

If the coherent coupling is off-resonant ($\delta_{\rm eff} \neq 0$), the energy profile is tilted and becomes asymmetric with respect to $Z = 0$, the absolute minimum corresponding always to a value of the polarization with the same sign as $\delta_{\rm eff}$. As for the resonant case, a secondary minimum appears in the half-plane $-\kappa n/\hbar\Omega > 1$ if $\delta_{\rm eff}$ is sufficiently small (see panels E, G); for very large detuning, the magnetization of the system will simply align with $\delta_{\rm eff}/\Omega$, showing a saturated-ferromagnet (S-FM) behaviour (panels D,H). The boundary between the FM and S-FM regions (the white solid line in Fig. 3.5) is determined by the value of $\delta_{\rm eff}$ for which the secondary minimum and the

maximum merge into a saddle point; the condition

$$\frac{\partial U}{\partial Z} = \frac{\partial^2 U}{\partial Z^2} = 0 \tag{3.53}$$

is fulfilled, only if $\kappa < 0$, for the critical magnetization:

$$Z_* = -\text{sign}(\delta_{\text{eff}})\sqrt{1 - \left(\frac{\hbar\Omega}{|\kappa|n}\right)^{2/3}} \tag{3.54}$$

at the critical detuning values $\delta_{\text{eff}} = \pm\delta^*_{\text{eff}}$, with:

$$\delta^*_{\text{eff}} = |\kappa|n\left[1 - \left(\frac{\hbar\Omega}{|\kappa|n}\right)^{2/3}\right]^{3/2} \tag{3.55}$$

It is also interesting to look at vertical cuts of the phase diagram: while on the PM side (left panel) the spin vector always remains aligned with δ_{eff}, in the FM regime (right panel) the system remains trapped in the relative minimum of the potential landscape, following an hysteresis cycle of size $\delta_{\text{hys}} = 2\delta^*_{\text{eff}}$. The criticality of the point $(-\kappa n/\hbar\Omega, \delta_{\text{eff}}/\Omega) = (1, 0)$ is confirmed by the divergence of the magnetic susceptibility: starting from (3.51) and recalling that the condition $\delta_{\text{eff}} = 0$ coincides with $Z = 0$ in the PM phase and with $1 - Z^2 = (\hbar\Omega/\kappa n)^2$ in the FM phase, the calculation gives:

$$\frac{1}{\chi} := \frac{1}{\Omega}\left|\frac{\partial Z}{\partial \delta_{\text{eff}}}\right|^{-1}_{\delta_{\text{eff}}=0} = \begin{cases} 1 + \dfrac{\kappa n}{\hbar\Omega} & \text{if } -\dfrac{\kappa n}{\hbar\Omega} < 1 \\ -\dfrac{\kappa n}{\hbar\Omega}\left[\left(\dfrac{\kappa n}{\hbar\Omega}\right)^2 - 1\right] & \text{if } -\dfrac{\kappa n}{\hbar\Omega} > 1 \end{cases} \tag{3.56}$$

Remarkably, the critical exponent is different on the two sides of the critical point.

3.5.2 Experimental measurement of the phase diagram

The phase diagram in Fig. 3.5, as well as the hysteresis width and magnetic susceptibility, has been recently measured experimentally in Ref. [77] using an immiscible mixture with $\kappa < 0$; we contributed to this work by providing theoretical and numerical support. More details on the experimental protocol and analysis of the results can be found in [96].

The horizontal axis in 3.5 can be explored in space thanks to the inhomogeneous density profile of the cloud in the harmonic trap: within a local density approximation, each position x is associated to a different value of $|\kappa|n(x)/\hbar\Omega$; if $|\kappa|n_0/\hbar\Omega > 1$ (where n_0 is the peak density), the central part of the cloud is FM or S-FM while the tails are PM. The vertical axis of Fig. 3.5 is instead scanned by varying the physical detuning δ in time: in order to guarantee that the system remains in a local minimum, the evolution needs to be adiabatic at all times.

The experimental results are shown in Fig. 3.6: panel (a) shows the real-time evolution starting from a single-component condensate in the $|\downarrow\rangle$ state with large and negative detuning, while panel (b) refers to the backward evolution starting from a condensate in the $|\uparrow\rangle$ state associated with a large and positive detuning. The

difference between the two is imputed to the ferromagnetic nature of the mixture: there exist an hysteretic region in which the state of the system depends on its history; in particular, the mixture can reside in a minimum of the energy landscape which does not coincide with the ground state. This is of crucial importance for the simulation of false vacuum decay, as we will discuss in detail in Chapter 6.

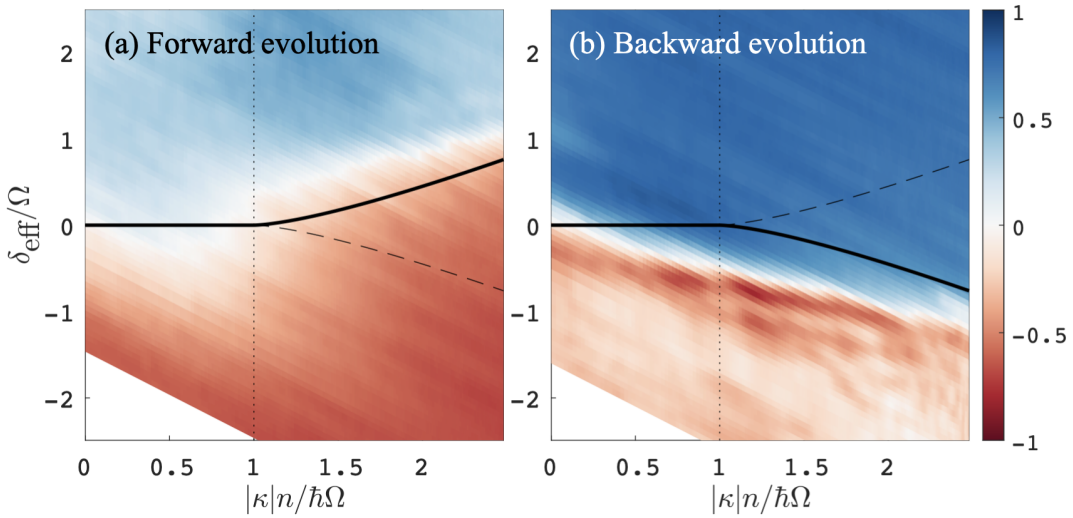

FIGURE 3.6: Experimental measurement of the phase diagram in Fig.3.5. The color-scale refers to the value of the magnetization Z. Panels (a) and (b) refer to the time-evolution observed starting from a polarized mixture in the $|\downarrow\rangle$ (red) and $|\uparrow\rangle$ (blue) states, respectively: in the former case, the detuning is initially large and negative and ramped up in time, while in the latter the initial detuning is large and positive, and it is ramped down in time. Black lines mark the theoretically predicted boundaries of the different phases (PM, FM and S-FM); in particular the solid line signals the expected location at which the magnetization jump takes place (that is, the critical detuning $\pm\delta^*_{\rm eff}$): discrepancies between the experimental data and the theoretical prediction are mainly imputed to imperfect adiabaticity (impossible to guarantee at the transition point) and dimensionality. More details can be found in Refs. [77, 96].

3.5.3 The magnetic analogy

Given the results presented in the previous Sections, the analogy with a quantum spin chain is evident: strenght and detuning of the coherent coupling play the role of the transverse and longitudinal component of an effective external magnetic field in spin space $\mathbf{B} = (B_1, 0, B_3) = (\Omega, 0, \delta_{\rm eff})$. The state of the system is determined by the interplay between such external field and an effective spin-spin interaction whose strength is given by κn. In the absence of the longitudinal field, if $\kappa > 0$ or B_1 dominates over $|\kappa|n$ (with $\kappa < 0$), the spin vector $\mathbf{S}$ remains aligned with the external field $\mathbf{B}$, that is, on the equator of the Bloch sphere: the ground state of the mixture is unpolarized ($Z = 0$); if instead spin-spin interactions dominate over B_1, it is energetically favourable for the spins to stay aligned either in the $|\uparrow\rangle$ state or $|\downarrow\rangle$

state, and the system shows two degenerate vacua with opposite polarization. A finite value of B_3 has the effect of shifting the magnetization value associated to the PM phase, and split the energy of the two vacua in the FM phase.

To stress the magnetic analogy, we could rewrite the Gross-Pitaevskii Hamiltonian density (3.45) in terms of $\mathbf{S}$: the first contribution is a quantum pressure term which accounts for the tendency of having a spatially uniform magnetization and inhibits short-wavelength modes; the second term describes spin-spin interactions; the third one is due to the coupling of the spins with the external magnetic field:

$$\mathscr{H} = \frac{1}{2}\left[\frac{\hbar^2}{4mn}|\vec{\nabla}\mathbf{S}|^2 + \frac{1}{2}\kappa S_3^2 - \hbar\mathbf{B}\cdot\mathbf{S}\right] \tag{3.57}$$

A FM phase can only be obtained if $\kappa < 0$, so that the spin-spin interaction term gives a negative contribution. For uniform systems (constant n, $K^\mu = 0$), the dynamics of the spin vector Eq. (3.13) can be cast in the form of a (dissipationless) Landau-Lifshitz equation [77]

$$\partial_t \mathbf{S} = \mathbf{S} \times \widetilde{\mathbf{H}} \tag{3.58}$$

namely, a nonlinear precession around the effective field

$$\widetilde{\mathbf{H}} = -\frac{2}{\hbar}\frac{\partial \mathscr{H}}{\partial \mathbf{S}} = \frac{\hbar}{2mn}\nabla^2\mathbf{S} - \frac{\kappa S_3}{\hbar}\hat{e}_3 + \mathbf{B} = \mathbf{H} + \frac{\hbar}{2mn}\nabla^2\mathbf{S} \tag{3.59}$$

where $\mathbf{H} = (\Omega, 0, \delta_{\text{eff}} - \kappa S_3/\hbar)$, as defined as in (3.11). Indeed, according to (3.8), if the total current K^μ is vanishing, the divergence of the spin current matrix F can be written as:

$$\vec{\nabla}\cdot F = -\frac{\hbar}{2mn}(\mathbf{S}\times\nabla^2\mathbf{S}) \tag{3.60}$$

If spin currents do not play a relevant role and $\widetilde{\mathbf{H}} \sim \mathbf{H}$, the dynamics of the system can be understood in terms of iso-energetic trajectories on the Bloch sphere: there exist one or two attractors depending on the parameters, and the time evolution is described either by an orbit around one of the minima or a two-lobe-shaped trajectory encircling both. The correction term $\propto \nabla^2\mathbf{S}$, appearing in Eq. (3.59), is instead responsible for a quantum torque effect [85] that significantly influences the dynamics of extended non-uniform systems, especially when driven far away from equilibrium.

It is worth pointing out that, despite the many analogies with a quantum spin chain, a few differences can be noticed as well: first, we are neglecting the dynamics some of the degrees of freedom of our system (total density and global phase), which, as we will discuss in the following Section, are not entirely independent on the spin vector dynamics. Consequences of this approximation are further discussed in Chapter 6. Moreover, spin chain Hamiltonians describe discrete systems, while Bose-Einstein condensates are associated to a continuous field theory and thus provide a larger number of degrees of freedom [such as the quantum torque term in Eq.(3.60)].

3.5.4 Bogoliubov excitations

The Bogoliubov problem for a mixture (3.14) is in general complex enough to require a numerical solution: for finite δ_{eff}, not even the values of magnetization Z associated

to the stationary states can be found analytically. However, if the mixture is uniform, excitations can be expanded in terms of plane waves of momentum $\mathbf{k}$ and the Bogoliubov matrix becomes algebraic. As shown in Sec. 3.4, the diagonalization of the Bogoliubov matrix for an unpolarized mixture becomes much easier if the spinor basis is rotated by $\theta/2$ [see Eq.(3.19)], where $\theta = \arccos(Z) = \pi/2$ is the polar angle in the Bloch sphere. For a polarized mixture, it is therefore convenient to apply the following transformation to the Bogoliubov spinor:

$$\widetilde{M} = \begin{pmatrix} \cos(\theta/2) & 0 & \sin(\theta/2) & 0 \\ 0 & \cos(\theta/2) & 0 & \sin(\theta/2) \\ -\sin(\theta/2) & 0 & \cos(\theta/2) & 0 \\ 0 & -\sin(\theta/2) & 0 & \cos(\theta/2) \end{pmatrix} \tag{3.61}$$

It is worth pointing our that this transformation is legitimate only if θ (that is, the magnetization) is uniform in space.

The new spinor, whose elements are hereafter identified with the labels d (density) and s (spin), involves combination of the original perturbations $\delta\psi_1, \delta\psi_2$ weighted with the local fraction of atoms in each component: indeed $\cos(\theta/2) = \sqrt{n_1/n}$ and $\sin(\theta/2) = \sqrt{n_2/n}$. Unfortunately, the transformed Bogoliubov matrix does not have a block diagonal structure, but simplifies to:

$$\widetilde{M}\mathcal{L}\widetilde{M}^{-1} = \left(\begin{array}{c|c} \widetilde{\mathcal{L}}_d & (\sigma_3\mathbb{I})\alpha/2 \\ \hline (\sigma_3\mathbb{I})\alpha/2 & \widetilde{\mathcal{L}}_s \end{array}\right) \tag{3.62}$$

where the two diagonal blocks have the usual Bogoliubov structure:

$$\widetilde{\mathcal{L}}_d = \begin{bmatrix} \hbar^2k^2/2m + \tilde{\mu}_d & \widetilde{\mu}_d \\ -\widetilde{\mu}_d & -\left(\hbar^2k^2/2m + \widetilde{\mu}_d\right) \end{bmatrix} \tag{3.63}$$

$$\widetilde{\mathcal{L}}_s = \begin{bmatrix} \hbar^2k^2/2m + \hbar\widetilde{\Omega} + \widetilde{\mu}_s & \tilde{\mu}_s \\ -\widetilde{\mu}_s & -\left(\hbar^2k^2/2m + \hbar\tilde{\Omega} + \widetilde{\mu}_s\right) \end{bmatrix} \tag{3.64}$$

provided the definition of some effective parameters:

$$\widetilde{\mu}_d = \mu_d + \mu_s Z^2 - \Delta n Z \qquad \widetilde{\mu}_s = (1 - Z^2)\mu_s \qquad \widetilde{\Omega} = \frac{\Omega}{\sqrt{1 - Z^2}} \tag{3.65}$$

These quantities reduce to $\mu_d = Gn/2 = (g + g_{12})n/2$, $\mu_s = \kappa n/2 = (g - g_{12})n/2$ and Ω once we set $Z = 0$, and we recover the results of Section 3.4.

The mixing between density and spin modes is encoded in a single parameter

$$\alpha = \sqrt{1 - Z^2}(\kappa Z - \Delta)n \tag{3.66}$$

which vanishes only in the following cases:

(a) For the symmetric unpolarized mixtures considered in Section 3.4, characterized by $\Delta = (g_{11} - g_{22})/2 = 0$ and $Z = 0$;

(b) If all interaction constants are identical, so that $\kappa = \Delta = 0$;

(c) If the solution $Z = \Delta/\kappa$ corresponds to a stationary state of the system, that is, satisfies Eq. (3.51).

The eigenvalues of the two diagonal blocks $\mathcal{L}_{d,s}$ of the Bogoliubov matrix lead to the density and spin dispersion, which have the same structure of (3.26), (3.27):

$$\hbar\widetilde{\omega}_d^2(k) = \frac{\hbar^2k^2}{2m}\left(\frac{\hbar^2k^2}{2m} + 2\widetilde{\mu}_d\right) \tag{3.67}$$

$$\hbar\widetilde{\omega}_s^2(k) = \left(\frac{\hbar^2k^2}{2m} + \hbar\widetilde{\Omega}\right)\left(\frac{\hbar^2k^2}{2m} + \hbar\widetilde{\Omega} + 2\widetilde{\mu}_s\right) \tag{3.68}$$

We notice that the density dispersion does not depend directly on Ω, but only indirectly through the value of Z appearing in the definition of $\widetilde{\mu}_d$; moreover, such dependence is weak as long as $G \gg |\kappa|, |\Delta|$. On the contrary, the spin dispersion has a strong dependence on both Ω and Z: in particular, spin modes have entirely different nature depending on which stationary state one is considering (the absolute minimum, the local one or the maximum). For instance, dynamical instabilities appear in the spin sector if one considers the magnetization associated to a maximum of the potential U, while the density branch remains stable.

The exact eigenvalues of the Bogoliubov problem have energies given by the avoided crossing between the two branches $\widetilde{\omega}_{d,s}$, namely:

$$\omega_\pm^2(k) = \frac{\widetilde{\omega}_d^2(k) + \widetilde{\omega}_s^2(k)}{2} \pm \sqrt{\left(\frac{\widetilde{\omega}_d^2(k) - \widetilde{\omega}_s^2(k)}{2}\right)^2 + \frac{\alpha^2}{\hbar^2}\cdot\frac{\hbar k^2}{2m}\left(\frac{\hbar k^2}{2m} + \hbar\widetilde{\Omega}\right)} \tag{3.69}$$

For small α, $\omega_\pm(k)$ will deviate from $\widetilde{\omega}_{d,s}(k)$ close to the region where they cross [see, as an example, panel (a) of Fig.3.7]. Hence the two eigenstates will have density character for small momenta and spin character for high momenta or vice-versa.

Finally, it is worth pointing out that, even if the spin channel is dynamically stable ($\widetilde{\omega}_s^2 \geq 0$ for all k), the ω_- branch might become unstable due to the presence of the coupling α. This cannot happen if one is considering excitations over the ground state of the mixture (which must be dynamically stable), but might occur if the stationary state of interest corresponds to the relative minimum of the potential U in the ferromagnetic sector ($\kappa < 0$); an example is shown in Fig. 3.7(b). In other words the ferromagnetic metastable state with Z anti-aligned with respect to the external field B_3 might be dynamically unstable if the crossing point between $\widetilde{\omega}_d$ and $\widetilde{\omega}_s$ is at very low k, or equivalently, when the gap in the spin dispersion

$$\widetilde{\omega}_p = \sqrt{\widetilde{\Omega}(\widetilde{\Omega} + 2\widetilde{\mu}_s/\hbar)} \tag{3.70}$$

becomes small enough with respect to α. In formulas:

$$\frac{\hbar\widetilde{\omega}_p}{2|\widetilde{\mu}_s|} = \frac{\hbar\Omega/|\kappa|n}{(1-Z^2)^{3/2}}\sqrt{1 - \frac{(1-Z^2)^{3/2}}{\hbar\Omega/|\kappa|n}} \ll 1 \tag{3.71}$$

Since the condition $\hbar\Omega/|\kappa|n \to 0$ also implies $\sqrt{1-Z^2} \propto \hbar\Omega/|\kappa|n \to 0$, the only way to close the gap is to set the quantity under square root to zero. Recalling Eq.

(3.54), we conclude that the gap in $\widetilde{\omega}_s$ closes only if $Z = Z_*$, or, equivalently, when the detuning is close enough to the critical value defining the edge of the FM region: hence, due to the non-zero coupling α with the density channel, the ω_- branch of the dispersion shows dynamical instabilities. In other words, at the edge of the hysteresis region, the secondary minimum becomes unstable at the level of quantum fluctuations and indeed the system jumps to the true ground state.

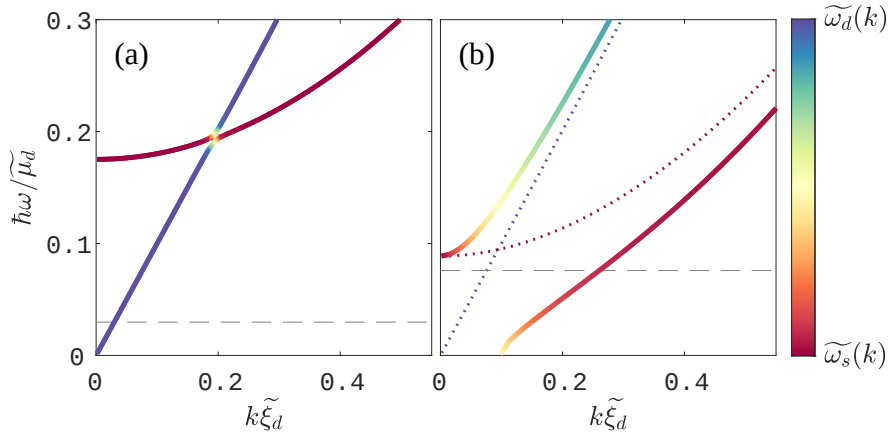

FIGURE 3.7: Dispersion relations $\hbar\omega_\pm(k)$ obtained for a ferromagnetic mixture with $\kappa/G = -0.1$, $\Delta = \kappa$ and $|\kappa|n/\hbar\Omega \simeq 1.5$. The effective detuning is set to $\delta_{\text{eff}} = 0.9\delta^*_{\text{eff}}$. Panels (a) and (b) refer to the stationary states associated to the absolute ($Z > 0$) and relative ($Z < 0$) minimum of the potential $U(Z, \varphi = 0)$. Notice how the interaction imbalance $\Delta \neq 0$ makes the coupling α between density and spin channels asymmetric with respect to the sign of Z. The dashed black line indicates the value of $\widetilde{\mu}_s$. The dotted curves represent the uncoupled spin and density dispersions $\widetilde{\omega}_{d,s}(k)$; the color scale is associated to the density/spin character of the modes.

3.6 Numerical details

Although the simplest configurations can be analysed analytically, most of those considered in this Thesis require a numerical solution. Simulations have been performed in one and two dimensions, typically in the presence of a trapping potential. Both physical (interactions, number of particles, temperature, etc...) and numeric (resolution, convergence threshold, etc...) parameters have been adapted to the various cases of interest. The main routines we used are listed in the following:

(a) The first task we needed to implement is the *initialization of the system in the ground state or in a stationary state of the Gross-Pitaevskii equations*. In the case of one-dimensional simulations, this is easily obtained with *imaginary time evolution*: the real time variable is replaced with an imaginary time $t \to \tau = it$ so that the time-evolution operator $e^{-i\mathcal{H}t} \to e^{-\mathcal{H}\tau}$ acts by lowering the energy of the system. We then solve the Gross-Pitaevskii equations in imaginary

time (by means of an Euler algorithm) until we converge in one of the minima of the energy landscape. For higher dimensional simulations (2D and above), imaginary-time evolution converges very slowly, thus it needs to be sped up by a *conjugate gradient algorithm* [103]: each imaginary time-step is chosen to minimize the energy of the state after the step itself.

As for all minimization algorithms, one must start sufficiently close to the stationary state of interest, to avoid getting stuck in a different minimum of the energy landscape. We typically choose as initial state the Thomas-Fermi solution of the stationary Gross-Pitaevskii equation and impose at every step eventual symmetries of the considered configuration.

(b) The *real-time evolution*, in the absence of both quantum and thermal fluctuations, is found by solving the time-dependent Gross-Pitaevskii equations by means of a *split-step algorithm*. At each step the time evolution operator is split into two parts: first the kinetic energy is applied in Fourier space, where it acts as a diagonal operator; then the wavefunction is transformed back to real space, where the potential acts trivially.

(c) The *exact diagonalization of the Bogoliubov problem* is performed using predefined routines in one dimension and for two-dimensional systems with cylindrical symmetry (so the problem could be reduced to an effectively one-dimensional one for the radial direction).

(d) The simplest way to include fluctuations in the simulation of the dynamics of BEC systems at low temperature T is via *truncated-Wigner simulations*: quantum and thermal fluctuations are included by averaging many Gross-Piteavskii time-evolutions obtained starting from different noisy initial configurations. The initial noise is built as follows: given some stationary state described by normalized wavefunctions (ψ_1, ψ_2), the associated Bogoliubov problem is solved to determine the mode profiles $\{u_{j\lambda}, v_{j\lambda}\}$, their eigenfrequencies ω_λ and their thermal populations $N_\lambda = \langle \hat{b}^\dagger_\lambda \hat{b}_\lambda \rangle = [\exp(\hbar\omega_\lambda / k_B T) - 1]^{-1}$. The initial state is:

$$\psi_j(x) = \beta_0 \phi_j(x) + \sum_{\lambda=1}^{\Lambda} \Big[\beta_\lambda u_{j,\lambda}(x) + \beta^*_\lambda v^*_{j\lambda}(x) \Big] \tag{3.72}$$

where all the coefficients $\beta_{\lambda\neq 0}$ are chosen so that $|\beta_\lambda|$ is a gaussian distributed variable with zero mean and variance $\sigma^2_\lambda = N_\lambda + 1/2 = [2\tanh(\hbar\omega_\lambda / 2k_B T)]^{-1}$, and $\arg(\beta_\lambda)$ is a random variable. The number of non-condensed particles associated to a single sample is then computed as:

$$N_{th} = \sum_{\lambda=1}^{\Lambda} \sum_{j=1,2} \int \left[\Big(|\beta_\lambda|^2 - \frac{1}{2} \Big) |u_{j\lambda}|^2 + \Big(|\beta_\lambda|^2 + \frac{1}{2} \Big) |v_{j\lambda}|^2 \right] \mathrm{d}x \tag{3.73}$$

and the first coefficient is set to $\beta_0 = \sqrt{N - N_{th}}$, N being the total number of atoms. Each sample is evolved classically using the Gross-Pitaevskii equation. Finally, statistical averages of all the fields' quadratures, namely of the elements

of the spin vector, is made, and from those we compute all the relevant quantities (total density, magnetization, relative phase, etc...)

Despite being commonly used to include the lowest quantum and thermal corrections to the Gross-Pitaevskii equation, Truncated-Wigner simulations can have implementation issues, especially for what concerns the long-time dynamics: it has been shown [104] that Wigner noise quickly thermalizes to a classical field distribution at a temperature T_Λ that is always larger than the physical temperature T and depends on the cutoff Λ on the number of Bogoliubov modes included in the simulation (or, equivalently, on the grid spacing `dx`).

In Chapter 6 we discuss a physical phenomenon for which Truncated-Wigner simulations have proven to be unreliable.

(e) The dynamics of the mixture at high temperature is computed with *classical field simulations*: given some stationary state defined by (ψ_1, ψ_2), we inject energy in the system by locally adding, independently to both components' densities, random noise of amplitude εn_j where n_j is the local density of the j-th component and $\varepsilon \ll 1$; the noise amplitude ε determines the amount of injected energy per particle $\delta E/N$. We then let the system thermalize. Under an ergodicity assumption, we can determine the dynamics of the system by averaging over many repetitions of the same time-evolution, each one obtained starting from a different noisy sample. In other words, we perform mean-field simulations in which initial noise plays the role of an effective temperature. Of course, these do not allow to investigate the role of quantum fluctuations: this procedure is thus justified only if the temperature is high enough to guarantee that the dynamics is driven by thermal noise.

Compared to other numerical techniques [105], our procedure does not allow to fix a priori the thermalization temperature. However it is much well-suited to reproduce experimental preparation procedures during which the system might be driven out of thermal equilibrium, and could be readily extended to simulate systems in more than one spatial dimension.

3.7 Experimental details

Chapter 6, as well as some of the results shown in this Chapter (see Figs. 3.4, 3.6) is the results of a collaboration with the experimental team of the Pitaevskii Center for Bose-Einstein condensation in Trento: despite the main focus of this Thesis will be on analytical and numerical calculations, attention is given to the experimental feasibility and/or limitations of the proposed set-ups.

The experiment starts from the preparation of a BEC of $N \sim 10^6$ Sodium-23 atoms in the $|F, m_F\rangle = |1, -1\rangle$ internal state, F being the total atomic angular momentum and m_F its projection on the quantization axis, set by a uniform magnetic field. The BEC is held in a axially symmetric optical trap that can be described as an harmonic external potential:

$$V(\mathbf{r}) = \frac{1}{2} m(\omega_r^2 r^2 + \omega_x^2 x^2) \tag{3.74}$$

where $r = \sqrt{y^2 + z^2}$ is the radial coordinate. The trapping frequencies are chosen so to have a much stronger confinement along the radial direction $\omega_r \gg \omega_x$: the condensate is thus cigar-shaped and elongated along x. Nonetheless, the radial trapping frequency is not large enough to make it a quasi-1D system: the ground state density is well approximated by Thomas-Fermi (TF) profile in all three space directions with TF radii $L = \sqrt{2\mu/m\omega_x^2}$ and $R = \sqrt{2\mu/m\omega_r^2} \ll L$. In other words, the transverse dimension of the cloud R is always larger than its healing length ξ or, equivalently, $\mu \gg \hbar\omega_r$.

Binary mixtures can be obtained by transferring atoms to other hyperfine levels by means of Rabi or Raman processes:

1. The mixture considered in Refs. [57, 106, 107] is characterized by $g_{12} = 0.93g$ (where $g = g_{11} = g_{22}$) and is prepared by transferring half of the population to the $|1, 1\rangle$ level. Since $\kappa := g - g_{12} = 0.07g > 0$, this mixture can only show a paramagnetic phase, but is miscible even if $\Omega = 0$.

2. The mixture considered in Chapter 6 and in Refs. [77, 85, 108] is characterized by $g_{12} \simeq g_{22} \simeq 1.2g_{11}$ and is obtained by transferring atoms to the $|2, -2\rangle$ hyperfine state. Since $\kappa \simeq \Delta \simeq -0.08g < 0$, the mixture is immiscible in the absence of coherent coupling, while it can show both a paramagnetic and a ferromagnetic phase depending on the value of $\Omega \neq 0$.

The experimental apparatus allows to independently tune the (spatially uniform) values of Ω, δ, so to explore the whole phase diagram of Fig. 3.5. The stability of the coherent coupling is guaranteed by a magnetic shield that suppresses fluctuations by several orders of magnitude [109].

The setup gives direct access to the atomic densities of the two components: the trapping potential is suddenly removed and the atoms in the two hyperfine states are selectively imaged after a short time of flight (TOF). Due to the short duration of the TOF stage and to the axial symmetry of the trapping potential, the elongated condensate expands only in the transverse directions, leaving the axial distribution practically unchanged. Integration of the absorption images along the transverse direction allows to compute the effective 1D atomic densities of the two components.

3.7.1 Geometrical reduction

Given the elongated shape of the system, and that the relevant dynamics occurs along the longitudinal direction x, it is convenient to treat the problem in a reduced dimensionality by integrating out the transverse degrees of freedom; this will require the definition of some effective parameters, to take into account the 3D geometry of the cloud. More specifically, we are interested in the effective dispersion relation for longitudinal Bogoliubov modes, whose frequency is expected to satisfy the condition $\omega_z \ll \omega \ll \omega_r$ [110]. Let us restrict to the simplest case of an unpolarized mixture, for which we can separately treat density and spin collective modes.

Our calculation starts from the Bogoliubov-de Gennes equations, with the assumptions $\mathbf{v} = 0$ (that, in turn, implies that the total density n does not vary in time) and $\delta n_j(\mathbf{r}, t) = w(r)f(x, t)$; the dimensionless function f describes the (effective) longitudinal mode, while $w(r)$ is the time-independent radial profile of the perturbation. For the sake of simplicity we neglect for the moment the presence of the longitudinal trap

($\omega_x = 0$), so that $n(\mathbf{r}) \to n(r)$. Moreover, we assume that $n(r)$ is well approximated by the TF density profile associated to the harmonic potential (3.74): in formulas, the density healing length is much smaller than the transverse size of the condensate, $\xi_d \ll R$. The TF assumption guarantees that the hydrodynamic regime is satisfied in the density channel and Eqs. (3.37) can be written as:

$$\partial_t^2(\delta n_d) + \frac{Gn(r)}{\hbar}\mathcal{D}(\delta n_d) = 0 \tag{3.75}$$

When the operator $\mathcal{D}$, defined as in (2.34), acts on a generic function that depends both the longitudinal and transverse coordinate, it provides multiple terms:

$$\mathcal{D}\big[w(r)f(x)\big] = -\frac{\hbar}{2m}\left\{w(r)\partial_x^2 f(x) + \left[\partial_r^2 w(r) + \partial_r w(r)\frac{\partial_r n(r)}{n(r)}\right] f(x)\right\} \tag{3.76}$$

Of these, those involving derivatives along the transverse direction give a contribution of the order of $\hbar/mR^2 \propto \omega_r^2$. Since we are looking for modes with frequencies well below the transverse trapping frequency [110], it is natural to choose $w(r) \propto n_0\Theta(R-r)$, where $n_0 = n(\mathbf{0})$ is the peak density; with this uniform radial profile, the operator $\mathcal{D}$ reduces to the kinetic energy along x:

$$\Theta(R-r)\partial_t^2 f(x,t) = \frac{Gn(r)}{2m}\partial_x^2 f(x,t) \tag{3.77}$$

Integration along r on both sides leads to an effective wave equation for the longitudinal profile of the mode, $\partial_t^2 f = (\mu_d/m)\partial_x^2 f$, with:

$$\mu_d = \frac{G}{2\pi R^2}\int n(r)\mathrm{d}\mathbf{r} = \frac{1}{2}\cdot\frac{Gn_0}{2} \tag{3.78}$$

We conclude that the effective longitudinal speed of density-sound $c_d = \sqrt{\mu_d/m}$ is reduced by a factor $\sqrt{2}$ with respect to the peak one, due to the harmonic trapping along the transverse direction [110].

Let us now repeat the same calculation for spin modes. Since the Thomas-Fermi assumption does not guarantee the validity of the hydrodynamic approximation in the spin channel, one must consider the full Bogoliubov-de Gennes equations:

$$\partial_t^2(\delta n_s) + n(r)(\mathcal{D}+\Omega)\left[\frac{\kappa n(r)}{\hbar} + \Omega + \mathcal{D}\right]\frac{\delta n_s}{n(r)} = 0 \tag{3.79}$$

If $\Omega = 0$ and spin modes are also hydrodynamic (that is, $R \gg \xi_s$ or $\mu_s \gg \omega_r$), Eq. (3.79) takes the same form as (3.75) apart from the substitution $G \to \kappa$: the effective longitudinal speed of spin-sound $c_s = \sqrt{\mu_s/m}$ is also reduced by a factor $\sqrt{2}$ with respect to its peak value, since $\mu_s = (1/2)\kappa n_0/2$.

On the contrary, if $\xi_s \gtrsim R$, the operator $\mathcal{D}$ dominates over $\kappa n/\hbar$ in the square bracket of Eq.(3.79); similarly, in the presence of a coherent coupling, the term Ω dominates over $\kappa n/\hbar$ for sufficiently large r, where the derivative $\partial_r n/n$ [see Eq. (3.76)] is largest. In both cases, modes with low frequency $\omega \ll \omega_r$ are found by assuming $w(r) = n(r)$, so that the magnetization $\delta n_s/n = f(x,t)$ is independent on

the transverse coordinate and almost all the derivatives with respect to r vanish:

$$n(r)\partial_t^2 f + \left(\Omega - \frac{\hbar}{2m}\partial_x^2\right)\left(\frac{\kappa n(r)}{\hbar} + \Omega - \frac{\hbar}{2m}\partial_x^2\right) n(r) f = \frac{\kappa}{2m}\vec{\nabla}(n\vec{\nabla}n) f \tag{3.80}$$

Integration along r makes the term on the right-hand-side vanish: indeed the density vanishes at the Thomas-Fermi radius; the remaining contributions give:

$$\partial_t^2 f(x,t) + \left(\Omega - \frac{\hbar}{2m}\partial_x^2\right)\left(2\mu_s + \Omega - \frac{\hbar}{2m}\partial_x^2\right) f(x,t) = 0 \tag{3.81}$$

where we have defined:

$$\mu_s = \frac{\kappa}{2}\frac{\int n^2(r)\mathrm{d}\mathbf{r}}{\int n(r)\mathrm{d}\mathbf{r}} = \frac{2}{3}\cdot\frac{\kappa n_0}{2} \tag{3.82}$$

The same factor 2/3 was found, starting from the Landau-Lifshitz equation (3.58), in Ref. [85]. This result implies that, in the absence of coherent coupling, the speed of spin sound is renormalized by a factor $\sqrt{2/3}$ with respect to its peak value. In other words, the hydrodynamic nature of spin excitations not only influences the curvature of the Bogoliubov dispersion at high k, but has also a non-negligible effect on the geometric renormalization of the value of the speed of sound. In particular, if $\xi_d \ll R \lesssim \xi_s$, the ratio between the effective speeds of sound of density and spin modes is $c_d/c_s = \sqrt{3G/4\kappa}$, roughly 15% smaller than the expected peak value $\sqrt{G/\kappa}$. This result has been experimentally verified in [57] (see Fig.3.4).

The same calculation can be performed for two-dimensional systems (or, equivalently, for radial collective modes of pancake-shaped condensates): since only one transverse dimension has to be integrated out, the geometric renormalization coefficients in Eq. (3.78), (3.82) are 2/3 and 4/5, respectively.

3.8 Summary

Coherently-coupled binary mixtures of atomic Bose-Einstein condensates are characterized by an extremely rich phase diagram, as shown in Fig. 3.5: in particular, the magnetic properties of these systems can be accurately controlled by tuning the strength and detuning of the external field coupling the two components [77]. In each magnetic phase, the binary mixture shows specific features which can be exploited in the context of *analog gravity*.

Paramagnetic unpolarized mixtures, both with and without a resonant coherent coupling, have two independent channels of elementary excitations (that we refer to as density and spin modes), associated to perturbations of the total and relative density. Within certain parameters ranges, long-wavelength modes of both branches show a phononic behaviour, with different speed of sound; hence, their dynamics is analog to that of a scalar field in a curved spacetime, whose geometry is encoded in a metric tensor with the same structure as (2.41). Moreover, the effective mass of spin excitations is tunable via the Rabi frequency: this represents the first conceptual advantage of working with binary mixtures rather than single-component condensates. In addition to this, exploring the gravitational analogy in the spin channel of a two-component BEC might be convenient in a practical sense, namely in the experimental

implementation of configurations of interest: typical parameters lead to a much smaller speed of sound for spin modes and thus to a much larger healing length; furthermore, all the field quadratures, including the relative phase between the two components, are experimentally accessible. In Chapters 4 and 5 we study the analog version of two astrophysical phenomena (*Hawking radiation* and *superradiance*, respectively) for which these properties of spin modes appear to be beneficial.

If spin interactions dominate over the coherent coupling, binary mixtures behave instead as ferromagnetic superfluids; as anticipated, this rare combination of features opens the possibility of studying magnetism in the absence of dissipation, defects and decoherence. In Chapter 6, we analyse the relaxation mechanism of the mixture when prepared in a metastable stationary state: this process, known as *false vacuum decay*, has important applications in cosmology.

4 Hawking radiation from spin-sonic black-holes

4.1 Introduction

As mentioned in Chapter 2, the astrophysical phenomenon that has attracted the most attention in the analog gravity community is *Hawking emission*: according to Hawking prediction [28, 29], black holes of mass M are expected to radiate as black bodies with temperature:

$$k_B T_H = \frac{\hbar c^3}{8\pi G M} \tag{4.1}$$

as a result of the interplay between quantum fluctuations and the curvature of space-time in the vicinity of the singularity. Without any accretion meccanism, Hawking emission eventually leads to the evaporation of the black hole [28]. For typical black-hole masses, the Hawking temperature (4.1) is orders of magnitude smaller than the cosmic microwave background (CMB) temperature ($\sim 2.7K$) and the evaporation time longer than the age of the Universe: these are among the reasons why Hawking emission has so far escaped direct observation in the astrophysical context.

The kinematic nature of the Hawking effect [111] offers the possibility, through the gravitational analogy [25], of observing this phenomenon (i.e. the spontaneous creation of particles due to vacuum fluctuations in a curved-space field theory) on experimentally accessible platforms, including classical fluids [8, 9], polaritons [11], optical systems [13] and ultracold gases [10]. In the analog context, sonic horizons are generated by engineering a steadily-flowing stationary state that features a point-of-no-return for elementary excitations, at which the flow velocity v exceeds the speed of sound c; for Bose-Einstein condensates in the hydrodynamic regime, the analog Hawking temperature is given by [30, 111]:

$$k_B T_H = \frac{\hbar}{2\pi} \frac{\partial (c - v)}{\partial n} \tag{4.2}$$

Despite the physical temperature of ultracold atomic gases being often larger than the analog Hawking temperature characterizing the emission, its direct observation is still possible by analysing the two-point correlations between excitations propagating on the two sides of the horizon [38, 39, 112]; indeed, this obervable is robust against temperature effects [38] and it has been exploited to claim the first experimental observation of the Hawking effect in a single component condensate [40–42].

This Chapter is devoted to the theoretical study of the Hawking process for spin modes in a binary mixture of Bose-Einstein condensates: after reviewing the spin-sonic black-hole configuration considered in Ref. [43], we extend it to include a resonant

coherent-coupling between the two components, in the spirit of Refs. [44, 45]. Our purpose is two-fold: on the one hand, dealing with spin modes in a mixture allows us to conceptually extend the analysis to massive excitations; on the other hand, we aim to identify observables that, as density correlations, encode a recognizable signal associated with Hawking emission, but might be more convenient or easier to measure in an experiment.

Differently from [44, 45], we do not restrict our analysis to small values of the Rabi frequency. All our calculations are based on zero-temperature Bogoliubov theory; since we do not make use of the gravitational analogy (that is, we do not restrict to the hydrodynamic regime), we can safely consider parameters regimes for which a one-by-one correspondence with the astrophysical context cannot be made, but that are closer to typical experimental conditions [57]. As we will see, the notion of analog horizon can be straightforwardly extended to parameters ranges that do not allow the definition of a speed of sound, and the features characterizing the emission are preserved in such non-relativistic regime.

4.2 The spin-sonic black hole

The first ingredient one needs to study analog Hawking radiation in a Bose-Einstein condensate is a fluid flow that mimics a black hole geometry. The simplest configuration with this property involves a uniform one-dimensional system steadily flowing with velocity v [38, 39, 112]; a step-like modulation of the interaction constant

$$g(x) = g_u\Theta(-x) + g_d\Theta(x) \tag{4.3}$$

where Θ is the Heaviside step function, separates the upstream region (for $x < 0$, labelled u) region, where the flow is subsonic, that is $c_u = \sqrt{g_u n/m} > v$, from the downstream region (for $x > 0$, labelled d), which is instead supersonic, $c_d = \sqrt{g_d n/m} < v$. The surface $x = 0$ plays thus the role of an analog sonic horizon. It is clear that the interaction profile (4.3) breaks the hydrodynamic approximation and indeed Eq.(4.2) would predict an infinite Hawking temperature. More realistic configurations involving a smoother horizon and/or inhomogeneous density profiles, which reproduce more closely the experimental conditions [40], have also been considered in the literature (see, for instance, [30, 112]), but, remarkably, the features of the Hawking signal are qualitatively identical. In particular, the emission temperature T_H is always finite and of the order of μ/k_B, where μ is the chemical potential of the system.

For the sake of simplicity, we will only analyse the simplest and analytically tractable case of a step modulation of the interaction constants in a uniform system. Our aim is, in particular, to generalize such configuration to the spin channel of an unpolarized binary mixture with $n_1 = n_2 = n/2$: as we discussed in Chapter 3, the $\mathbb{Z}_2$ symmetry of the system implies a complete decoupling between the dynamics of excitations of the total and relative density. Let us then consider a uniform binary mixture of total density n and assume that a spin-sonic horizon is generated by a step modulation of the spin interaction constant:

$$\kappa(x) = \kappa_u\Theta(-x) + \kappa_d\Theta(x) \tag{4.4}$$

whereas the density interaction constant $G = g + g_{12}$ is uniform in space, so that no analog horizon is seen by density modes. A similar configuration was analysed in [43]. In addition to a modulation of the interaction constant, we also assume that a resonant Rabi field couples the two components:

$$\Omega(x) = \Omega_u \Theta(-x) + \Omega_d \Theta(x) \tag{4.5}$$

According to (3.17), there exists a stationary state of the mixture of the form

$$\psi_1(x,t) = \psi_2(x,t) = \sqrt{n/2}\, e^{iqx} e^{-i\mu t/\hbar} \tag{4.6}$$

where $q = mv/\hbar$ is the momentum associated with the fluid flow and

$$\mu = \frac{\hbar^2 q^2}{2m} + V(x) + \frac{1}{2}Gn - \frac{\hbar\Omega(x)}{2} \tag{4.7}$$

is the chemical potential. Notice that if $\Omega_u \neq \Omega_d$, the jump at $x = 0$ in the Rabi frequency has to be compensated by an external potential, $V(x) = \hbar\Omega(x)/2$, in order to guarantee the stationarity of the state (4.6). If v does not exceed the speed of density-sound, the stationary flow is everywhere subsonic with respect to density excitations; in other words, it is possible to generate a spin-sonic horizon without generating a density-sonic one.

It is worth pointing out that, in order to reproduce this toy model in the lab, it is not necessary to realize quasi-onedimensional condensates: indeed, as discussed in Chapter 3, the dynamics of spin modes can be effectively one-dimensional, even though the density profile is well approximated by the Thomas-Fermi solution.

Since the dynamics of density modes is trivial, throughout this Chapter we will exclusively consider spin excitations; let us then avoid using the index s associated to quantities (dispersion relation, speed of sound, structure factor, etc...) in the spin channel, for legibility; the indexes u, d will be instead used to distinguish parameters' values in the upstream and downstream regions, respectively.

In the presence of a coherent coupling, the dispersion relation for spin modes in the comoving frame (3.27) is gapped and a definition of the speed of sound is only possible in a limited range of parameters' values, that is, in the regimes of validity of the gravitational analogy (3.40),(3.41). In any other case, the role of the speed of sound is played by the Landau critical velocity, defined as

$$c_{d,u} \equiv \min_k \frac{\omega^+(k, x \gtrless 0)}{|k|} \tag{4.8}$$

In other words, in order to generate an analog horizon for spin modes, it is necessary to fix the parameters (4.4), (4.5) so that the Landau critical speed is larger than the flow velocity in the upstream region, $c_u > v$, and smaller than the flow velocity in the downstream region, $c_d < v$. As already pointed out, only in the absence of a gap in the spin dispersion, $c_{u,d}$ coincides with the sound-speed; however, by analogy with the gapless case, in the following we will sometimes refer to the upstream and downstream regions as subsonic and supersonic, respectively.

It is worth noticing that the condition $c_d < v$ is necessary to obtain an analog horizon: negative norm modes in the downstream region, once Doppler-shifted, acquire

positive frequency and thus have negative energy in the lab frame. The existence of these solutions is the key ingredient that enables the onset of Hawking physics: pairs of particles with opposite energy can be emitted on the two sides of the horizon, while conserving the total energy of the system.

A schematic drawing of the spin-sonic black hole configuration that we consider throughout this Chapter is shown in Fig. 4.1. Typical examples of dispersion relations in some regimes of interest are reported in Figs. 4.2 - 4.6.

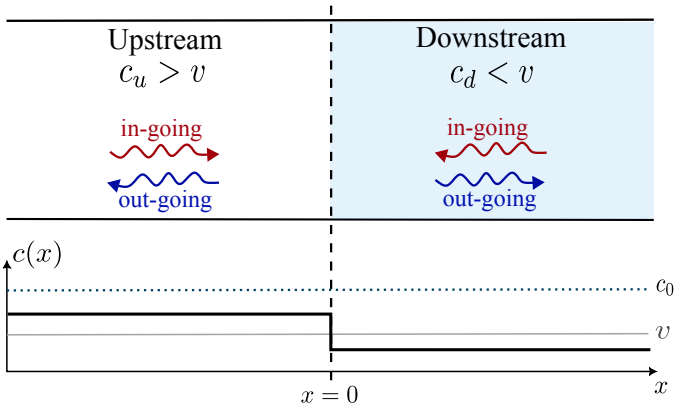

FIGURE 4.1: Schematic of the analog black-hole configuration considered in the text. The analog horizon, located at $x = 0$, separates a subsonic (upstream, u) region where the Landau critical speed for spin modes c_u exceeds the flow velocity v, from a supersonic (downstream, d) region, where instead the opposite holds $v > c_d$. This step configuration can be realized while keeping the speed of density-sound $c_0 = \sqrt{Gn/2m}$ uniform and larger than v, so that the density channel is everywhere subsonic. The red (blue) arrows indicate the group velocity direction for in-going (out-going) modes.

Analog Hawking radiation of massive particles in a spin-sonic black-hole configuration with homogeneous coherent coupling ($\Omega_u = \Omega_d \neq 0$) has been characterized in Ref. [44, 45]: in this case the requirement $c_u > v > c_d$, necessary to have an horizon, constraints the Rabi frequency in a limited range of extremely small values. In order to be able to explore different regimes, we allow the coherent coupling to have different intensities on the two sides of the horizon, $\Omega_u \neq \Omega_d$. Moreover, since the presence of a gap in the upstream region reduces the intensity of particles emitted in the black-hole exterior [44], we also set $\Omega_u = 0$. The absence of a gap in the upstream region allows us to define a speed of sound $c_u = \sqrt{\kappa_u n/2m}$, interaction energy $\mu_u = \kappa_u n/2$ and a healing length $\xi_u = \hbar/mc_u$ for spin modes propagating in the black-hole exterior, whose frequency is given by a Doppler-shifted gapless Bogoliubov dispersion:

$$\omega_u^{\pm}(k) = vk \pm c_u|k|\sqrt{1 + \frac{\xi_u^2 k^2}{4}} \tag{4.9}$$

The condition $c_u > v$ guarantees that propagating modes with real wave-vector and positive frequency necessarily have positive norm.

On the contrary, let us assume the coherent coupling is not necessarily vanishing in the downstream region. We will focus on four regimes of conceptual interest:

(a) The standard gapless case in the absence of coherent coupling ($\Omega_d = 0, \kappa_d > 0$), already analysed in Ref.[43] and shown in Fig. 4.2.

(b) The relativistic gapped case, obtained with $\Omega_d \ll \kappa_d n/\hbar$ and κ_d positive, shown in Fig. 4.4. This regime was considered in Ref.[44] for a uniform Rabi frequency. Notice that typical values of the interaction constants lead to $\kappa \ll G$, so this relativistic regime is hardly accessible experimentally: as an example, for the mixture in [57], $\kappa n \sim 300$ Hz, thus it would be necessary to control the Rabi frequency at the level of a few Hz.

(c) The vicinity of the critical point for the para-to-ferromagnetic phase transition ($\hbar\Omega_d + \kappa_d n \sim 0$, with κ_d negative, as in Fig. 4.5). Once again, an experimental realization of this configuration seems hard to achieve, mostly due to the change of sign of κ on the two sides of the horizon, which would necessarily require the availability of a Feshbach resonance [113]; moreover, in the proximity of a critical point the system is extremely sensitive to any source of noise. However, it is interesting to compare the Hawking emission in cases (b) and (c), due to the very different properties of spin modes in these two relativistic regimes.

(d) The non-relativistic case $\hbar\Omega_d \gg |\kappa_d| n$, to which the gravitational analogy does not apply (shown in Fig. 4.6). Despite the absence of a one-by-one correspondence with a curved spacetime geometry, this regime is the easiest to access in a lab among the ones with $\Omega_d \neq 0$.

From the perspective of the gravitational analogy, varying the intensity of the coherent coupling in the downstream region Ω_d keeping $\Omega_u = 0$ amounts to changing the nature of the analog black-hole (in particular its greybody factor, as we will see later on), without affecting the spacetime geometry of the black-hole exterior.

For generic values of Ω_d, the role of the speed of sound is replaced by the Landau critical velocity. A direct calculation from (4.8) leads to:

$$mc_d^2 = \frac{\kappa_d n}{2} + \hbar\Omega_d + \sqrt{\hbar\Omega_d(\hbar\Omega_d + \kappa_d n)} \tag{4.10}$$

Notice that $c_d \simeq \sqrt{|\kappa_d| n/2m}$ coincides with the speed of sound in the two relativistic regimes $\Omega_d \sim 0$ and $\Omega_d + \kappa_d n/\hbar \sim 0$, while, in the opposite limit $\hbar\Omega_d \gg |\kappa_d| n$, in which the gravitational analogy breaks, we find the density-independent value $c_d \sim \sqrt{2\hbar\Omega_d/m}$. The supersonic condition $c_d < v$ is verified by choosing the parameters in the downstream region such that:

$$1 - \frac{\kappa_d n}{2mv^2} > \sqrt{\frac{2\hbar\Omega_d}{mv^2}} \tag{4.11}$$

As already pointed out, this requirement guarantees the existence of a range of positive frequencies ($0 < \omega < \omega_*$) for which both positive and negative norm modes with real momentum exist in the downstream region, with dispersion given by:

$$\omega_d^{\pm}(k) = kv \pm \sqrt{\left(\frac{\hbar k^2}{2m} + \Omega_d\right)\left(\frac{\hbar k^2}{2m} + \Omega_d + \frac{\kappa_d n}{\hbar}\right)} \tag{4.12}$$

The threshold frequency is $\omega_* = \max[\omega_d^-(x)]$.

4.3 The scattering matrix formalism

As a first step towards the study of analog Hawking physics in BEC mixtures, we analyse the scattering properties of the spin-sonic horizon. The formalism has been first developed to characterize single component systems [38, 39], and then extended to treat two-component mixtures in the absence of coherent coupling [43] or in the relativistic regime $\hbar\Omega \ll \kappa n$ [44, 45]. Since it does not rely on the gravitational analogy but exclusively on the validity of Bogoliubov theory, it can be exploited in any parameters' range.

As already pointed out, we consider the analytically tractable case of a uniform unpolarized mixture of total density n, so that field perturbations are easily written as a sum of plane waves. However, given the stationarity of our configuration, it is convenient to work in frequency rather than momentum space. Due to particle-hole symmetry, we can restrict to positive frequencies provided we account for both signs of the Bogoliubov norm. For each frequency $\omega > 0$ in the laboratory frame, there exist four solutions to the equation $\omega^{\pm}_{u,d}(k) = \omega$ in both the subsonic and supersonic regions. In the upstream region, we find two positive norm modes with real k (green dots in Figs. 4.2 - 4.6, labelled u), in addition to two negative norm modes with complex conjugate momenta $\Re(k) \pm i\Im(k)$ (not shown): of these, one is exponentially growing for $x \to -\infty$, and thus represents an unphysical solution, while the other is evanescent in the same limit and contributes to the perturbation only close to the horizon. The same holds in the downstream region if $\omega > \omega_*$; if instead $\omega < \omega_*$ four propagating solutions with real momentum exist, two with positive norm (red dots in Figs. 4.2 - 4.6, labelled $d1$) and two with negative norm (blue dots in Figs. 4.2 - 4.6, labelled $d2$). Among all the real-k modes, some move towards the sonic horizon (in-going, labelled *in*), while others propagate away from it (outgoing, labelled *out*), depending on the sign of their group velocity $w_k \equiv \partial\omega/\partial k$.

Table 4.1 summarizes all the main properties (wavevector, group velocity, norm) of the available spin modes, including evanescent ones, in the upstream and downstream regions, for all the different frequency ranges.

Mode	Region	Wave-vector	Group velocity	Frequency range	Norm
u|in	$x<0$	$k_u^{\rm in}(\omega)>0$	$w_u^{\rm in}(\omega)>0$	$\omega>0$	$+1$
u|out	$x<0$	$k_u^{\rm out}(\omega)<0$	$w_u^{\rm out}(\omega)<0$	$\omega>0$	$+1$
u|ev	$x<0$	$\Im(k_u^{\rm ev})<0$	–	$\omega>0$	–
$d1$|in	$x>0$	$k_{d1}^{\rm in}(\omega)<0$	$w_{d1}^{\rm in}(\omega)<0$	$\omega>0$	$+1$
$d1$|out	$x>0$	$k_{d1}^{\rm out}(\omega)>0$	$w_{d1}^{\rm out}(\omega)>0$	$\omega>0$	$+1$
d|ev	$x>0$	$\Im(k_d^{\rm ev})>0$	–	$\omega>\omega_*$	–
$d2$|in	$x>0$	$k_{d2}^{\rm in}(\omega)>0$	$w_{d2}^{\rm in}(\omega)<0$	$0<\omega<\omega_*$	-1
$d2$|out	$x>0$	$k_{d2}^{\rm out}(\omega)>0$	$w_{d2}^{\rm out}(\omega)>0$	$0<\omega<\omega_*$	-1

TABLE 4.1: Summary of the main properties of the available Bogoliubov spin-modes for the analog black-hole configuration in Fig. 4.1.

Far from the sonic horizon ($|x| \to \infty$), the generic scattering solution at frequency ω is a eigenfunction of the spin Bogoliubov operator (3.22) of the form:

$$\begin{aligned}\begin{bmatrix}\mathscr{U}(x,\omega)\\ \mathscr{V}(x,\omega)\end{bmatrix} = &\sum_r \alpha_r \begin{bmatrix}U_r^{\rm in}(\omega)\\ V_r^{\rm in}(\omega)\end{bmatrix} \frac{e^{ik_r^{\rm in}(\omega)x}}{\sqrt{|w_r^{\rm in}(\omega)|}}\Theta_r(x)\\ &+\sum_r \beta_r \begin{bmatrix}U_r^{\rm out}(\omega)\\ V_r^{\rm out}(\omega)\end{bmatrix} \frac{e^{ik_r^{\rm out}(\omega)x}}{\sqrt{|w_r^{\rm out}(\omega)|}}\Theta_r(x)\end{aligned} \tag{4.13}$$

where the sum runs over the three branches and includes all the propagating modes available at frequency ω, separated into ingoing and outgoing ones. In particular, $r \in \{u, d1, d2\}$ if $\omega < \omega_*$ and $r \in \{u, d1\}$ if $\omega > \omega_*$.

In the vicinity of the horizon ($x \sim 0$), one must include exponentially suppressed modes in the expansion by adding to Eq.(4.13) a term of the form:

$$+\sum_r \gamma_r \begin{bmatrix}U_r^{\rm ev}(\omega)\\ V_r^{\rm ev}(\omega)\end{bmatrix} e^{ik_r^{\rm ev}(\omega)x}\Theta_r(x) \tag{4.14}$$

where $r \in \{u\}$ if $\omega < \omega_*$ and $r \in \{u, d\}$ if $\omega > \omega_*$.

The Heaviside Theta functions $\Theta_r(x)$ are necessary to ensure that the mode u (the modes $d1, d2$) contributes to the solution only in the upstream (downstream) region $x < 0$ ($x > 0$):

$$\Theta_u(-x) = \Theta_{d1}(x) = \Theta_{d2}(x) = \begin{cases}0 & \text{if } x < 0\\ 1 & \text{if } x > 0\end{cases} \tag{4.15}$$

The normalization involving the group velocity guarantees that the orthonormality condition is fulfilled in frequency space. The particle and antiparticle components (U, V) are solutions of the Bogoliubov problem in the comoving frame; as such

$$|U_r^{\rm in}(\omega)|^2 - |V_r^{\rm in}(\omega)|^2 = |U_r^{\rm out}(\omega)|^2 - |V_r^{\rm out}(\omega)|^2 = \sigma_r \tag{4.16}$$

where $\sigma_u = \sigma_{d1} = -\sigma_{d2} = +1$ is the Bogoliubov norm of the mode.

In general the coefficients of in-going and out-going modes are related through a scattering matrix $\mathcal{M}(\omega)$ of dimension $D \times D$, where D is the number of in-going and out-going modes available at frequency ω. More specifically, if $\omega < \omega_*$ propagating modes are available in all three branches:

$$\begin{bmatrix}\beta_u\\ \beta_{d1}\\ \beta_{d2}\end{bmatrix} = \mathcal{M}(\omega) \begin{bmatrix}\alpha_u\\ \alpha_{d1}\\ \alpha_{d2}\end{bmatrix} \tag{4.17}$$

while, if $\omega > \omega_*$ (or if neither of the two regions is supersonic), we find:

$$\begin{bmatrix}\beta_u\\ \beta_{d1}\end{bmatrix} = \mathcal{M}(\omega) \begin{bmatrix}\alpha_u\\ \alpha_{d1}\end{bmatrix} \tag{4.18}$$

The coefficient $\mathcal{M}_{rr'}(\omega)$ describes the scattering of the r'-th in-going mode onto the r-th out-going one. The square modulus $|\mathcal{M}_{rr'}(\omega)|^2$ represents therefore the reflectivity/transmittivity of the in-going mode r' into the out-going mode r. In order to

guarantee energy conservation, $\mathcal{M}$ must satisfy the normalization condition:

$$\mathcal{M}^\dagger \eta \mathcal{M} = \eta = \mathcal{M} \eta \mathcal{M}^\dagger \tag{4.19}$$

where η is a diagonal square matrix of dimension D whose diagonal elements coincide with the norm of the available modes, that is $\eta_{rr'} = \sigma_r \delta_{rr'}$. If the $d2$ branch is not available, $\eta = \mathrm{diag}(1,1)$ coincides with the identity matrix and $\mathcal{M}$ is unitary: we deal with a standard scattering problem in which only positive energy modes are involved; each incoming packet is partially transmitted and partially reflected, and the transmittivity and reflectivity sum up to 1:

$$|\mathcal{M}_{ur}|^2 + |\mathcal{M}_{d1r}|^2 = 1 \qquad r = u, d1 \tag{4.20}$$

The unitarity of the scattering matrix also proves the equivalence of the basis of in-going and out-going modes in the decomposition of the field perturbation.

All of this does not apply if propagating $d2$ modes are available, that is, for $\omega < \omega_*$; energy conservation is satisfied with $\eta = \mathrm{diag}(1,1,-1)$, thus:

$$|\mathcal{M}_{ur}|^2 + |\mathcal{M}_{d1r}|^2 - |\mathcal{M}_{d2r}|^2 = \sigma_r \qquad r = u, d1, d2 \tag{4.21}$$

As a consequence of the minus sign, reflectivities and transmittivities are not bound to be smaller than 1. Also, the scattering matrix is not unitary, but pseudo-unitary, signalling the inequivalence between the representation of the perturbation in terms of in-going and out-going modes: this mathematical fact is at the basis of spontaneous particle creation in quantum field theories on curved spacetimes.

Thanks to the relation between in-going and out-going modes coefficients α_r, β_r in terms of the scattering matrix, the generic scattering solutions (4.13) can be written as a linear combination of scattering modes rather than quasi-particle modes. We call *in-going scattering mode* the solution of the Bogoliubov problem initiated by a single in-going quasi-particle mode:

$$\begin{bmatrix} \mathcal{U}_r(x) \\ \mathcal{V}_r(x) \end{bmatrix} = \begin{bmatrix} U_r^{\mathrm{in}} \\ V_r^{\mathrm{in}} \end{bmatrix} \frac{e^{ik_r^{\mathrm{in}} x}}{|w_r^{\mathrm{in}}|^{1/2}} \Theta_r(x) + \sum_{r'} \mathcal{M}_{r'r} \begin{bmatrix} U_{r'}^{\mathrm{out}} \\ V_{r'}^{\mathrm{out}} \end{bmatrix} \frac{e^{ik_{r'}^{\mathrm{out}} x}}{|w_{r'}^{\mathrm{out}}|^{1/2}} \Theta_{r'}(x) \tag{4.22}$$

Similarly an *out-going scattering mode* is a solution of the Bogoliubov problem involving a single out-going quasi-particle mode:

$$\begin{bmatrix} \overline{\mathcal{U}}_r(x) \\ \overline{\mathcal{V}}_r(x) \end{bmatrix} = \begin{bmatrix} U_r^{\mathrm{out}} \\ V_r^{\mathrm{out}} \end{bmatrix} \frac{e^{ik_r^{\mathrm{out}} x}}{|w_r^{\mathrm{out}}|^{1/2}} \Theta_r(x) + \sum_{r'} (\mathcal{M}^{-1})_{r'r} \begin{bmatrix} U_{r'}^{\mathrm{in}} \\ V_{r'}^{\mathrm{in}} \end{bmatrix} \frac{e^{ik_{r'}^{\mathrm{in}} x}}{|w_{r'}^{\mathrm{in}}|^{1/2}} \Theta_{r'}(x) \tag{4.23}$$

Notice that the pseudo-unitarity (4.19) of the scattering matrix allows to write the elements of $\mathcal{M}^{-1}$ in terms of those of $\mathcal{M}$: in particular, since $\mathcal{M}^{-1} = \eta \mathcal{M}^\dagger \eta$, one has $(\mathcal{M}^{-1})_{r'r} = \sigma_r \sigma_{r'} (\mathcal{M}^\dagger)_{r'r} = \sigma_r \sigma_{r'} \mathcal{M}^*_{rr'}$. Moreover, if $\mathcal{M}$ is pseudo-unitary, also $\mathcal{M}^{-1}$ has the same property. The full scattering solution can thus be equivalently written as a linear combination of in-going or out-going scattering modes:

$$\begin{bmatrix} \mathscr{U}(x,\omega) \\ \mathscr{V}(x,\omega) \end{bmatrix} = \sum_r \alpha_r \begin{bmatrix} \mathcal{U}_r(x,\omega) \\ \mathcal{V}_r(x,\omega) \end{bmatrix} = \sum_r \beta_r \begin{bmatrix} \overline{\mathcal{U}}_r(x,\omega) \\ \overline{\mathcal{V}}_r(x,\omega) \end{bmatrix} \tag{4.24}$$

with coefficients related by the scattering matrix as:

$$\beta_{r'} = \sum_r \mathcal{M}_{r'r}\alpha_r \tag{4.25}$$

The computation of the scattering matrix coefficients typically requires to fully solve the Bogoliubov problem, taking into account the exact profile of the sonic horizon. A semi-analytical solution can be easily determined for the step-like configuration in Fig. 4.1. Indeed, physical profiles for the Bogoliubov amplitudes (4.13) are found by matching the solutions in the subsonic and supersonic regions at the location of the horizon. In practice, the amplitudes α_r of the in-going modes are fixed as initial conditions for the scattering problem, while those of the out-going modes β_r are computed by matching the $x = 0$ values of $\mathcal{U}, \mathcal{V}$ and of their first derivatives. This amounts to solving a linear system of four equations for each in-going mode an for each frequency ω. Since the matching is done at the position of the horizon, one must include exponentially suppressed modes in the calculations; from a mathematical point of view, this is necessary to get unambiguous results, since the number of unknown coefficients to be determined (β_r and γ_r) needs to be equal to the number of imposed constraints.

Despite the scattering problem analysed so far represents a (classical) stimulated version of the Hawking process [114], the elements of the scattering matrix carry important information about its spontaneous counterpart. In particular, as we will discuss later on, the coefficient $|\mathcal{M}_{ud2}(\omega)|^2$ can be thought as the (zero-temperature) Hawking emission spectrum [38, 39], since it is associated to the number of u particles, that are spontaneously emitted by the analog horizon in the black-hole exterior, even in the absence of any in-going mode. Moreover, the transmittivity of d modes into the u mode (or, equivalently, the reflectivity of the horizon with respect to the u mode)

$$\Gamma(\omega) = |\mathcal{M}_{d1u}(\omega)|^2 - |\mathcal{M}_{d2u}(\omega)|^2 = 1 - |\mathcal{M}_{uu}(\omega)|^2 \tag{4.26}$$

can be thought as a greybody factor of the analog black-hole.

4.4 The Hawking spectrum

Results of the semi-analytical calculation of the scattering coefficients as a function of frequency are shown in Figs. 4.2 - 4.6 for various configurations. Before discussing the single cases separately, let us point out some general properties of the scattering matrix coefficients which are always satisfied:

(a) In contrast to the astrophysical case, the sonic horizon does not act as a perfect black body: indeed the reflectivity of the u mode, $|\mathcal{M}_{uu}(\omega)|^2$, is non-vanishing. In other words, the Hawking emission spectrum $|\mathcal{M}_{ud2}(\omega)|^2$ does not coincide with a black-body thermal spectrum, but features a (possibly frequency-dependent) grey-body factor $\Gamma(\omega)$.

(b) As expected for astrophysical non-rotating black-holes, no superradiant amplification of the in-going u mode is observed, as $|\mathcal{M}_{uu}(\omega)|^2 < 1$ for all frequencies.

(c) Superradiant amplification is instead observed for downstream modes $d1, d2$ inside the analog black-hole; for instance $|\mathcal{M}_{d2d2}(\omega)|^2 > 1$ for all frequencies. This phenomenon has no counterpart in the gravitational context, since the propagation of particles in the black-hole interior towards the event horizon is not allowed, as it would be the results of a superluminal dispersion relation.

4.4.1 Uncoupled binary mixture

Fig. 4.2(c) shows the reflectivity/transmittivity of the sonic horizon with respect to the $d2$ mode for the uncoupled mixture considered in Ref. [43], which is analogous to the case of a single condensate [39]. The dispersion relation of spin modes is gapless in both the subsonic and supersonic regions, as shown in panels (a) and (b) of Fig. 4.2. Due to the possibility of exciting modes with opposite energies, all the scattering matrix coefficients are unbounded and indeed reflectivity and transmittivity diverge as $1/\omega$ in the low-frequency regime.

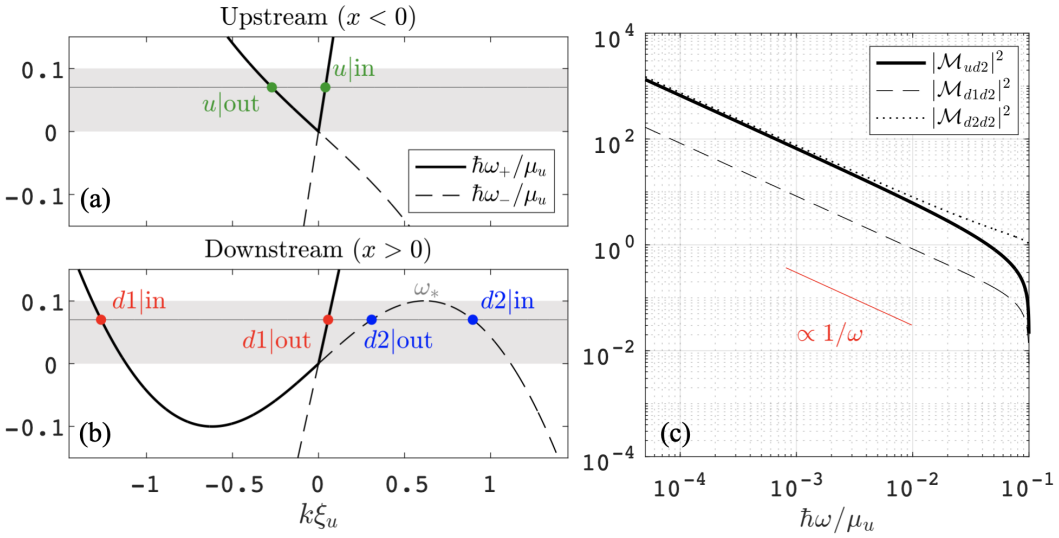

FIGURE 4.2: Dispersion relation for spin collective modes in the upstream (a) and downstream (b) regions; the positive (negative) norm branch is represented as a solid (dashed) black line. The gray area indicates the range of frequencies in which the $d2$ mode is available: all the propagating solutions available within this range are highlighted in green (u mode), red ($d1$ mode) and blue ($d2$ mode). Panel (c) reports the trasmittivity/reflectivities of the horizon for an incoming $d2$ mode. Parameters: $c_u/v = 4/3, \kappa_d/\kappa_u = 0.25, \Omega_u = \Omega_d = 0$, corresponding to the standard gapless case considered in [43].

Let us assume that the Hawking emission spectrum can be written as:

$$|\mathcal{M}_{ud2}(\omega)|^2 = \frac{\Gamma(\omega)}{\exp\left[\hbar\omega/k_B T_H(\omega)\right] - 1} \tag{4.27}$$

where $\Gamma(\omega) = 1 - |\mathcal{M}_{uu}(\omega)|^2$ is the greybody factor and $T_H(\omega)$ is the Hawking temperature. A thermal spectrum would require a frequency-independent T_H: however, let us keep a frequency dependence to account for deviations from thermality.

Notice that the Hawking temperature T_H is completely unrelated to the physical temperature T of the BEC system under consideration: indeed all the results presented in this Chapter are derived assuming $T = 0$.

Given the $1/\omega$ dependence of $|\mathcal{M}_{ud2}|^2$, in the low-frequency limit Eq.(4.27) holds with constant T_H and its value is uniquely determined by the ratios v/c_u and v/c_d [30, 43]. On the contrary, if $\omega \sim \omega_*$, T_H acquires a frequency dependence: in particular, it must be vanishing for $\omega \geq \omega_*$, since $\mathcal{M}_{ud2}$ is identically zero if the $d2$ mode is not available. This is often considered a weak deviation from thermality due to non-hydrodynamic effects, since the maximum intensity of emitted particles is found in the $\omega \to 0$ regime, where T_H is approximately constant, although it could in principle be detected in experiments [115].

The numerically computed results for the Hawking temperature and for the greybody factor are shown in Fig.4.3. With the parameters in Fig. 4.2, we find $\Gamma(\omega \to 0) \simeq 0.98$ and $k_B T_H(\omega \to 0)/\hbar\omega_* \simeq 0.68$; these values are in excellent agreement with the analytical results of [43]. Typical experimental parameters for Sodium atoms [57] give a Hawking temperature of the order of 1-10 nK. A physical temperature much lower than T_H would be necessary to directly observe the Hawking effect: otherwise thermal flutuations would hide it.

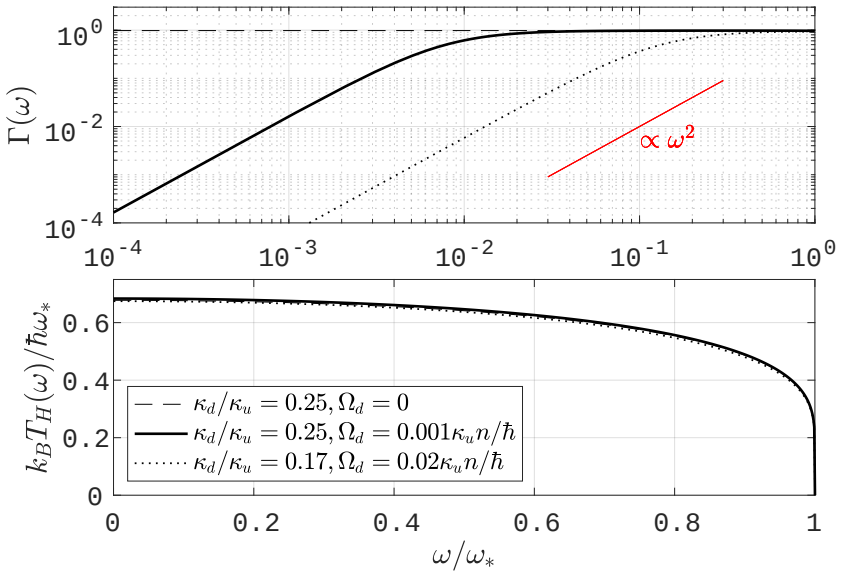

FIGURE 4.3: Frequency dependence of the greybody factor (upper panel) and Hawking temperature (lower panel) in the three configurations of Figs. 4.2, 4.4 and 4.6 (dashed, solid and dotted lines, respectively). The parameters were chosen so to have similar values of $\omega_* \sim 0.1\mu_u/\hbar$. The greybody factor is computed as $\Gamma(\omega) = 1 - |\mathcal{M}_{uu}(\omega)|^2$; the Hawking temperature is then derived by inverting Eq. (4.27).

4.4.2 Coupled binary mixture

As visible in Figs. 4.4 - 4.6, a finite value of Ω regularizes all the scattering matrix elements, eliminating their infrared divergence [116]: zero-frequency u (d) modes cannot be transmitted in the downstream (upstream) region, thus all the transmittivities vanish in the limit $\omega \to 0$, while all the reflectivities tend to constant values [116]. In particular, $|\mathcal{M}_{uu}(\omega \to 0)|^2 \to 1$ and $|\mathcal{M}_{ud2}(\omega \to 0)|^2 \propto \omega$.

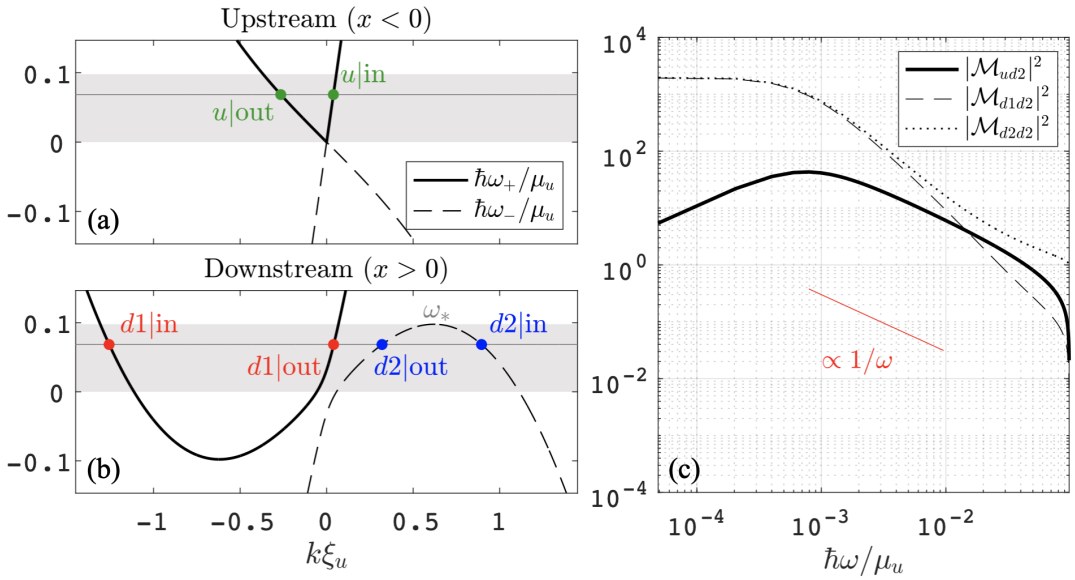

FIGURE 4.4: Same as Fig. 4.2. Parameters: $c_u/v = 4/3$, $\Omega_u = 0$, $\kappa_d/\kappa_u = 0.25$, $\Omega_d = 0.001\kappa_u n/\hbar = 0.004\kappa_d n/\hbar$, defining the relativistic regime $\hbar\Omega_d \ll \kappa_d n$.

As shown in the upper panel of Fig. 4.3, this affects the greybody factor, which, for finite gaps, acquires a quadratic frequency dependence in the low-frequency regime. In the gravitational context, this behaviour has been found, for instance, for non-minimally coupled massless scalar fields in a Schwarzschild spacetime [117, 118], where the coupling with the curvature effectively acts as a mass term in the Klein-Gordon equation. As long as $\Omega_d \ll \kappa_d n/\hbar$ (see Fig.4.4), the greybody factor reaches an asymptotic value close to unity at a frequency $\overline{\omega} \ll \omega^*$, which also corresponds to a maximum in the Hawking emission spectrum: above this frequency, the $1/\omega$ dependence of the Hawking emission spectrum is recovered. As the Rabi frequency Ω_d increases, $\overline{\omega}$ approaches ω_* (see Fig. 4.6) until, in the limit $\Omega_d > \kappa_d n/\hbar$ and for $\kappa_d < 0$ (see Fig. 4.5), the greybody factor can be considered quadratic in almost the whole range $[0, \omega_*]$. Fig. 4.7 summarized how $\overline{\omega}$ varies with the Rabi frequency: in the small coupling limit, it grows linearly with $\hbar\Omega_d/\kappa_d n$.

Remarkably, the presence of a coherent coupling in the downstream region has little effect on the Hawking temperature $T_H(\omega)$ (see the lower panel of Fig. 4.3): the degree of thermality in the emission spectrum is preserved, despite the inaccuracy of the gravitational analogy if $\hbar\Omega_d \sim \kappa_d n$.

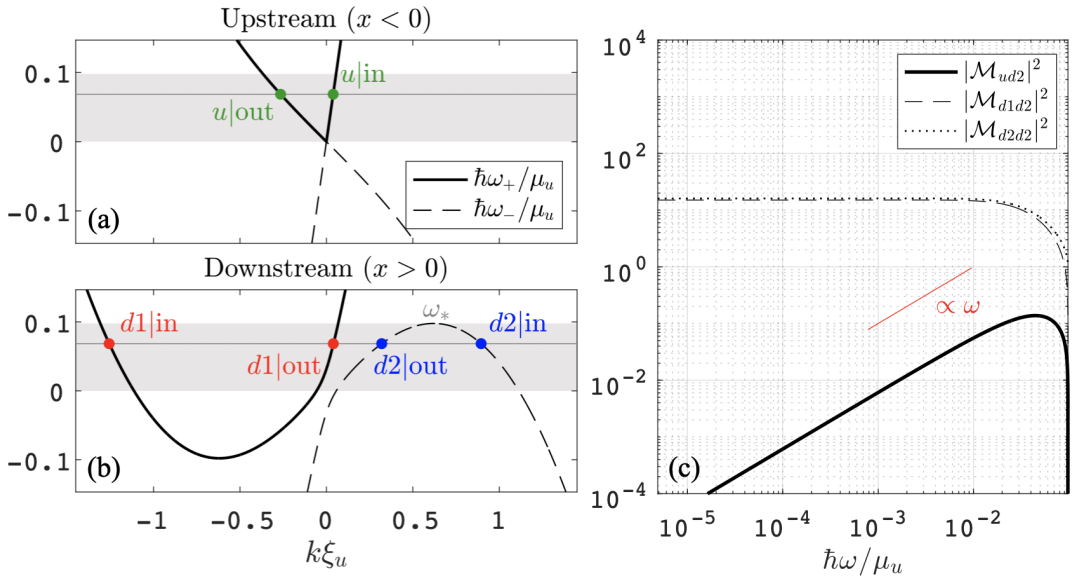

FIGURE 4.5: Same as Fig. 4.2. Parameters: $c_u/v = 4/3$, $\Omega_u = 0$, $\kappa_d/\kappa_u = -0.25$, $\Omega_d = 0.251\kappa_u n/\hbar$, defining the relativistic regime in the vicinity of the critical point for the para-to-ferromagnetic phase transition, $\hbar\Omega_d + \kappa_d n \gtrsim 0$. Notice that, despite the different sign of κ_d, the dispersion relation in the downstream region is identical to that of Fig. 4.4.

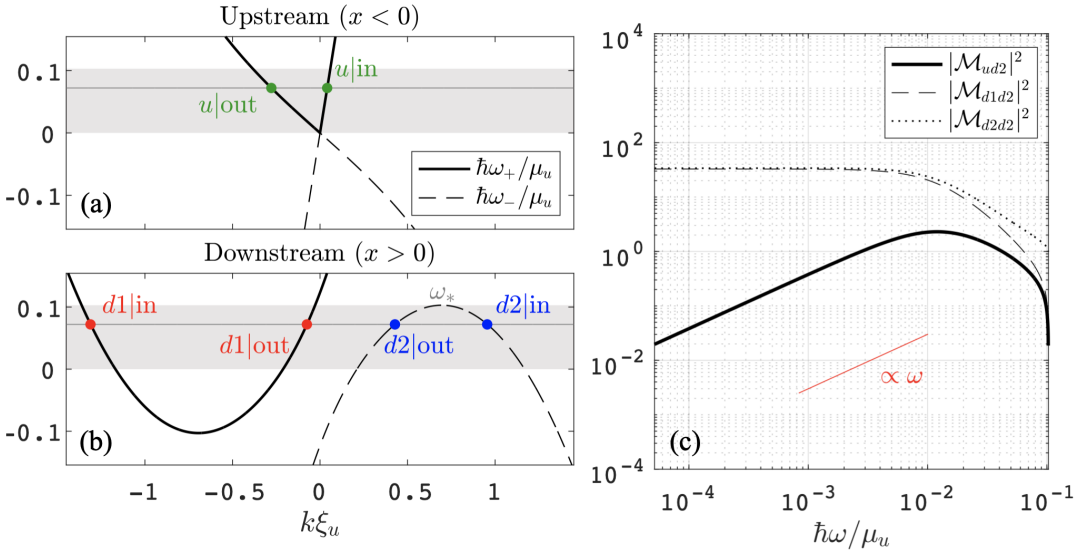

FIGURE 4.6: Same as Fig. 4.2. Parameters: $c_u/v = 4/3$, $\Omega_u = 0$, $\kappa_d/\kappa_u = 0.17$, $\Omega_d = 0.02\kappa_u n/\hbar \simeq 0.12\kappa_d n/\hbar$, defining the non-relativistic regime with $\hbar\Omega_d \sim \mu_d \equiv \kappa_d n/2$.

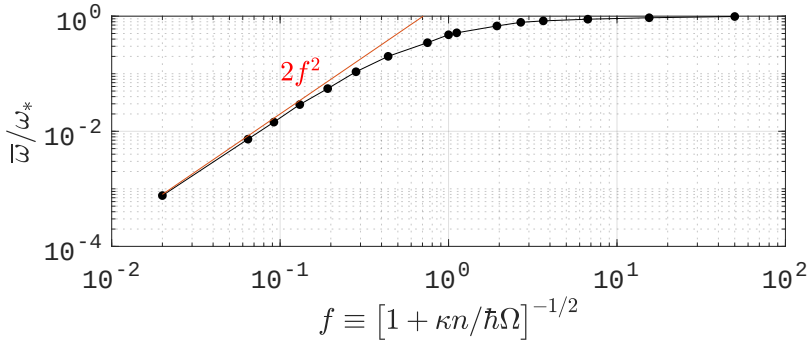

FIGURE 4.7: Saturation frequency $\overline{\omega}$ (computed as the frequency at which the Hawking spectrum is maximum) as a function of the strenght of the coherent coupling in the downstream region. The value of κ has been tuned to have $\omega_* \sim 0.1\mu_u/\hbar$ for all the points in the plot. The dimensionless quantity on the horizontal axis allows to easily distinguish the various regimes we considered: $f \ll 1$ identifies the relativistic case $\hbar\Omega \ll \kappa n$, $f \to \infty$ represents the critical point for the para-to-ferromagnetic phase transition, while $f \sim 1$ is related to the non-relativistic regime $\hbar\Omega \sim |\kappa| n$. For the parameters in Fig. 4.4 - 4.6, we have $f = 0.06, 16, 0.32$, respectively.

4.5 Quantization of the field

The spectral properties of the analog horizon we discussed so far can be probed in a stimulated way: in other words, a classical version of the Hawking effect can be observed in the scattering of plane waves in a purely mean field description [39, 114]. However, here we are mostly interested in the characterization of the spontaneously emitted radiation and in determining which observables would allow to detect it experimentally. We therefore need to quantize the theory.

The standard quantization procedure consists in replacing the complex coefficients α_r, β_r in the field expansion (4.24) with creation/annihilation operators. In terms of in-going scattering modes, we have:

$$\delta\hat{\Psi}(x,t) = \int_0^\infty \frac{\mathrm{d}\omega}{\sqrt{2\pi}} \sum_r \left[\mathcal{U}_r(x,\omega)e^{-i\omega t}\hat{a}_r + \mathcal{V}_r^*(x,\omega)e^{i\omega t}\hat{a}_r^\dagger\right] \tag{4.28}$$

where the sum runs over all the modes available at a given frequency, that is $r \in \{u, d1, d2\}$ if $\omega < \omega_*$ and $r \in \{u, d1\}$ if $\omega > \omega_*$. Analogously, one could expand the field in terms of out-going scattering modes $\hat{b}_r, \hat{b}_r^\dagger$.

In principle, in order to expand $\delta\Psi$ over a complete basis set, one would need to explicitly include two unconventional eigenstates of the Bogoliubov matrix $\mathcal{L}$ with eigenvalue $\omega = 0$ [115]. In a single component BEC, these zero-frequency modes are due to the Gauge symmetry associated with the global phase of the system, or, equivalently, to the conservation of the total number of particles. In the case of the spin channel of a symmetric binary mixture, they exist only in the absence of a coherent coupling, when the same Gauge freedom applies to the relative phase and the relative number of particles is conserved. Within our framework, involving a uniform density profile, the Bogoliubov coefficients of these two zero-frequency modes

would also be position-independent. As a consequence, without coherent coupling, they would contribute, at most, as a uniform shift to the observables we will define in the following; if $\Omega \neq 0$ in the downstream region, the continuity of the wavefunction fixes the relative phase in the upstream region as well, effectively eliminating the Goldstone mode. For these reasons, we avoid including the zero-frequency modes in the field expansion (4.28) and in the following calculations.

Let us also point out that Eq.(4.28) is not exact in the vicinity of the analog horizon ($x \neq 0$), since evanescent modes have not been included.

In the following, when unnecessary, we will omit the frequency dependence in the Bogoliubov coefficients, momenta and group velocity of the modes, for legibility.

In Eq.(4.28) we have associated annihilation (creation) operators to the U (V) component for all the modes; as discussed in Chapter 2, in order to guarantee the proper commutation relations for the field, we have to treat negative norm modes as anti-particles, for which the roles of creation and annihilation operators are exchanged[1]. This reflects on the commutation relations for $\hat{a}_r, \hat{b}_r$:

$$[\hat{a}_r(\omega), \hat{a}^\dagger_{r'}(\omega')] = \sigma_r \delta_{rr'} \delta(\omega - \omega') \tag{4.29}$$

$$[\hat{b}_r(\omega), \hat{b}^\dagger_{r'}(\omega')] = \sigma_r \delta_{rr'} \delta(\omega - \omega') \tag{4.30}$$

as well as on their expectation values. If the symbol $\langle \cdot \rangle$ indicates the average value over the vacuum of in-going particles, at zero physical temperature $T = 0$ we have:

$$\langle \hat{a}^\dagger_r(\omega) \hat{a}_{r'}(\omega') \rangle = \left(\frac{1 - \sigma_r}{2} \right) \delta_{rr'} \delta(\omega - \omega') \tag{4.31}$$

$$\langle \hat{a}_{r'}(\omega') \hat{a}^\dagger_r(\omega) \rangle = \left(\frac{1 + \sigma_r}{2} \right) \delta_{rr'} \delta(\omega - \omega') \tag{4.32}$$

Expectation values of out-going modes operators over the vacuum of in-going modes can be determined starting from the input-output relation (4.17):

$$\hat{b}_r(\omega) = \sum_{r'} \mathcal{M}_{rr'}(\omega) \hat{a}_{r'}(\omega) \tag{4.33}$$

A direct calculation gives:

$$\langle \hat{b}^\dagger_r(\omega) \hat{b}_{r'}(\omega') \rangle = \mathcal{M}^*_{rd2}(\omega) \mathcal{M}_{r'd2}(\omega) \delta(\omega - \omega') \tag{4.34}$$

$$\langle \hat{b}_{r'}(\omega') \hat{b}^\dagger_r(\omega) \rangle = \left[\mathcal{M}^*_{rd2}(\omega) \mathcal{M}_{r'd2}(\omega) + \sigma_r \delta_{rr'} \right] \delta(\omega - \omega') \tag{4.35}$$

Notice that, as long as the $d2$ mode is available, the expectation values of in-going and out-going modes do not coincide: this signals that a process of spontaneous particle creation is taking place. In particular, the energy emitted by the sonic horizon in the

[1] An equivalent expansion for the field perturbation (4.28) is obtained by separating the sum over positive norm and negative norm modes and associating annihilation (creation) operators to the V (U) component for negative norm modes, as commonly done in previous literature [39, 112]. This replacement allows to treat all modes, including the negative norm ones, as particles fulfilling canonical commutation relations.

u out-going mode (that is, towards the black-hole exterior) is:

$$\frac{\mathrm{d}I_u^{\mathrm{out}}}{\mathrm{d}t} = \int_0^{\omega_*} \frac{\mathrm{d}\omega}{2\pi} \langle \hat{b}_u^\dagger(\omega)\hat{b}_u(\omega)\rangle = \int_0^{\omega_*} \frac{\mathrm{d}\omega}{2\pi} |\mathcal{M}_{ud2}(\omega)|^2 \tag{4.36}$$

Hence, as we anticipated, the scattering coefficient $|\mathcal{M}_{ud2}(\omega)|^2$ is typically referred to as the *Hawking emission spectrum* of the analog black-hole.

With the chosen normalization in Eq.(4.28) , the field commutator is:

$$[\delta\hat{\Psi}(x), \delta\hat{\Psi}^\dagger(x')] = \int_0^\infty \frac{\mathrm{d}\omega}{2\pi} \sum_r \sigma_r \Big[\mathcal{U}_r(x)\mathcal{U}_r^*(x') - \mathcal{V}_r^*(x)\mathcal{V}_r(x')\Big] = \tag{4.37}$$

$$= \sum_{I\in\{\mathrm{in,out}\}} \int_0^\infty \frac{\mathrm{d}\omega}{2\pi} \sum_r \frac{e^{ik_r^I(x-x')}}{|w_r^I|} \Theta_r(x)\Theta_r(x') \tag{4.38}$$

Notice that it does not coincide with a Dirac delta function because the zero-frequency modes have not been included in the calculation.

The second and third spin vector components (3.31), (3.32) are expanded as:

$$\hat{S}_2(x,t) = \sqrt{n}\int_0^\infty \frac{\mathrm{d}\omega}{\sqrt{2\pi}} \sum_r \Big[i\mathcal{Q}_r(x)e^{-i\omega t}\hat{b}_r + \mathrm{h.c.}\Big]\,\Theta_r(x) \tag{4.39}$$

$$\hat{S}_3(x,t) = \sqrt{n}\int_0^\infty \frac{\mathrm{d}\omega}{\sqrt{2\pi}} \sum_r \Big[\mathcal{R}_r(x)e^{-i\omega t}\hat{b}_r + \mathrm{h.c.}\Big]\,\Theta_r(x) \tag{4.40}$$

where, to simplify the notation, we have defined the sum and difference of the Bogoliubov components describing the scattering modes as $\mathcal{R}_r(x) = \mathcal{U}_r(x) + \mathcal{V}_r(x)$ and $\mathcal{Q}_r(x) = \mathcal{U}_r(x) - \mathcal{V}_r(x)$. The same quantities can be defined for the Bogoliubov coefficients associated to each quasi-particle mode; moreover, if U_r^I, V_r^I are properly normalized, they can be expressed in terms of the static structure factor for spin modes as:

$$R_r^I = U_r^I + V_r^I = \big[\mathcal{S}(k_r^I)\big]^{1/2} \tag{4.41}$$

$$Q_r^I = U_r^I - V_r^I = \sigma_r\big[\mathcal{S}(k_r^I)\big]^{-1/2} \tag{4.42}$$

where $I \in \{\mathrm{in},\ \mathrm{out}\}$ and $r = u, d1, d2$. In particular $R_r^I Q_r^I = \sigma_r$.

The full expression for $\mathcal{R}_r, \mathcal{Q}_r$ for in-going scattering modes (4.22) is:

$$\mathcal{R}_r(x) = \frac{R_r^{\mathrm{in}} e^{ik_r^{\mathrm{in}}x}}{|w_r^{\mathrm{in}}|^{1/2}}\Theta_r(x) + \sum_{r'} \mathcal{M}_{r'r} \frac{R_{r'}^{\mathrm{out}} e^{ik_{r'}^{\mathrm{out}}x}}{|w_{r'}^{\mathrm{out}}|^{1/2}}\Theta_{r'}(x) \tag{4.43}$$

$$\mathcal{Q}_r(x) = \frac{Q_r^{\mathrm{in}} e^{ik_r^{\mathrm{in}}x}}{|w_r^{\mathrm{in}}|^{1/2}}\Theta_r(x) + \sum_{r'} \mathcal{M}_{r'r} \frac{Q_{r'}^{\mathrm{out}} e^{ik_{r'}^{\mathrm{out}}x}}{|w_{r'}^{\mathrm{out}}|^{1/2}}\Theta_{r'}(x) \tag{4.44}$$

4.6 Correlation functions

The observable which has typically been considered in previous works [38, 39, 43, 44, 112] is the equal-time density-density correlation function, which displays a characteristic signal associated to the spontaneous creation of pairs of particles which travel on opposite sides of the sonic horizon. Such signal has been observed experimentally in a single-component condensate [40–42]. In the case of an unpolarized mixture, an analogous signal is expected in relative density correlations [43], that is, in the equal time correlations of the third component of the spin vector:

$$n^2\mathcal{G}_{33}(x,x') = \langle \hat{S}_3(x)\hat{S}_3(x')\rangle - n\big[\delta\hat{\Psi}(x), \delta\hat{\Psi}^\dagger(x')\big] \tag{4.45}$$

After expanding $\hat{S}_3$ in terms of scattering modes as in Eq.(4.40), we find:

$$\mathcal{G}_{33}(x,x') = \frac{1}{n}\Re\left\{\int_0^\infty \frac{\mathrm{d}\omega}{2\pi}\sum_r \Big[\mathcal{R}_r(x) - \sigma_r\mathcal{Q}_r(x)\Big]\mathcal{R}_r^*(x')\right\} \tag{4.46}$$

A further expansion of $\mathcal{R}_r, \mathcal{Q}_r$ in terms of quasi-particle modes as in Eqs.(4.43)-(4.44), combined with the pseudo-unitarity of the scattering matrix, leads to the result:

$$\mathcal{G}_{33}(x,x') = \mathcal{C}_3(x,x') + \sum_{rr'}\mathcal{G}_{33}^{(rr')}(x,x') \tag{4.47}$$

The first contribution:

$$\mathcal{C}_3(x,x') = \frac{1}{n}\Re\left\{\sum_{I\in\{\mathrm{in,out}\}}\int_0^\infty \frac{\mathrm{d}\omega}{2\pi}\sum_r \frac{|R_r^I|^2-1}{|w_r^I|}e^{ik_r^I(x-x')}\Theta_r(x)\Theta_r(x')\right\} \tag{4.48}$$

is present even in the absence of an analog horizon and represents an antibunching (bunching) term resulting from repulsive (attractive) spin interactions [112]. When written in momentum space rather than frequency space, $\mathcal{C}_3(x,x')$ coincides with the Fourier transform of the structure factor reduced by 1, computed at $x-x'$: as a consequence it diverges at the critical point for the para-to-ferromagnetic phase transition, where $\mathcal{S}(k\to 0)\propto 1/k$, while it vanishes in the absence of spin interactions, $\kappa = 0$, since $\mathcal{S}(k) = 1$. A typical example is given in Fig. 4.8(a,c): for $\kappa > 0$, $\mathcal{C}_3(x,x')$ is a negative correlation peaked along the main diagonal $x = x'$; the difference in the signal found in the two sectors $x,x' > 0$ and $x,x' < 0$ is due to the different value of spin interaction energy κ in the upstream and downstream regions.

The additional correlation term in Eq.(4.47) contributes only if the $d2$ mode is available, that is, only in the presence of a sonic horizon. For this reason, it can be directly associated to the analog of the Hawking effect in a BEC system. We can distinguish between self-correlation terms ($r = r'$):

$$\mathcal{G}_{33}^{(rr)}(x,x') = \frac{1}{n}\Re\left\{\int_0^{\omega_*}\frac{\mathrm{d}\omega}{2\pi}\left[\frac{|R_r^{\mathrm{out}}|^2 e^{ik_r^{\mathrm{out}}(x-x')}}{|w_r^{\mathrm{out}}|}\left(|\mathcal{M}_{rd2}|^2 + \frac{\sigma_r - 1}{2}\right)\right]\Theta_r(x)\Theta_r(x')\right\} + (x\leftrightarrow x') \tag{4.49}$$

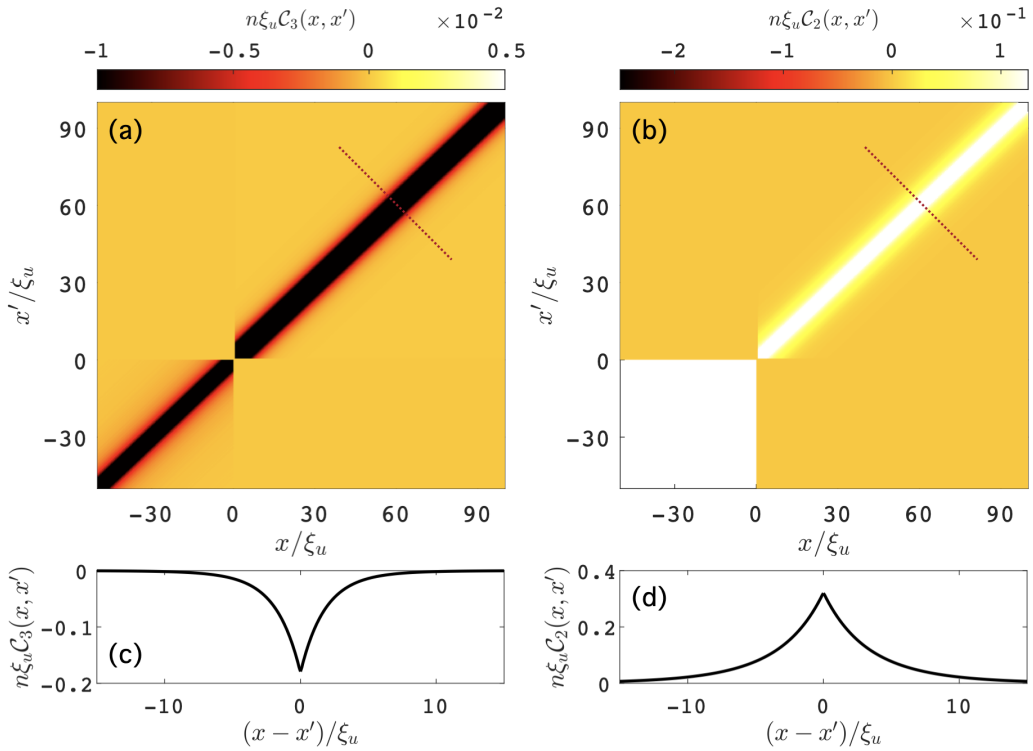

FIGURE 4.8: Trivial contribution to the relative density (4.48) [panels (a) and (c)] and relative phase (4.54) [panels (b) and (d)] correlation signal due to spin interactions. Parameters: $\kappa_d/\kappa_u = 0.1$, $\Omega_u = 0$ and $\hbar\Omega_d/\kappa_d n = 0.1$. Panels (b) and (d) represents cuts of the 2D plots at $x + x' \sim 120\xi_u$. Notice that relative phase correlations diverge in the upstream region $(x, x' < 0)$ due to the $1/\omega$ behaviour of $|Q_u^I|^2$ (both for $I = \text{in, out}$) in the absence of coupling.

and cross correlation terms ($r \neq r'$):

$$\mathcal{G}_{33}^{(r\neq r')}(x,x') = \frac{1}{n}\Re\left\{\int_0^{\omega_*}\frac{\mathrm{d}\omega}{2\pi}\left[\frac{R_r^{\rm out}R_{r'}^{\rm out}e^{i(k_r^{\rm out}x-k_{r'}^{\rm out}x')}}{|w_r^{\rm out}w_{r'}^{\rm out}|^{1/2}}\mathcal{M}_{rd2}\mathcal{M}^*_{r'd2}\right]\Theta_r(x)\Theta_{r'}(x')\right\} + (x\leftrightarrow x') \tag{4.50}$$

While the former gives, once again, a signal along the main diagonal $x = x'$, the latter might contribute away from it, producing a signal which is clearly distinguishable from the usual bunching/antibunching term (4.48). In particular cross-correlations are non-vanishing in the quadrants $xx' < 0$: physically such correlation signal is interpreted as due to pairs of quasi-particles which are spontanously emitted on the two sides of the sonic horizon, in close analogy with what is expected in gravitational context.

According to (3.31), (3.32), the spin field perturbation not only affects the relative density $S_3(x)$ but also the second component of the spin vector $S_2(x)$, related to the relative phase between the two components of the mixture. It is therefore natural to

define relative phase correlations as:

$$n^2\mathcal{G}_{22}(x,x') = \langle \hat{S}_2(x)\hat{S}_2(x')\rangle - n\big[\delta\hat{\Psi}(x), \delta\hat{\Psi}^\dagger(x')\big] \tag{4.51}$$

Notice that $S_2(x)$ is accessible in experiments by applying a $\pi/2$ pulse before measuring the spin density $S_3(x)$.

By expanding the second component of the spin vector as in Eq.(4.39) we obtain:

$$\mathcal{G}_{22}(x,x') = \frac{1}{n}\Re\left\{\int_0^\infty \frac{\mathrm{d}\omega}{2\pi}\sum_r \Big[\mathcal{Q}_r(x) - \sigma_r\mathcal{R}_r(x)\Big]\mathcal{Q}_r^*(x')\right\} \tag{4.52}$$

$$= \mathcal{C}_2(x,x') + \sum_{rr'}\mathcal{G}_{22}^{(rr')}(x,x') \tag{4.53}$$

Analogously to density correlations, also phase correlations can be written as the sum of various contributions, including a trivial term due to spin interactions:

$$\mathcal{C}_2(x,x') = \frac{1}{n}\left\{\Re\sum_{I\in\{\mathrm{in,out}\}}\int_0^\infty\frac{\mathrm{d}\omega}{2\pi}\sum_r\frac{|Q_r^I|^2-1}{|w_r^I|}e^{ik_r^I(x-x')}\Theta_r(x)\Theta_r(x')\right\} \tag{4.54}$$

It consists in a positive (negative) contribution for $\kappa > 0$ ($\kappa < 0$), localized around the main diagonal $x = x'$. When written in momentum space, it coincides with the Fourier transform of the inverse of the structure factor reduced by 1: therefore it diverges in the absence of a coherent coupling, while it vanishes in the absence of spin interactions. A typical example is given in Fig.4.8(b,d).

The additional contributions, which are only found if an analog horizon is present, can be distinguished between self-correlations ($r = r'$)

$$\mathcal{G}_{22}^{(rr)}(x,x') = \frac{1}{n}\Re\left\{\int_0^{\omega_*}\frac{\mathrm{d}\omega}{2\pi}\left[\frac{|Q_r^{\mathrm{out}}|^2e^{ik_r^{\mathrm{out}}(x-x')}}{|w_r^{\mathrm{out}}|}\left(|\mathcal{M}_{rd2}|^2+\frac{\sigma_r-1}{2}\right)\right]\Theta_r(x)\Theta_r(x')\right\} + (x\leftrightarrow x') \tag{4.55}$$

and cross correlations ($r \neq r'$)

$$\mathcal{G}_{22}^{(r\neq r')}(x,x') = \frac{1}{n}\Re\left\{\int_0^{\omega_*}\frac{\mathrm{d}\omega}{2\pi}\left[\frac{Q_r^{\mathrm{out}}Q_{r'}^{\mathrm{out}}e^{i(k_r^{\mathrm{out}}x-k_{r'}^{\mathrm{out}}x')}}{|w_r^{\mathrm{out}}w_{r'}^{\mathrm{out}}|^{1/2}}\mathcal{M}_{rd2}\mathcal{M}_{r'd2}^*\right]\Theta_r(x)\Theta_{r'}(x')\right\} + (x\leftrightarrow x') \tag{4.56}$$

Once again, only the latter are expected to produce a signal that is clearly distinguishable from the trivial contribution along the main diagonal. In particular, the (ud) contributions in the sectors with $xx' < 0$ are associated to correlations between the Hawking particles emitted in the black-hole exterior and their partners.

As a last observable, let us define a symmetrized density-phase correlation:

$$n^2\mathcal{G}_{23}(x,x') = \frac{1}{2}\Big[\langle\hat{S}_2(x)\hat{S}_3(x')\rangle + \langle\hat{S}_3(x)\hat{S}_2(x')\rangle\Big] \tag{4.57}$$

Once expressed in terms of quasi-particle modes using Eqs.(4.39),(4.40) and, subsequently, Eqs.(4.43),(4.44), it reads:

$$\mathcal{G}_{23}(x,x') = \frac{1}{n}\Im\left\{\int_0^\infty \frac{\mathrm{d}\omega}{2\pi}\sum_r \left[\mathcal{R}_r(x)\mathcal{Q}_r^*(x') - \mathcal{Q}_r(x)\mathcal{R}_r^*(x')\right]\right\} \tag{4.58}$$

$$= \sum_{r\neq r'} \mathcal{G}_{23}^{(rr')}(x,x') \tag{4.59}$$

where the contribution coming from each pair $(r \neq r')$ is:

$$\mathcal{G}_{23}^{(rr')}(x,x') = \frac{1}{n}\Im\left\{\int_0^{\omega_*} \frac{\mathrm{d}\omega}{2\pi}\left[\frac{R_r^{\mathrm{out}}Q_{r'}^{\mathrm{out}}e^{i(k_r^{\mathrm{out}}x - k_{r'}^{\mathrm{out}}x')}}{|w_r^{\mathrm{out}}w_{r'}^{\mathrm{out}}|^{1/2}}\mathcal{M}_{rd2}\mathcal{M}_{r'd2}^*\right]\Theta_r(x)\Theta_{r'}(x')\right\} + (x\leftrightarrow x') \tag{4.60}$$

The real part appearing in Eq. (4.55), (4.49) is replaced by an imaginary part for density-phase correlations due to the imaginary unit in the expansion of S_2, see Eq. (4.39). As a consequence, all self-correlation terms vanish and $\mathcal{G}_{23}(x,x')$ is exclusively given by the cross-correlations. In other words, this mixed correlation signal is entirely due to the Hawking process and would be absent without an horizon.

In the following Sections, we report the results of our semi-analytical calculation for the correlation signals in several cases of interest. Let us point out that, since we are considering a stationary configuration, our results can be considered valid at infinitely long times after the creation of the analog horizon. In a realistic experimental setup, it is only possible to observe the Hawking emission for a limited time after initializing the analog black-hole, and this might lead to different patterns or signals in the correlations. An approximate yet straightforward way of estimating $\mathcal{G}_{\nu\nu'}(x,x')$ $(\nu,\nu'=2,3)$ at a time t after the creation of the horizon, consists in setting an infrared cutoff, namely replacing the lower bound (0) of the integrals in Eqs. (4.46), (4.52), (4.58) with a small frequency $\epsilon \sim 1/t$ [119]. For instance, the trivial contribution $\mathcal{C}_2(x,x')$ to phase correlations in Eq.(4.54) diverges in the standard uncoupled case because the inverse of the structure factor goes as $1/\omega$; hence in a time-dependent setup it should grow logarithmically with time, as $\propto \log(1/\epsilon) \sim \log(t)$.

4.6.1 Uncoupled binary mixture

Let us start from the straightforward generalization of a black-hole configuration for an uncoupled symmetric mixture, already considered in Ref. [43]: in the absence of coherent coupling, the dispersion relation for spin modes is gapless both in the subsonic and supersonic region (see an example in Fig. 4.2) and the sonic horizon is generated by a step in the spin interaction constant κ, which also translates into a step-like behaviour of the speed of spin-sound $c = \sqrt{\kappa n/2m}$.

All the main features appearing in the two-point correlation functions, shown in Fig. 4.9, can be explained through approximated analytical calculations of the integrals defined in the previous Section: since they run over the frequency range $[0,\omega_*]$ in which the $d2$ mode is available and typically $\hbar\omega_* \ll \mu_u$, we can Taylor expand the quantities appearing in the formulas around $\omega = 0$, up to first order in ω. For instance, the

momenta of the out-going modes can be considered linear with respect to ω:

$$k_r^{\rm out}(\omega \to 0) \simeq \omega / w_r^{\rm out}(0) \tag{4.61}$$

As a consequence, the phase factor

$$\Phi_{rr'}(x, x', \omega) \equiv k_r^{\rm out}(\omega) x - k_{r'}^{\rm out}(\omega) x' \tag{4.62}$$

is also approximatively linear in ω:

$$\Phi_{rr'}(x, x', \omega \to 0) \simeq \omega \left(\frac{x}{w_r^{\rm out}(0)} - \frac{x'}{w_{r'}^{\rm out}(0)} \right) \equiv \omega \Pi_{rr'}(x, x') \tag{4.63}$$

The proportionality factor $\Pi_{rr'}(x, x')$ is defined as the difference between the time that a low-frequency $r|$out and $r'|$out modes take, after being emitted at the sonic horizon, to reach positions x and x'.

The linear behaviour of momenta also affects the structure factor for spin modes, which is also linear in frequency: $\mathcal{S}(k_r^{\rm out}) \propto \omega$; therefore we have:

$$R_r^{\rm out}(\omega \to 0) \propto \sqrt{\omega} \tag{4.64}$$

$$Q_r^{\rm out}(\omega \to 0) \propto \sigma_r / \sqrt{\omega} \tag{4.65}$$

Moreover, in the low-frequency regime, the solution of the scattering problem gives the following results for the scattering matrix elements:

$$\Re\big[\mathcal{M}_{rd2}(\omega \to 0) \mathcal{M}^*_{r'd2}(\omega \to 0)\big] \propto 1/\omega \tag{4.66}$$

$$\Im\big[\mathcal{M}_{rd2}(\omega \to 0) \mathcal{M}^*_{r'd2}(\omega \to 0)\big] \simeq \text{const} \tag{4.67}$$

so that we can safely neglect their imaginary part in the following calculation.

Putting all together, we find that the main contribution to the density correlation signal $\mathcal{G}_{33}(x, x')$ is a sum of oscillating functions, one for each pair of modes:

$$\mathcal{G}_{33}^{(rr')}(x, x') \propto \int_0^{\omega_*} \cos\big[\omega \Pi_{rr'}(x, x')\big] \, {\rm d}\omega = \omega_* \, \mathrm{sinc}\big[\omega_* \Pi_{rr'}(x, x')\big] \tag{4.68}$$

where $\mathrm{sinc}(z) \equiv \sin(z)/z$. Each of these terms is peaked at the locus of points fulfilling $\Pi_{rr'}(x, x') = 0$, that is, on the straight lines defined by:

$$x' = \frac{w_{r'}^{\rm out}(0)}{w_r^{\rm out}(0)} x \tag{4.69}$$

Self-correlations ($r = r'$) contribute, as expected, on the main diagonal, whereas cross-correlations ($r \neq r'$) produce additional signals away from the diagonal, due to the different group velocities of the modes. The expected location of these *mustaches* is represented with dashed lines in Fig. 4.9(a), where we report the exact correlation signal, numerically computed from (4.49), (4.50). Our results are analogous to those shown in previous works on single-component [38, 39, 112] and two-component BECs [43]. In particular, the strongest contribution is due to a negative correlation between the Hawking particle emitted outside the analog black hole and its anti-particle partner

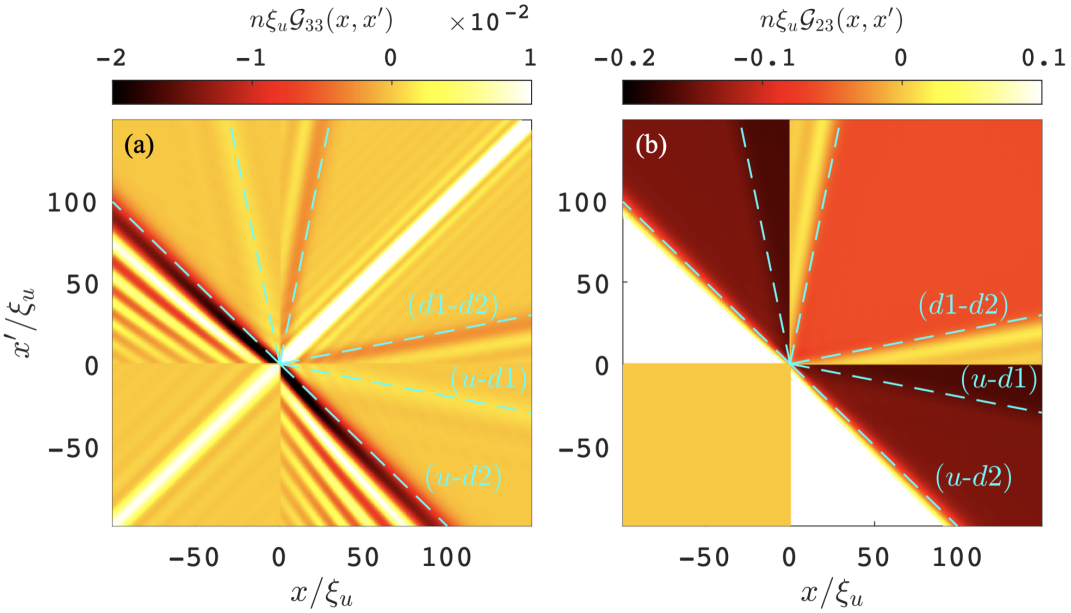

FIGURE 4.9: Density correlations $\mathcal{G}_{33}(x,x')$ [panel (a)] and density-phase correlations $\mathcal{G}_{23}(x,x')$ [panel (b)] for a symmetric uncoupled mixture, computed numerically using Eqs. (4.49), (4.50) and Eq. (4.60), respectively; same parameters as in Fig. 4.2. Dashed lines indicate the expected position of the cross-correlation signals, given by Eq. (4.69).

emitted in its interior (see the u-$d2$ signal in Fig.4.9).

Following the same procedure, we can also compute mixed density-phase correlations $\mathcal{G}_{23}(x,x')$ and phase correlations $\mathcal{G}_{22}(x,x')$. The main contribution to the former is given by terms of the form:

$$\mathcal{G}_{23}^{(rr')}(x,x') \propto \int_0^{\omega_*} \frac{\sin[\omega\Pi_{rr'}(x,x')]}{\omega}\mathrm{d}\omega = \mathrm{Si}\big[\omega_*\Pi_{rr'}(x,x')\big] \tag{4.70}$$

where $\mathrm{Si}(z) = \int_0^z \mathrm{sinc}(z')\mathrm{d}z'$ is the sine integral function: its asymptotic values at $\pm\infty$ are $\pm\pi/2$, respectively, and it crosses zero when $z = 0$. The full correlation, shown in Fig. 4.9(b), is therefore a collection of patches in which $\mathcal{G}_{23}$ has different, almost constant values, separated by smooth jumps whose location is determined, once again, by the solution of $\Pi_{rr'}(x,x') = 0$. In other words, jumps in $\mathcal{G}_{23}(x,x')$ correspond to peaks in $\mathcal{G}_{33}(x,x')$: the higher the jump in density-phase correlations, the more intense the signal in density-density correlations. More specifically, for each pair of modes $r \neq r'$:

$$\mathcal{G}_{33}^{(rr')}(x,x') \propto \frac{\partial}{\partial x}\mathcal{G}_{23}^{(rr')}(x,x') \tag{4.71}$$

Lastly, phase-phase correlations $\mathcal{G}_{22}$ show an infrared divergence: indeed the $1/\omega$ behaviour of the scattering matrix coefficients is not compensated and even worsened by the Q_r^{out} coefficients, which provide a factor which is also inversely proportional to

the frequency. Given some infrared cut-off ϵ, the most relevant contribution is:

$$\mathcal{G}_{22}^{(rr')}(x,x') \propto \int_{\epsilon}^{\omega_*} \frac{\cos[\omega \Pi_{rr'}(x,x')]}{\omega^2} \mathrm{d}\omega \tag{4.72}$$

and diverges as $1/\epsilon$; hence, in a time-dependent setup, it should grow approximately linearly with time. Recall that the trivial phase correlations $\mathcal{C}_2(x,x')$ in Eq.(4.54) also diverge in the absence of coherent coupling, but as $\log(1/\epsilon)$. From a physical point of view, we interpret the infrared divergence of relative phase correlations as due to the Gauge symmetry of the system, or, equivalently, to the presence of a Goldstone mode associated to the relative phase: in each statistical sample (or experimental realization) the phase of both components at any given point x is chosen randomly. Indeed, as we will see in the following Sections, phase correlations are regularized by the presence of a coherent coupling, which fixes the relative phase between the two components to be $\varphi = 0$ in the ground state.

Alternatively, the divergence can be cured by replacing, in the definition of phase correlations (4.51), $\hat{S}_2(x,t) \to \hat{S}_2(x,t) - \hat{S}_2(0,t)$, namely, by measuring $\hat{S}_2$ with respect to some reference point (the sonic horizon $x = 0$ is the most natural choice). This amounts to substituting, in formulas (4.54), (4.55), (4.56):

$$e^{i(k_r^{\mathrm{out}} x - k_{r'}^{\mathrm{out}} x')} \longrightarrow \left(e^{ik_r^{\mathrm{out}} x} - 1\right)\left(e^{ik_{r'}^{\mathrm{out}} x'} - 1\right) \tag{4.73}$$

Notice that, in principle, Eq. (4.39) is only valid away from the sonic horizon because it does not include evanescent modes. However, these are damped out over distances of a few healing lengths, and long range coherence in BEC system guarantees that the error we make by estimating the phase at $x = 0$ with Eq.(4.39) is negligible.

In the low-frequency limit, the complex exponentials (4.73) can be expanded at first order in ω and the phase factor $e^{i\omega\Pi(x,x')}$ is replaced by $k_r^{\mathrm{out}} k_{r'}^{\mathrm{out}} xx' \propto \omega^2 xx'$: the ω^2 dependence cancels the denominator in Eq.(4.72), leaving a finite correlation signal $\mathcal{G}_{22}(x,x') \propto xx'$, that only diverges at infinite distance from the two axis $x = 0, x' = 0$, where instead it vanishes, by definition.

An example is reported in Fig. 4.10(a); although the signal might appear featureless, the typical Hawking *mustaches* are recovered by eliminating the linear dependence of $\mathcal{G}_{22}$ on the coordinates x, x', namely, by taking its first derivative with respect to both x and x'. The result is shown in Fig. 4.10(b): notice that, despite phase correlations are orders of magnitude larger than density correlations, the amplitude of the signal in Fig. 4.10(b) is comparable to the one of Fig. 4.9(a), being roughly twice as large. Similarly, a single derivative of $\mathcal{G}_{22}$ with respect to either x or x', followed by a symmetrization of the signal, would produce a correlation pattern similar to Fig. 4.9(b), with slightly larger amplitude (not shown).

While considering the phase degree of freedom might not be of great practical advantage in the experimental measurement of analog Hawking emission for an uncoupled binary mixture, our results show that phase correlations carry the same information of density correlations; hence, once regularized by the presence of a coherent coupling, they represent a promising observable to detect Hawking emission. Examples are discussed in the next Section.

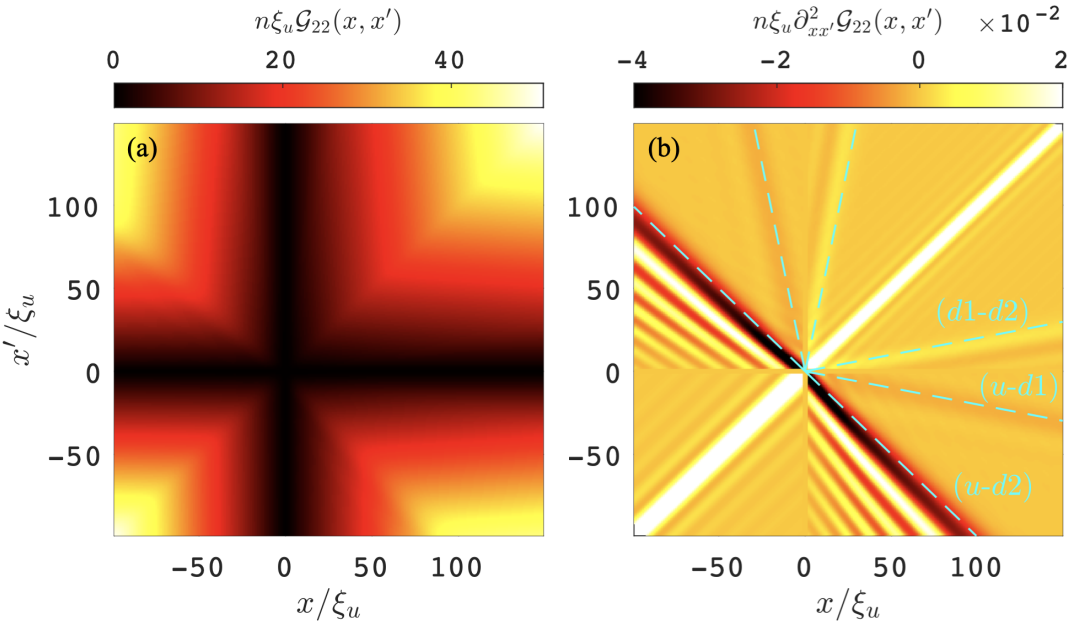

FIGURE 4.10: (a) Phase correlations $\mathcal{G}_{22}(x,x')$ computed using (4.54), (4.56) after replacing the phase factors as in (4.73). (b) Double derivative of $\mathcal{G}_{22}(x,x')$ with respect to both x and x' revealing the standard Hawking *mustaches* that appear in density correlations $\mathcal{G}_{33}(x,x')$, see Fig. 4.9(a). Same parameters as in Fig. 4.2.

4.6.2 Coupled binary mixture

Let us now analyse the effects of a non-vanishing coherent coupling in the downstream region. The main consequences of having $\Omega_d \neq 0$ can be summarized as follows:

(a) There exist, in the downstream region, zero-frequency out-going modes with non-zero wavevector; in particular $k^{\rm out}_{d1}(0) = -k_0$ and $k^{\rm out}_{d2}(0) = +k_0$. As we will see, the existence of such modes produces oscillations in the correlations pattern, since modes with non-zero momentum can be excited without paying energy; this phenomenon is sometimes referred to as *undulation* [116].

(b) The group velocity of the two zero-frequency modes is identical:

$$\frac{w^{\rm out}_{d1}(0)}{v} = \frac{w^{\rm out}_{d2}(0)}{v} \equiv \frac{w_0}{v} = \sqrt{\left(1-\frac{\mu_d}{mv^2}\right)^2 - \frac{2\hbar\Omega_d}{mv^2}} \tag{4.74}$$

therefore, oscillations with momentum k_0 appear in the correlation signal, parallel to either of the two diagonals, $x+x'=0$ or $x-x'=0$. A combination of the two gives a checkerboard pattern, analogous to the one observed for white-hole configurations [119].

(c) The Gauge symmetry associated to the conservation of the relative number of particles is broken, thus relative phase correlations $\mathcal{G}_{22}(x,x')$ are regularized.

In the following we repeat the analytical calculations of the previous Section, with the aim of analysing the various contributions to the correlation signals in the presence

of a coherent coupling. Since the gap is only present in the downstream region, we have to treat separately the u mode and the $d1, d2$ modes. A Taylor expansion of the out-going momenta in the low-frequency limit (up to linear terms in ω) leads to:

$$k_u^{\rm out}(\omega \to 0) \simeq \omega / w_u^{\rm out}(0) \tag{4.75}$$

$$k_d^{\rm out}(\omega \to 0) \simeq -\sigma_d k_0 + \omega / w_0 \qquad d = d1, d2 \tag{4.76}$$

while the structure factors are approximately given by:

$$\mathcal{S}(k_u^{\rm out}(\omega \to 0)) \simeq \frac{1}{2}\xi_u \frac{\omega}{|w_u^{\rm out}(0)|} \tag{4.77}$$

$$\mathcal{S}(k_d^{\rm out}(\omega \to 0)) \simeq \mathcal{S}_0 \equiv \mathcal{S}(k_0) \qquad d = d1, d2 \tag{4.78}$$

This translates on the phase factors as follows:

$$\Phi_{uu}(x, x', \omega \to 0) = \omega \Pi_{uu}(x, x') = \omega \, \frac{(x - x')}{w_u^{\rm out}(0)} \tag{4.79}$$

$$\Phi_{ud}(x, x', \omega \to 0) = \omega \Pi_{ud}(x, x') + \sigma_d k_0 x' \qquad d = d1, d2 \tag{4.80}$$

$$\begin{aligned} \Phi_{dd'}(x, x', \omega \to 0) &= -\sigma_d k_0 x + \sigma_{d'} k_0 x' + \omega \Pi_{dd'}(x, x') \\ &= -k_0(\sigma_d x - \sigma_{d'} x') + \omega \frac{(x - x')}{w_0} \qquad d, d' = d1, d2 \end{aligned} \tag{4.81}$$

where $\Pi_{rr'}(x, x')$ is defined as in (4.63). In general, the phase factor $\Phi_{rr'}(x, x', \omega)$ contains a frequency-independent contribution, which, as we will see, produces an oscillating correlation signal with momentum k_0, as well as a term proportional to ω, that determines the locus of points in the (x, x') plane in which the signal is peaked: self-correlations contribute only close to the main diagonal, since $\Pi_{rr}(x, x') \propto (x - x')$. The same holds for ($d1$-$d2$) cross-correlations, due to the identical group velocity for the two modes. On the contrary, (u-$d1$) and (u-$d2$) correlations are expected to be superimposed on a line defined by:

$$\Pi_{ud}(x, x') = \frac{x}{w_u^{\rm out}(0)} - \frac{x'}{w_0} = 0 \tag{4.82}$$

The solution of the scattering problem gives the following results for the scattering matrix coefficients: those involving d modes tend to a constant value, while $\mathcal{M}_{ud2}$ tends to zero in the zero-frequency limit. More specifically, we find:

$$\begin{aligned} |\mathcal{M}_{ud2}(\omega \to 0)|^2 &\propto \omega \\ \mathcal{M}_{ud2}(\omega \to 0)\mathcal{M}^*_{dd2}(\omega \to 0) &\propto \sqrt{\omega} \qquad d = d1, d2 \\ \mathcal{M}_{dd2}(\omega \to 0)\mathcal{M}^*_{d'd2}(\omega \to 0) &\simeq \text{const} \qquad d, d' = d1, d2 \end{aligned} \tag{4.83}$$

Notice that, while the asymptotic behaviour at $\omega \to 0$ we just discussed is valid for any finite value of Ω_d, in the relativistic regimes (see Figs. 4.4 and 4.5) it is reached at extremely small frequencies: in other words, the saturation frequency $\overline{\omega}$ can be much smaller than the threshold value ω_* (see Fig. 4.7). If this is the case, correlations might be not entirely determined by the asymptotic behaviour at $\omega \to 0$. Moreover,

in realistic experimental setups (or time-dependent numerical simulations) such small frequencies might not be resolved, since they require extremely long time-scales.

Non relativistic regime For these reasons, let us first consider the non-relativistic case $\hbar\Omega_d \sim |\kappa_d| n$, shown in Fig. 4.6, for which the above Taylor expansions (for momenta, structure factors and scattering matrix coefficients) are approximately valid in the whole range $[0, \omega_*]$. We can therefore easily derive approximate results for the different contributions to the correlation signals, which are shown in Fig. 4.11. We will not discuss the self-correlation terms due to the u-mode, $\mathcal{G}^{(uu)}_{\nu\nu}(x, x')$, since it always gives a trivial signal peaked on the main diagonal $x = x'$, sometimes hidden by the infrared divergence of $\mathcal{C}_2$, unless the latter is regularized by considering phase differences, as we already discussed.

Let us start our calculation from density-density correlations; cross terms in the (ud) sector (characterized by $xx' < 0$), give:

$$\sum_{d=d1,d2} \mathcal{G}^{(ud)}_{33}(x, x') \propto \sin\big(k_0 x'\big) \int_0^{\omega_*} \omega \sin\big[\omega \Pi_{ud}(x, x')\big] \mathrm{d}\omega + (x \leftrightarrow x') \tag{4.84}$$

The signal is not peaked, but rather vanishing along the correlation line (4.82), because the above integral is anti-symmetric with respect to a change of sign of Π_{ud}; moreover, it is accompanied by an oscillation with wavelength $2\pi/k_0$. A similar feature is present for density correlations in the analog black-hole interior: the signal consists indeed in a checkerboard pattern with wavelength $2\pi/k_0$ whose amplitude is maximum along the main diagonal $x = x'$:

$$\sum_{d,d'=d1,d2} \mathcal{G}^{(dd')}_{33}(x, x') \propto \sin(k_0 x) \sin\big(k_0 x'\big) \mathrm{sinc}\left[\omega_* \frac{(x - x')}{w_0}\right] \tag{4.85}$$

Notice that, in contrast with the case of an acoustic white-hole [119], this checkerboard pattern is not infrared divergent. The numerical calculations shown in Fig. 4.11(a) confirm these results.

Analogous calculations can be performed to compute phase correlations $\mathcal{G}_{22}(x, x')$ and density-phase correlations $\mathcal{G}_{23}(x, x')$. The general result is a sinc contribution, peaked along either the main diagonal $x = x'$ or along the straight lines defined by $\Pi_{ud}(x, x') = 0$, multiplied by an oscillating term with characteristic wavelength $2\pi/k_0$, due to the zero-frequency modes.

Cross correlations between u and d modes in the $xx' < 0$ quadrants give:

$$\sum_{d=d1,d2} \mathcal{G}^{(ud)}_{22}(x, x') \propto \cos(k_0 x) \mathrm{sinc}\big[\omega_* \Pi_{ud}(x, x')\big] + (x \leftrightarrow x') \tag{4.86}$$

Notice that the signal is symmetric with respect to a change of sign in $\Pi_{ud}(x, x')$, contrary to what happens to density correlations. In the (dd) quadrant $(x, x' > 0)$ we find a checkerboard pattern analogous to (4.85), apart from a $\pi/2$ phase shift:

$$\sum_{d,d'=d1,d2} \mathcal{G}^{(dd')}_{22}(x, x') \propto \cos(k_0 x) \cos\big(k_0 x'\big) \mathrm{sinc}\left[\omega_* \frac{(x - x')}{w_0}\right] \tag{4.87}$$

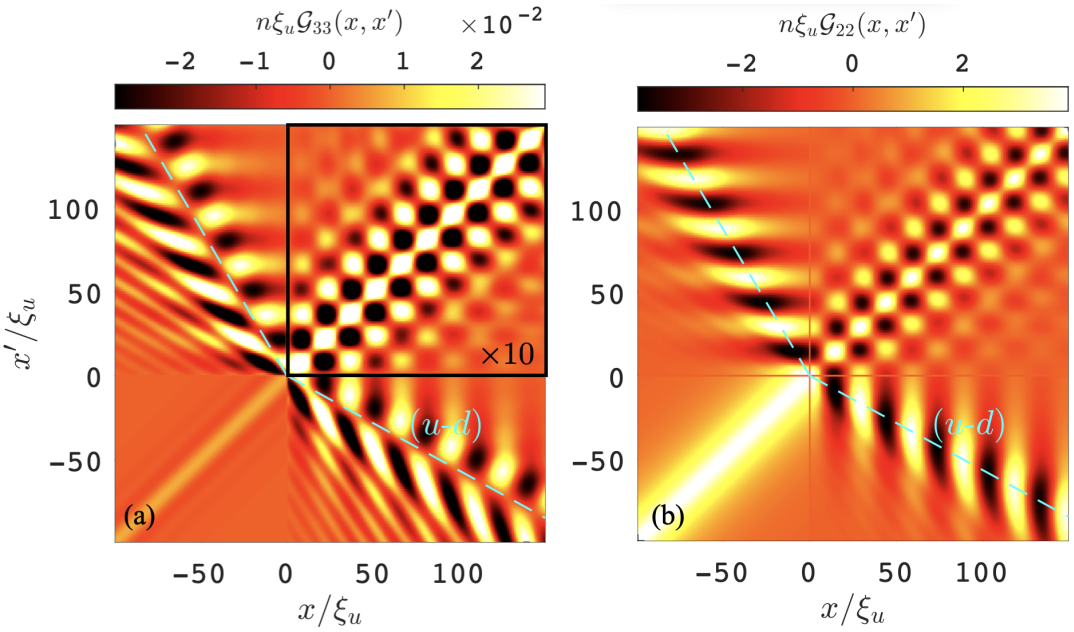

FIGURE 4.11: Density-density (a) and phase-phase (b) correlations in the non-relativistic gapped case, numerically computed using (4.49), (4.50) and (4.55), (4.56), respectively; the parameters are the same as in Fig. 4.6: the dispersion relation for modes in the downstream region is almost parabolic. The momentum of zero-frequency modes is approximatively $k_0\xi_u \sim 0.2$, leading to oscillating patterns with characteristic wavelength $2\pi/k_0 \sim 30\xi_u$. Cyan dashed lines identify the solution of (4.82), on which the (ud) cross-correlation is peaked. In panel (a), the (dd) correlation signal in the $x, x' > 0$ quadrant (within the black square) has been reduced by a factor 10, in order to show it on the same scale as the (ud) contribution.

Once again, these results are consistent with numerical results shown in Fig. 4.11(b): in particular, the signal is two orders of magnitude stronger than the standard mustache visible in density correlations for the uncoupled case [see Fig. 4.9(a)]; moreover, phase correlations between the interior and exterior of the analog black-hole appear as an *oscillating Hawking mustache*, which carries information about the massive nature of the emitted particles in the downstream region.

We obtain similar results for density-phase correlations (not shown):

$$\sum_{d=d1,d2} \mathcal{G}_{23}^{(du)}(x,x') \propto \sin(k_0 x)\mathrm{sinc}\left[\omega_* \Pi_{ud}(x,x')\right] + (x \leftrightarrow x') \tag{4.88}$$

$$\sum_{d,d'=d1,d2} \mathcal{G}_{23}^{(d\neq d')}(x,x') \propto \sin[k_0(x+x')]\mathrm{sinc}\left[\omega_* \frac{(x-x')}{w_0}\right] \tag{4.89}$$

Since only cross-correlations contribute to the signal, the checkerboard pattern in the (dd) sector is replaced by an oscillation orthogonal to the main diagonal.

Relativistic regimes As anticipated, the analytical calculations done so far might not

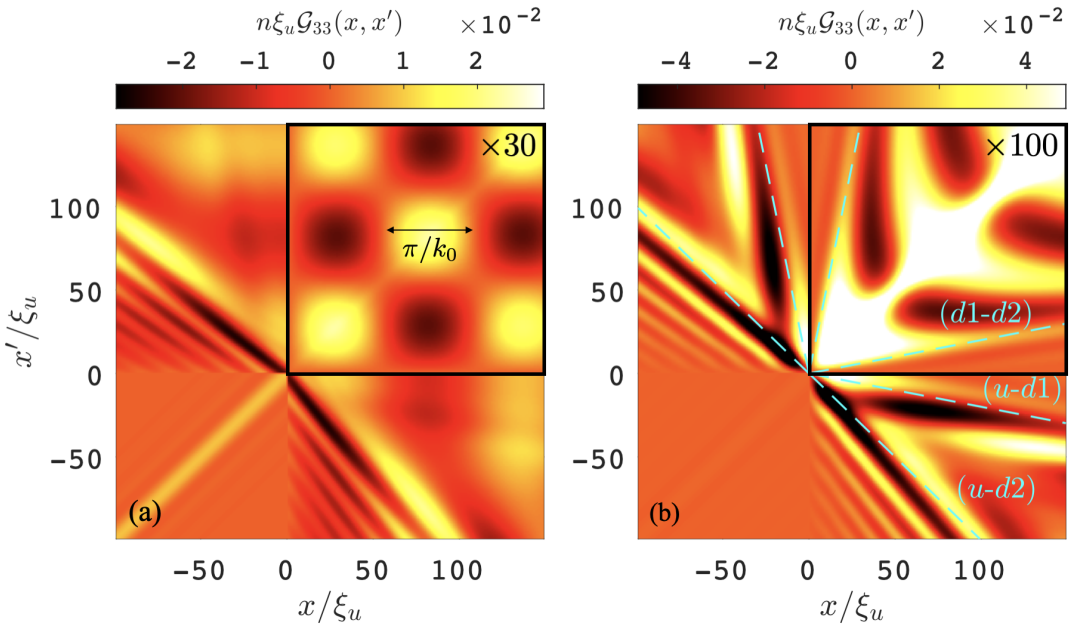

FIGURE 4.12: Relative density correlations $\mathcal{G}_{33}(x,x')$ in the two relativistic regimes $\hbar\Omega_d \ll \kappa_d n$ [panel (a)] and $\hbar\Omega_d + \kappa_d n \sim 0$ [panel (b)]. The (dd) correlation signal in the $x, x' > 0$ quadrant (within the black square) has been reduced by a factor 30 (100) in panel (a) [panel (b)], in order to show it on the same scale as the (ud) contribution. Parameters are chosen as in Fig. 4.4. In both cases $k_0\xi_u \simeq 0.057$, which leads to $\pi/k_0 \simeq 55\xi_u$.

be valid for the two relativistic regimes $\Omega_d \sim 0$ and $\hbar\Omega_d + \kappa_d n \sim 0$, for which the asymptotic low-frequency behaviour is only reached at extremely small frequencies $\overline{\omega} \ll \omega_*$ (or, equivalently, long time-scales). This is particularly true for density correlations in the (ud) sectors, since the main contribution to the integral in Eq. (4.84) does not come from the $\omega \to 0$ limit. Even when this is not the case, in a time-dependent setup, the correlation signal might converge to the stationary result only at extremely long times and have completely different features prior to convergence; in particular, regular *undulations*, such as those predicted by Eqs. (4.85), (4.87) or (4.86), are expected to appear only at times of the order of $1/\overline{\omega}$.

Let us consider, for instance, the relativistic regime $\Omega_d \sim 0$ of Fig. 4.4: in the frequency range $[\overline{\omega}, \omega_*]$ wavevectors of all the propagating out-going modes can be considered approximatively linear with frequency [see Eq. (4.61)], as in the uncoupled case. This implies a linear dependence on ω of the structure factor as well. As for the scattering matrix coefficients, we find approximately:

$$\Re\big[\mathcal{M}^*_{rd2}(\omega)\mathcal{M}_{r'd2}(\omega)\big] \propto \frac{1}{\omega^\alpha} \qquad \alpha = \begin{cases} 1 & \text{if } r = r' = u \\ 3/2 & \text{if } r = u, r' = d1, d2 \\ 2 & \text{if } r, r' = d1, d2 \end{cases} \tag{4.90}$$

while imaginary parts have much weaker dependence on frequency. The completely different behaviour of these quantities with respect to that in the zero-frequency limit

can manifest in the correlation signal, as visible in the (ud) sector of the density-density correlation plot reported in Fig.4.12(a): in particular $(u\text{-}d1)$ and $(u\text{-}d2)$ correlations are not superimposed, due to the different group velocities of the downstream modes, and undulations, although slightly visible, are not dominating the signal. On the contrary, in the (dd) sector of $\mathcal{G}_{33}$, as well as for $\mathcal{G}_{22}$ and $\mathcal{G}_{23}$, reported in Fig. 4.14(a) and 4.13(a), correlations are entirely given by undulations: this is due to the extremely high asymptotic values of the scattering coefficients involving the d modes as $\omega \to 0$ [see Fig. 4.4(c)].

The situation is slightly different in the vicinity of the critical point, see Fig. 4.5: at intermediate frequencies $\omega \lesssim \omega_*$, the wavevectors of all the out-going modes are linear with ω, but the structure factor in the downstream region is inversely proportional to ω, thus the roles of $R_d^{\rm out}$ and $Q_d^{\rm out}$ $(d = d1, d2)$ coefficients are exchanged with respect to the standard gapless case. The scattering matrix elements are instead well approximated by the zero frequency results of Eqs.(4.83) [see Fig. 4.5]. As a consequence, density correlations in the (ud) channel are, once again, dominated by the standard *mustaches*, rather than *undulations*, as shown in Fig. 4.12(b). In the (dd) sector, as well as in phase correlations [shown in Fig. 4.14(b)] and mixed density-phase ones [reported in Fig. 4.13(b)], the two contributions compete and both features (the *mustaches* along the correlation lines (4.69) and *undulations* with wavevector k_0) are visible. In particular the $(u\text{-}d2)$ cross correlation between the positive energy Hawking particle propagating in the black-hole exterior and its negative energy partner propagating in the black-hole interior is not only present in the signal for $\mathcal{G}_{33}$, but also in phase correlations $\mathcal{G}_{22}$, where its amplitude is larger by an order of magnitude.

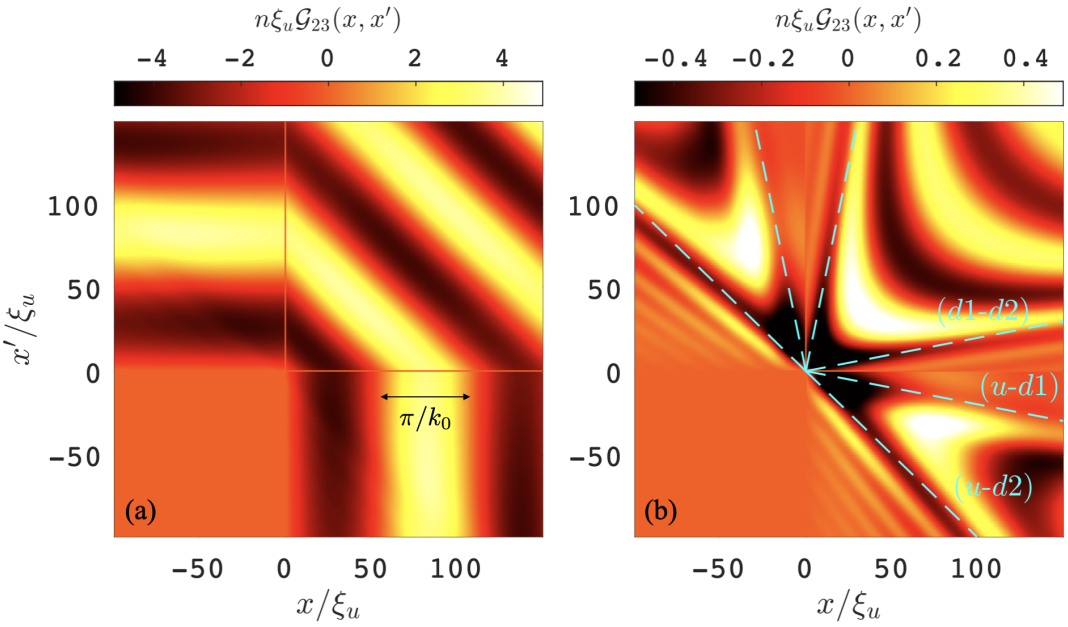

FIGURE 4.13: Density-phase correlations $\mathcal{G}_{23}(x, x')$ in the two relativistic regimes $\hbar\Omega_d \ll \kappa_d n$ [panel (a)] and $\hbar\Omega_d + \kappa_d n \sim 0$ [panel (b)]. Parameters are chosen as in Fig. 4.4. In both cases $k_0\xi_u \simeq 0.057$, which leads to $\pi/k_0 \simeq 55\xi_u$.

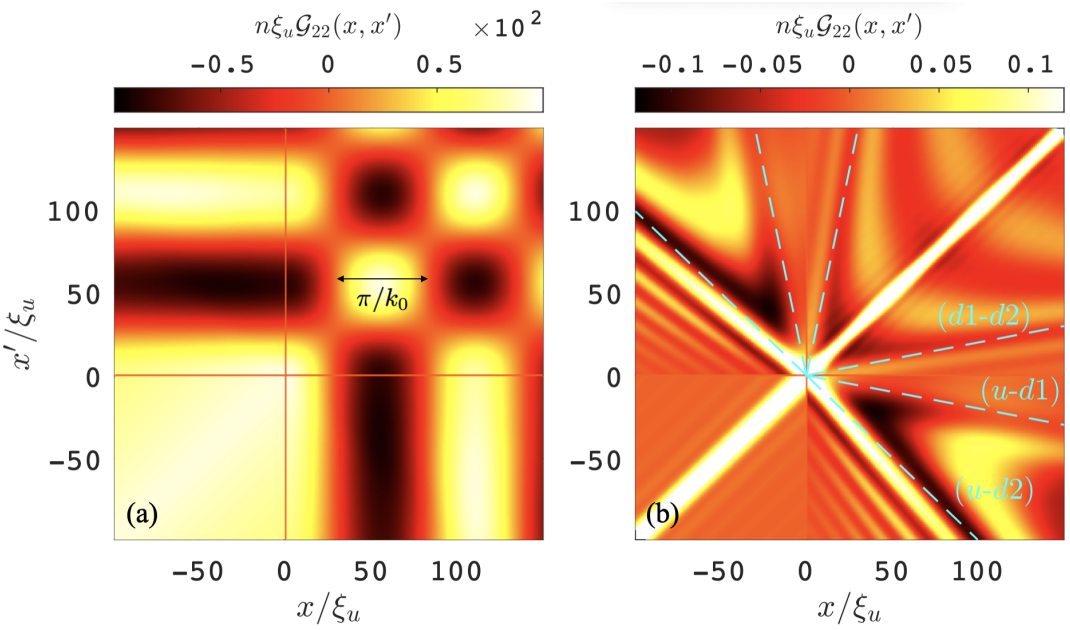

FIGURE 4.14: Relative phase correlations $\mathcal{G}_{22}(x,x')$ in the two relativistic regimes $\hbar\Omega_d \ll \kappa_d n$ [panel (a)] and $\hbar\Omega_d + \kappa_d n \sim 0$ [panel (b)]. Parameters are chosen as in Fig. 4.4. In both cases $k_0\xi_u \simeq 0.057$, which leads to $\pi/k_0 \simeq 55\xi_u$.

Let us, once again, stress that the results we just discussed are valid, strictly speaking, at infinitely long time after the creation of the sonic horizon. A more rigorous study of the development of the signal through time-dependent numerical simulation will be the subject of future work.

4.7 Conclusions and future perspectives

In this Chapter we have studied analog Hawking emission of spin modes from a sonic horizon in a binary mixture of Bose-Einstein condensates, both with and without a coherent-coupling between the two components.

We started from an analysis of the scattering properties of the analog horizon, which carry information about the Hawking emission spectrum: we have interpreted the presence of a coherent coupling in the downstream region as a modification of the grey-body factor of the analog black-hole, which acquires a quadratic frequency dependence in the limit $\omega \to 0$; moreover, we have verified that the thermal character of the emission is not affected by the value of the Rabi frequency: this is remarkable considering that both the step configuration and the parameters regime we considered break the hydrodynamic approximation, and thus prevent a straightforward application of the gravitational analogy.

We have also exploited the scattering matrix formalism to compute two-point correlation functions; in addition to density-density correlations, previously considered in the literature, we have computed phase-phase and density-phase correlation functions, with the aim of finding an observable in which Hawking radiation manifests through a signal with larger intensity and, as such, easier to measure in a lab. In particular,

we found that in the limit of a large Rabi frequency ($\hbar\Omega_d \gg |\kappa_d|n$), phase correlations show an *oscillating Hawking mustache*, characterized by the typical *undulation* expected when massive particles are involved in the emission process; the signal is orders of magnitude stronger than the one observed in density correlations and the parameters we consider seem within reach of currently available experiments [57].

Our results are not only relevant for atomic Bose-Einstein condensates, but also for polariton systems: in the latter case, mixtures are generated by exploiting the polarization degree of freedom and the gap in the dispersion relation opens if the pump laser is detuned with respect to the polariton interaction energy [32].

A natural extension of our work concerns the analysis of more realistic configurations, involving a (smooth) jump in the density profile and/or in the flow velocity, rather than in the spin interaction constant [45, 112]. Given that typical values of the interaction constants lead to $\kappa \ll G$ [57, 77], an analog horizon for spin modes can be generated by leaving the density channel subsonic everywhere; nonetheless, having different densities on the two sides of the horizon might affect the signal in the correlations. In addition to this, time-dependent numerical simulations based on Gross-Pitaevskii or Bogoliubov theory would be necessary to support our semi-analytical results: it would be useful to identify the most convenient initialization procedure to generate the analog horizon, expecially in the presence of the coherent coupling, and to analyse the robustness of the Hawking *mustache* to a finite temperature. Along the same lines, a further development of our work could be the study of the effect of a small imbalance between the number of atoms in each component, that would lead to a weak coupling between density and spin modes [57].

Simple one-dimensional configurations similar to the one we considered throughout this Chapter are also suited, in principle, to analyse black-hole related phenomena other than Hawking radiation. For instance, the addition of a finite coherent coupling in the upstream region, might allow to observe a phenomenon known as *boomerang effect* [120]: modes with frequency smaller than the gap in the upstream region are emitted by the analog horizon but, instead of propagating to infinity, they bounce and are dragged back in the black-hole interior.

Another phenomenon that is expected to occur in black-hole spacetimes is *rotational superradiance* [47]: as already pointed out, the toy model of Fig. 4.1 does not allow to observe superradiant amplification of upstream modes because its analog geometry does not account for rotation. However, as suggested in Refs. [81, 121], superradiance-related phenomena could be analysed in a planar configuration if rotation was mimicked through a synthetic vector potential. Alternatively, one must consider stationary states whose analog metric shares the same features of a rotating spacetime, such as two-dimensional quantized vortices. This will be the main subject of the following Chapter.

5 Superradiant instabilities in analog rotating spacetimes

5.1 Introduction

In the previous Chapter we discussed Hawking emission in an analog spacetime with a sonic horizon. This Chapter is devoted to another astrophysical phenomenon which instead relies on the presence of a so-called *ergoregion*, known as superradiance.

The term *rotational superradiance* refers to the amplified scattering of waves from a rotating object at the expenses of the rotational energy of the object itself [47]. It is a fully classical phenomenon, that was first predicted for elecromagnetic waves impinging on a rotating cylinder [48]; it has been experimentally observed for surface waves in a classical fluid [49], acoustic waves scattered by a rotating disk [50] and in optical systems [51]. Rotational superradiance relies on the possibility of extracting energy from the rotating object, so that the excess energy of the amplified reflected wave is compensated by such energy loss [47]; from a different perspective, one could argue that superradiant amplification can occur whenever there exist negative energy states that can store the extra energy associated to the amplification [81].

In the gravitational context, superradiance is predicted to occur in a variety of spacetime geometries, in particular in the surroundings of massive rotating objects, such as Kerr black holes [46]: the dragging of spacetime by the rotating object gives rise to an ergoregion, namely a spatial region supporting negative-energy light and matter modes. In this case, the process of superradiance can be microscopically explained as the amplified reflection of a positive-energy wave impinging onto the boundary of the ergoregion, accompanied by the transmission of a negative-energy wave inside the ergoregion. In the presence of some reflecting element, self-amplification of one of the outgoing modes may take place, leading to an exponentially growing perturbation (see the sketch in Fig. 5.1). Depending on the location of the reflecting element on either the inner or the outer side of the ergosurface, the instability takes the name of ergoregion instability [52, 53, 122–124] or black hole-bomb instability [54, 125, 126].

For what concerns the specific case of rotating black holes in an asymptotically flat spacetime, dynamical stability is guaranteed by the possibility of amplified reflected radiation to propagate away to infinity and by the presence of an event horizon, which, being a one-way membrane, provides a dissipation mechanism that suppresses self-amplification of negative norm modes inside the ergoregion. A reflecting boundary outside the ergoregion might be provided by asymptotically anti-de-Sitter spacetime geometries [54] or by the *boomerang effect* if the amplified field is massive [127, 128]. Ergoregion instabilities, instead, are likely to develop in rotating spacetimes which feature an ergoregion but not an event horizon [47].

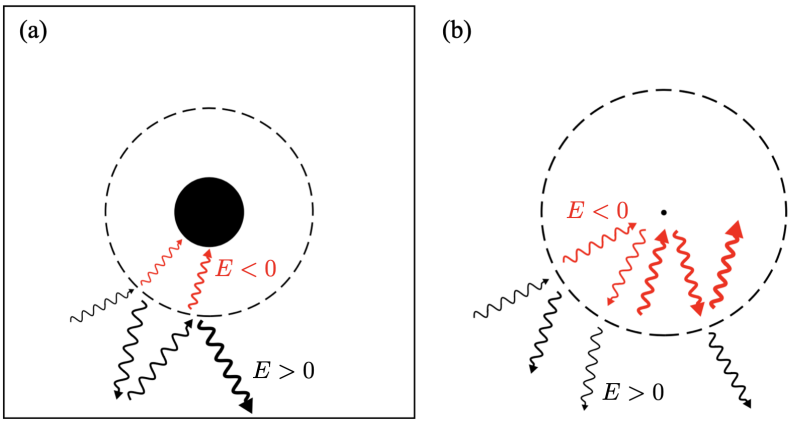

FIGURE 5.1: Illustrative sketch of the development of a black-hole bomb [panel (a)] and of an ergoregion [panel (b)] instability: in the former case, negative energy states inside the ergoregion are absorbed or dissipated while positive energy ones are reflected and amplified; in the latter, positive energy modes can propagate away, while negative energy ones, bound inside the ergoregion, are self-amplified due to the absence of an absorption or dissipation mechanism. Image adapted from [81].

Rotating Bose-Einstein condensates are promising platforms to study superradiant phenomena [47, 129]. A number of theoretical studies have investigated superradiance in configurations featuring a single vortex located at the center of a cylindrically symmetric trap. In particular, the analog gravity perspective has offered transparent physical explanations for the hydrodynamic instability of multiply-charged single vortex configurations [130–133] by connecting them to ergoregion instabilities of rotating massive objects in gravitation [56].

Within this general framework, in this Chapter, we explore ergoregion instability phenomena in two-component BECs displaying a single quantized vortex in both components. Thanks to the very different value of the density- and spin-sound speeds, the ergosurface for spin waves is no longer bound to sit inside or in the close vicinity of the vortex core as it instead happens in single component BECs, but can be pushed far away from the vortex core into the external region where the density is approximately constant. This is of great interest for analog gravity as it leaves a wider space to investigate the dynamics of the quantum field in the ergoregion and disentangle the different effects at play.

Beyond analog gravity, an active interest for this physics is also coming from a purely quantum gas perspective: a recent numerical work [134] has pointed out the rich phenomenology of vortex splitting in harmonically trapped two-component BECs: singly-charged vortices are dynamically unstable for sufficiently strong repulsive inter-component interactions, whereas doubly-charged vortices dispose of several decay channels. Experimentally, the splitting of a singly-charged vortex into a pair of half-quantized vortices has been observed in spinor exciton-polariton superfluids [135] and antiferromagnetic spinor BECs [136].

Here, we take advantage of the analog gravity point of view to develop a transparent physical interpretation of vortex physics in two-component BECs in terms of

superradiance effects. Use of this formalism allows us to highlight a number of features that are specific to two-components BECs and characterize them in view of forthcoming experimental studies. In addition to recovering the main predictions of previous works, e.g. on vortex splitting instabilities, we identify regimes where a clean analog of the ergoregion instability of massive rotating objects is visible.

5.2 Draining vortices as analogs of rotating black holes

The simplest configuration which reproduces the main features of a rotating black-hole geometry in an analog system is the two-dimensional draining vortex [3, 47], whose fluid flow is characterized by a drain and a circulation term:

$$\mathbf{v} = -\frac{A}{r}\hat{r} + \frac{B}{r}\hat{\theta} \equiv -v_r\hat{r} + v_\theta\hat{\theta} \tag{5.1}$$

where (r, θ) are polar coordinates and $A > 0$. The analog metric (2.41) associated to this vortical flow, when written in polar coordinates, leads to the line element:

$$\mathrm{d}s^2 = -\left(c^2 - \frac{A^2+B^2}{r^2}\right)\mathrm{d}t^2 + \frac{2A}{r}\mathrm{d}t\mathrm{d}r - 2B\mathrm{d}t\mathrm{d}\theta + \mathrm{d}r^2 + r^2\mathrm{d}\theta^2 \tag{5.2}$$

The following coordinate transformation [3, 47, 137]:

$$c\,\mathrm{d}t' \equiv c\,\mathrm{d}t + \frac{v_r/c}{1-(v_r/c)^2}\mathrm{d}r \tag{5.3}$$

$$r\,\mathrm{d}\theta' \equiv r\,\mathrm{d}\theta + \frac{v_r v_\theta/c^2}{1-(v_r/c)^2}\mathrm{d}r \tag{5.4}$$

allows to write the line element (5.2) in a form that resembles the equatorial slice of the Kerr black-hole line element:

$$\mathrm{d}s^2 = -\left(c^2 - |\mathbf{v}|^2\right)\mathrm{d}t^2 + \frac{\mathrm{d}r^2}{1-(v_r/c)^2} - 2B\mathrm{d}t\mathrm{d}\theta + r^2\mathrm{d}\theta^2 \tag{5.5}$$

and that facilitates the identification of an ergoregion and an event horizon: the former is located at the radius r_E at which the first component of the metric vanishes ($g_{tt} = 0$), while the position of the analog horizon r_H is signalled by a singularity of the coordinate system (more specifically of g_{rr}):

$$r_H = \frac{A}{c} \qquad r_E = \frac{\sqrt{A^2+B^2}}{c} \tag{5.6}$$

Moreover, if $\Omega_H \equiv B/r_H^2$ is the angular velocity of the analog horizon, modes with azimuthal number M undergo superradiant amplification if their frequency is low enough, that is $\omega < M\Omega_H = MBc^2/A^2$ [137].

As expected, r_H and r_E coincide with the locations at which the modulus $|\mathbf{v}|$ and the radial component v_r of the velocity flow exceed the speed of sound, respectively. Moreover, in order for the analog metric to display an horizon, it is necessary to engineer a flow with drain, $A \neq 0$. It is possible to do so with classical fluids [49],

through a physical drainage hole, or with polaritons [138] and optical systems [12], which naturally possess dissipation channels. On the contrary, thanks to particle-number conservation, atomic Bose-Einstein condensates support quantized vortices with non-zero circulation but vanishing drain [55], whose analog metric displays an ergoregion but no horizon, and are therefore the ideal background to study analogs of the ergoregion instabilities of rotating spacetimes. From a different perspective, if $A = 0$ the superradiance condition translates to $\omega < \infty$, therefore all modes are amplified at the ergoregion: any small perturbation of the system triggers superradiant scattering, which, due to self-amplification, leads to a dynamical instability.

5.3 Quantized vortices in atomic BECs

Let us consider a two-dimensional BEC. Even though condensation is strictly speaking not possible in 2D, effectively two-dimensional atomic superfluids can be realized experimentally by tightly confining the condensate along one direction, say z, imposing a much weaker confinement in the orthogonal plane (x, y); the main effect of the transverse confinement is a geometrical renormalization of the interaction strength, while the dynamics of the order parameter can be described with an effectively two-dimensional Gross-Pitaevskii equation [14].

More specifically we are interested in an unpolarized binary mixture with equal intraspecies interactions $g_{11} = g_{22} = g$. For the sake of simplicity, let us assume there is no coherent coupling between the two components, $\Omega = 0$; we will briefly discuss the effect of a coupling later on. We also assume $\kappa \equiv g - g_{12} > 0$ so that the mixture is miscible. The system is subject to an external potential $V(r)$ that only depends on the radial coordinate $r = \sqrt{x^2 + y^2}$ and not on the polar angle $\theta = \arctan(y/x)$. Stationary states are characterized by identical order parameters for the two components satisfying the time-independent GP equation:

$$\mu\psi(\mathbf{r}) = \left[-\frac{\hbar^2\nabla^2}{2m} + V(r) + G\frac{n(\mathbf{r})}{2}\right]\psi(\mathbf{r}) \tag{5.7}$$

where μ is the oscillation frequency of the matter field and $G = g + g_{12}$. Of course μ takes the meaning of chemical potential when we consider the lowest-order stationary state of (5.7) corresponding to the ground state of the condensate.

Spin-symmetric quantized vortices are factorizable solutions of (5.7) the form [14]:

$$\psi(r, \theta) = f(r)e^{iL\theta}e^{-i\mu t/\hbar} \tag{5.8}$$

where the integer-valued parameter L is referred to as the *charge* of the vortex and the vortex profile $f(r)$ is a solution of:

$$-\frac{\hbar^2}{2m}\frac{\partial}{\partial r}\left(r\frac{\partial f}{\partial r}\right) + \left[V(r) + \frac{\hbar^2L^2}{2mr^2} - \mu\right]f + Gf^3 = 0 \tag{5.9}$$

In the limit $r \to 0$, where only the kinetic energy contribution is relevant, Eq.(5.9) is solved by $f(r \to 0) \propto r^{|L|}$, thus the density of atoms vanishes at $r = 0$. On the contrary, far from the vortex line, the density profile is well approximated by the

Thomas-Fermi solution for the ground state:

$$f^2(r \to \infty) \simeq \frac{n_{\rm TF}(r)}{2} \equiv \frac{\mu_{\rm TF} - V(r)}{G} \tag{5.10}$$

where $\mu_{\rm TF}$ is determined through the normalization condition for the total particle number N. For instance, for a uniform mixture in a box of radius R, one has:

$$\mu_{\rm TF} = \frac{GN}{2\pi R^2} \tag{5.11}$$

while, in the case of a system in an harmonic trap with frequency ω_0 and of TF radius R, we find:

$$\mu_{\rm TF} = \frac{1}{2} m\omega_0^2 R^2 = \frac{GN}{\pi R^2} \tag{5.12}$$

The exact solution for $f(r)$ has to be found numerically by either solving (5.9) or the time-dependent Gross-Pitaevskii equation in imaginary-time. In the former case, Eq.(5.1) has to be solved self-consistently so to determine the proper value of μ, while in the latter μ can be computed as an integral over space [see Eq.(2.6)], once the profile $f(r)$ has been determined.

The velocity flow associated to the quantized vortex (5.8) is purely tangential

$$\mathbf{v}(r) = \frac{\hbar L}{mr}\hat{\theta} \tag{5.13}$$

and coincides with (5.1) if $A = 0$ and $B = \hbar L/m$. As we already pointed out, the associated analog metric displays an ergoregion but not an horizon, and this makes quantized vortices the ideal configuration to analyse the development of ergoregion instabilities. Strictly speaking, the ergosurface position r_E is well defined only if all modes move at the same speed: for a quantized vortex in a BEC this assumption is not only violated by the quadratic dispersion of high-frequency modes, but also by the inhomogeneity of the density profile, and in particular by the density drop in the vortex core, that breaks the hydrodynamic approximation.

As a consequence, we deal, once again, with a configuration to which we cannot straightforwardly apply the gravitational analogy: however, as in Chapter 4, we will see that the main features of superradiance-related instabilities are preserved and that dynamical instabilities of vortex configurations in BECs can be intrepreted as due to self-amplification of negative norm modes at an analog ergoregion.

Although the analogy can be exploited for single component condensates [56], working with symmetric binary mixtures might lead to practical advantages in the experimental observation of the development of analog ergoregion instabilities: as already discussed in Chapter 3, there exists two classes of elementary excitations of a binary mixture, density and spin modes; both are subject to an analog metric with the same structure as (2.41), but with different sound speed. For an inhomogeneous density profile, these acquire a radial dependence as well:

$$c_{d,s}(r) = \sqrt{\frac{g \pm g_{12}}{2m}}\, f(r) \tag{5.14}$$

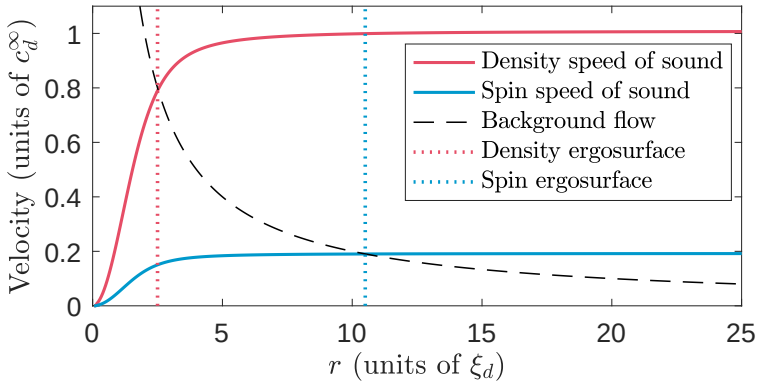

FIGURE 5.2: Comparison between the density and spin sound speed (red and blue line respectively), and the flow velocity (dashed black line) in a vortex configuration. The location of the ergosurface for density (spin) excitations, indicated by the dotted red (blue) line, is found as the intersection between $|\mathbf{v}(r)|$ and $c_d(r)$ $[c_s(r)]$. All velocities are normalized to the large-distance value of the speed of density sound, $c_d^\infty \equiv c_d(r \to \infty)$. The plot is obtained using the numerically calculated density profile of a vortex of charge $L = 2$; interactions are set to the experimentally relevant value $g_{12} = 0.93g$, giving $c_d/c_s = \xi_s/\xi_d \sim 5.25$ [57].

The local sound velocities for an $L = 2$ vortex configuration are shown in Fig. 5.2 (red and blue solid lines, respectively). Since $f(r)$ must vanish at the vortex line $r = 0$, while the velocity flow (dashed black line) diverges as $1/r$ in the same limit, there exist two different positions, that roughly coincide with the ergosurface location r_E, at which the fluid becomes supersonic with respect to density and spin modes (red and blue dotted lines, respectively). If the system is asymptotically homogeneous with density $n^\infty \equiv n(r \to \infty)$, it is possible to define asymptotic sound speeds $c_{d,s}^\infty \equiv c_{d,s}(r \to \infty)$ and healing lengths $\xi_{d,s} \equiv \hbar/mc_{d,s}^\infty$; the two analog ergoregions are thus approximately found at $r_E \sim L\xi_{d,s}$. It is clear that, for mixtures with $\kappa \ll G$ (that is $g_{12} \lesssim g$), spin modes are subject to an analog spacetime featuring a much larger ergoregion than density ones, since $\xi_s \gg \xi_d$ (see Fig. 5.2); in particular, while density ergoregion instabilities are bound to develop inside the vortex core, which is typically characterized by very small size and low atomic density, the development of dynamically unstable spin modes might be much more accessible in a lab.

Notice that, in contrast to the spin-sonic black-hole configuration analized in Chapter 4, the analog spacetime associated to a quantized vortex necessarily features an ergoregion for both spin and density modes: in principle, it could be possible to generate an analog spacetime featuring only a spin ergoregion through the stabilization of the vortex, either by pinning it or filling it with atoms of an additional component. This will be the subject of future work.

5.3.1 Bogoliubov modes on top of a quantized vortex

In this work we exploit the analysis of the Bogoliubov spectrum [15] to study the stability of spin-symmetric vortex configurations in two-component BECs. In stable

configurations, all frequencies are real-valued and, for each excitation mode, have the same sign as the norm. Modes with positive (real) frequency and negative norm, or vice versa, have instead a negative energy and their existence is a signature of an energetic (or thermodynamic) instability: these modes cannot be excited in an energy-conserving setup, but would destabilize the system if dissipation was included in the GP equation and the system let to thermalize.

The appearance of modes with complex frequency implies instead dynamical instability for the considered configuration: indeed these zero-norm, zero-energy modes always come in pairs, whose frequencies share the same real part and have opposite imaginary parts, $\omega = \eta \pm i\Gamma$. The imaginary part Γ represents the rate of exponential growth of the dynamically unstable mode. Such mode can develop in an energy-conserving problem because it physically corresponds to the simultaneous creation of particles and antiparticles, a process that leaves the total energy unchanged.

Taking advantage of the radial symmetry, the Bogoliubov excitations of frequency ω and angular momentum M on top of a charge-L vortex can be written in the factorized form ($j = d, s$)

$$u_j(\mathbf{r}) = U_j(r)e^{i(M+L)\theta} \tag{5.15}$$

$$v_j(\mathbf{r}) = V_j(r)e^{i(M-L)\theta} \tag{5.16}$$

and the stability of the vortex configuration can be assessed by solving the effectively 1D radial Bogoliubov problem. The frequencies and spatial profile of the collective excitation modes on top of the vortex are computed as the eigenvalues and eigenvectors of the Bogoliubov operators (3.21), (3.22) in the density d and spin s sectors. Notice that the kinetic energy operator, written in polar coordinates, acts differently on the particle and antiparticle component of the mode:

$$\nabla^2 = \frac{\partial^2}{\partial r^2} + \frac{1}{r}\frac{\partial}{\partial r} - \frac{(L \pm M)^2}{r^2} \tag{5.17}$$

where the $+$ ($-$) sign must be chosen when applying the operator to U (V).

5.4 Local density approximation

In general, the Bogoliubov problem on top of a spatially inhomogeneous vortex configuration can hardly be solved analytically. Before proceeding with the numerical diagonalization of the Bogoliubov matrices which will be the subject of the next Section, we start here with an intuitive discussion of the physics on the basis of a local density approximation (LDA).

Let us assume that the condensate is enclosed in a large box trap, so that the density can be considered approximately uniform far from the vortex core, $n(r \gg L\xi_d) \simeq n^\infty$. Within a small spatial region around $\mathbf{r}$, excitations of angular momentum M can be approximated as plane waves with wavevector $\mathbf{k} = k\mathbf{u}_r + (M/r)\mathbf{u}_\theta$, so that the Bogoliubov wavefunctions are $u(\mathbf{r}), v(\mathbf{r}) \propto e^{ikr}e^{iM\theta}$. By exploiting the LDA, the k-dependent Bogoliubov dispersion relation in the radial direction is obtained by taking the uniform result (3.27) and replacing $k^2 \to k^2 + M^2/r^2$. The effect of the finite M is thus to open a gap in the dispersion relation and is equivalent to having

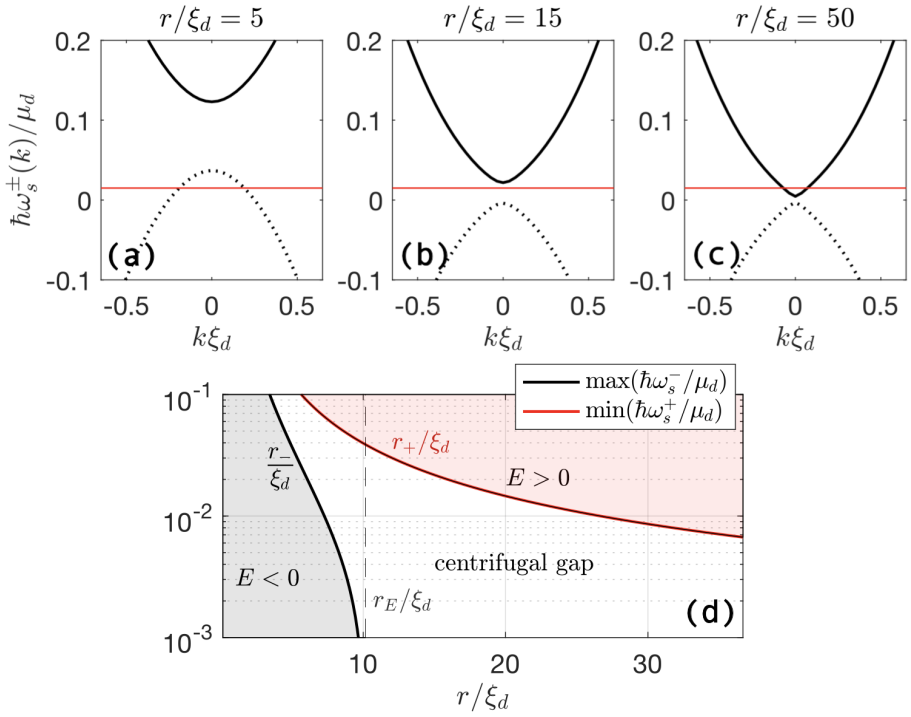

FIGURE 5.3: Properties of the dispersion relation in the LDA (5.18) (obtained with $L = 2, M = 1, g_{12}/g = 0.93, \Omega = 0$, $\mu_d/\mu_s = 27.5$). (a-c) Plot of the dispersion at different radii, showing the availability of positive and negative norm modes at a generic frequency ω, indicated by the red horizontal line: solid (dotted) black lines refer to the upper (lower) branch. (d) Plot of the maximum frequency of the lower branch (black line) and minimum frequency of the upper branch (red line); the red (gray) area indicates the region of the plot where positive (negative) energy modes are available. The white area represents the centrifugal gap. The dashed black line indicates the spin ergosurface location, given by (5.19).

a space-dependent coherent coupling $\Omega(r) = \hbar M^2/2mr^2$. On top of this, one needs to include the overall M-dependent Doppler shift $\delta(r) \equiv \mathbf{k}\cdot\mathbf{v} = \hbar LM/mr^2$ due to the tangential velocity flow. Due to the absence of in-going flow, this Doppler term does not tilt the dispersion relation as a function of the radial wavevector k, but only rigidly shifts it vertically along the frequency axis. This shift is crucial to bring negative-norm (positive-norm) modes up (down) to positive (negative) frequencies.

Combining all these elements together, we obtain the final formula

$$\omega_s^{\pm}(k) = \frac{\hbar LM}{mr^2} \pm \sqrt{\left(\frac{\hbar k^2}{2m} + \frac{\hbar M^2}{2mr^2}\right)\left(\frac{\hbar k^2}{2m} + \frac{\hbar M^2}{2mr^2} + \kappa n^{\infty}\right)} \tag{5.18}$$

where the sign $\pm$ refers to the positive and negative branches, respectively. From this formula, the space-dependent centrifugal gap is $\Delta(r) \equiv \sqrt{\Omega(r)[\Omega(r) + \kappa n^{\infty}]}$. It is worth noticing that in the perfect hydrodynamic limit of a sonic dispersion, the centrifugal gap would instead depend linearly on M as the Doppler shift: $\Delta_{\rm hydro}(r) =$

$\sqrt{\Omega(r)} = \sqrt{\hbar/2mr^2}\, M$. Also notice that including a finite physical coherent coupling would simply result in a larger centrifugal gap for all r.

Because of the Doppler shift and the centrifugal gap, for a generic positive frequency ω, there can be positive norm, negative norm or no modes available depending on the radial position r. Three specific examples for different radial positions r are shown in Fig. 5.3(a-c). A summary of the results for generic $(r, \omega > 0)$ is displayed in panel (d): here, the red and gray shaded areas indicate the (r, ω) regions where positive and negative norm modes are available, respectively. The boundaries of these regions identify two frequency-dependent positions in real space, $r_{\pm}(\omega)$, indicated by the red and black solid lines in Fig. 5.3(d). In particular, $r_{-}(\omega)$ can be thought as an effective frequency-dependent ergosurface position.

An ergoregion instability occurs when a negative norm mode in the inner part of the system is coupled to a positive norm mode living in the outer region, so that the two combine into a pair of zero-norm modes with complex frequencies $\omega \pm i\Gamma$ [56]. In other words, the dynamical instability can be thought as resulting from a tunnelling process between the red- and gray-shaded regions in Fig. 5.3(d), with a tunneling-mediated instability rate determined by the real-space width of the forbidden white region separating them. According to this interpretation, modes with smaller frequency, that is, hydrodynamic excitations, have a more extended antiparticle component, but also a smaller instability rate since they have to cross a much wider forbidden region.

In general, a necessary (but not sufficient) requirement for the occurrence of an ergoregion instability is the presence of negative norm modes in the inner region, which translates in the condition $\delta(r) \geq \Delta(r)$ between the Doppler shift and the centrifugal gap. The limiting radius r_E for which such condition is satisfied can be thought as the boundary of the ergoregion:

$$r_E = L\xi_s \sqrt{1 - \frac{M^2}{4L^2}}\,. \tag{5.19}$$

This value is slightly reduced with respect to the hydrodynamic prediction $L\xi_s$, which is recovered in the $M/L \to 0$ limit, with the correction being due to the non-linear behaviour of the dispersion relation; since the centrifugal gap Δ grows with M faster than the Doppler shift δ, as M increases the ergoregion shrinks in space and eventually disappears for angular momentum modes with $M \geq 2L$. This simple reasoning explains the disagreement of our results with respect to previous works studying ergoregion instabilities with hydrodynamic vortices [55] and in horizonless gravitational spacetimes [124].

As mentioned above, the presence of a physical coherent coupling results in a larger centrifugal gap [white region in Fig. 5.3(d)], so the matching between the external positive-norm modes (red-shading) and the negative-norm ones in the ergoregion (grey-shading) modes is harder to obtain and the unstable modes, if present, are more localized and display a weaker instability rate.

While this discussion based on the LDA provides an intuitive understanding of the microscopic process underlying the ergoregion instability, it completely misses all

those features that stem from the quantization of the radial wavevector k in a finite-size system[1]. Since the radial wavevector is associated to the radial kinetic energy contribution $\hbar^2 k^2/2m$, we expect that for tight enough ergoregions, the minimum value of the kinetic energy set by the quantization of the negative norm mode may increase the size of the effective gap so much that it prevents the development of the instability. Assessing all these features in a quantitative way requires going beyond the LDA and solving the full Bogoliubov problem with numerical tools. This will be the subject of the next Section.

5.5 Bogoliubov spectra

The numerical solution of the Bogoliubov problem is performed as follows. For the chosen value of the vortex charge L, we first find the radial function $f(r)$ that describes the density profile of the stationary vortex and the associated oscillation frequency μ. This is achieved by means of an imaginary-time evolution of the radial Gross-Pitaevskii equation.

We consider two experimentally relevant cases: the harmonic trap and the asymptotically uniform system in a box. The free parameters of the simulation are the interaction constants ratio g_{12}/g, the radial size of the system R and the expected chemical potential in the TF regime (i.e. without vortices) $\mu_{\rm TF}$. The remaining parameters, i.e. the number of particles N and the trapping frequency ω_0, are chosen to satisfy the normalization condition (5.11), (5.12). For all the numerical results shown in the rest of this Chapter, the system size R is much larger than the vortex size $\sim L\xi_d$, which implies $\mu \simeq \mu_{\rm TF}$.

Once the vortex profile $f(r)$ is known, for each value of angular momentum $1 \leq M < 2L$, we build the density and spin Bogoliubov matrices and diagonalize them: the eigenvalues form the Bogoliubov spectrum of the vortex, while the eigenvectors give the real-space profiles of the modes.

In order to assess the dependence of dynamical instabilities on the size of the system and on the external potential applied to the atoms, we performed a calculation of the Bogoliubov spectra as a function of R: the value of g is tuned to keep $\mu_{\rm TF}$ constant. The spectrum of $M = 1$ spin modes over an $L = 1$ vortex are shown in Fig. 5.4, both for a system in an harmonic trap [panels (a)-(c)] and in a box [panels (d)-(f)]. Results are in agreement with Ref. [56]: we find alternate intervals of dynamical stability and instability; in correspondence of the crossing points between a positive and a negative energy mode, we observe the appearance of dynamically unstable modes (red dots) with an associated imaginary frequency bubble. The insets (panels c, f) show examples of the spatial profiles of the particle and antiparticle components of the dynamically unstable modes: the common feature consists in the localization of the antiparticle component (red solid line) in the inner portion of the system, while the particle component (black solid line) is spread throughout the whole volume occupied by the fluid. Notice that there is no qualitative difference in the real-space profiles of

[1] Differently from the planar configurations with synthetic vector potentials considered in [121], in our vortex configuration the irrotational nature of the superfluid flow fixes the characteristic spatial length on which the variation of $\mathbf{v}(r)$ can occur. As a result, it is not possible to find a rigorous limiting procedure in which the LDA is exactly verified.

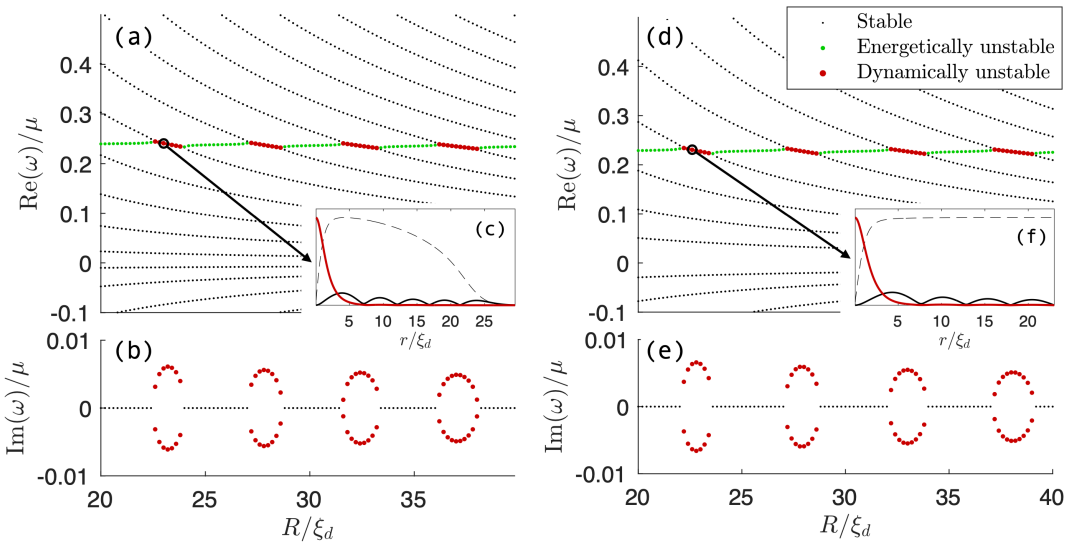

FIGURE 5.4: Bogoliubov spectra for $M = 1$ spin excitations over a vortex of charge $L = 1$ with $g_{12} = 0.93g$. Panels (a-c) refer to an harmonically trapped system of TF radius R, while panels (d-f) refer to a uniform mixture in a box of radius R. Panels (c) and (f) show the real-space profile of the particle (black solid line) and antiparticle (red solid line) components of the dynamically unstable mode for $R = 23\xi_d$; the dashed line represents the rescaled vortex profile $f(r)$.

the unstable modes for the two examined external potentials. We verified that this is true also for other values of vortex charge L and angular momentum M (not shown). Therefore, in the rest of this Chapter we focus on results obtained with an harmonic trapping potential.

As shown in panels (b) and (e), the instability bubbles acquire a larger width but smaller amplitude as R increases. It is therefore convenient, if possible, to simulate the real-time dynamics of systems with relatively small size ($R \sim 20\xi_d$): in addition to the advantage of allowing for a better resolution in space, such configurations also feature a faster development of the instabilities.

Fig. 5.5 and Fig. 5.6 show the Bogoliubov spectra in the spin channel for different angular momenta M as a function of the interaction strength ratio g_{12}/g for vortices of charge $L = 1, 2$. For singly-charged $L = 1$ vortices, in the density channel a negative energy density mode is always present, but its frequency remains below that of positive norm modes (not shown); hence a dynamical instability never develops, in agreement with previous works [56]. On the other hand, the spin channel shows energetic stability for attractive interspecies interactions $g_{12} < 0$ (not shown) and alternated intervals of dynamical stability and instability for repulsive interactions $g_{12} > 0$ [see Fig. 5.5(a-b)]. Similarly to what happens for density fluctuations of multiple-charged vortices in single-component BECs, this originates from the crossing of a spectrally isolated negative norm mode with the band of positive norm ones; the discreteness of the band, due to the finite size of the cloud, explains the existence of instability bubbles separated by intervals of dynamical stability. Note that this is in contrast to the case of an infinitely large system, where a dynamical instability

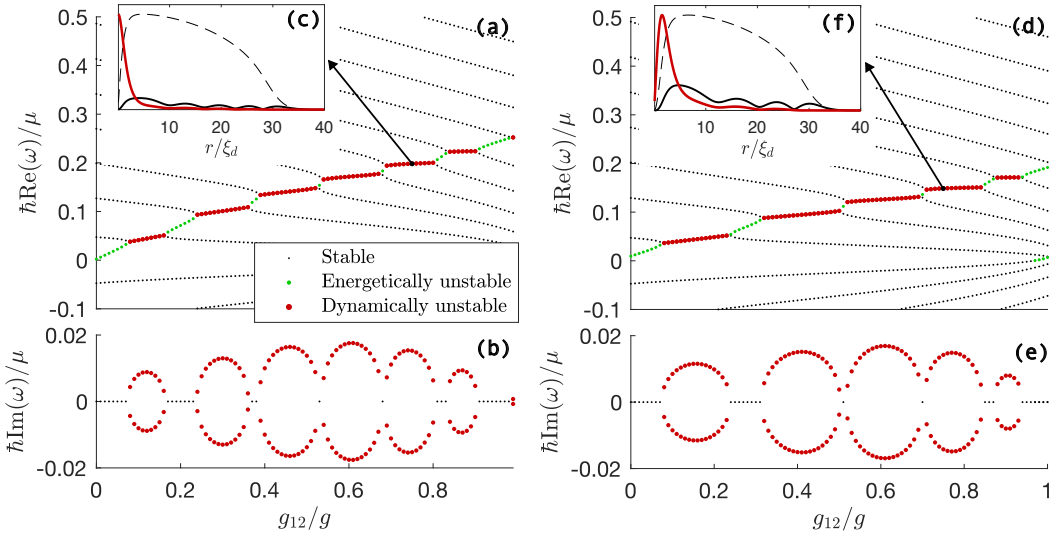

FIGURE 5.5: Bogoliubov spectrum for $M = 1$ spin excitations on top of a $L = 1$ (panels a-c) or $L = 2$ (panels d-f) vortex located at the center of a harmonically trapped mixture of TF radius $R = 30\xi_d$. Panels (c) and (f) show, together with the radial profile of the BEC density (grey dashed line), an example of the real-space profile of the particle $|u(x)|$ (black solid line) and antiparticle $|v(x)|$ (red solid line) components of the dynamically unstable mode for $g_{12} = 0.75g$.

is found for all values of the interactions [56]. Moreover, since the frequency of the isolated mode can be arbitrarily high, the associated instabilities are typically well localized in the vortex core [see Fig. 5.3(d)].

As it is well known [130], when multiply-charged $L > 1$ vortices are considered, dynamical instabilities of the same nature appear in the density channel too: since the energy of a vortex with charge L is larger than that of L singly-charged vortices, multiply charged vortices may be unstable against splitting into several lower-charge vortices. For instance, for $L = 2$ vortices, we find, as a function of the interparticle interaction, alternate intervals of dynamical stability and instability in the $M = 2$ channel of the density Bogoliubov problem (not shown), again in agreement with previous works [56].

An additional class of dynamical instabilities occur in the spin channel: besides the high-frequency isolated modes crossing the positive energy band discussed above, which are present for all angular momenta $1 \leq M < 2L$ [see Fig. 5.5(d) and Fig. 5.6(a,e)] and which are related to the deformation of the vortex core and/or its splitting, low-frequency and spatially extended instabilities may also appear. As visible in Fig. 5.6(a), such an instability may originate from the crossing of the two bands of closely spaced positive and negative norm modes that extend throughout the ergoregion. As such it belongs to the class of superradiant ergoregion instabilities closer to the hydrodynamic regime. The possibility of observing instabilities of this superradiant kind is one of the main interests of replacing single-component systems with spin mixtures with a much wider ergoregion.

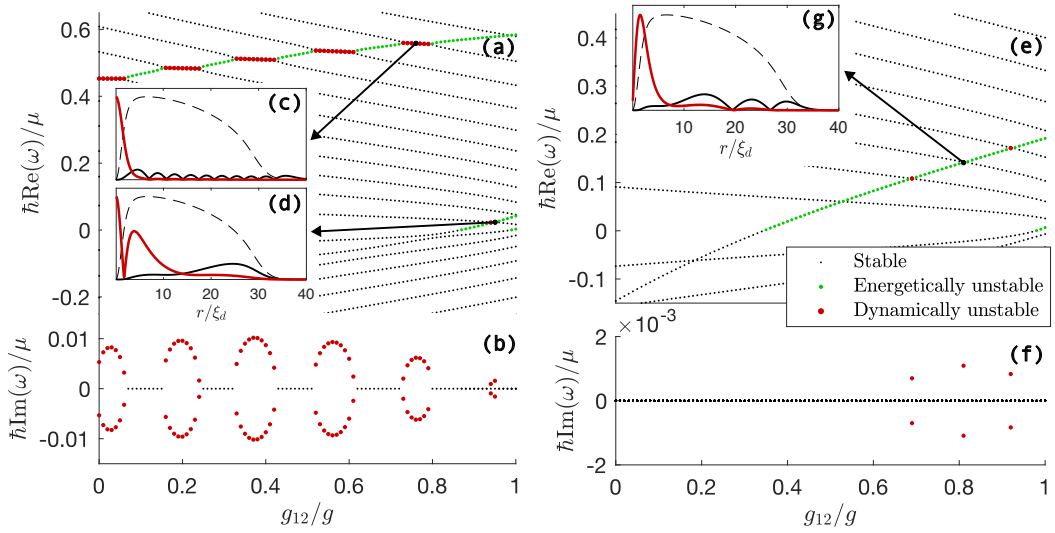

FIGURE 5.6: Bogoliubov spectrum for $M = 2$ (panels a-d) and $M = 3$ (panels e-g) spin excitations on top of an $L = 2$ vortex in a harmonically trapped mixture of TF radius $R = 30\xi_d$. Two dynamical instabilities are present in the $M = 2$ channel: the real-space profile of the particle (black solid line) and antiparticle (red solid line) components of these modes is shown in panels (c) and (d) for $g_{12} = 0.75g$ and $g_{12} = 0.95$, respectively. The main difference between the two modes is in the localization of the antiparticle component, which dominates up to $r_- \sim 3\xi_d$ for the former, and up to $r_- \sim 14\xi_d$ for the latter; indeed, according to our LDA treatment, lower frequency modes are more extended. Remarkably, the low frequency mode is only present for $g_{12} \sim g$. The $M = 3$ channel shows a single instability: an example of the real-space profile of the mode is shown in panel (g) for $g_{12} = 0.81g$.

Due to their different origin, these additional modes appear only around zero frequency for $g_{12} \lesssim g$ close to the demixing point: most importantly, their antiparticle component extends well outside the vortex core [see Fig. 5.6(d) as compared with Fig. 5.6(c)]. Physically, this means that long-wavelength spin waves are involved in the instability mechanism. From a quantum gas perspective, the instability can be understood as a demixing instability whose appearance is facilitated by the presence of a vortex which lowers its threshold. From the point of view of the gravitational analogy, this instability is of superradiant nature: as it happens for ergoregion instabilities around massive rotating objects, the positive energy of the wave in the outer region is compensated by the negative energy of the wave inside the ergoregion.

Analogously, in the presence of a coherent coupling, low-frequency instabilities are expected to appear close to the ferromagnetic phase transition point $g_{12} \lesssim g + 2\Omega/n$, where the massive gap in the spin dispersion closes and the spin healing length diverges. This will be the subject of future work.

In general, depending on the parameters' values, multiple dynamically unstable modes can be found for the same configuration. When observing the time evolution of the system starting from an unperturbed L-charged vortex, after a short transient in

which all the unstable modes compete, the mode with the largest imaginary frequency will eventually win over the others and dominate the intermediate-time evolution. In most cases, the dominating mode is a high-frequency localized one. However, it is possible to play with the system size R and with the interaction constants ratio g_{12}/g to make all localized modes dynamically stable, while keeping a spatially extended mode unstable via superradiant mechanisms. In this case the dynamical instability is associated to the generation of long-wavelength phonon within the ergoregion, as expected from the gravitational analogy with ergoregion instabilities of massive rotating objects [47]. At very long times, nonlinear effects set in, resulting in complex mode mixing phenomena and additional instabilities. A study of this physics will be the subject of the next Section.

5.6 Long-time dynamics

It is well-known that the linearized Bogoliubov theory holds as long as the the excited modes are small perturbations on top of the stationary vortex state. When dealing with a dynamical instability, this approximation is valid for a limited amount of time, roughly given by the inverse of the growth rate Γ of the unstable mode. After that, the radial symmetry of the problem is likely to be broken by complex non-linear processes, and mixing phenomena start occurring. Therefore, while we can take advantage of the axial symmetry of the system to compute the Bogoliubov spectra, in order to access the long-time dynamics of the spin mixture, it is necessary to simulate the full Gross-Pitaevskii equations in two dimensions.

The numerical protocol is the following: we first identify, thanks to the Bogoliubov spectra, a set of parameters $(L, g_{12}/g, R)$ leading to a dynamical instability; we calculate the 2D profile of a stationary vortex of charge L sitting at $r = 0$ via a conjugate gradient algorithm [103], where the azymuthal profile of the wavefunction phase is enforced at every step. The stationary state is perturbed with some weak random noise, applied independently on the total and relative density, to trigger the instability. We then simulate the time evolution of the system given by the GPE using a split-step method.

Examples of the simulated time-evolution are presented in Figs. 5.7 - 5.10 for vortices of charge $L = 1, 2$. As already discussed, $L = 1$ vortices have a single $M = 1$ potentially unstable mode in the spin channel. On the other hand, $L = 2$ vortices can feature up to five unstable modes, four of which in the spin channel (one for $M = 1$, two for $M = 2$, one for $M = 3$). For the sake of simplicity, the simulation parameters are chosen in a way to have a single dynamical instability in the spin channel: in practice, this is done by keeping the interaction ratio g_{12}/g fixed and tuning the system size R to select the desired mode.

In all these figures, the short- and intermediate-time dynamics is consistent with our expectations based on the Bogoliubov theory: the instability develops initially as a well visible perturbation characterized by $2M$ lobes in the azymuthal direction, where M is the angular momentum of the unstable mode. For high-frequency instabilities, this excitation has a larger-amplitude part localized around $r = 0$ and a smaller-amplitude one visible as interference fringes at larger radii [see panel (b2) of Figs. 5.7 - 5.9]; for low-frequencies instabilities instead, the localized part of the mode is itself

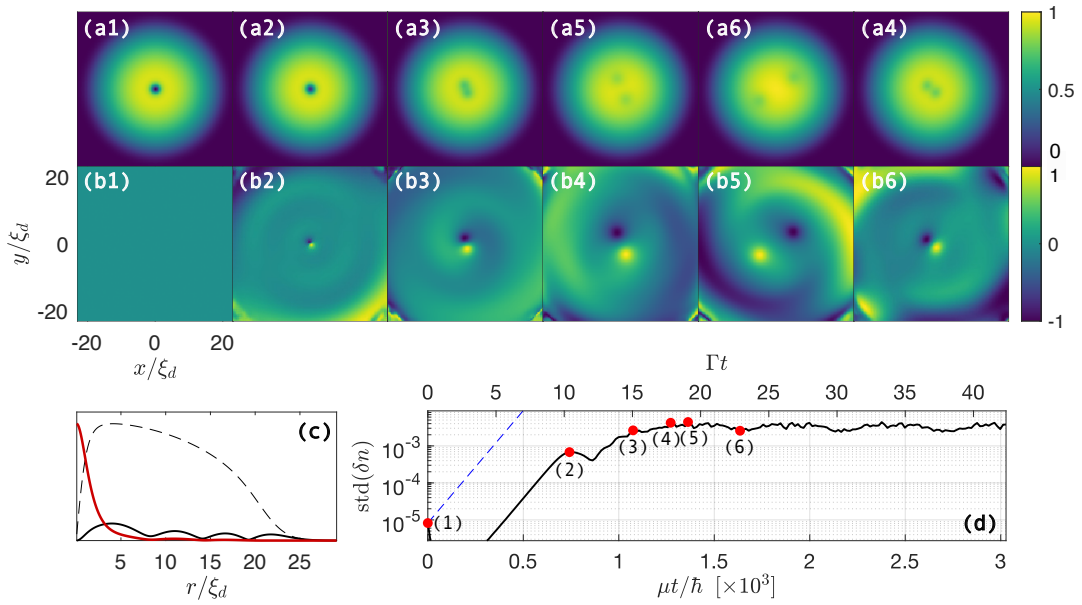

FIGURE 5.7: Dynamics of the vortex splitting instability. Real time evolution of a $L = 1$ vortex with $R = 21\xi_d$ and $g_{12} = 0.8g$. Panel (c) shows, together with the radial profile of the BEC density (grey dashed line), the real-space profile of the particle $|u(x)|$ (black solid line) and antiparticle $|v(x)|$ (red solid line) components of the $M = 1$ dynamically unstable mode, whose growth rate, for these parameters, is $\hbar\Gamma/\mu \simeq 0.014$. Panels (a1-a6): total density $n = n_1 + n_2$, measured in units of the peak Thomas-Fermi density $2n_{\mathrm{TF}}(r = 0) = 2\mu/(g + g_{12})$. Panels (b1-b6): polarization, $Z = (n_1 - n_2)/n$. Each column is computed at the time indicated by one of red dots in panel (d), which shows the temporal evolution of the standard deviation of the spin density $\delta n = n_1 - n_2$ (black solid line), compared with the analytical exponential growth $\exp(\Gamma t)$ (blue dashed line).

spread over a larger portion of the system [see panel (b2) of Fig. 5.10].

In panel (d) of Figs. 5.7 - 5.10, we show the standard deviation (STD) of the spin density $\delta n = n_1 - n_2$ from its ground state vanishing value, defined as

$$\mathrm{std}(\delta n) = \sqrt{\frac{1}{Q^2 - 1} \sum_{i,j=1}^{Q} \delta n^2(x_i, y_j)} \tag{5.20}$$

where $Q \times Q$ is the number of points in the 2D numerical grid. As expected, this quantity is exponentially growing at a rate equal to the imaginary part Γ of the frequency of the dynamically unstable mode, whereas the total density remains almost unperturbed.

At longer times, $t\Gamma \gg 1$, for the intermediate values of g_{12}/g considered in Figs. 5.7 and 5.8, the high-frequency dynamically unstable modes lead to the splitting of the original vortex into smaller vortices and/or pairs of coreless vortices[2]. Two examples

[2]With the term *coreless vortex* we indicate a singly-charged vortex in one component, filled with atoms belonging to the other component.

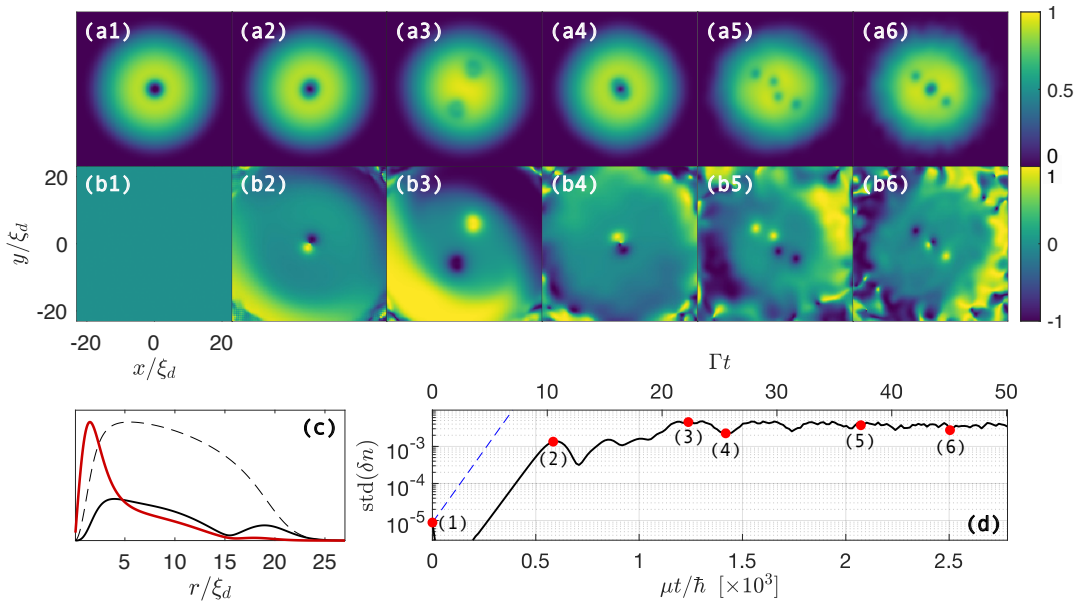

FIGURE 5.8: Dynamics of the vortex splitting instability. Same plots as in Fig. 5.7 for an $L = 2$ vortex with $R = 20\xi_d$ and $g_{12} = 0.52g$. For these parameters, the instability rate of the $M = 1$ unstable mode, whose real-space profile is shown in panel (c), is $\hbar\Gamma/\mu = 0.018$.

are shown in Figs. 5.7 and 5.8 for $L = 1$ and $L = 2$ vortices, respectively, and closely resemble the results of Ref. [134]. Interestingly, the splitting is often followed by a recombination process; similar dynamics was predicted for multiply-charged vortices in a single-component BEC in [139]. We attribute this phenomenon to energy conservation and to the finite size of the system: once the vortex is split, the excess of energy is released in the form of spin excitations, whose interference, after bouncing on the trap walls, reverses the splitting process. This typically occurs multiple times, before, in the absence of a dissipation mechanism, the evolution becomes turbulent, with additional vortices being nucleated from the boundaries and/or deformation of the (otherwise circular) cloud [see panels (a6-b6) of Fig. 5.8]. All these complex nonlinear features go beyond this work and will be the subject of future studies.

The physics is more intriguing in the $g_{12} \lesssim g$ regime close to the demixing point, where vortex splitting is much harder to observe and, if it does so, only occurs at much longer times scales: in addition to the reduced value of the instability rate Γ, the softness of spin modes prevents in fact the cloud from absorbing the excess energy that would derive from vortex splitting. This result is confirmed by looking at the Bogoliubov spectra in Figs. 5.5 and 5.6: for $g_{12}/g \lesssim 1$, the instability bubbles disappear or become tiny, and instability rates drop by roughly an order of magnitude. As a consequence, when approaching the demixing point, vortices in condensate mixtures remain stable for a very long time, while their spin dynamics is ruled by linear Bogoliubov theory.

Two examples of the real-time dynamics in this regime are shown in Figs. 5.9 and 5.10 for $L = 1, 2$ vortices, respectively, and $g_{12}/g = 0.97$. In the former case, the unstable Bogoliubov mode is spatially localized around the vortex and corresponds to

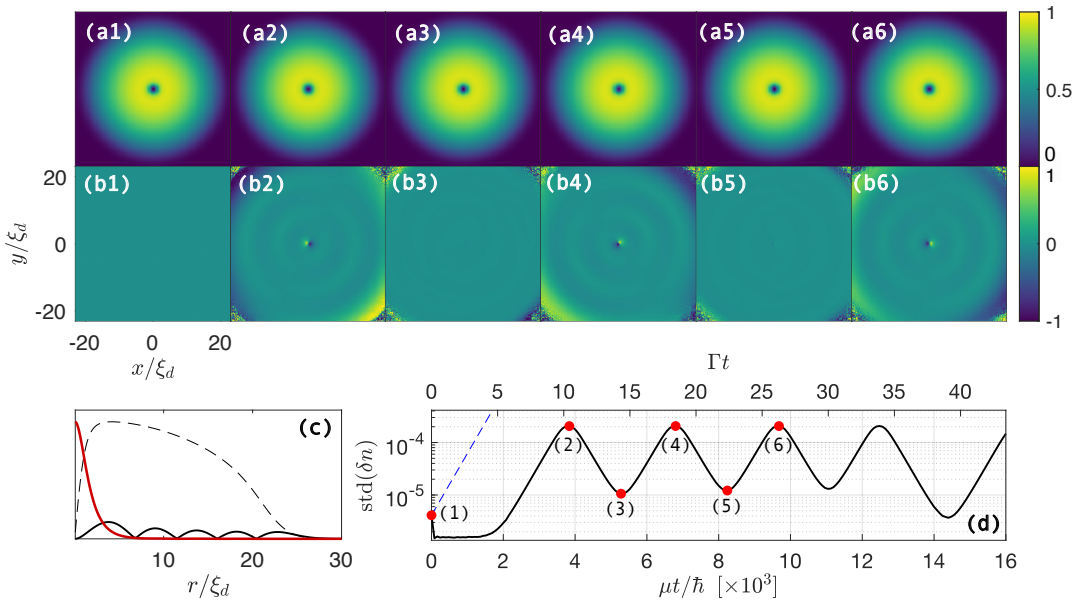

FIGURE 5.9: Real time evolution of a $L = 1$ vortex with $R = 22\xi_d$ and $g_{12} = 0.97g$. For these parameters, the growth rate of the $M = 1$ unstable mode, whose real-space profile is shown in panel (c), is $\hbar\Gamma/\mu \simeq 0.0016$. Same plots as in Fig. 5.7.

a displacement of the cores in the two components, with the consequent appearance of a net polarization. This process, however, does not lead to a full splitting of the vortex. We rather observe a sequence of intervals of suppression and revival of the instability, as witnessed by the oscillation in time of the standard deviation (STD) of the relative density. The underlying mechanism is rooted in the finite-size of the system and is analogous to the one leading to the sequence of vortex splitting and recombination events seen above.

The temporal evolution associated to a superradiant instability is finally visible in Fig. 5.10. At intermediate times [panel (b2)], a spatially extended $M = 2$ modulation is clearly visible in association to the vortex core deformation. Its characteristic size corresponds to the spatial profile of the unstable mode shown in panel (c) and, in particular, its antiparticle component matches the extension of the ergoregion. This is the smoking gun of the superradiant nature of the instability.

At later times, the dynamics develops instead a more complicated behaviour that involves strong nonlinear mode-mixing effects: the perturbation of the spin density, due to the development of the instability, is large enough to excite the $M = 2$ waves with higher radial momentum and several radial nodes that are visible in panel (b3). These different excitation patterns are in competition, eventually leading to a marked deformation of the vortex and a significant modulation also of the total density [see panel (a6)]. Once again, the accurate analysis of these complex mode-mixing processes goes beyond the scope of the present work.

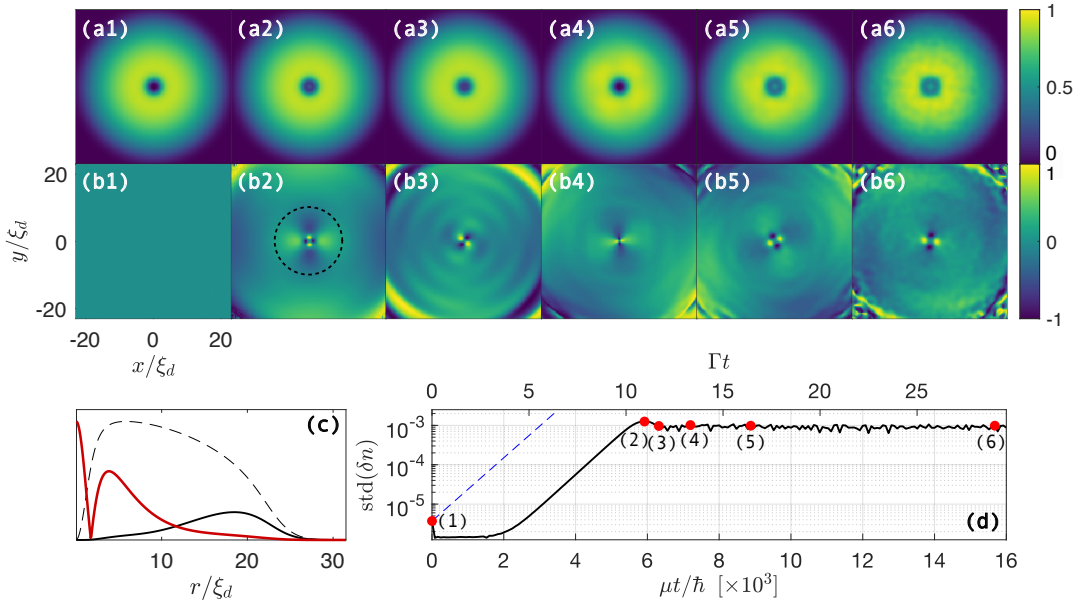

FIGURE 5.10: Real time evolution of a $L = 2$ vortex with $R = 23\xi_d$ and $g_{12} = 0.97g$. For these parameters, the growth rate of the $M = 2$ unstable mode, whose real-space profile is shown in panel (c), is $\hbar\Gamma/\mu \simeq 0.0019$. Same plots as in Fig. 5.7; the dotted black line in panel (b2) indicates the size of the region where the antiparticle component of the unstable mode dominates.

5.7 Conclusions and perspectives

In this Chapter, we have theoretically analysed the stability of quantized vortices in symmetric two-component atomic Bose-Einstein condensates (BEC) and we have interpreted the results within an analog gravity context in terms of ergoregion instabilities. In addition to instabilities related to high-frequency Bogoliubov modes localized in the vortex core and associated to the distortion or the splitting of the vortex core like in single-component BECs [56], suitable regimes are found where the physics is determined by low-frequency and long-wavelength spin excitations. In this case, the superradiant scattering process underlying the ergoregion instability involves the excitation of a Doppler-shifted, negative-energy spin-sound wave spread over the ergoregion and the simultaneous emission of positive-energy spin waves into the outer part of the BEC, in close analogy with the ergoregion instability of space-time around a rotating massive object.

On the theoretical side, the most challenging open questions concern the late time dynamics of unstable configurations. First studies of this physics focused on the simpler case of black hole laser instabilities [140] and first hints of the remarkable complexity of the superradiant case are visible in the simulations reported in this work. In this long-term adventure, a special attention has to be paid to the role of nonlinear processes in saturating the instability, in analogy with related phenomena predicted in the gravitational context and with potential application to particle physics: more specifically, numerical simulations in this context have predicted the growth, near the unstable object, of a bosonic cloud, usually referred to as *black hole hair* [122,

125, 126, 141], that extracts energy and angular momentum from the black hole and subsequently slowly dissipates them through emission of gravitational waves [47].

On the experimental side, two-component condensates can be obtained in fluids of atoms and of light. In the atomic case, vortices can be generated by means of suitably chosen stirring potential [131, 142] and the different components can be chosen within the atomic hyperfine structure in a way to obtain slow spin-sound waves [57]. In the optical case, the polarization degree of freedom can be used to obtain two-component condensates and arbitrary velocity patterns can be imprinted onto the fluid by suitably designing the phase profile of the pump beam so to generate rotating configurations [78]. In both cases, the control of the coherent coupling strength via either an external electromagnetic dressing of the atoms or the optical birefringence of the cavity material may be used to tune the mass of the quantum field.

The remarkable experimental advances in both fields make us confident that it will be soon possible to validate our conclusions using state-of-the-art set-ups. As a more ambitious challenge, the analysis of correlations in the spirit of [38–40], will allow to investigate superradiant processes at the quantum level, so to prove superradiant amplification is intrinsically connected to the spontaneous creation of correlated pairs of Bogoliubov modes with opposite energy at the ergosurface.

6 False vacuum decay in a ferromagnetic superfluid

6.1 Introduction

Up to now, we have discussed astrophysical phenomena that are expected to occur in black-hole geometries, or, more specifically, in spacetimes with an event horizon or an ergoregion. In addition to black-hole related phenomena, analog systems provide a platform to investigate cosmological processes: examples include cosmological particle creation during *preheating* [4, 5, 17, 18, 97, 98] or in asymptotically curved spacetimes [23, 143]. This Chapter is devoted to the realization, with a ferromagnetic binary mixture, of the analog version of another phenomenon which has applications to cosmology, known as *false vacuum decay* [101]. The project was carried on in collaboration with the experimental group of the Pitaevskii BEC Center in Trento and with Ian Moss (and collaborators) from the University of Newcastle, which provided theoretical support.

False vaccum decay (FVD) can be thought of as the relaxation process of a quantum field from a metastable state. Metastability is a well known phenomenon in physics: it occurs when a system is in a local mininum (also referred to as *false vacuum*, FV) of its free energy landscape that is not its ground state (or *true vacuum*, TV). Typical examples are supercooled liquids or ferromagnets misaligned with respect to an externally applied magnetic field. In order to reach its ground state, a metastable system needs to overcome or tunnel through a potential barrier. The generalization of this process to a quantum field has attracted extensive attention in cosmology, due to its consequences on the stability of the Higgs vacuum and its application to inflationary models describing the early Universe [72–75]. In its purest form, false vacuum decay would take place through quantum fluctuations [69, 70]; however in realistic scenarios it is likely to be boosted by thermal fluctuations [71] or seeded by the presence of "impurities" in the system [144], such as black holes.

In an energy conserving setup, false vacuum decay is believed to take place via the probabilistic formation of resonant bubbles of true vacuum, when the energy gain provided by the bulk is compensated by the surface tension of the walls. Each bubble then grows in size with time and the whole system ends up in the ground state as the energy of the false vacuum is released in the form of excitations around the true vacuum. A complete analysis of the decay from a false vacuum requires therefore the calculation of the bubble nucleation rate, as well as an analysis of the dynamics of bubbles after they are formed.

The analytical computation of the tunnelling times is non-trivial due to the highly non-perturbative nature of the process; the stardard approach is a semiclassical calculation based on an *instanton* solution, first proposed by Coleman in [69]. According

to it, the rate of bubble formation is expected to be exponentially small with the system's parameters. This makes numerical and experimental studies extremely challenging, due to the long-time scales on which the decay occurs. So far, there have been proposals to realize an analog version of false vacuum decay with quantum spin chains [145] and with unpolarized binary BEC mixtures with a periodically modulated coherent coupling [58]. In the former case, the double well potential is due to the system being just across a first-order phase transition (the para-to-ferromagnetic one), while in the latter it is engineered through a fast periodic driving of the Rabi frequency. The main drawbacks of the two proposals are discretization of space, which could affect the results, and the excitation of parametric instabilities on the same time-scales of bubble nucleation, respectively. We propose here an alternative and much more straightforward approach which exploits the ferromagnetic properties of polarized coherently-coupled binary mixtures, and does not require a fast modulation of the Rabi frequency in order to generate the double well potential [101].

We first briefly summarize the magnetic properties of a coherently-coupled binary mixture, that we already discussed in detail in Chapter 3, focusing on how the profile of the double-well potential can be arbitrarily engineered by tuning the Rabi frequency Ω and detuning δ of the coupling. We then review the instanton theory, first developed by Coleman in [69], that is often used to predict the bubble nucleation rates, and we report the results of the application of such theory to our specific system [101]. Lastly, we focus on our contribution to the project, that is, a numerical analysis of the bubble nucleation process and of the decay rates: we compare our results both with the instanton analytical prediction and with the experimental data of Ref. [101].

6.2 False vacuum decay with a ferromagnetic superfluid

Let us consider a uniform one-dimensional two-component condensate: as we already saw in Chapter 3, it is possible to identify an effective potential, which, if $\kappa < 0$, naturally has a double-well profile with respect to the magnetization Z. Let us define, for the sake of simplicity, the dimensionless parameters:

$$h_1 := \frac{\hbar\Omega}{|\kappa|n} > 0 \qquad h_3 := \frac{\hbar\delta_{\text{eff}}}{|\kappa|n} \tag{6.1}$$

so that the potential (3.46) can be written as:

$$\frac{U(Z,\varphi=0)}{|\kappa|n} = -\left(\frac{1}{2}Z^2 + h_3 Z + h_1\sqrt{1-Z^2}\right) \tag{6.2}$$

The phase diagram of the mixture is summarized again in Fig. 6.1: the system is ferromagnetic if $h_1 < 1$ and $|h_3| < h_3^* = [1-h_1^{2/3}]^{3/2}$ [see Eq. (3.55)]. The longitudinal field h_3 determines the symmetry of the potential: at resonance, $h_3 = 0$, the energy landscape is symmetric, so the system has two degenerate ground states with opposite magnetization $\pm Z_0$, $Z_0 = \sqrt{1-h_1^2}$ [see Eq. (3.52)]. As the value of h_3 is increased, the potential gets linearly tilted: while the absolute minimum Z_{TV} represents the ground state (or true vacuum, TV) of the mixture, the local one at Z_{FV} is a metastable false vacuum (FV). At the edge of the ferromagnetic region, defined by $|h_3| = h_3^*$,

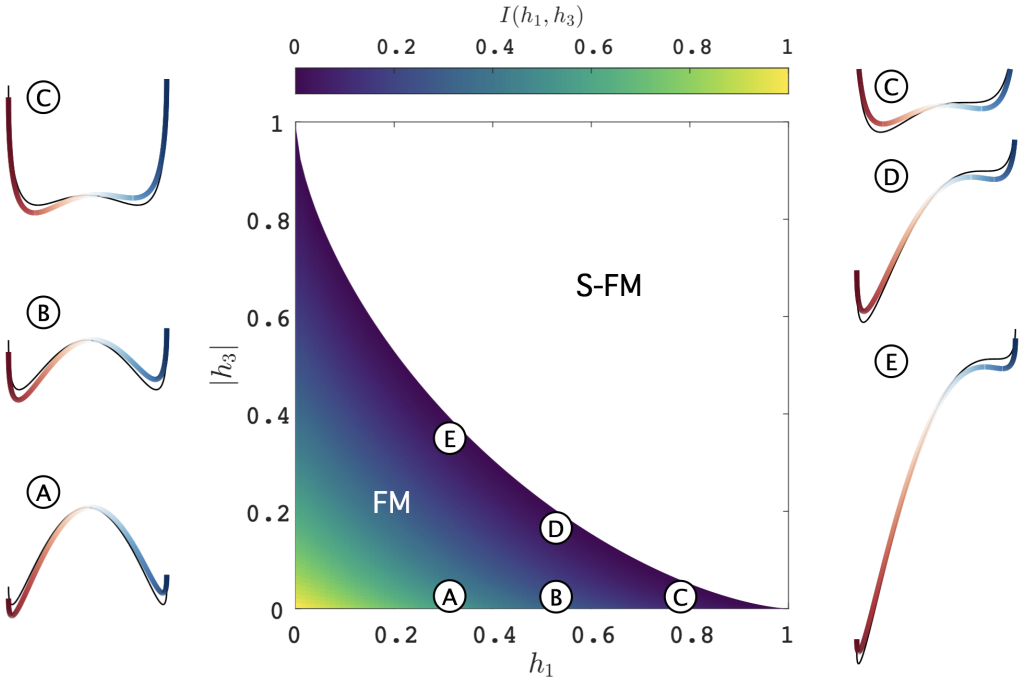

FIGURE 6.1: Phase diagram of a ferromagnetic mixture as a function of the external field components h_1, h_3. The colored area identifies the parameters' values for which the potential has a double-well profile, whose boundary is defined by $|h_3| = h_3^*$. Examples of the potential profile in some points of interest are shown in panels A-E. Panels A-C are obtained with $|h_3| = 0.03 \ll 1$ (solid black lines refer to $h_3 = 0$, for comparison): in the almost resonant regime, $|h_3| \ll 1$, changing h_1 has effect on the height of the potential barrier. Panels C-E are obtained with $h_3^* - |h_3| = 0.03 \ll 1$ (solid black lines refer to $|h_3| = h_3^*$, for comparison): in the vicinity of the critical detuning, $h_3^* - |h_3| \ll 1$, changing h_1 has effect on the energy imbalance between false and true vacuum. The color scale refers to the (numerically-computed) value of the integral I in Eq. (6.11).

the secondary minimum becomes a saddle point, located at $Z_* = -\text{sign}(h_3) h_3^{*1/3}$ [see Eq. (3.54)], and metastability is lost.

Without loss of generality, in the following we will assume $h_3 \propto \delta_{\text{eff}} < 0$, so that $Z_{TV} < 0$ and $Z_{FV} > 0$ (results for $h_3 > 0$ are easily get through $Z \to -Z$). Let us consider two regimes of interest, which allow to perform approximate analytical calculations (results are summarized in Table 6.1):

(a) $|h_3| \ll 1$. Close to resonance, an expansion keeping only linear terms in the longitudinal field can be performed: both the potential barrier width (given by $Z_{FV} - Z_{TV}$) and the energy imbalance between the two minima depend on $Z_0 \propto (1 - h_1)^{1/2}$, while the barrier height has a much stronger dependence on $(1 - h_1)^2 \propto Z_0^4$ (see the difference between panels A-C of Fig. 6.1). Given some value of $|h_3| \ll 1$, we therefore expect the false vacuum decay to be more and more suppressed as $h_1 \to 0$, since the potential barrier to tunnel through becomes larger and larger in the same limit. On the other hand, the dynamics

after the nucleation, which is determined by the amount of energy to be released during the bubble growth, is likely to depend only weakly on h_1.

Spin collective modes on top of either one of the two minima are approximately described by the following (dynamically stable) dispersion relation:

$$(\hbar\widetilde{\omega}_s)^2 \simeq \left(\frac{\hbar^2k^2}{2m} + |\kappa|n\right)\left(\frac{\hbar^2k^2}{2m} + |\kappa|nZ_0^2\right) \tag{6.3}$$

Hence they have free particle character in the limit $h_1 \to 0$ (for which $Z_0 \sim 1$) and phononic character in the proximity of the critical point $h_1 \sim 1$ ($Z_0 \sim 0$). However the coupling between the density and spin branches (3.66) is given by $\alpha \propto \sqrt{1-Z_0^2} = h_1$; thus spin modes are more likely to become dynamically unstable in the proximity of the critical point $h_1 \to 1$, due to the interplay between the closing gap and the coupling with the total density dynamics.

(b) $h_3^* - |h_3| \ll 1$. Close to the critical detuning that defines the edge of the FM region, we can expand the potential profile around the saddle point Z_*:

$$\frac{U(Z_{FV}+\zeta) - U(Z_{FV})}{|\kappa|n} = \sqrt{\frac{3Z_*}{2h_1^{2/3}}}\left(h_3^* - |h_3|\right)^{1/2}\zeta^2 + \frac{Z_*}{2h_1^{2/3}}\zeta^3 \tag{6.4}$$

As visible in panels C-E of Fig. 6.1, given some value of $h_3^* - |h_3| \ll 1$, the height of the potential barrier has a weak dependence on h_1, whereas the energy difference between true and false vacua increases significantly as $h_1 \to 0$: an approximate estimate is given by $2|\kappa|nh_3^*Z_* = 2|\kappa|nZ_*^4 = 2|\kappa|n(1-h_1^{2/3})^2$. Hence, we expect the bubble nucleation rate to be almost independent on h_1 and the dynamics after the decay to be highly influenced by the value of the transverse field.

Spin collective modes on top of the false vacuum have the following dispersion:

$$(\hbar\widetilde{\omega}_s)^2 \simeq \left(\frac{\hbar^2k^2}{2m} + |\kappa|nh_1^{2/3}\right)\left(\frac{\hbar^2k^2}{2m} + 3|\kappa|nh_1^{1/3}\sqrt{\frac{3Z_*}{2}}\left(h_3^* - |h_3|\right)^{1/2}\right) \tag{6.5}$$

If $h_3^* - |h_3|$ is sufficiently small, these have phononic character with speed of sound $\tilde{c}_s = h_1^{1/3}\sqrt{|\kappa|n/2m}$. However, dynamical instabilities might arise from the coupling with density modes (3.66), given by $\alpha \propto \sqrt{1-Z_*^2} = h_1^{1/3}$; once again, this is more likely to happen in the vicinity of the critical point, $h_1 \sim 1$.

It is worth mentioning that the two regimes (that is $|h_3| \ll 1$ and $h_3^* - |h_3| \ll 1$) become indistinguishable in the proximity of the critical point $h_1 \to 1$, since the size of the FM region h_3^* shrinks. In view of numerical and experimental studies of false vacuum decay, the condition $h_1 \sim 1$ might be convenient since it allows to explore the whole FM region without having to deal with extremely long time-scales. On the other hand, being close to a critical point magnifies any source of noise or fluctuations, possibly affecting the accuracy of the measurements or even the decay process itself. For instance, we have just shown that dynamical instabilities might arise due the non-negligible coupling with the total density dynamics.

	$\lvert h_3\rvert \ll 1$	$h_3^* - \lvert h_3\rvert \ll 1$
Z_{TV}	$-Z_0 - \frac{h_1^2}{Z_0^2}\lvert h_3\rvert$	–
Z_{FV}	$Z_0 - \frac{h_1^2}{Z_0^2}\lvert h_3\rvert$	$Z_* + \sqrt{\frac{2h_1^{2/3}}{3Z_*}}\left(h_3^* - \lvert h_3\rvert\right)^{1/2}$
Z_{max}	$\frac{\lvert h_3\rvert}{1-h_1}$	$Z_* - \sqrt{\frac{2h_1^{2/3}}{3Z_*}}\left(h_3^* - \lvert h_3\rvert\right)^{1/2}$
$\frac{U(Z_{FV}) - U(Z_{TV})}{\lvert\kappa\rvert n}$	$2Z_0\lvert h_3\rvert$	–
$\frac{U(Z_{max}) - U(Z_{FV})}{\lvert\kappa\rvert n}$	$\frac{1}{2}(1-h_1)^2 - Z_0\lvert h_3\rvert$	$\frac{4}{3}\sqrt{\frac{2h_1^{2/3}}{3Z_*}}\left(h_3^* - \lvert h_3\rvert\right)^{3/2}$

TABLE 6.1: Approximate values for magnetization corresponding to false and true vacuum and to the maximum, for the barrier height and for the energy imbalance between true and false vacuum.

6.3 Analytical results for the bubble nucleation rate: the instanton solution

Given the applications of false vacuum decay to cosmological models, bubble nucleation rates are usually computed [69, 71] for field theories described by relativistic Lagrangian densities of the form $\mathscr{L} = \frac{1}{2}\partial_\mu\phi\partial^\mu\phi - U(\phi)$, where ϕ is a scalar field and the potential $U(\phi)$ has an asymmetric double-well profile. For the sake of simplicity, let us assume the potential is shifted such that the false vacuum state ϕ_{FV} has $U(\phi_{FV}) = 0$.

In principle, the decay rate can be computed exactly as the transition amplitude from the false vacuum to a bubble state in a path integral formulation [146]. However the calculation is notably simplified by performing a Wick rotation to Euclidean time ($it \to \tau$): this amounts to a change of sign of the potential $U(\phi) \to -U(\phi)$. Since the false vacuum becomes an unstable maximum of the inverted potential, there exists a classical trajectory (called *instanton*) from it to a *resonant bubble state*, that is, a configuration such that the bulk energy gain is compensated by the presence of walls separating the two vacua.

The path integral can be approximated with its most relevant contribution, that is, the one coming from the classical path that minimizes the $(d+1)$-Euclidean action (d being the number of space dimensions):

$$S_E^{(d+1)} = \int \mathrm{d}\tau\mathrm{d}\mathbf{x}\mathscr{L}_E := \int \mathrm{d}\tau\mathrm{d}\mathbf{x}\left[\frac{1}{2}\partial_\mu\phi\partial^\mu\phi + U(\phi)\right] \tag{6.6}$$

where $\mathscr{L}_E$ is the Euclidean Lagrangian density. The general result for the decay rate is therefore $\Gamma = A\exp(-\overline{S}_E^{(d+1)}/\hbar)$, where $\overline{S}_E^{(d+1)}$ is the minimum action and A is a typically unknown prefactor that includes the first quantum corrections to the classical instanton solution [70]. Being non-trivial to compute, it is generally neglected assuming that the main dependence on the systems' parameters is in the exponential

factor. In other words, the simplest estimation of the nucleation rates can be obtained by minimizing the Euclidean action (6.6), that is, computing the action associated to the (classical) instanton solution.

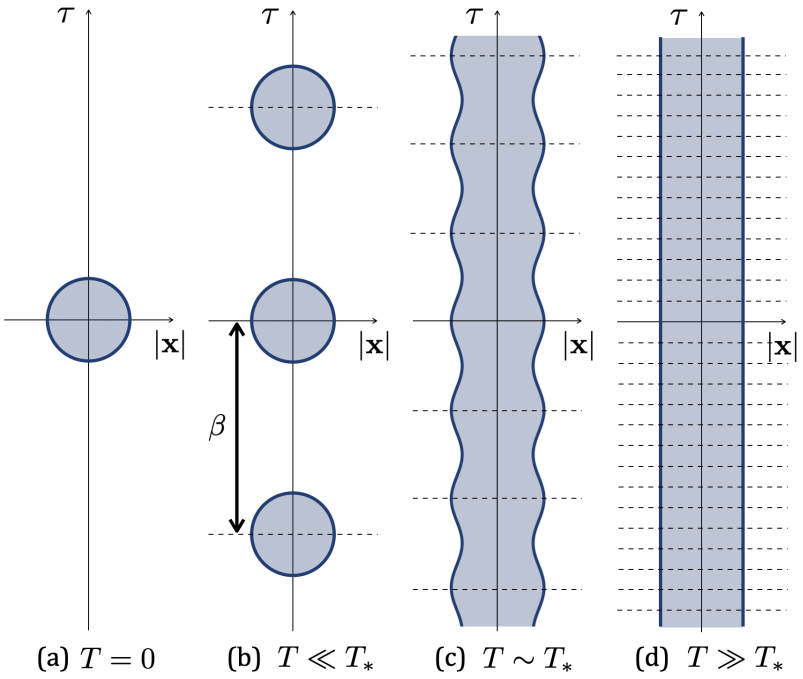

FIGURE 6.2: Sketch showing how the instanton solution changes as a function of temperature [71]. For $T = 0$ one can assume the instanton is invariant under rotations in Euclidean spacetime (a), while at finite temperature $T \neq 0$ the solution is symmetric in space, but periodic in Euclidean time with period $\beta = 1/k_B T$. In the limit of high temperatures, when the periodic copies are highly superimposed, the derivative $\partial_\tau \phi$ can be neglected and one gets a thermal instanton solution (d).

The calculation proceeds differently depending on the temperature T of the system. At zero temperature, where only quantum fluctuations matter, one generally assumes that the field ϕ only depends on $\rho = \sqrt{\mathbf{x}^2 + \tau^2}$ [69], based on the Lorentz invariant form of the Lagrangian density [see panel (a) of Fig. 6.2]. Let ρ_0 be the size of the bubble solution that minimizes the action.

At finite temperature T, one must integrate the decay rates over all possible initial excited states of energy $\varepsilon > 0$ above the false vacuum, with weights given by the Boltzmann factor $\exp(-\beta\varepsilon)$, where $\beta = 1/k_B T$ [147]. This amounts to assume that the instanton solution is periodic in Euclidean time, with period β given by the temperature [71]. As long as β is much larger than the typical bubble size ρ_0 [see panel (b) of Fig.6.2], the decay rate coincides with the $T = 0$ one, that is, quantum fluctuations dominate. The thermal-to-quantum threshold temperature T^* can be defined as the one for which the periodic copies start overlapping [see panel (c) of Fig. 6.2]. In the high-temperature regime $T \gg T_*$ [panel (d) of Fig. 6.2], one gets a cylindrically symmetric thermal instanton solution: the derivative with respect to Euclidean time

$\partial_\tau \phi$ is negligible and the Euclidean action simplifies to:

$$S_E^{(d+1)} = \beta S_E^{(d)} := \beta \int \mathrm{d}\mathbf{x} \left[\frac{1}{2} (\nabla \phi)^2 + U(\phi, T) \right] \tag{6.7}$$

where we assume that temperature not only influences the bubble shape in Euclidean spacetime, but might also potentially affect the landscape of the potential U. The minimal reduced action $\overline{S}_E^{(d)}$ is sometimes referred to as *instanton energy* and represents the many-body barrier that the system needs to overcome to decay.

Despite the instanton solution is typically used to compute false vacuum decay rates in the cosmological context, the procedure does not rely on the relativistic nature of the Lagrangian density. Therefore the same calculation can be performed, in principle, also for our case of interest, starting from the Lagrangian density of a uniform coherently-coupled BEC mixture:

$$\mathscr{L} = -\frac{n}{2} \left\{ \hbar \varphi \frac{\partial Z}{\partial t} + \frac{\hbar^2}{4m} \left[\frac{|\vec{\nabla} Z|^2}{1 - Z^2} + (1 - Z^2) |\vec{\nabla} \varphi|^2 \right] + U(Z, \varphi) \right\} \tag{6.8}$$

However, the non-relativistic nature of the system, as well as the presence of two dynamical fields (Z and φ) instead of only one, make calculations cumbersome. A simplified analytical results is only available [101] if a certain number of approximations and assumptions are made:

(a) The relative phase dynamics is negligible, that is $|\vec{\nabla} \varphi|^2 \ll \varphi^2 \ll 1$. This allows to derive an effectively reduced field theory for the magnetization Z only, with potential $U(Z) := U(Z, \varphi = 0)$.

(b) The temperature T is high enough to ensure that the decay is thermally-induced but smaller than the energy barrier that the system needs to overcome to decay, so that the Euclidean action takes the simple form in Eq. (6.7), with $\beta S_E^{(d)} > 1$.

(c) The potential $U(Z)$ is not affected in a relevant way by the temperature.

(d) The system is one-dimensional: together with (a), this assumption allows to use identity (3.49) both to express the kinetic energy contribution in terms of the potential and to change integration variable from x to Z.

Putting all together, the minimum thermal instanton action can be written as [101]:

$$\overline{S}_E^{(1+1)} = \beta \overline{S}_E^{(1)} = \hbar \frac{|\kappa| n}{k_B T} Q \, I(h_1, h_3) \tag{6.9}$$

where Q is a dilution parameter that determines its order of magnitude:

$$Q := n \xi_\kappa \qquad \xi_\kappa := \frac{\hbar}{\sqrt{m |\kappa| n / 2}} \tag{6.10}$$

and I is a WKB-type integral which encodes its dependence on the external field components $h_1 := \hbar\Omega/|\kappa|n, h_3 := \hbar\delta_{\text{eff}}/|\kappa|n$:

$$I(h_1, h_3) = \frac{1}{2}\int_{Z_{TP}}^{Z_{FV}} \sqrt{\frac{2U(Z)}{|\kappa|n}} \frac{\mathrm{d}Z}{\sqrt{1-Z^2}} \tag{6.11}$$

Here, Z_{TP} is the magnetization of the turning point in the inverted potential $-U(Z)$, that is the point defined by the condition $U(Z_{TP}) = U(Z_{FV})$.

Typical values of the parameters for Sodium-23 atoms [77, 101] are $|\kappa|n \sim 2\pi\hbar \times 1.1kHz$ and $n \sim 4000$ atoms/μm, which give $Q \sim 3400$. The (dimensionless) integral I in (6.11) can be computed numerically for all values of the parameters (see Fig. 6.1) and its value ranges from 0 (when $|h_3| = h_3^*$) to 1 (for $h_1 = h_3 = 0$). An analytical result is easily found in the critical regime $h_3^* - |h_3| \ll 1$, since the potential around the false vacuum state can be approximated as (6.4):

$$I(h_1, h_3) \sim 1.25 h_1^{1/6} (h_3^*)^{-1/4} \left(h_3^* - |h_3|\right)^{5/4} \tag{6.12}$$

The nucleation rate is thus expected to depend exponentially on the distance from the edge of the FM region, that is $h_3^* - |h_3|$. The exponential suppression of the tunnelling leading to bubble formation as a function of the system's parameters is a typical feature of the decay from the false vacuum (see, for instance [69, 145]) and what makes it an extremely hard problem to simulate and study experimentally, due to the involved time-scales. In particular, for values of Q of the order of 10^3, we expect to be able to observe the decay from the false vacuum only if either the temperature is high, $|\kappa|n/k_BT \ll 1$, or the potential barrier is small, $I \ll 1$.

6.4 The role of inhomogeneity

So far, we have considered the simplest case of a uniform infinite system. However, in most experimental setups, condensed atoms are confined in space through a trapping potential, so the atomic density is a function of the position, $n \to n(x)$. As a straightforward consenquence, both the transverse and longitudinal fields h_1, h_3 also depend on x. Within a local density approximation (LDA), we can associate to each position x a different point in the phase diagram of Fig. 3.5 and a different bubble nucleation rate $\Gamma(x)$: bubbles nucleate stochastically, but appear with a higher probability in the positions associated to the highest Γ.

For the sake of simplicity, let us focus on the experimental setup of the Pitaevskii BEC Center in Trento [77, 96, 101]: the coherent coupling is uniformly applied to the whole cloud, so δ and Ω do not depend on x; atoms are harmonically trapped, thus their integrated density profile is parabolic:

$$n(x) = n_0 \left(1 - \frac{x^2}{L^2}\right) \tag{6.13}$$

where $n_0 \sim 4000\mu m^{-1}$ is the effective 1D peak density and $L \sim 200\mu m$ the Thomas-Fermi radius. Moreover, the interaction constants for Sodium give $\Delta = \kappa < 0$, so the effective detuning is $\delta_{\text{eff}}(x) = \delta - |\kappa|n(x)$. In other words, a single, spatially extended

sample is represented on the phase diagram by a line with slope $-\Delta/\kappa = -1$ [see the yellow line in Fig. 6.3(a)]:

$$\frac{h_3(x)}{h_1(x)} = \frac{\delta}{\Omega} - \frac{1}{h_1(x)} \tag{6.14}$$

By changing the physical detuning δ (which amounts to a vertical shift of such line) in time, one can probe the entire phase diagram of the mixture [77].

More specifically, by properly choosing the values of the δ, Ω, all the different phases (PM, S-FM and FM) can coexist in the same sample: an example is given in Fig. 6.3(b). The tails of the cloud are always paramagnetic (PM), due to the low atomic density. The condition $h_1(x) = 1$ defines the separation between the paramagnetic region and a saturated-ferromagnetic (S-FM) region, which extends up to the position satisfying $h_3(x) = h_3^*(x)$. The central part of the cloud is instead ferromagnetic (FM): within this region the mixture can occupy, locally in space, either the absolute or the relative minimum of the potential. In the former case the system is in its ground state: the local magnetization has everywhere the same sign as h_3, thus two domain-walls are present at the positions $\pm x_*$ satisfying the identity $h_3(x_*) = 0$ [see upper plot of Fig. 6.3(b)]. In the latter case, a false vacuum region of size $2x_*$ is present in the central part of the cloud, where Z is positive but h_3 is negative [solid black line in Fig. 6.3(a)]; moreover, since the magnetization is everywhere positive, the state of the mixture shows no domain-walls.

The absence of domain-wall in the false vacuum state, as well as the paramagnetic nature of the tails, is a fundamental ingredient to observe *spontaneous* bubble nucleation: indeed, it has been proven [63] that trap edges and topological defects act as seeds for the false vacuum decay process. In other words, if the false vacuum configuration features domain-walls, the system reaches the ground state by simply moving them, rather than nucleating true vacuum bubbles.

The false vacuum configuration in the lower plot of Fig. 6.3(b) can be initialized by preparing the mixture in the ground state associated to a large and positive δ, and then adiabatically lowering the detuning until the central part of the cloud is on the wrong side of the hysteresis cycle [77]. With reference to Fig. 6.3(a), this corresponds to starting from a configuration in which the yellow line is entirely in the upper half-plane and shifting it downwards until part of it (the solid portion, associated to the highest densities) falls below the $h_3 = 0$ line.

Let us point out that, for $\Delta < 0$, an analogous configuration with a false vacuum region with negative magnetization and no domain-walls does not exist; in other words, even though the physics of uniform systems is invariant under the transformation $h_3 \to -h_3$, spontaneous generation of bubbles can be observed in trapped clouds only if h_3 has the same sign of Δ in the false vacuum region. More specifically, it would not be possible to perform the same study with a perfectly symmetric mixture with $\Delta = 0$, since false vacuum configurations would always present domain-walls.

The interaction imbalance is therefore necessary to be able to observe spontaneous bubble nucleation in non-uniform systems: this given, inhomogeneity has two additional consequences on the decay process itself:

(a) We already mentioned that the central region of false vacuum has size $2x_*$, where x_* satisfies $h_3(x_*) = 0$. For an harmonic trapping potential, this gives $x_*/L = \sqrt{|h_3(x=0)|}$. This quantity shrinks to zero close to resonance and in

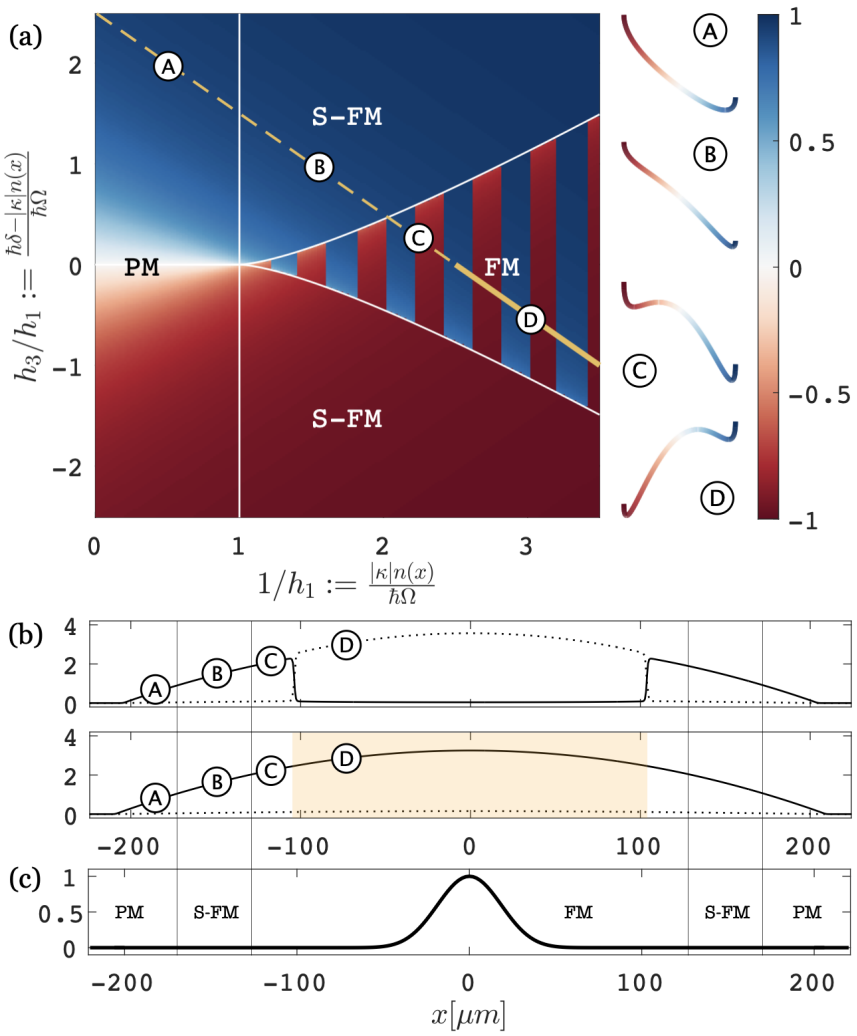

FIGURE 6.3: Effects of inhomogeneity. (a) Phase diagram of the mixture: colors refer to the magnetization Z of stationary states as a function of the parameters h_1, h_3. The yellow line represents an harmonically trapped cloud with $|\kappa|n_0/\hbar\Omega = 3.5$, $\delta/\Omega = 2.5$ and $\kappa = \Delta < 0$. Panels A-D show the profile of the potential $U(Z)$ along the cloud: while the low-density tails are paramagnetic (A) or saturated-ferromagnetic (B), the high-density central part of the system (C,D) can be characterized by both signs of magnetization. (b) Real space density profiles of stationary states for the harmonically trapped mixture represented by the yellow line in panel (a). The dotted and solid lines represent $|\kappa|n/\hbar\Omega$ for the two spin components, respectively. The upper plot shows the ground state of the system: Z has everywhere the same sign as h_3. The lower plot is a stationary state with $Z > 0$ for all x: the central part of the cloud (yellow region) is therefore in a false vacuum state, namely it is locally in a relative minimum of $U(Z)$. Bubble nucleation can only occur within this region, which is represented as the solid part of the yellow line in panel (a). Panel (c) shows the probability distribution $\Gamma(x)$ of the position in which true vacuum bubbles appear, normalized by $\Gamma(x = 0)$. Obtained using the thermal instanton solution (6.9), after setting $k_B T = 20|\kappa|n$.

proximity of the critical point (where $h_3^* \to 0$), preventing the observation of bubble nucleation or, at least, introducing finite size effects.

Nevertheless, both these regimes are difficult to access due to the extremely long time scales and the enhancement of noise at the critical point, respectively.

(b) Since n, h_1, h_3, depend on x, the nucleation rate depends on x, as well: bubbles are more likely to appear at certain positions. According to the thermal instanton prediction (6.9), if $\Delta = \kappa$, the probability distribution of the position at which bubbles appear is approximately a gaussian centered at $x = 0$ and width proportional to the temperature [see Fig. 6.3(c)]:

$$\Gamma(x \ll L) \simeq \Gamma_0 \exp\left[\frac{|\kappa| n_0}{k_B T} Q_0 \left(\frac{3}{2} I_0 + n_0 \left.\frac{\partial I}{\partial n}\right|_{n_0}\right) \frac{x^2}{L^2}\right] \tag{6.15}$$

Notice that this is a non-trivial consequence of how the integral I in Eq. (6.11) depends on the effective external field components: indeed, if h_1, h_3 were constant over the whole cloud, one would expect the decay to take place in low-density regions, where the effect of fluctuations is the largest.

6.5 Numerical simulations

Given the estimates in the previous sections, we performed most of the numerical simulations in the critical regime $h_3^* - |h_3| < 0.08$. The physical parameters (interaction constants, peak density, number of particles, etc...) are those of the available immiscible mixture at the Pitaevskii BEC Center in Trento [77, 85, 108]. In particular $\kappa = \Delta$ in all that follows.

The mixture is initialized in the false vacuum state and subsequently evolved in real time without changing any parameter in the Hamiltonian. We look at both single realizations and statistical averages, that we indicate with the symbol $\langle\cdot\rangle$. It has been proven [145] that there exists a time interval in which the following quantity

$$P(t) = \frac{\langle Z(t)\rangle - Z_{TV}}{Z_{FV} - Z_{TV}}, \tag{6.16}$$

that represents the probability that no bubbles nucleate up to time t, decays exponentially to zero with rate given by the false vacuum decay rate Γ. We will therefore use this quantity to determine how Γ depends on the parameters h_1, h_3, and compare the results with the instanton prediction (6.9).

As an alternative observable, we also compute the tunnelling time τ defined as $P(\tau) = 1/2$ (which is more easily accessible experimentally) and compare it with $1/\Gamma$.

6.5.1 The validity of the Truncated-Wigner approach

With the aim of seeing quantum effects at play, we started performing Truncated-Wigner simulations at small temperature ($k_B T < |\kappa| n$); the mixture has uniform density over a box of length L with periodic boundary conditions. This strategy is usually carried on when studying false vacuum decay in BEC mixtures [58, 60, 63]:

the uniform density allows to easily populate the Bogoliubov modes so to reproduce both quantum and thermal fluctuations.

Physical parameters are chosen to reproduce realistic experimental conditions for a Sodium mixture [77]: in particular $n \simeq 4000$ atoms/μm, $|\kappa|n \simeq 2\pi\hbar \times 1.1kHz$ and $L \simeq 250\mu m$, so to have a total of $N = 10^6$ atoms. A typical example of a single realization showing bubble nucleation is reported in Fig. 6.4(a): we observe that bubbles nucleate stochastically both in space and time, as expected. The dynamics after bubble nucleation is a complicated subject that goes beyond the scope of this work; a brief discussion, accompanied by some preliminary results, can be found in the Conclusions of this Chapter (Sec. 6.7). For the parameters of Fig. 6.4(a), bubbles grow at approximatively constant speed until the whole mixture is in the true vacuum; the eccess of energy is released in the form of small perturbations of the ground state.

While the dynamics observed in single numerical realizations is consistent with the expectations and with previous works on the subject [58, 60], statistical averages lead to inconsistent results: in particular, bubble nucleation rates are cut-off dependent, especially at the smallest temperatures [148, 149]. Moreover, thermalization of Wigner noise to a classical distribution [104] occurs on time scales shorter than those characterizing the false vacuum decay, making the results inconclusive on the role of quantum fluctuations. Truncated-Wigner simulations seem thus not reliable when used to compute the bubble nucleation rates, due to the extremely long time-scales that characterize the decay process.

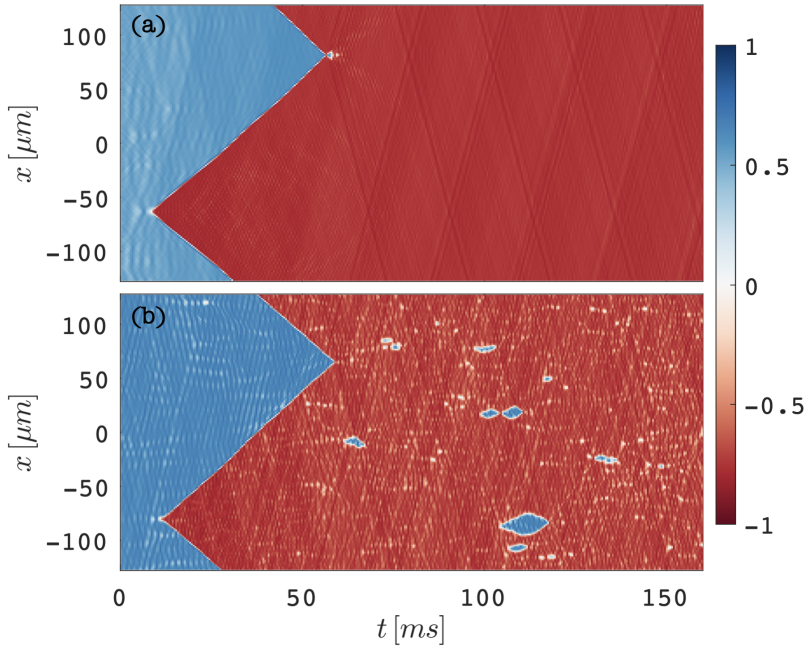

FIGURE 6.4: Bubble nucleation in a ferromagnetic mixture. Colors refer to the magnetization Z. (a) Obtained with Truncated-Wigner simulations at $T = 22nK$, corresponding to $|\kappa|n/k_BT = 2.5$. Physical parameters: $h_1 \simeq 0.73$, $h_3^* - |h_3| \simeq 0.017$. (b) Obtained with classical field simulations. Physical parameters: $h_1 \simeq 0.73$, $h_3^* - |h_3| \simeq 0.058$.

6.5.2 Classical field simulations at finite temperature

Given the inconsistencies, we decided to abandon the Truncated-Wigner approach and perform classical field simulations at finite temperature (see Chapter 3 for more details). This implies working in a classical regime where the false vacuum decay is driven by thermal fluctuations. Our goal is to compute the decay rate through the function $P(t)$ in (6.16) and compare it to the thermal instanton prediction:

$$\Gamma \propto \exp\left[-\frac{|\kappa|n}{k_B T} QI(h_1, h_3)\right] \tag{6.17}$$

We started from the simulation of a uniform mixture in a box. The parameters are chosen to reproduce the experimental ones; in particular $n \sim 4000\mu m^{-1}$ and $|\kappa|n/\hbar \sim 2\pi \times 1.1\,\mathrm{kHz}$, which give $Q \sim 3400$. In order to obtain a total number of particle of $N \sim 10^6$, we set the box length to $L \simeq 250\mu m$. We inject energy in the system by adding, independently to both components' densities, random noise of amplitude εn, where n is the total density and $\varepsilon \ll 1$. We then let the system thermalize for $1.5s$. We verified that the results of the simulations do not vary if we double this thermalization time, proving that the system has indeed reached equilibrium. The mixture is initialized in the false vacuum state following the experimental preparation procedure of [77]: starting from the (noisy) ground state associated with a large and positive $\delta = 2\pi \times 1\,\mathrm{kHz}$, we ramp the detuning down in time at a speed of $50\,\mathrm{Hz}/ms$ so that, at the end of the ramp, h_3 is negative and the cloud is in a metastable state with positive magnetization. We verified that the results shown in the following do not change if we initialize the false vacuum state with a slower (more adiabatic) ramp, proving that the formation of bubbles is not triggered by the ramp itself.

Estimation of the temperature As already pointed out in Chapter 3, our numerical simulations do not allow to fix a priori the temperature of the system in the false vacuum state at the end of the detuning ramp. Assuming the system is at thermal equilibrium and such temperature exists, a rough estimation of it is obtained by exploiting the fluctuation-dissipation theorem as explained in the following.

Let us first point out that, since false vacuum decay occurs for the magnetization degree of freedom, we expect the nucleation rate to depend from an effective temperature associated to the occupation of spin modes, or, equivalently, to the fluctuations of the magnetization σ_Z. This quantity is computed by dividing the cloud, of total lenght L, into windows of lenght $W\mathtt{dx}$, $\mathtt{dx}$ being the resolution of the simulation; the variance of the magnetization Z is calculated in each window and then averaged:

$$\sigma_Z^2(W) = \left\langle \sum_{j=i}^{i+W} \left[Z(x_j) - \frac{1}{W} \sum_{j'=i}^{i+W} Z(x_{j'}) \right]^2 \right\rangle_{i=1,\dots,\frac{L}{\mathtt{dx}}-W} \tag{6.18}$$

For one-dimensional system of large size $L \to \infty$ and uniform density $n = N/L$, assuming the temperature T is small enough to guarantee the validity of Bogoliubov theory, σ_Z and T are related according to the identity [86]:

$$N^2 \lim_{W\to\infty} \sigma_Z^2(W) = \mathcal{S}_s(k = 0, T) \tag{6.19}$$

where $\mathcal{S}_s(k,T)$ is the static structure factor associated to the system's respons to perturbations of the relative density $n_2 - n_1$. The analytical computation of $\mathcal{S}_s(k,T)$ is cumbersome as it requires the eigenvectors of the Bogoliubov matrix (3.14) in the basis defined by $(\delta\psi_1, \delta\psi_2)$ [86]. At high temperature $T \gg |\kappa|n/k_B \simeq 50nK$ a numerical diagonalization of the Bogoliubov problem leads to a structure factor with an approximately Lorentzian shape, with its peak value at $k = 0$ proportional to the temperature T. The large window limit appearing in Eq.(6.19) is therefore extracted through a fit of $\sigma_Z^2(W)$ with a Lorentzian function.

Eq. (6.19) provides a protocol to measure the effective temperature of spin modes starting from the fluctuations of Z after the detuning ramp. Also it suggests that, given some preparation protocol, such temperature is different depending on the parameters h_1, h_3. For most of the simulations presented in the following we find $T \in [250, 500]\mu K$ [see Fig. 6.7(c)]. Let us however stress that these values have to be taken as an indication of the order of magnitude rather than precise numbers, since the just described protocol relies on strong assumptions, such as the system being at thermal equiliubrium after the detuning ramp and the validity of Bogoliubov theory. A more accurate analysis would require the calculation of the density-density correlation function and will be the subject of future work.

Numerical results An example of single realization in which a bubble nucleates is shown in Fig. 6.4(b). A comparison with Fig. 6.4(a) reveals no qualitative difference with respect to Truncated-Wigner simulations: bubbles form stocastically both in space and time and their size grows in time. Increasing the amount of fluctuations allows to investigate larger values of $h_3^* - |h_3|$, thus probing the FM region close to resonance, at least in the limit $h_1 \lesssim 1$. As an unwanted additional effect, we observe that, if the energy difference between true and false vacua is small enough, fluctuations do not only cause small perturbations of the ground state after the decay has taken place, but they might generate bubbles of false vacuum, too [clearly visible in Fig. 6.4(b)]. Despite such bubbles are short lived, their presence affects the measurement of $P(t)$ and, consequently, the calculation of the nucleation rate Γ. To avoid this effect, in what follows we avoid the regime $h_1 \sim 1$ and set $h_1 < 0.5$.

Fig. 6.5 shows a statistical average of the magnetization $Z(x,t)$ obtained from 1000 different realization with different initial (thermalized) noise. As expected, it smoothly decreases from the false vacuum value $Z_{FV} \sim +1$ to the true vacuum value $Z_{TV} \sim -1$. This happens uniformly in space, due to the uniform total density within the box. The probability $P(t)$ in Eq.(6.16) can thus be computed after averaging $\langle Z(x,t)\rangle$ in space over the whole numerical box: the result is shown in the lower panel of Fig. 6.5. Consistently with recent results of [145], obtained for a quantum spin chain, $P(t)$ shows an initial plateau, followed by an interval of exponential decay. The associated nucleation rate Γ is obtained from a linear fit of $\log P$ (dashed red line) in such time interval, whose extremes are typically defined by the condition $P(t) \in [0.3, 0.7]$. The tunnelling time τ is also easily computed by solving $P(\tau) = 1/2$. The two analysed observables Γ^{-1} and τ have the same order of magnitude but do not coincide due to the presence of the initial plateau, whose length depends in a non-trivial way on the system's parameters. Despite this feature is commonly found in numerical studies on false vacuum decay [145, 150], it is not predicted by the theory of instantons and has not been fully understood yet.

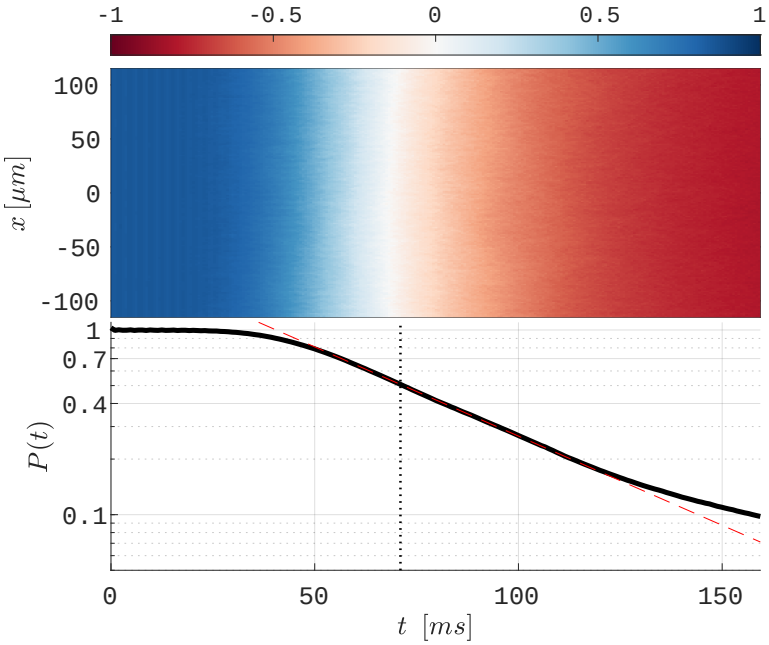

FIGURE 6.5: (Upper panel) Statistical average of the magnetization $Z(x,t)$ obtained from 1000 different realizations with different initial noise. Parameters: $h_1 = 0.27$ (which gives $h_3^* = 0.44$) and $h_3^* - |h_3| \sim 0.04$. The temperature in the spin channel, estimated by exploiting the fluctuation-dissipation theorem (6.19), is $T \sim 320nK$. (Lower panel) Probability $P(t)$ computed as in Eq.(6.16) where $Z(t)$ is also averaged in space over the whole numerical box. The dashed black line represents a linear fit of $\log P$ in the interval defined by $P \in [0.3, 0.7]$. The dotted line indicates the tunnelling time τ, satisfying $P(\tau) = 1/2$.

Depencence on the temperature As a first step in the analysis of false vacuum decay rates, we report in Fig. 6.6 its dependence on the effective spin temperature, which is varied by changing the initial noise amplitude between 4% and 15% of the total density. The numerical results show an exponential trend of Γ as a function of $1/T$, as expected for a thermally induced decay process. According to instanton theory, a linear fit of $-\log\Gamma$ as a function of $\beta = 1/k_B T$ would allow to compute the many-body energy barrier that the system needs to overcome to undergo false vacuum decay: for the parameters in Fig.6.6, we find $\overline{S}_E^{(1)} \simeq k_B \times 750\, nK$. The instanton prediction (6.9) gives instead, for the same parameters, $\overline{S}_E^{(1)} = \hbar|\kappa|nQI(h_1, h_3) \simeq k_B \times 3.8\mu K$, roughly 5 times larger than the one extracted from the simulation.

Dependence on the effective detuning The smoking gun of a decay from a metastable state is the exponential dependence of the time-scales on the barrier height, which, for our system of interest, is controlled through the parameter $h_3^* - |h_3|$. Figure 6.7(a) summarizes the numerical results obtained by varying the effective detuning h_3 at fixed $h_1 = 0.27$: as expected, the decay rate shows an exponential dependence on $h_3^* - |h_3|$. In order to quantitatively compare the numerical data with the analytical

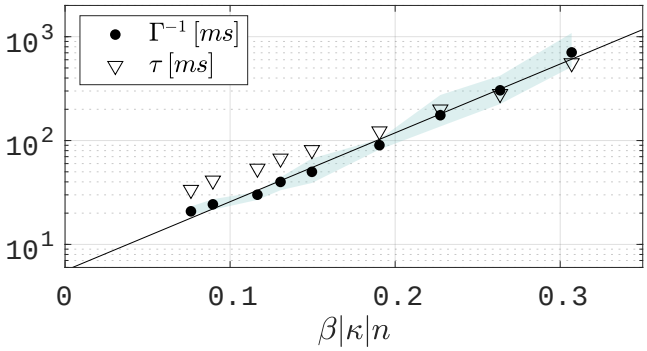

FIGURE 6.6: Tunnelling times as a function of the effective spin temperature [which is estimated using Eq. (6.19) and varied by changing the amount of initial noise] for $h_1 = 0.27$ and $h_3^* - h_3 = 0.04$. Nucleation times are computed by averaging over 1000 different realization of the dynamics. The shaded area represents the maximum dispersion of the FVD rate values Γ^{-1} computed from 10 different sets of 100 samples each. The solid line is a linear fit of Γ^{-1} in logarithmic scale: according to instanton theory, its slope $\overline{S}_E^{(1)} \simeq k_B \times 750nK$ (0.07 on the horizontal axis) represents the height of many-body energy barrier that the system needs to overcome in order to decay.

instanton result we performed a three-parameter fit with the formula:

$$\log \Gamma^{-1} = A(h_3^* - |h_3|)^{\nu} + \log \Gamma_0^{-1} \tag{6.20}$$

According to Eq.(6.9), $\nu = 1.25$ and A should encode the dependence on h_1, T. The fit gives instead $\nu > 1.75$, the exact value depending on how many points are included in the fit: remarkably, as the points associated to the largest decay times are added to the fit, the exponent ν becomes larger, reaching $\nu > 2$ when all the data are used (dotted black line). Such discrepancy with the instanton result is imputed to a residual dependence of the effective spin temperature from h_3 [see the inset in panel (c) of Fig. 6.7]: at larger $h_3^* - |h_3|$, the occupation of spin modes is smaller due to the larger gap in the dispersion relation; the nucleation rate therefore not only decreases because of the increasing height of the many-body barrier, but also due to the lower spin temperature, resulting in a stronger dependence of Γ on $h_3^* - |h_3|$.

After correcting the nucleation rates to account for the different spin temperatures, the results become perfectly compatible with a power-law dependence with exponent 5/4; the two-parameter fit with the formula:

$$\frac{k_B T}{|\kappa|n} \log \left(\frac{\Gamma}{\Gamma_0} \right)^{-1} = A(h_3^* - |h_3|)^{5/4} \tag{6.21}$$

gives $\Gamma_0^{-1} \sim 7ms$ and $A = 790$. According to the instanton result (6.9), the former is related to the unknown prefactor, while the latter only depends on $\Omega, |\kappa|n$ through $A = 1.25 Q h_1^{1/6} (h_3^*)^{-1/4} \simeq 4164$; once again, this value is roughly a factor 5 larger than the one resulting from the fitted numerical data. The instanton theory, thus, would predict either higher temperatures or smaller decay rates. A possible explanation for

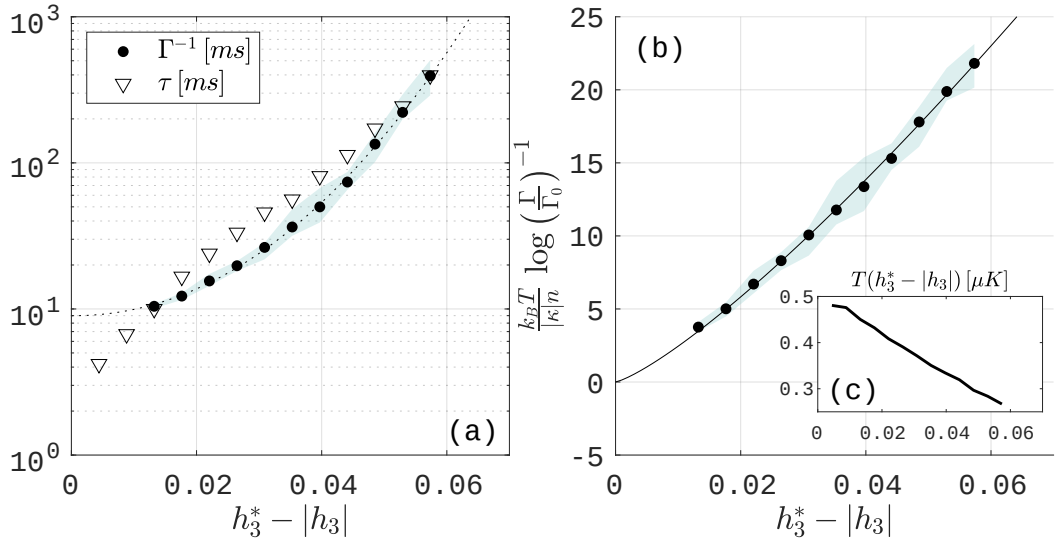

FIGURE 6.7: (a) Inverse of the nucleation rates Γ^{-1} (black dots) and tunnelling times τ (empty triangles), computed by averaging over 1000 different realization of the dynamics, as a function of h_3 for fixed $h_1 = 0.27$. The shaded area represents the maximum dispersion of the FVD rate values computed from 10 different sets of 100 samples each. The dotted black line represents a three-parameter fit with formula (6.20), which gives $\nu = 2.04$. (b) Nucleation rates Γ^{-1} corrected to account for the different spin temperatures, which are estimated by exploiting the fluctuation-dissipation theorem (6.19) and whose dependence on h_3 is reported in inset (c). The solid black line represents a fit using formula (6.21).

such discrepancy is discussed in the conclusions.

Effect of an harmonic trap As a last point in the analysis, we included the harmonic trapping potential in our numerical simulations; the longitudinal trapping frequency is set to $16Hz$, so to obtain a Thomas-Fermi radius of $L \simeq 200\mu m$ and a peak density of $n_0 \sim 3680\mu m^{-1}$ with a total of $N = 10^6$ atoms. The amount of noise injected in the system before letting it thermalize is chosen to approximately match the decay rates obtained for the uniform mixture with the same parameters; in the central part of the cloud, it amounts to roughly 10% of the peak density.

The results of the simulations are analogous to those obtained in the uniform case; as already discussed, the main effect of the trapping potential can be seen in the probability distribution of the position in which bubbles appear: in particular the nucleation rate is higher where the density is higher, which causes bubbles to appear more likely around $x = 0$. Nonetheless, the process remains stochastic and unseeded, as proven by the histogram in Fig. 6.8, showing that bubbles appear as far as $60\mu m$ from the center, only with much lower probability. As shown in the upper panel of Fig. 6.9, once formed, bubbles grow in size until they fill the central region of the cloud that was originally in the false vacuum state; the magnetization at the tails remains instead positive. The final size of the bubble perfectly matches the theoretical

expectation $2x_* = 2L\sqrt{|h_3|}$, which, for the parameters of Fig. 6.9, gives $\simeq 250\mu m$.

In order to avoid effects arising from the inhomogeneous density, the function $P(t)$, reported in the lower panel of Fig.6.9, is computed by averaging the magnetization only over the central $20\mu m$ of the cloud, where the density is approximatively constant. Once again, it shows an initial plateau followed by an interval of exponential decay; the latter can be fitted to determine the decay rate.

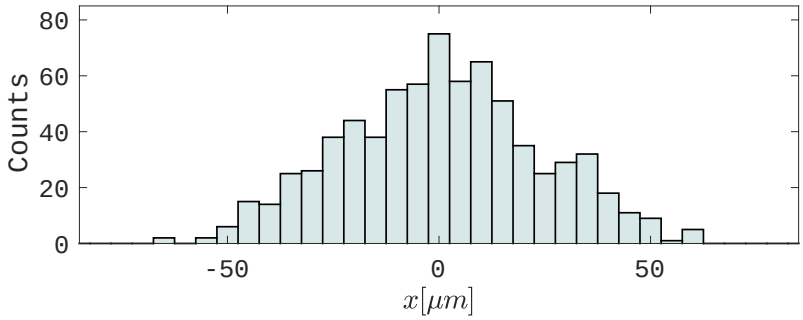

FIGURE 6.8: Statistical distribution of the position in which the bubble appears for a total of 1000 different realization. Parameters: $h_1 = 0.27$ (which gives $h_3^* = 0.44$) and $h_3^* - |h_3| \sim 0.04$. The temperature, estimated with Eq. (6.19), is $T \sim 370nK$.

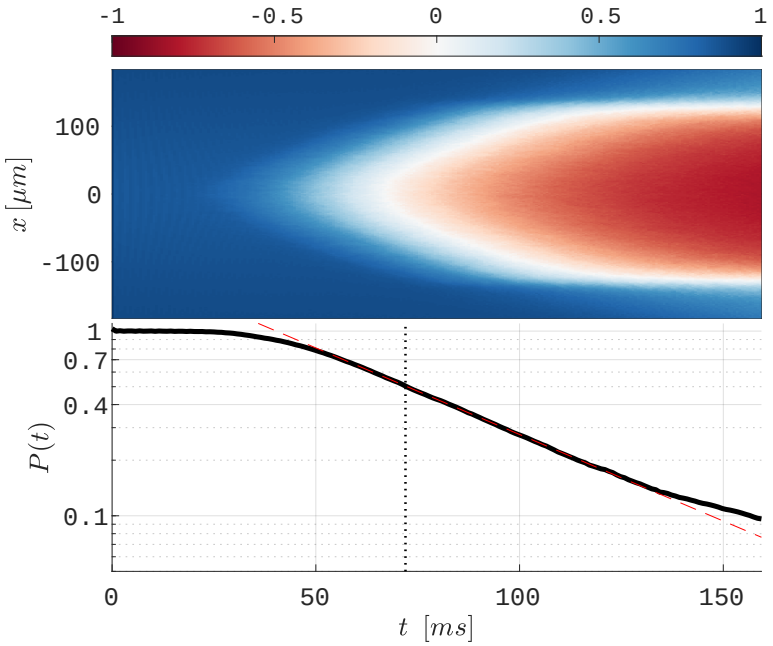

FIGURE 6.9: (Upper panel) Statistical average of the magnetization $Z(x,t)$ obtained from 1000 different realization with different initial noise. Same simulation as in Fig. 6.8. (Lower panel) Probability $P(t)$ computed as in Eq. (6.16) where $Z(t)$ is also averaged in space over the central $20\mu m$ of the cloud. The dashed black line represents a linear fit of $\log P$ in the interval defined by $P \in [0.3, 0.7]$. The dotted line indicates the tunnelling time τ, satisfying $P(\tau) = 1/2$.

6.6 Comparison with experimental results

Numerical simulations in the presence of the harmonic trap have been performed for different values of the physical detuning and of the Rabi frequency, in order to compare them with experimental data. The results are summarized in Fig. 6.10; more details about the experimental procedure, measurements and data analysis can be found in Refs. [96, 101].

We find the same qualitative behaviour in numerical results and experimental data: for both, the dependence on h_3 can be fitted with the formula (6.20) after setting $\nu = 5/4$ (solid lines in the plot). As we already pointed out earlier, the parameters extracted from the fit are not compatible with the instanton prediction: in particular, if they were used to estimate the system's temperature, the result would be Ω-dependent and higher than the condensation temperature for the experimental system. Additionally, both the numerical results and experimental data suggest that, for fixed detuning $h_3^* - |h_3|$, the bubble nucleation time decreases as the Rabi frequency Ω approaches the critical value $|\kappa| n/\hbar = 2\pi \times 1.1$ kHz (above which the system becomes paramagnetic); the instanton theory would instead predict the opposite behaviour. A possible explanation of these discrepancies is given in the Conclusions.

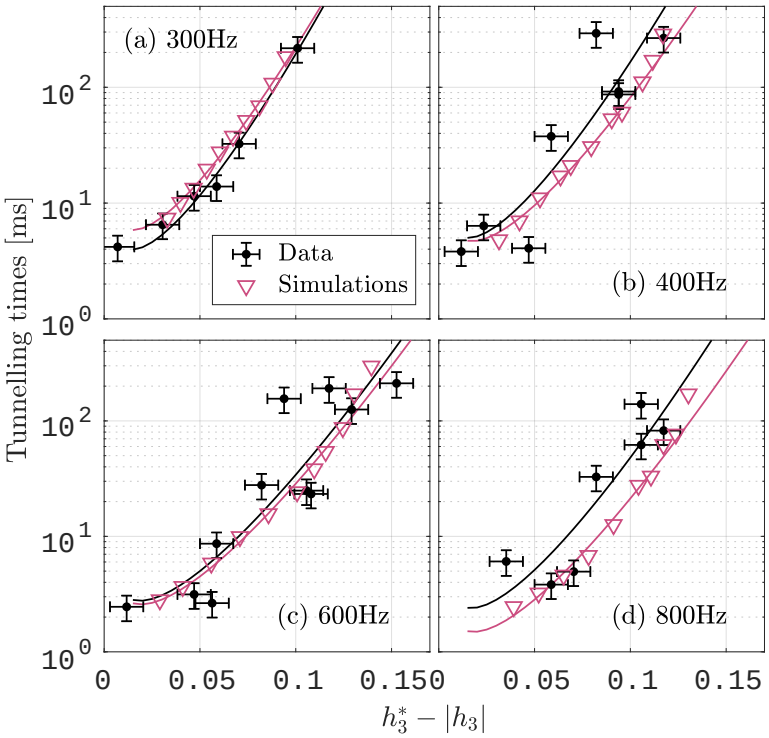

FIGURE 6.10: Comparison between numerical simulations (red triangles) and experimental data (black dots), for different Rabi frequencies: the values of $\Omega/2\pi$ are indicated in the various panels; for the numerical points, the horizontal axis has been rescaled by a factor 0.64 (see text). Solid lines represents two-parameter fits with formula (6.20) after setting $\nu = 5/4$.

Quantitative agreement between simulations and experimental data is recovered, for all the four values of Ω we considered, with a rescaling of the horizontal axis in Fig. 6.10 by a factor 0.64 (the numerical points shown in the plot are already rescaled). The discrepancy is believed to be caused by the different dimensionality (1D in the simulations, 3D for the experiment): it has indeed been proved in Ref. [77] that dimensionality can significantly affect the phase diagram of the mixture (see also Fig. 3.6); it could have an even stronger effect on the FVD rates, since the ratio between surface and volume of a bubble is different according to its shape and dimensionality. Another element that might explain the need of a rescaling factor to match simulations and experimental data is an discrepancy in the temperature, which, unfortunately, cannot be accurately controlled in neither of the two.

6.7 Conclusions

In this Chapter, we have numerically studied the process of relaxation of a ferromagnetic binary mixture from a metastable state to its ground state; we have shown that the decay occurs through the *spontaneous* nucleation of bubbles of true vacuum which then expand in time, in agreement with expectations and with previous works on the subject. We have first attemped to analyse the phenomenon in the quantum regime, but, given the extremely long time-scales and the unreliability of Wigner simulations, we have restricted to a regime in which thermal noise dominates over quantum fluctuations, but temperature is still smaller than the many-body energy barrier that the system needs to overcome in order to decay.

We have identified an observable $P(t)$ in Eq. (6.16) which, after a transient, decays exponentially in time; the decay rate Γ shows an evident exponential dependence both on the system's temperature and on the many-body barrier, which is controlled through the quantity $h_3^* - |h_3|$. Such dependence is qualitatively captured by a simplified instanton model based on a reduced energy functional for the magnetization only. We also investigated the role of an harmonic trapping potential and found remarkable agreement between numerical simulation and experimental data [101].

To summarize, our results present all the main features of *false vacuum decay at finite temperature* [71], that is, of a thermally-induced macroscopic tunnelling from a metastable state in a spatially extended system. Our work thus confirms the potential of ferromagnetic coherently-coupled binary BEC mixtures as an experimentally accessible and highly-tunable platform to reach a better understanding of the early Universe, as well as of the physics of dissipationless magnetic materials across a first-order phase transition.

Future research directions are diverse and include:

(a) a better understanding of the discrepancy between numerical results and the instanton prediction: on one side, working at fixed temperature, by means of stochastic-GPE simulations [105], would facilitate a quantitative comparison with analytical results; on the other side, the instanton solution (6.9) relies on strong assumptions which need to be relaxed, such as neglecting the relative phase dynamics and the coupling with the density channel. While the latter is likely to have a secondary effect on the decay rates, especially for uniform

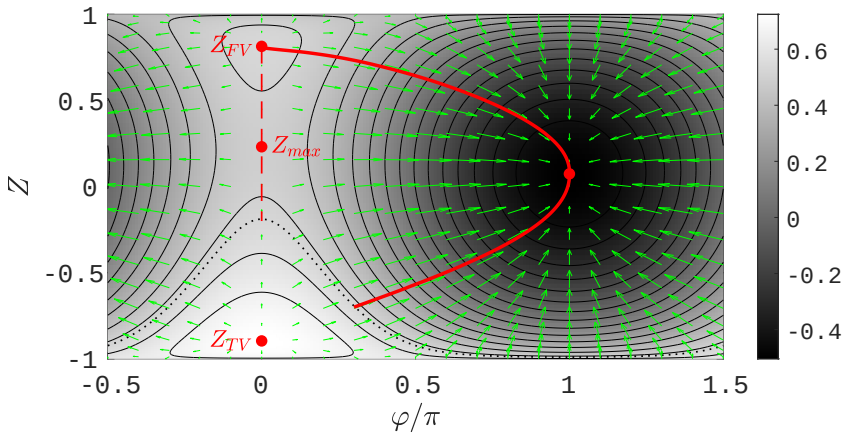

FIGURE 6.11: Contour plot (in gray scale) of the inverted potential $-U(Z,\varphi)/|\kappa|n$ that is solved to determine the instanton solution (6.9); green arrows indicate the gradient of the potential; the dotted black line represents the locus of turning points for which $U(Z,\varphi) = U(Z_{FV},0)$. Red dots indicate the four stationary points: the FV and TV states are maxima in the inverted potential; there exist a saddle point (a minimum along Z, but a maximum along φ) at $\varphi = 0, Z = Z_{max}$ and a global minimum at $\varphi = \pi$. The dashed red line represents the instanton solution considered up to now, which passes through the saddle point ($\varphi = 0$ at all times), while the solid red curve represents an alternative path which, by allowing a non-zero relative phase, is possibly associated to a lower action.

systems, the former might be significant both for what concerns the absolute values of Γ and their dependence on the Rabi frequency h_1.

As shown in Fig. 6.11, allowing for a non-zero relative phase enlarges dramatically the space of possible paths in the inverted potential $-U(Z,\varphi)$; an example is shown as a solid red line. A more rigorous calculation is necessary to determine if some of such paths lead to a smaller action, and thus to a reduction of the tunnelling times; if this is the case, since the relative phase enters in the potential through a term proportional to Ω, we expect that relaxing the assumption $\varphi \sim 0$ would mostly affect the dependence of Γ on h_1.

(b) an analysis of the effect of dimensionality on the false vacuum decay rates: since the process occurs through the formation of a *resonant* bubble, whose size is such that the bulk energy gain is compensated by the tension at the walls, we expect Γ to depend on the ratio between surface and volume of the bubble, which, in turn, depends on the dimensionality of the bubble itself. In particular, we expect the decay to be favoured in higher dimension.

The role of dimensionality could be investigated, for instance, with an axially symmetric harmonically trapped mixture by measuring how the decay rate varies with the ratio between the trapping frequencies $\omega_\perp/\omega_{||}$ at fixed peak density.

(c) an analysis of the role of temperature and of the quantum-to-thermal threshold, in the spirit of [61]. Approaching the regime in which quantum fluctuations

play a relevant is however challenging, since it requires the development of more sophisticated numerical techniques and/or an improvement of the experimental apparatus accuracy. In general, it might be helpful to work with smaller densities, so to avoid impossibly long time-scales.

In addition to a deeper analysis of the decay rates Γ, a natural extension of our work would be a study of the dynamics of the bubble after the nucleation: while in the cosmological context bubbles of true vacuum are expected to grow indefinitely at the speed of light, studies on the nature of elementary excitations in magnetic systems have proven the existence of mesonic-like kink-antikink bound states, suggesting that domain-walls should be confined to stay close to each other. We expect the dynamics after the decay to stem from a complicated interplay between energy conservation and the available "dissipation" channels: as a bubble grows in size, the energy difference between the true and false vacuum states can be either stored as kinetic energy in the domain-walls, or released in the form of Bogoliubov modes and thermal noise, or even generate other excitations, such as solitons.

As visible in Fig. 6.1 (panels C-E), in our platform the energy imbalance between the false and true vacuum states depends strongly on Ω: we thus expect the domain-wall dynamics after the formation of the bubble to vary significantly with the Rabi frequency. Preliminary numerical results seem to confirm this prediction: while for the parameters of Fig. 6.4(a), for which the energy difference between true and false vacuum is $\delta U \sim 0.03|\kappa|n$, after an initial acceleration the size of the bubble grows at constant speed, for those in Fig. 6.12, giving $\delta U \sim 0.17|\kappa|n$, the dynamics is much more complicated: the bubble size initially oscillates rather than increasing, as if the two domain-walls were bound; in the meanwhile, Bogoliubov excitations are emitted (visible as a cone of waves around the bubble); these trigger the formation of additional bubbles leading to a cascade effect that eventually flips the magnetization of the whole cloud. A deeper study of the dynamics of domain-walls, including confinement and scattering, and of how such dynamics depends on the physical parameters (Rabi frequency, detuning, temperature) will be the subject of future works.

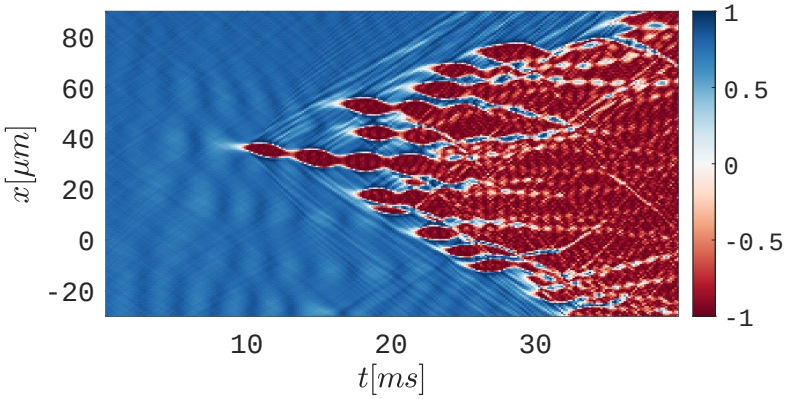

FIGURE 6.12: Bubble nucleation in an harmonically trapped ferromagnetic mixture. Colors refer to the magnetization Z. Obtained with truncated-Wigner simulations at $T = 22\,nK$; Parameters: $h_1 \simeq 0.36$, $h_3^* - |h_3| \simeq 0.01$.

7 Conclusions and future perspectives

In this Thesis we discussed the possibility of exploiting two-component mixtures of atomic Bose-Einstein condensates to investigate astrophysical and cosmological phenomena, in the context of *analog gravity* [3]: this research field is based on the use of table-top set-ups to simulate the physics of quantum fields on curved spacetimes, based on the formal equivalence of the equations of motion governing the dynamics of the two systems under suitable conditions. The strength of this approach resides in the possibility of experimentally observe gravitational phenomena which would otherwise escape direct investigation, as those occurring in the vicinity of a black hole or during the fast expansion of the early universe.

Due to their superfluid character, intrinsic quantum nature and impressive experimental tunability, Bose-Einstein condensates represent one of the most promising platforms to realize analog spacetimes and emulate gravitational phenomena, potentially even those stemming from the interplay between the effectively curved geometry and quantum fluctuations. In this Thesis we go beyond the standard single-component BEC and focus on binary mixtures of atomic condensates, possibly in the presence of a coherent coupling between the two-components [14, 86]. Our goal is to exploit the additional degrees of freedom that such systems display in order to explore a broader spectrum of gravitational phenomena, as well as to potentially facilitate their experimental observation.

In Chapter 3 we discussed all the relevant features of binary BEC mixtures, which are characterized by an extremely rich phase diagram, and whose properties are accurately controlled by tuning the strength and detuning of the external field coupling the two components [77]. Without such coupling, the system has two independent branches of elementary excitations, associated to perturbations of the total and relative density, that we referred to as *density* and *spin* modes; both are phononic in the low-frequency regime, but with very different sound-speed [57]. Hence, the availability of both density and spin modes allows to simulate the dynamics of a massless scalar field subject to two different spacetime geometries, despite the total density profile of the background atomic condensate is fixed. When a non-vanishing coherent coupling is switched on, it affects the dispersion relation of spin modes by opening a gap, thus allowing, within certain parameters' regimes, to conceptually extend the analysis to massive scalar fields.

In Chapters 4 and 5 we discussed two configurations of gravitational interest whose realization with unpolarized binary mixtures makes full use of their novel features listed above.

Specifically, in Chapter 4 we considered a one-dimensional analog black-hole spacetime featuring a sonic horizon for spin modes and analysed its stimulated and spontaneous Hawking radiation at zero temperature; the background flow of the condensate can be engineered so that the analog geometry felt by density modes is trivial, making the configuration robust against total density perturbations. The much larger value of the healing length for spin modes ξ_s (with respect to that of density modes ξ_d) allows to obtain an effectively one-dimensional dynamics without the need to work with a quasi-1D condensate and even to generate an horizon that is steeper than ξ_s.

A finite Rabi frequency in the black-hole interior modifies its grey-body factor, without affecting the thermal character of the (relativistic) Hawking particles emitted in the black-hole exterior. The different nature of excitations on the two sides of the analog horizon significantly changes instead the spectral properties of the emission, and, as a consequence, the typical *mustache* observed in density-density correlations [38–40], which shows characteristic features known as *undulations*. A non-vanishing coherent coupling also fixes the relative phase between the two components and regularizes its perturbations, making phase-phase correlations an equivalently powerful observable, in which the Hawking signal potentially appears with much larger intensity, thus facilitating its experimental observation.

In Chapter 5 we focused on a two-dimensional rotating spacetime featuring an analog ergoregion, which is obtained with quantized vortices, and analysed dynamical instabilities arising from self-stimulated superradiance. While the size of the non-hydrodynamic vortex core is fixed by the density healing length ξ_d, the dimension of the analog ergoregion for spin modes depends on $\xi_s \gg \xi_d$: this will significantly facilitate the experimental observation of the development of ergoregion instabilities in Bose-Einstein condensates. A remarkable consequence of the existence of dynamically unstable modes which extend outside of the vortex core is their property of having extremely low frequencies. Their hydrodynamic nature influences their long-time fate: instead of being associated with vortex splitting, they cause phononic emission from the ergosurface, in closer analogy with the astrophysical context.

While unpolarized $\mathbb{Z}_2$ symmetric mixture offer the possibility of straightforwardly apply the gravitational analogy to the dynamics of both density and spin modes, such one-by-one correspondence with the relativistic context cannot be found for polarized mixtures. However, the coexistence of superfluidity and ferromagnetic character make it possible, for instance, to initialize the system in a metastable state and study the relaxation process to the ground state. When occurring to a field, this phenomenon takes the name of *false vacuum decay* and has relevant applications to cosmology, being associated to the stability of the electroweak vacuum.

In Chapter 6 we reported a numerical analysis of thermally-induced false vacuum decay in a ferromagnetic binary BEC mixture, whose results are in agreement with the first experimental observation of the phenomenon [101]; the experiment, to which we provided numerical support, was performed at the Pitaevskii BEC Center in Trento. Despite the observed nucleation rates and bubble dynamics are not sufficient to directly draw conclusions on cosmological false vacuum decay and the stability of the Higgs field, an accurate comparison of the numerical and experimental data with the

theoretical prediction of the instanton model would allow to validate or disprove it; indeed, this theory is commonly used to study false vacuum decay in cosmology and to put constraints on models describing the early universe, but its application is not restricted to relativistic scenarios.

In general, our results confirm the potential of atomic Bose-Einstein condensates as gravitational analogs and highlight the practical and conceptual advantages brought by coherently-coupled binary mixtures over single-component systems, even for configurations in which the gravitational analogy is not directly applicable. Future work will focus on more realistic implementations of the ideal configurations considered in the Thesis, taking into account, for instance, the effects of a small asymmetry in the number of particles, finite temperature, external potentials, and transverse dimensions. For what concerns Hawking emission, time-dependent numerical simulations are necessary to support the simple semi-analytical results we discussed in Chapter 4, and analyse the correlation features that appear at short and intermediate times after the creation of the analog horizon.

A more ambitious challenge consists in reaching a regime that would allow to see quantum fluctuations at play. In particular, with reference to the vortex geometry considered in Chapter 5, an analysis of correlations will allow to investigate superradiant processes at the quantum level, so to prove that the amplification is intrinsically connected to the spontaneous creation of correlated pairs of Bogoliubov modes with opposite energy at the ergosurface. Similarly, the development of more sophisticated numerical techniques is necessary to investigate false vacuum decay from vacuum initial conditions, in order to determine the thermal-to-quantum threshold temperature and identify potential limitations in the experimental observation of this phenomenon in the quantum limit with our platform.

Besides the realization of processes of astrophysical and cosmological interest, the richness of the phase diagram of two-component condensates (see Fig. 3.5) suggests the possibility of exploiting them in the study of magnetism in the absence of dissipation, decoherence and defects, conditions that are challenging to achieve in other condensed matter platforms [77]. As briefly mentioned in Chapter 6, examples include the dynamics of domain walls and their scattering properties, or the study of kink-antikink bound states and domain-wall confinement.

Related publications

The results presented in this Thesis (in Chapters 3, 5 and 6) have been partially published in the following papers:

- "*Observation of Massless and Massive Collective Excitations with Faraday Patterns in a Two-Component Superfluid*",
  R. Cominotti, A. Berti, A. Farolfi, A. Zenesini, G. Lamporesi, I. Carusotto, A. Recati and G. Ferrari, Phys. Rev. Lett. 128, 210401 (2022)

- "*Ferromagnetism in an extended coherently-coupled atomic superfluid*",
  R. Cominotti, A. Berti, C. Dulin, C. Rogora, G. Lamporesi, I. Carusotto, A. Recati, A. Zenesini and G. Ferrari, Physical Review X 13 (2), 021037 (2023)

- "*Superradiant phononic emission from the analog spin ergoregion in a two-component Bose–Einstein condensate*",
  A. Berti, L. Giacomelli and I. Carusotto, Comptes Rendus Physique 24 (S3), 1-20 (2023)

- "*False vacuum decay via bubble formation in ferromagnetic superfluids*",
  A. Zenesini, A. Berti, R. Cominotti, C. Rogora, I. G. Moss, T. P. Billam, I. Carusotto, G. Lamporesi, A. Recati and Gabriele Ferrari, Nature Physics, 1-6 (2024)

The results of Chapter 4 are part of a manuscript under preparation:

- "*Analog Hawking radiation from a spin-sonic horizon in a coherently-coupled Bose-Einstein condensate*",
  A. Berti, L. Fernandes, S. G. Butera, A. Recati and I. Carusotto

Other related publications not included in this Thesis:

- "*Monte Carlo matrix-product-state approach to the false vacuum decay in the monitored quantum Ising chain*",
  J. Maki, A. Berti, I. Carusotto and A. Biella, SciPost Physics 15 (4), 152 (2023)

Bibliography

[1]W. G. Unruh, "Experimental black-hole evaporation?", Physical Review Letters **46**, 1351 (1981).

[2]W. Unruh, "Dumb holes: analogues for black holes", Philosophical Transactions of the Royal Society A: Mathematical, Physical and Engineering Sciences **366**, 2905–2913 (2008).

[3]C. Barcelo, S. Liberati, and M. Visser, "Analogue gravity", Living reviews in relativity **14**, 1–159 (2011).

[4]S. Robertson, F. Michel, and R. Parentani, "Nonlinearities induced by parametric resonance in effectively 1d atomic bose condensates", Physical Review D **98**, 056003 (2018).

[5]S. Butera and I. Carusotto, "Numerical studies of back reaction effects in an analog model of cosmological preheating", Phys. Rev. Lett. **130**, 241501 (2023).

[6]S. Weinfurtner, S. Liberati, and M. Visser, "Modelling planck-scale lorentz violation via analogue models", in Journal of physics: conference series, Vol. 33, 1 (IOP Publishing, 2006), p. 373.

[7]M. Visser, C. Barcelo, and S. Liberati, "Acoustics in bose-einstein condensates as an example of broken lorentz symmetry", in *Cpt and lorentz symmetry* (World Scientific, 2002), pp. 336–340.

[8]G. Rousseaux, C. Mathis, P. Maïssa, T. G. Philbin, and U. Leonhardt, "Observation of negative-frequency waves in a water tank: a classical analogue to the hawking effect?", New Journal of Physics **10**, 053015 (2008).

[9]G. Rousseaux, P. Maïssa, C. Mathis, P. Coullet, T. G. Philbin, and U. Leonhardt, "Horizon effects with surface waves on moving water", New Journal of Physics **12**, 095018 (2010).

[10]O. Lahav, A. Itah, A. Blumkin, C. Gordon, S. Rinott, A. Zayats, and J. Steinhauer, "Realization of a sonic black hole analog in a bose-einstein condensate", Physical review letters **105**, 240401 (2010).

[11]H. S. Nguyen, D. Gerace, I. Carusotto, D. Sanvitto, E. Galopin, A Lemaître, I. Sagnes, J. Bloch, and A. Amo, "Acoustic black hole in a stationary hydrodynamic flow of microcavity polaritons", Physical review letters **114**, 036402 (2015).

[12]D. Vocke, C. Maitland, A. Prain, K. E. Wilson, F. Biancalana, E. M. Wright, F. Marino, and D. Faccio, "Rotating black hole geometries in a two-dimensional photon superfluid", Optica **5**, 1099–1103 (2018).

[13]T. G. Philbin, C. Kuklewicz, S. Robertson, S. Hill, F. Konig, and U. Leonhardt, "Fiber-optical analog of the event horizon", Science **319**, 1367–1370 (2008).

[14]L. Pitaevskii and S. Stringari, *Bose-einstein condensation and superfluidity*, Vol. 164 (Oxford University Press, 2016).

[15]Y. Castin, "Bose-einstein condensates in atomic gases: simple theoretical results", in *Coherent atomic matter waves: 27 july–27 august 1999* (Springer, 2002), pp. 1–136.

[16]M. Visser, "Acoustic black holes: horizons, ergospheres and hawking radiation", Classical and Quantum Gravity **15**, 1767 (1998).

[17]A. Chatrchyan, K. T. Geier, M. K. Oberthaler, J. Berges, and P. Hauke, "Analog cosmological reheating in an ultracold bose gas", Physical Review A **104**, 023302 (2021).

[18]J.-C. Jaskula, G. B. Partridge, M. Bonneau, R. Lopes, J. Ruaudel, D. Boiron, and C. I. Westbrook, "Acoustic analog to the dynamical casimir effect in a bose-einstein condensate", Physical Review Letters **109**, 220401 (2012).

[19]S. Butera and I. Carusotto, "Particle creation in the spin modes of a dynamically oscillating two-component bose-einstein condensate", Physical Review D **104**, 083503 (2021).

[20]T. V. Zache, V. Kasper, and J. Berges, "Inflationary preheating dynamics with two-species condensates", Physical Review A **95**, 063629 (2017).

[21]P. Jain, S. Weinfurtner, M. Visser, and C. W. Gardiner, "Analog model of a friedmann-robertson-walker universe in bose-einstein condensates: application of the classical field method", Phys. Rev. A **76**, 033616 (2007).

[22]S. Eckel, A. Kumar, T. Jacobson, I. B. Spielman, and G. K. Campbell, "A rapidly expanding bose-einstein condensate: an expanding universe in the lab", Physical Review X **8**, 021021 (2018).

[23]C. Viermann, M. Sparn, N. Liebster, M. Hans, E. Kath, Á. Parra-López, M. Tolosa-Simeón, N. Sánchez-Kuntz, T. Haas, H. Strobel, et al., "Quantum field simulator for dynamics in curved spacetime", Nature **611**, 260–264 (2022).

[24]Y. Kawaguchi and M. Ueda, "Spinor bose–einstein condensates", Physics Reports **520**, 253–381 (2012).

[25]S. Liberati, M. Visser, and S. Weinfurtner, "Analogue quantum gravity phenomenology from a two-component bose–einstein condensate", Classical and Quantum Gravity **23**, 3129 (2006).

[26]M. Visser and S. Weinfurtner, "Massive klein-gordon equation from a bose-einstein-condensation-based analogue spacetime", Physical Review D **72**, 044020 (2005).

[27]S. Weinfurtner, S. Liberati, and M. Visser, "Analogue space-time based on 2-component bose-einstein condensates", Quantum Analogues: From Phase Transitions to Black Holes and Cosmology, 115–163 (2007).

[28]S. W. Hawking, "Black hole explosions?", Nature **248**, 30–31 (1974).

[29]S. W. Hawking, "Particle creation by black holes", Communications in mathematical physics **43**, 199–220 (1975).

[30]J. Macher and R. Parentani, "Black-hole radiation in bose-einstein condensates", Physical Review A **80**, 043601 (2009).

[31]S. Finazzi and I. Carusotto, "Entangled phonons in atomic bose-einstein condensates", Physical Review A **90**, 033607 (2014).

[32]M. Jacquet, M. Joly, F. Claude, L. Giacomelli, Q. Glorieux, A. Bramati, I. Carusotto, and E. Giacobino, "Analogue quantum simulation of the hawking effect in a polariton superfluid", The European Physical Journal D **76**, 152 (2022).

[33]B. Horstmann, B. Reznik, S. Fagnocchi, and J. I. Cirac, "Hawking radiation from an acoustic black hole on an ion ring", Physical review letters **104**, 250403 (2010).

[34]L.-P. Euvé, F. Michel, R. Parentani, T. G. Philbin, and G. Rousseaux, "Observation of noise correlated by the hawking effect in a water tank", Physical review letters **117**, 121301 (2016).

[35]S. Weinfurtner, E. W. Tedford, M. C. Penrice, W. G. Unruh, and G. A. Lawrence, "Measurement of stimulated hawking emission in an analogue system", Physical review letters **106**, 021302 (2011).

[36]F. Belgiorno, S. L. Cacciatori, M. Clerici, V. Gorini, G. Ortenzi, L. Rizzi, E. Rubino, V. G. Sala, and D. Faccio, "Hawking radiation from ultrashort laser pulse filaments", Physical review letters **105**, 203901 (2010).

[37]J. Drori, Y. Rosenberg, D. Bermudez, Y. Silberberg, and U. Leonhardt, "Observation of stimulated hawking radiation in an optical analogue", Physical Review Letters **122**, 010404 (2019).

[38]I. Carusotto, S. Fagnocchi, A. Recati, R. Balbinot, and A. Fabbri, "Numerical observation of hawking radiation from acoustic black holes in atomic bose–einstein condensates", New Journal of Physics **10**, 103001 (2008).

[39]A Recati, N Pavloff, and I. Carusotto, "Bogoliubov theory of acoustic hawking radiation in bose-einstein condensates", Physical Review A **80**, 043603 (2009).

[40]J. Steinhauer, "Observation of quantum hawking radiation and its entanglement in an analogue black hole", Nature Physics **12**, 959–965 (2016).

[41]J. R. Muñoz de Nova, K. Golubkov, V. I. Kolobov, and J. Steinhauer, "Observation of thermal hawking radiation and its temperature in an analogue black hole", Nature **569**, 688–691 (2019).

[42]V. I. Kolobov, K. Golubkov, J. R. Muñoz de Nova, and J. Steinhauer, "Observation of stationary spontaneous hawking radiation and the time evolution of an analogue black hole", Nature Physics **17**, 362–367 (2021).

[43]P.-É. Larré and N Pavloff, "Hawking radiation in a two-component bose-einstein condensate", EPL (Europhysics Letters) **103**, 60001 (2013).

[44]W.-C. Syu, D.-S. Lee, and C.-Y. Lin, "Analogous hawking radiation and quantum entanglement in two-component bose-einstein condensates: the gapped excitations", Physical Review D **106**, 044016 (2022).

[45]W.-C. Syu and D.-S. Lee, "Analogous hawking radiation from gapped excitations in a transonic flow of binary bose-einstein condensates", Physical Review D **107**, 084049 (2023).

[46]R. Penrose and R. Floyd, "Extraction of rotational energy from a black hole", Nature Physical Science **229**, 177–179 (1971).

[47]R. Brito, V. Cardoso, and P. Pani, *Superradiance*, Vol. 10 (Springer, 2020).

[48]I. Zeldovich, "Amplification of cylindrical electromagnetic waves reflected from a rotating body", Soviet Physics-JETP **35**, 1085–1087 (1972).

[49]T. Torres, S. Patrick, A. Coutant, M. Richartz, E. W. Tedford, and S. Weinfurtner, "Rotational superradiant scattering in a vortex flow", Nature Physics **13**, 833–836 (2017).

[50]M. Cromb, G. M. Gibson, E. Toninelli, M. J. Padgett, E. M. Wright, and D. Faccio, "Amplification of waves from a rotating body", Nature Physics **16**, 1069–1073 (2020).

[51]M. C. Braidotti, R. Prizia, C. Maitland, F. Marino, A. Prain, I. Starshynov, N. Westerberg, E. M. Wright, and D. Faccio, "Measurement of penrose superradiance in a photon superfluid", Physical Review Letters **128**, 013901 (2022).

[52]J. L. Friedman, "Ergosphere instability", Communications in Mathematical Physics **63**, 243–255 (1978).

[53]N. Comins and B. F. Schutz, "On the ergoregion instability", Proceedings of the Royal Society of London. A. Mathematical and Physical Sciences **364**, 211–226 (1978).

[54]V. Cardoso, O. J. Dias, J. P. Lemos, and S. Yoshida, "Black-hole bomb and superradiant instabilities", Physical Review D **70**, 044039 (2004).

[55]L. A. Oliveira, V. Cardoso, and L. C. Crispino, "Ergoregion instability: the hydrodynamic vortex", Physical Review D **89**, 124008 (2014).

[56]L. Giacomelli and I. Carusotto, "Ergoregion instabilities in rotating two-dimensional bose-einstein condensates: perspectives on the stability of quantized vortices", Physical Review Research **2**, 033139 (2020).

[57]R. Cominotti, A. Berti, A. Farolfi, A. Zenesini, G. Lamporesi, I. Carusotto, A. Recati, and G Ferrari, "Observation of massless and massive collective excitations with faraday patterns in a two-component superfluid", Physical Review Letters **128**, 210401 (2022).

[58]O. Fialko, B. Opanchuk, A. Sidorov, P. Drummond, and J. Brand, "Fate of the false vacuum: towards realization with ultra-cold atoms", Europhysics Letters **110**, 56001 (2015).

[59]O. Fialko, B. Opanchuk, A. I. Sidorov, P. D. Drummond, and J. Brand, "The universe on a table top: engineering quantum decay of a relativistic scalar field from a metastable vacuum", Journal of Physics B: Atomic, Molecular and Optical Physics **50**, 024003 (2017).

[60]K. L. Ng, B. Opanchuk, M. Thenabadu, M. Reid, and P. D. Drummond, "Fate of the false vacuum: finite temperature, entropy, and topological phase in quantum simulations of the early universe", PRX Quantum **2**, 010350 (2021).

[61]M. G. Abed and I. G. Moss, "Bubble nucleation at zero and non-zero temperatures", Physical Review D **107**, 076027 (2023).

[62]J. Braden, M. C. Johnson, H. V. Peiris, and S. Weinfurtner, "Towards the cold atom analog false vacuum", Journal of High Energy Physics **2018**, 1–39 (2018).

[63]T. P. Billam, R. Gregory, F. Michel, and I. G. Moss, "Simulating seeded vacuum decay in a cold atom system", Physical Review D **100**, 065016 (2019).

[64]J. Braden, M. C. Johnson, H. V. Peiris, A. Pontzen, and S. Weinfurtner, "Nonlinear dynamics of the cold atom analog false vacuum", Journal of High Energy Physics **2019** (2019).

[65]T. P. Billam, K. Brown, and I. G. Moss, "False-vacuum decay in an ultracold spin-1 bose gas", Physical Review A **105**, L041301 (2022).

[66]T. P. Billam, K. Brown, and I. G. Moss, "Bubble nucleation in a cold spin 1 gas", New Journal of Physics **25**, 043028 (2023).

[67]A. C. Jenkins, I. G. Moss, T. P. Billam, Z. Hadzibabic, H. V. Peiris, and A. Pontzen, "Generalized cold-atom simulators for vacuum decay", arXiv preprint arXiv:2311.02156 (2023).

[68]A. C. Jenkins, J. Braden, H. V. Peiris, A. Pontzen, M. C. Johnson, and S. Weinfurtner, "Analog vacuum decay from vacuum initial conditions", Physical Review D **109**, 023506 (2024).

[69]S. Coleman, "Fate of the false vacuum: semiclassical theory", Physical Review D **15**, 2929 (1977).

[70]C. G. Callan Jr and S. Coleman, "Fate of the false vacuum. ii. first quantum corrections", Physical Review D **16**, 1762 (1977).

[71]A. D. Linde, "Decay of the false vacuum at finite temperature", Nuclear Physics B **216**, 421–445 (1983).

[72]J. Elias-Miro, J. R. Espinosa, G. F. Giudice, G. Isidori, A. Riotto, and A. Strumia, "Higgs mass implications on the stability of the electroweak vacuum", Physics Letters B **709**, 222–228 (2012).

[73]M. Sher, "Electroweak higgs potential and vacuum stability", Physics Reports **179**, 273–418 (1989).

[74]S Alekhin, A. Djouadi, and S Moch, "The top quark and higgs boson masses and the stability of the electroweak vacuum", Physics Letters B **716**, 214–219 (2012).

[75]T. Markkanen, A. Rajantie, and S. Stopyra, "Cosmological aspects of higgs vacuum metastability", Frontiers in Astronomy and Space Sciences **5**, 40 (2018).

[76]R. Bousso, D. Harlow, and L. Senatore, "Inflation after false vacuum decay: observational prospects after planck", Physical Review D **91**, 083527 (2015).

[77]R Cominotti, A Berti, C Dulin, C Rogora, G Lamporesi, I Carusotto, A Recati, A Zenesini, and G Ferrari, "Ferromagnetism in an extended coherently coupled atomic superfluid", Physical Review X **13**, 021037 (2023).

[78]I. Carusotto and C. Ciuti, "Quantum fluids of light", Reviews of Modern Physics **85**, 299 (2013).

[79]M. H. Anderson, J. R. Ensher, M. R. Matthews, C. E. Wieman, and E. A. Cornell, "Observation of bose-einstein condensation in a dilute atomic vapor", science **269**, 198–201 (1995).

[80]K. B. Davis, M.-O. Mewes, M. R. Andrews, N. J. van Druten, D. S. Durfee, D. Kurn, and W. Ketterle, "Bose-einstein condensation in a gas of sodium atoms", Physical review letters **75**, 3969 (1995).

[81]L. Giacomelli, "Superradiant phenomena: lessons from and for bose–einstein condensates", PhD thesis (University of Trento, 2021).

[82]T. Jacobson, "Black-hole evaporation and ultrashort distances", Physical Review D **44**, 1731 (1991).

[83]R. Brout, S. Massar, R. Parentani, and P. Spindel, "Hawking radiation without trans-planckian frequencies", Physical Review D **52**, 4559 (1995).

[84]A. Recati and S. Stringari, "Coherently coupled mixtures of ultracold atomic gases", Annual Review of Condensed Matter Physics **13**, 407–432 (2022).

[85]A. Farolfi, A. Zenesini, D. Trypogeorgos, C. Mordini, A. Gallemì, A. Roy, A. Recati, G. Lamporesi, and G. Ferrari, "Quantum-torque-induced breaking of magnetic interfaces in ultracold gases", Nature Physics **17**, 1359–1363 (2021).

[86]M. Abad and A. Recati, "A study of coherently coupled two-component bose-einstein condensates", The European Physical Journal D **67**, 1–11 (2013).

[87]J Steinhauer, R Ozeri, N Katz, and N Davidson, "Excitation spectrum of a bose-einstein condensate", Physical review letters **88**, 120407 (2002).

[88]C. Schori, T. Stöferle, H. Moritz, M. Köhl, and T. Esslinger, "Excitations of a superfluid in a three-dimensional optical lattice", Physical review letters **93**, 240402 (2004).

[89]M Krämer, C Tozzo, and F. Dalfovo, "Parametric excitation of a bose-einstein condensate in a one-dimensional optical lattice", Physical Review A **71**, 061602 (2005).

[90]P. Engels, C. Atherton, and M. Hoefer, "Observation of faraday waves in a bose-einstein condensate", Physical review letters **98**, 095301 (2007).

[91]S. Pollack, D Dries, R. Hulet, K. M. F. Magalhães, E. Henn, E. Ramos, M. Caracanhas, and V. S. Bagnato, "Collective excitation of a bose-einstein condensate by modulation of the atomic scattering length", Physical Review A **81**, 053627 (2010).

[92]J. Nguyen, M. Tsatsos, D Luo, A. Lode, G. D. Telles, V. S. Bagnato, and R. Hulet, "Parametric excitation of a bose-einstein condensate: from faraday waves to granulation", Physical Review X **9**, 011052 (2019).

[93]Z. Zhang, K.-X. Yao, L. Feng, J. Hu, and C. Chin, "Pattern formation in a driven bose-einstein condensate", Nature Physics **16**, 652–656 (2020).

[94]A. I. Nicolin, R Carretero-González, and P. Kevrekidis, "Faraday waves in bose-einstein condensates", Physical Review A **76**, 063609 (2007).

[95]C.-L. Hung, V. Gurarie, and C. Chin, "From cosmology to cold atoms: observation of sakharov oscillations in a quenched atomic superfluid", Science **341**, 1213–1215 (2013).

[96]R. Cominotti, "Experiments with coherently-coupled bose-einstein condensates: from magnetism to cosmology", PhD thesis (University of Trento, 2023).

[97]P. O. Fedichev and U. R. Fischer, "Cosmological quasiparticle production in harmonically trapped superfluid gases", Physical Review A **69**, 033602 (2004).

[98]V. S. Barroso, A. Geelmuyden, Z. Fifer, S. Erne, A. Avgoustidis, R. J. Hill, and S. Weinfurtner, "Primary thermalisation mechanism of early universe observed from faraday-wave scattering on liquid-liquid interfaces", arXiv preprint arXiv:2207.02199 (2022).

[99]L. Kofman, A. Linde, and A. A. Starobinsky, "Reheating after inflation", Physical Review Letters **73**, 3195 (1994).

[100]L. Kofman, A. Linde, and A. A. Starobinsky, "Towards the theory of reheating after inflation", Physical Review D **56**, 3258 (1997).

[101]A. Zenesini, A. Berti, R. Cominotti, C. Rogora, I. G. Moss, T. P. Billam, I. Carusotto, G. Lamporesi, A. Recati, and G. Ferrari, "False vacuum decay via bubble formation in ferromagnetic superfluids", Nature Physics, 1–6 (2024).

[102]C. Qu, M. Tylutki, S. Stringari, and L. P. Pitaevskii, "Magnetic solitons in rabi-coupled bose-einstein condensates", Physical Review A **95**, 033614 (2017).

[103]X. Antoine, A. Levitt, and Q. Tang, "Efficient spectral computation of the stationary states of rotating bose-einstein condensates by preconditioned nonlinear conjugate gradient methods", Journal of Computational Physics **343**, 92–109 (2017).

[104]A. Sinatra, C. Lobo, and Y. Castin, "The truncated wigner method for bose-condensed gases: limits of validity and applications1", Journal of Physics B: Atomic, Molecular and Optical Physics **35**, 3599 (2002).

[105]N. P. Proukakis, S. A. Gardiner, M. Davis, and M. Szymanska, *Quantum gases: finite temperature and non-equilibrium dynamics*, Vol. 1 (World Scientific, 2013).

[106]T. Bienaimé, E. Fava, G. Colzi, C. Mordini, S. Serafini, C. Qu, S. Stringari, G. Lamporesi, and G. Ferrari, "Spin-dipole oscillation and polarizability of a binary bose-einstein condensate near the miscible-immiscible phase transition", Physical Review A **94**, 063652 (2016).

[107]E. Fava, T. Bienaimé, C. Mordini, G. Colzi, C. Qu, S. Stringari, G. Lamporesi, and G. Ferrari, "Observation of spin superfluidity in a bose gas mixture", Physical Review Letters **120**, 170401 (2018).

[108]A Farolfi, D Trypogeorgos, C Mordini, G Lamporesi, and G Ferrari, "Observation of magnetic solitons in two-component bose-einstein condensates", Physical Review Letters **125**, 030401 (2020).

[109]A. Farolfi, D. Trypogeorgos, G. Colzi, E. Fava, G. Lamporesi, and G. Ferrari, "Design and characterization of a compact magnetic shield for ultracold atomic gas experiments", Review of Scientific Instruments **90** (2019).

[110]S Stringari, "Dynamics of bose-einstein condensed gases in highly deformed traps", Physical Review A **58**, 2385 (1998).

[111]M. Visser, "Hawking radiation without black hole entropy", Physical Review Letters **80**, 3436 (1998).

[112]P.-É. Larré, A Recati, I. Carusotto, and N Pavloff, "Quantum fluctuations around black hole horizons in bose-einstein condensates", Physical Review A **85**, 013621 (2012).

[113]C. Chin, R. Grimm, P. Julienne, and E. Tiesinga, "Feshbach resonances in ultracold gases", Reviews of Modern Physics **82**, 1225 (2010).

[114]L. Fernandes, "Fluctuations in multicomponent quantum fluids", PhD thesis (University of Antwerp, 2024).

[115]M Isoard and N Pavloff, "Departing from thermality of analogue hawking radiation in a bose-einstein condensate", Physical Review Letters **124**, 060401 (2020).

[116]A. Coutant, A. Fabbri, R. Parentani, R. Balbinot, and P. R. Anderson, "Hawking radiation of massive modes and undulations", Physical Review D **86**, 064022 (2012).

[117]L. C. Crispino, A. Higuchi, E. S. Oliveira, and J. V. Rocha, "Greybody factors for nonminimally coupled scalar fields in schwarzschild–de sitter spacetime", Physical Review D **87**, 104034 (2013).

[118]P. Kanti, T. Pappas, and N. Pappas, "Greybody factors for scalar fields emitted by a higher-dimensional schwarzschild–de sitter black hole", Physical Review D **90**, 124077 (2014).

[119]C. Mayoral, A. Recati, A. Fabbri, R. Parentani, R. Balbinot, and I. Carusotto, "Acoustic white holes in flowing atomic bose–einstein condensates", New Journal of Physics **13**, 025007 (2011).

[120]G. Jannes, T. G. Maïssa Philippe and, and G. Rousseaux, "Hawking radiation and the boomerang behavior of massive modes near a horizon", Physical Review D **83**, 104028 (2011).

[121]L. Giacomelli and I. Carusotto, "Understanding superradiant phenomena with synthetic vector potentials in atomic bose-einstein condensates", Physical Review A **103**, 043309 (2021).

[122]W. E. East and F. Pretorius, "Superradiant instability and backreaction of massive vector fields around kerr black holes", Physical review letters **119**, 041101 (2017).

[123]G. Moschidis, "A proof of friedman's ergosphere instability for scalar waves", Communications in Mathematical Physics **358**, 437–520 (2018).

[124]Z. Zhong, V. Cardoso, and E. Maggio, "Instability of ultracompact horizonless spacetimes", Physical Review D **107**, 044035 (2023).

[125]N. Sanchis-Gual, J. C. Degollado, P. J. Montero, J. A. Font, and C. Herdeiro, "Explosion and final state of an unstable reissner-nordström black hole", Physical review letters **116**, 141101 (2016).

[126]P. Bosch, S. R. Green, and L. Lehner, "Nonlinear evolution and final fate of charged anti–de sitter black hole superradiant instability", Physical Review Letters **116**, 141102 (2016).

[127]T. J. Zouros and D. M. Eardley, "Instabilities of massive scalar perturbations of a rotating black hole", Annals of physics **118**, 139–155 (1979).

[128]S. Detweiler, "Klein-gordon equation and rotating black holes", Physical Review D **22**, 2323 (1980).

[129]L. A. Oliveira, L. J. Garay, and L. C. Crispino, "Ergoregion instability of a rotating quantum system", Physical Review D **97**, 124063 (2018).

[130]A. L. Fetter and A. A. Svidzinsky, "Vortices in a trapped dilute bose-einstein condensate", Journal of Physics: Condensed Matter **13**, R135 (2001).

[131]A. L. Fetter, "Rotating trapped bose-einstein condensates", Reviews of Modern Physics **81**, 647 (2009).

[132]P. Fedichev and G. Shlyapnikov, "Dissipative dynamics of a vortex state in a trapped bose-condensed gas", Physical Review A **60**, R1779 (1999).

[133]D. Rokhsar, "Vortex stability and persistent currents in trapped bose gases", Physical review letters **79**, 2164 (1997).

[134]P. Kuopanportti, S. Bandyopadhyay, A. Roy, and D Angom, "Splitting of singly and doubly quantized composite vortices in two-component bose-einstein condensates", Physical Review A **100**, 033615 (2019).

[135]F Manni, K. Lagoudakis, T. Liew, R. André, V Savona, and B Deveaud, "Dissociation dynamics of singly charged vortices into half-quantum vortex pairs", Nature communications **3**, 1–7 (2012).

[136]S. W. Seo, S. Kang, W. J. Kwon, and Y.-i. Shin, "Half-quantum vortices in an antiferromagnetic spinor bose-einstein condensate", Physical Review Letters **115**, 015301 (2015).

[137]S. Basak and P. Majumdar, "Superresonance from a rotating acoustic black hole", Classical and Quantum Gravity **20**, 3907 (2003).

[138]M. Jacquet, T Boulier, F Claude, A Maître, E Cancellieri, C. Adrados, A Amo, S Pigeon, Q Glorieux, A Bramati, et al., "Polariton fluids for analogue gravity physics", Philosophical Transactions of the Royal Society A **378**, 20190225 (2020).

[139]S. Patrick, A. Geelmuyden, S. Erne, C. F. Barenghi, and S. Weinfurtner, "Origin and evolution of the multiply quantized vortex instability", Physical Review Research **4**, 043104 (2022).

[140]J. De Nova, S Finazzi, and I Carusotto, "Time-dependent study of a black-hole laser in a flowing atomic condensate", Physical Review A **94**, 043616 (2016).

[141]T. Ikeda, R. Brito, and V. Cardoso, "Blasts of light from axions", Physical Review Letters **122**, 081101 (2019).

[142]K. W. Madison, F. Chevy, W. Wohlleben, and J. Dalibard, "Vortex formation in a stirred bose-einstein condensate", Physical review letters **84**, 806 (2000).

[143]M. Tolosa-Simeón, A. Parra-López, N. Sánchez-Kuntz, T. Haas, C. Viermann, M. Sparn, N. Liebster, M. Hans, E. Kath, H. Strobel, M. K. Oberthaler, and S. Floerchinger, "Curved and expanding spacetime geometries in bose-einstein condensates", Phys. Rev. A **106**, 033313 (2022).

[144]N. Tetradis, "Black holes and higgs stability", Journal of Cosmology and Astroparticle Physics **2016**, 036 (2016).

[145]G. Lagnese, F. M. Surace, M. Kormos, and P. Calabrese, "False vacuum decay in quantum spin chains", Physical Review B **104**, L201106 (2021).

[146]F. Devoto, S. Devoto, L. Di Luzio, and G. Ridolfi, "False vacuum decay: an introductory review", Journal of Physics G: Nuclear and Particle Physics (2022).

[147]A. R. Brown and E. J. Weinberg, "Thermal derivation of the coleman-de luccia tunneling prescription", Physical Review D **76**, 064003 (2007).

[148]J. Braden, M. C. Johnson, H. V. Peiris, A. Pontzen, and S. Weinfurtner, "Erratum: new semiclassical picture of vacuum decay [phys. rev. lett. 123, 031601 (2019)]", Physical Review Letters **129**, 059901 (2022).

[149]J. Braden, M. C. Johnson, H. V. Peiris, A. Pontzen, and S. Weinfurtner, "Mass renormalization in lattice simulations of false vacuum decay", Physical Review D **107**, 083509 (2023).

[150]D. Szász-Schagrin and G. Takács, "False vacuum decay in the $(1 + 1)$-dimensional φ^4 theory", Physical Review D **106**, 025008 (2022).

Acknowledgements

One might think that a PhD Thesis is mainly the product of its author's effort. But, if there is one thing I have learned in the past three years, it is that scientific research is always the result of teamwork. Therefore, I cannot conclude without mentioning the many people (both colleagues and non-physicists) whose support and collaboration have been essential to my personal and professional growth throughout my academic journey.

I owe my deepest and most sincere gratitude:

To Iacopo, for guiding me in the exciting world of scientific research since my undergraduate studies and for continuously stimulating me with new challenges along the way. His contagious enthusiasm for physics is second only to his unmatched ability to draw connections between seemingly unrelated fields, which has often amazed me and deepened my understanding of the problem at hand.

To Gabriele and the whole experimental group of the BEC Center (especially Giacomo, Alessandro, Arturo, Riccardo and Chiara) for letting me in their lab, and for trusting my numerical simulations more than I did myself.

To all the theoretical physicists (both internal and external colleagues) I have had the pleasure to work with: Alessio, who first explained to me the idea behind analog gravity, as well as Luca, Lennart, Giulio, Alberto, Jeff, Prof. Ian Moss and many more. Without their help, I could not have completed this Thesis.

To my fellow doctoral students, with whom I have shared the good and the bad of a wannabe physicist's life amidst aperitifs, climbing lessons, and volleyball matches.

To my friends, especially the ones I can count in this category despite the long-distance, who have distracted me from work through several (anti)social activities, thus preserving my mental health during the past years. Thanks for bearing with my weirdest obsessions, from sunsets to cliffs to chocolate, and for all the first times together.

To my family, for their unconditional support and for being there to celebrate all my achievements, despite having no idea of what I am doing. In my sister's words:

Sara: "What do you do for a living?"
Anna: "I am a researcher"
Sara: "And what are you looking for? The missing DNA?"

And lastly, to Toni, for being the most loyal companion during the writing process. And for all the biscuits.

Ringraziamenti

Verrebbe da pensare che il contenuto di una tesi di dottorato sia il prodotto del lavoro dell'autore. Ma, se c'è una cosa che ho imparato in questi ultimi tre anni, è che la ricerca scientifica è lavoro di squadra: non mi resta quindi che ricordare le molte persone (colleghi e non) senza il cui sostegno e collaborazione non avrei potuto completare questa tesi e che hanno contribuito alla mia crescita non soltanto a livello professionale, ma anche personale.

Un ringraziamento speciale va quindi:

A Iacopo, per avermi fatto da guida nel mondo della ricerca fin dalla tesi di laurea magistrale e per avermi sempre stimolato con nuove sfide durante questo percorso. Il suo entusiasmo contagioso per la fisica è superato soltanto alla sua impareggiabile abilità di vedere i collegamenti più originali fra sistemi diversi, che spesso mi ha lasciata di stucco, e con una comprensione molto più ricca della materia.

A Gabriele e tutto il gruppo sperimentale del centro BEC (in particolare Giacomo, Alessandro, Arturo, Riccardo e Chiara) per avermi accolto nel loro laboratorio e per essersi fidati delle mie simulazioni più di quanto lo facessi io.

A tutti i colleghi teorici (interni ed esterni al gruppo BEC) con cui ho avuto il piacere di collaborare e senza il cui contributo la mia conoscenza della fisica discussa in questa tesi sarebbe decisamente più povera e superficiale: Alessio, che per primo mi ha introdotto al campo della gravità analoga, ma anche Luca, Lennart, Giulio, Alberto, Jeff, il prof. Ian Moss, e non solo.

Ai compagni dottorandi, che, fra aperitivi, sedute di arrampicata e partite di pallavolo, hanno condiviso con me le gioie e i dolori della vita da aspiranti fisici.

Agli amici, specialmente a quelli che lo sono rimasti anche a distanza, per avermi distratto dal lavoro contribuendo così a preservare la mia vita (anti)sociale e la mia sanità mentale in questi anni. Grazie di assecondare le mie ossessioni più disparate, dai tramonti ai precipizi al cioccolato, e per tutte le prime volte insieme.

Alla mia famiglia, per aver supportato incondizionatamente le mie scelte e festeggiato i miei traguardi nonostante non abbiano idea di cosa io stia facendo. Per dirlo con le parole di mia sorella:

Lei: "Mi spieghi che cosa fai tu di lavoro?"
Io: "Faccio ricerca"
Lei: "E che cosa cerchi? Il DNA scomparso?"

E infine, a Toni, per la strenua compagnia nella scrittura di questa tesi. E per tutti i biscotti.

Anna